UNIVERSITY OF LONDON THESIS

Degree PhD Year 2007 Name of Author NGIAM, Shi Shong

The Influence of Surface Residual Stress On Fatigue Crack Growth

Shi Song Ngiam

Submitted for the Degree of
Doctor of Philosophy

Department of Mechanical Engineering
University College London

March 2007

ProQuest LLC
789 East Eisenhower Parkway
P.O. Box 1346
Ann Arbor, MI 48106-1346

DECLARATION

I declare that:

This submission is entirely my own work. Any uses made within it of the works of other authors in any form, wherever published, unpublished, printed, electronic or other information sources have been used as a contribution or component of this work, these are explicitly, clearly and individually acknowledged by appropriate use of quotation marks, citations, references and statements in text. A full list of the references employed is included.

SIGNATURE:

DATE: 06/07/07

ABSTRACT

Residual stress exists in most structures and although it has been recognised for a long time, its complex mechanism and characteristics are still being intensively studied. Residual stress can be stratified into damaging residual stress and beneficial residual stress. Surface tensile residual stresses are generally known to reduce the mechanical properties of materials while compressive residual stresses improve the fatigue performance of components. This Ph.D. thesis reports the analytical and experimental work conducted to investigate both the damaging and beneficial effects of residual stress on fatigue crack growth in structural components.

The detrimental effect of tensile residual stresses is studied through large scale fatigue testing of T-butt welded plates fabricated from High Strength Steels (HSS). Despite the growing use of HSSs in the offshore industry, the fatigue performance and corrosion resistance of welded joints made from such steels are still not clear. Due to their complex metallurgy and relatively poor weldability, there is still a lack of understanding of the residual stresses that arise from the welding process. This study involved modification and development conducted on a variable amplitude (VA) load-time sequence generator for the investigation of long life fatigue performance of HSS. Emphasis was given to the generation of a stationary load-time history and numerous analyses were presented to demonstrate the importance of the long term statistical nature of the load-time sequence on fatigue testing. Fatigue test results obtained were extensively compared with previous HSS corrosion fatigue studies. The effect of tensile residual stress on fatigue crack growth was investigated using a SIF weight function-based fatigue crack growth model.

Two newly developed preferential cold working techniques termed *stitch cold rolling* and *stitch shot peening* were explored to investigate the beneficial effect of surface compressive residual stress on fatigue crack growth in mild steel plates. One of the main objectives of this study was to control the fatigue crack shape by the manipulation of surface residual stress fields. The stitch cold rolling technique was implemented using a custom-built cold rolling jig. The feasibility of preferential cold working techniques was further investigated by the fatigue testing of stitch shot peened specimens. Both experimental programmes yielded unprecedented fatigue crack growth results. A residual stress monitoring programme was conducted to study the residual stress relaxation behaviour under cyclic loading. The experimental test results enabled the investigation of SIF solutions in non-uniform stress fields. A novel fatigue crack growth evolution model, which takes into account residual stress relaxation effects, was developed using the powerful SIF weight function methods.

ACKNOWLEDGEMENTS

First of all, I wish to acknowledge the continuous supervision and support provided by Professor Feargal Brennan and Professor Bill Dover throughout this Ph.D. study. I would like to express my deep and sincere gratitude to Feargal for being an excellent mentor and providing the opportunity to pursue such an inspiring research topic. His constant encouragement and tireless personal guidance have provided a good basis for the present study.

I would like to take this opportunity to thank my parents, sister and brother, for their continued love and support. I am deeply indebted to my parents and I am very grateful for their endless patience and understanding throughout these years. I wish to thank my sister, Sheau Huey, for her golden advice and help whenever I needed them.

I wish to express my sincere gratitude to Emily for always being there for me. Your loving support and help have been priceless and they will always be remembered.

Special thanks go to all my colleagues at the NDE Centre, especially Abdul, Amir, Andy, Bart, Bello, Bijan and Tanya. It has been a pleasure working with you guys and I will always remember those tedious but extremely rewarding days in the laboratory. The completion of this study would be impossible without your assistance. To Amir, Andy and Bijan, I will always miss those fruitful and constructive discussion sessions. I warmly thank Bart for being such a good friend and your advice and help have been invaluable.

I sincerely express my gratefulness to Metal Improvement Company for their first-rate advice and assistance on the shot peening work.

I would also like to thank the hall of residence team at Goldsmid House for their support.

Last but not least I wish to thank my colleagues at the Department of Mechanical Engineering. Credits must be given to Charlotte and Margaret for being ever so helpful. My thanks go to all the workshop technicians especially Terry, Neil and Phil for providing the valuable technical assistance.

TABLE OF CONTENTS

DECLARATION 2

ABSTRACT 3

ACKNOWLEDGEMENTS 4

TABLE OF CONTENTS 5

LIST OF TABLES 11

LIST OF FIGURES 13

NOMENCLATURE 20

CHAPTER 1

1.0 Introduction and Background 25

1.1 Introduction 25

1.2 Stress Life (*S-N*) Approach 27

1.2.1 The Implications of Other Factors on Fatigue Endurance 29

1.2.1.1 Thickness Effects 29

1.2.1.2 Environmental Effects 31

1.3 Fracture Mechanics Approach 33

1.3.1 Linear Elastic Fracture Mechanics (LEFM) 33

1.3.2 The Stress Intensity Factor (SIF) 34

1.3.3 Fatigue Crack Growth and The SIF 35

1.3.4 SIF Solutions 37

1.3.5 Calculation of SIFs Using Weight Functions 39

1.4 Residual Stress 43

1.4.1 Sources of Residual Stress 45

1.4.1.1 Welding 45

1.4.1.2 Cold Rolling 47

1.4.1.3 Shot Peening 48

1.4.2 Measurement of Residual Stress 50

1.4.2.1 Neutron Diffraction Methods 53

1.4.2.2 The Hole-Drilling Methods 55
1.4.3 Residual Stress Relaxation Due to Cyclic Loading 58
1.5 Summary and Overview of Thesis 62
1.6 References 64

CHAPTER 2

2.0 Variable Load-Time History Generation **73**
2.1 Introduction 73
2.2 Service Load Simulation for Fatigue Testing 74
2.2.1 Parameters in a Wave Loading Model 74
2.2.2 Standardised Load-Time Histories for Offshore Structures 76
2.3 Jack-up Offshore Standard load History (JOSH) 78
2.3.1 Operation of JOSH Sequence Generator 80
2.4 Analysis of Generated Sequences 81
2.4.1 Basic Parameters of the JOSH Sequence 83
2.4.2 Stationary Point 85
2.4.3 Equivalent Stress Range (ESR) 86
2.4.4 Power Spectrum Density 89
2.4.5 Sub-block Duration 92
2.4.6 Starting Sea states 93
2.5 Summary 99
2.6 References 99

CHAPTER 3

3.0 Variable Amplitude Corrosion Fatigue (VACF) Testing of High Strength Steel **103**
3.1 Introduction 103
3.2 Corrosion Fatigue of Offshore Structures 104
3.2.1 Hydrogen Embrittlement in HSSs 105
3.2.2 Effect of Cathodic Protection on Fatigue Crack Growth 106

3.3 Residual Stresses in Welded Joints 108
3.3.1 Residual Stress Distributions in Welded Joints 109
3.3.2 Residual Stress Measurements in T-butt Welded Plates Using a Neutron Diffraction Technique 113
3.4 Experimental Test Details 117
3.4.1 Test Specimens 117
3.4.2 Fatigue Test Set-up 119
3.4.3 Test Control and Data Acquisition 120
3.4.4 Simulation of Environmental Conditions 122
3.5 Fatigue Test Results 123
3.5.1 *S-N* Data 123
3.5.2 Fatigue Crack Growth Data 126
3.5.3 Crack Shape Evolution Data 129
3.6 Discussion of Fatigue Test Results 133
3.6.1 Fatigue Life 133
3.6.2 Fatigue Crack Growth 136
3.7 Fracture Mechanics Analysis of Fatigue Test Results 138
3.7.1 Fatigue Crack Growth Rate in VA Loading 138
3.7.2 Experimental Stress Intensity Factors 139
3.7.2.1 SIF Prediction for a Surface Crack in a T-butt Welded Plate 139
3.7.2.2 SIF Prediction for an Edge Crack in a T-butt Welded Plate 143
3.7.2.3 Inclusion of Surface Tensile Residual Stress Fields into SIF Predictions .. 145
3.7.3 Discussion of Fatigue Crack Growth Rate Results 148
3.8 Summary 159
3.9 References 159

CHAPTER 4

4.0 Experimental Investigation of Fatigue Crack Shape Evolution in Residual Stress Fields **165**
4.1 Introduction 165
4.2 The Significance of Fatigue Crack Shape on Crack Propagation 166

4.3 Fatigue Crack Shape Control Using Stitch Cold Rolling 168
4.4 Experimental Test Details 170
4.4.1 Test Specimens 170
4.4.2 Stitch Cold Rolling Parameters 172
4.4.3 Fatigue Test Set-up 175
4.5 Fatigue Test Results 176
4.5.1 Fatigue Crack Initiation Data 177
4.5.2 Fatigue Crack Growth Data 178
4.5.3 Crack Shape Evolution Data 182
4.5.4 Fatigue Crack Surfaces 185
4.6 Discussion of Results 187
4.7 Summary 191
4.8 References 192

CHAPTER 5

5.0 Fatigue Crack Shape Control Using Stitch Shot Peening 195
5.1 Introduction 195
5.2 Stitch Cold Rolling versus Stitch Shot Peening 196
5.3 Experimental Test Details 197
5.3.1 Test Specimens 197
5.3.2 Stitch Shot Peening Parameters 198
5.3.3 Fatigue Test Set-up 200
5.3.4 Residual Stress Monitoring Using the ICHD Technique 203
5.4 Fatigue Test Results 205
5.4.1 Fatigue Crack Growth Data 205
5.4.2 Crack Shape Evolution Data 211
5.4.3 Fatigue Crack Surfaces 213
5.5 Discussion of Fatigue Test Results 216
5.6 Summary 218
5.7 References 219

CHAPTER 6

6.0 Development of a SIF Weight Function-Based Fatigue Crack Growth Evolution Prediction Model for Stitch Shot Peened Specimens 221

6.1 Introduction 221

6.2 Residual Stress Analyses 222

6.2.1 The Equivalent Uniform Stress Method 222

6.2.2 The Integral Method 228

6.2.3 The Strain Hardening Effect Induced by Shot Peening 233

6.2.4 Residual Stress Relaxation Data 237

6.3 A SIF Weight Function-Based Fatigue Crack Growth Prediction Model 239

6.3.1 Compact Tension (CT) Tests 239

6.3.1.1 CT Test Details 239

6.3.1.2 CT Test Results 240

6.3.2 Incorporation of the Residual Stress Data into the Fatigue Crack Growth Evolution Model 243

6.3.3 SIF Weight Functions for Flat Plate Surface Cracks 245

6.3.4 Discussion 249

6.4 Summary 254

6.5 References 255

CHAPTER 7

7.0 Conclusions and Recommendations for Future Work 260

7.1 Conclusions 260

7.1.1 JOSH and VACF of SE 702 260

7.1.2 Residual Stresses in T-butt Welded Joints 261

7.1.3 Preferential Cold Working Methods 262

7.1.4 Residual Stress Monitoring and Analyses 263

7.1.5 Surface Crack Growth Evolution Prediction Using a SIF Weight Function-Based Method 264

7.2 Summary of Main Conclusions and Findings 264

7.3 Recommendations for Future Work 265
7.4 References 267

APPENDICES

Appendix A **268**
Appendix B **270**
Appendix C **275**
Appendix D **277**
Appendix E **280**
Appendix F **285**
Appendix G **288**
Appendix H **291**
Appendix J **296**
Appendix K **298**

LIST OF TABLES

CHAPTER 1

Table 1.1 : Comparison of the residual stress measurement techniques 52

CHAPTER 2

Table 2.1 : Statistic and fatigue damage data for simulated North Sea condition proposed by Wirsching 77
Table 2.2 : Sea state data proposed by WASH 77
Table 2.3 : Sea states data employed in JOSH 83
Table 2.4 : Sea states transition matrix for 10 minutes sub-block 84
Table 2.5 : Percentage of occurrence of sea states for different sub-block durations 93
Table 2.6 : Distribution of sea states of JOSH sequence with different starting sea state 96
Table 2.7 : Distribution of sea states with 12 different starting sea state obtained from Reference 2.27 97

CHAPTER 3

Table 3.1 : Summary of weld parameters 113
Table 3.2 : Quoted chemical composition and mechanical properties of SE 702 118
Table 3.3 : JOSH sequence parameters 119
Table 3.4 : Summary of fatigue test parameters 120
Table 3.5 : Summary of fatigue test results and durations 124
Table 3.6 : Comparison of fatigue life with BS EN 10025 Grade S355J2G3 124
Table 3.7 : The Paris material coefficients for SE 702 155
Table 3.8 : Comparison between experimental and predicted fatigue crack propagation lives 156

CHAPTER 4

Table 4.1 : Chemical composition and mechanical properties of BS EN 10025 S275JR steel 171
Table 4.2 : Dimensions of original and cold rolled notch 171

Table 4.3 : Test specimen details 174
Table 4.4 : Summary of fatigue test results 176

CHAPTER 5

Table 5.1 : Comparison of the stitch cold rolling and stitch shot peening technique 196
Table 5.2 : Summary of stitch shot peening parameters 199
Table 5.3 : Summary of fatigue pre-cracking data 206
Table 5.4 : Summary of fatigue test results 206

CHAPTER 6

Table 6.1 : Measured Vicker's diamond hardness data 235
Table 6.2 : Estimate of the material's yield strength from hardness data 235

LIST OF FIGURES

CHAPTER 1

Figure 1.1 : Stress gradient in a T-butt welded joint for different plate thickness 30

Figure 1.2 : *S-N* design curves for T-butt welded plates in different environmental conditions 32

Figure 1.3 : The three modes of crack opening 34

Figure 1.4 : Schematic sigmoidal behaviour of fatigue crack growth rate versus ΔK 36

Figure 1.5 : Newman-Raju normalised SIFs under bending for $a/c = 0.2$ 38

Figure 1.6 : Normalised weld toe SIFs under bending obtained using Brennan et al [1.32] parametric equations 38

Figure 1.7 : Crack loaded by body tractions 39

Figure 1.8 : Stress distribution along a crack 40

Figure 1.9 : Principle of the Niu-Glinka weight function composition technique 42

Figure 1.10 : Superimposition of residual stress 44

Figure 1.11 : Formation of residual stress as a result of welding: (a) Natural longitudinal shrinkage of unrestrained (unattached) weld; (b) Longitudinal shrinkage of restrained weld 46

Figure 1.12 : Induced residual stress in welded joint: (a) Longitudinal residual stress; (b) Transverse residual stress 46

Figure 1.13 : (a) Cold rolling process (b) Material thickness reduction after cold rolling 47

Figure 1.14 : Residual stress generation mechanism during cold rolling 48

Figure 1.15 : Simple illustration of the mechanism of shot peening 49

Figure 1.16 : Popularity of residual stress measurement techniques [1.64] 51

Figure 1.17 : Typical set-up of a neutron diffractometer 55

Figure 1.18 : (a) Centre-hole-drilling technique (b) Ring-core technique 56

Figure 1.19 : The RS-200 Milling guide used in the incremental centre-hole-drilling technique 57

Figure 1.20 : (a) Induction of residual stress by cold rolling; (b) Proof loading; (c) Relaxation of residual stress 58

CHAPTER 2

Figure 2.1 : A typical wave loading power spectrum 75

Figure 2.2 : A typical jack-up platform (Texas Pride, Gulf of Mexico, USA) 78

Figure 2.3 : A simplified two-dimensional model of jack-up platform 80
Figure 2.4 : Summary of the load-time history generation of JOSH 82
Figure 2.5 : Power spectra for the 8 sea states used in JOSH 84
Figure 2.6 : A 32-point power spectrum used in JOSH 84
Figure 2.7 : Variable amplitude load-time sequence generated using JOSH 86
Figure 2.8 : Sea state distributions for the entire sequence 86
Figure 2.9 : Stress range distribution obtained using rainflow cycle counting 87
Figure 2.10 : Convergence of the ESR 87
Figure 2.11 : Load-time history plot of the JOSH sequence used in Reference 2.27 88
Figure 2.12 : Percentage error in ESR of JOSH sequence for different sequence duration 88
Figure 2.13 : Percentage error in the normalised power density for the dominant frequency of the sequence 90
Figure 2.14 : Power spectral density for one complete JOSH sequence 90
Figure 2.15 : Convergence of the JOSH power spectrum 91
Figure 2.16 : Percentage error in normalised PSD of the dominant frequency in the JOSH sequence 91
Figure 2.17 : Stress range distribution for different sequence length 92
Figure 2.18 : Finalised transition matrix for the 8 sea states used in the JOSH sequence 94
Figure 2.19 : Real-time sea state occurrences for JOSH sequence 94
Figure 2.20 : Load-time history plots of the JOSH sequence with 8 different starting sea state 95
Figure 2.21 : Load-time history plots of the JOSH sequence with 12 different starting sea state obtained from Tantbirojn's study [2.27] 96
Figure 2.22 : ESR of the JOSH sequence with different starting sea state 98
Figure 2.23 : Percentage difference in ESR of the JOSH sequence with different starting sea state 98
Figure 2.24 : Stress range distributions of the JOSH sequence with different starting sea state 99

CHAPTER 3

Figure 3.1 : Directions of residual stresses in a T-butt welded plate 108
Figure 3.2 : Recommended transverse residual stress distributions 111
Figure 3.3 : Longitudinal through-thickness residual stress distributions 114
Figure 3.4 : Normal through-thickness residual stress distributions 115
Figure 3.5 : Transverse through-thickness residual stress distributions 115

Figure 3.6 : Normalised transverse residual stress distributions of SE 702 and S355J2G3 116
Figure 3.7 : Comparison of normalised transverse residual stress distributions 117
Figure 3.8 : Detail dimensions of T-butt welded specimens 118
Figure 3.9 : Samples of weld toe SCFs 118
Figure 3.10 : Test set-up on the Instron 1000kN fatigue test machine 120
Figure 3.11 : (a) U10 Crack Microgauge (b) Spot-welded ACPD probes and (c) Figure showing an array of spot-welded ACPD probes on a T-butt test specimen 121
Figure 3.12 : Environment chamber and impressed current cathodic protection set-up for corrosion fatigue tests 122
Figure 3.13 : S-N plots of experimental data and Class P Design Curves 125
Figure 3.14 : Fatigue crack growth data for Test 1 126
Figure 3.15 : Fatigue crack growth data for Test 2 126
Figure 3.16 : Fatigue crack growth data for Test 3 127
Figure 3.17 : Fatigue crack growth data for Test 4 127
Figure 3.18 : Fatigue crack growth data for Test 5 128
Figure 3.19 : Fatigue crack growth data for all tests 128
Figure 3.20 : Early crack shape evolution data for Test 2 130
Figure 3.21 : Early crack shape evolution data for Test 3 130
Figure 3.22 : Crack shape evolution data for Test 1 131
Figure 3.23 : Crack shape evolution data for Test 2 131
Figure 3.24 : Crack shape evolution data for Test 3 132
Figure 3.25 : Crack shape evolution data for Test 4 132
Figure 3.26 : Crack shape evolution data for Test 5 133
Figure 3.27 : Comparison of experimental fatigue lives with results obtained from the study conducted by Tantbirojn 135
Figure 3.28 : Fatigue crack growth data obtained from Reference 3.23 137
Figure 3.29 : Fatigue crack growth data obtained from Reference 3.24 137
Figure 3.30 : A graphical illustration of Niu-Glinka's SIG weight function composition method 140
Figure 3.31 : Normalised full-field stress distribution ahead of the weld toe in a T-butt welded Plate under bending 142
Figure 3.32 : Normalised T-butt surface crack SIF prediction under bending using Niu-Glinka's [3.47] weight Function 143
Figure 3.33 : Normalised T-butt edge crack SIF prediction under bending using Niu-Glinka's [3.48] weight function 144
Figure 3.34 : Comparison of the T-butt weld toe normalised SIFs under bending 145

Figure 3.35 : Proposed tri-linear upper bound transverse residual stress distribution 146
Figure 3.36 : Expression of the transverse residual stress distribution using piecewise continuous linear function 146
Figure 3.37 : Normalised SIF prediction for an edge crack in a T-butt welded plate under bending with the inclusion of the surface tensile residual stress 147
Figure 3.38 : Normalised SIF predictions for semi-elliptical surface cracks in a T-butt welded plate under bending with the inclusion of the surface tensile residual stress..... 148
Figure 3.39 : Fatigue crack growth rate data analysed using Niu-Glinka T-butt welded plate surface crack (deepest point) weight function 151
Figure 3.40 : Fatigue crack growth rate data analysed using Niu-Glinka T-butt welded plate edge crack weight function 152
Figure 3.41 : Fatigue crack growth rate data analysed using Niu-Glinka T-butt weld toe semi-elliptical surface crack weight function with the incorporation of residual stress field 153
Figure 3.42 : Fatigue crack growth rate data analysed using Niu-Glinka T-butt weld toe edge crack weight function with the incorporation of residual stress..... 154
Figure 3.43 : Comparison of the fatigue crack growth rates data for all tests 157
Figure 3.44 : Comparison between the experimental and the predicted fatigue crack propagation lives 158

CHAPTER 4

Figure 4.1 : Newman & Raju normalised surface crack SIFs under tension for a/T = 0.4..... 166
Figure 4.2 : Newman & Raju normalised SIFs under tension for a/c = 0.2..... 167
Figure 4.3 : Newman & Raju normalised SIFs under bending for a/c = 0.2 168
Figure 4.4 : Crack aspect ratio (a/c) at failure: (a) High asepct ratio failure (b) Low aspect ratio failure..... 169
Figure 4.5 : BS EN 10025 Grade S275JR mild steel plate..... 170
Figure 4.6 : Geometry of test specimen machined-notch..... 170
Figure 4.7 : A 2D FE mesh of the notch root 172
Figure 4.8 : Determination of theoretical SCF using FEA..... 172
Figure 4.9 : Induced compressive residual stress during cold rolling..... 173
Figure 4.10 : Preferential cold working..... 173
Figure 4.11 : Stitch cold rolling set-up 173
Figure 4.12 : Roller used for stitch cold rolling..... 173
Figure 4.13 : Four point bending fatigue test set-up..... 175
Figure 4.14 : Early fatigue crack growth data for Test CR1..... 177

Figure 4.15 : Fatigue crack growth data for Test CR1 178
Figure 4.16 : Fatigue crack growth data for Test CR2 (unrolled length = 20mm) 179
Figure 4.17 : Fatigue crack growth data for Test CR3 (unrolled length = 40mm) 180
Figure 4.18 : Fatigue crack growth data for Test CR4 (unrolled length = 20mm) 180
Figure 4.19 : Fatigue crack growth data for Test CR5 (unrolled length = 20mm) 181
Figure 4.20 : Fatigue crack growth data for Test CR6 (unrolled length = 40mm) 181
Figure 4.21 : Fatigue crack growth data for all tests 182
Figure 4.22 : Crack shape evolution data for Test CR1 183
Figure 4.23 : Crack shape evolution data for Test CR2 183
Figure 4.24 : Crack shape evolution data for Test CR3 184
Figure 4.25 : Crack shape evolution data for Test CR4 184
Figure 4.26 : Crack shape evolution data for Test CR5 185
Figure 4.27 : Crack shape evolution data for Test CR6 185
Figure 4.28 : Fracture surfaces 186
Figure 4.29 : Comparison of fatigue propagation life for 40mm-thick specimens 188
Figure 4.30 : Comparison of fatigue propagation life for 20mm-thick specimens 189
Figure 4.31 : Crack aspect ratio evolution prediction using RMS SIF 190
Figure 4.32 : Crack aspect ratio evolution data for all stitch cold rolled specimens 191

CHAPTER 5

Figure 5.1 : BS EN 10025 Grade S275JR test specimen 198
Figure 5.2 : A quarter-symmetry 3-D finite element mesh of the test specimens 198
Figure 5.3 : An example of a stitch shot peened test specimen 200
Figure 5.4 : Shot peened bands on Test SP6 200
Figure 5.5 : Fatigue test set-up on the Instron 1000kN test machine 202
Figure 5.6 : Comparison between theoretical and experimental strain data 202
Figure 5.7 : Fatigue pre-cracking of test specimen 203
Figure 5.8 : Removal of dimple peaks on shot peened surfaces 204
Figure 5.9 : An example of ICHD set-up 205
Figure 5.10 : In-situ residual stress monitoring on Test SP6 205
Figure 5.11 : Crack initiation data for Test SP2 during fatigue pre-cracking 207
Figure 5.12 : Crack shape evolution data for Test SP2 during fatigue pre-cracking 207
Figure 5.13 : Fatigue crack growth data for Test SP5 208
Figure 5.14 : Fatigue crack growth data for Test SP1 209
Figure 5.15 : Fatigue crack growth data for Test SP2 209
Figure 5.16 : Fatigue crack growth data for Test SP3 210

Figure 5.17 : Fatigue crack growth data for Test SP4 210
Figure 5.18 : Comparison of fatigue crack growth data for Tests SP1 to SP4 211
Figure 5.19 : A through-thickness crack in Test SP3 211
Figure 5.20 : Crack shape evolution data for Test SP1 212
Figure 5.21 : Crack shape evolution data for Test SP2 212
Figure 5.22 : Crack shape evolution data for Test SP3 213
Figure 5.23 : Crack shape evolution data for Test SP4 213
Figure 5.24 : Crack shape evolution data for Test SP5 214
Figure 5.25 : Fracture surfaces 214
Figure 5.26 : Comparison of crack depth and crack length growth for Tests SP1 and SP2 217
Figure 5.27 : Comparison of crack aspect ratio evolution data 218

CHAPTER 6

Figure 6.1 : Schematic diagram showing a typical strain gauge rosette arrangement and the hole- drilling geometry used in the ICHD technique 223
Figure 6.2 : An example of the strain relaxation data obtained from the 3C-6C shot peened band prior to fatigue loading 224
Figure 6.3 : An example of the strain relaxation data obtained from the 12C-16C shot peened band prior to fatigue loading 224
Figure 6.4 : The principal residual stresses evaluated from the 12C-16C shot peened band prior to fatigue loading 225
Figure 6.5 : Residual stress data for the 12A-16A shot peened band (EUS Method) 226
Figure 6.6 : Residual stress data for the 3C-6C shot peened band (EUS Method) 227
Figure 6.7 : Residual stress data for the 12C-16C shot peened band (EUS Method) 227
Figure 6.8 : Comparison between the Rendler-Vigness percentage relieved-strain curves and the measured strain relaxation data 229
Figure 6.9 : An illustration of the main difference between the EUS Method and the Integral Method 230
Figure 6.10 : Comparison of the initial residual stress data analysed using the EUS Method and the Integral Method 232
Figure 6.11 : Residual stress data for the 3C-6C shot peened band (Integral Method) 232
Figure 6.12 : Residual stress data for the 12C-16C shot peened band (Integral Method) 233
Figure 6.13 : Residual stress relaxation data for the 3C-6C shot peened surface 238
Figure 6.14 : Residual stress relaxation data for the 12C-16C shot peened surface 238
Figure 6.15 : Examples of residual stress relaxation curves for an SAE 1045 steel [6.24] 239
Figure 6.16 : An example of the CT test set-up on an Instron 1251 100kN fatigue test

machine 240
Figure 6.17 : (a) Test CT1 (b) Fracture surfaces of Test CT1 241
Figure 6.18 : Fracture surfaces of (a) Test CT2 and (b) Test CT3 241
Figure 6.19 : Fatigue crack growth data for all CT tests 242
Figure 6.20 : Fatigue crack growth rate vs. SIF range for all CT tests 242
Figure 6.21 : Combined fatigue crack growth data of Tests CT1 to CT3 243
Figure 6.22 : Linear extrapolation of the sub-surface residual stresses to the plate's surface point 244
Figure 6.23 : Comparison of weight function-based SIFs with Newman-Raju [6.40] SIFs for deepest point of semi-elliptical cracks in a finite thickness plate under uniform tension 246
Figure 6.24 : Schematic flowchart of the crack growth evolution model 247
Figure 6.25 : Simulation of the stitch shot peening effect 248
Figure 6.26 : Fatigue crack growth prediction 250
Figure 6.27 : Half-crack length growth prediction 250
Figure 6.28 : Simulation of crack aspect ratio evolutions 251
Figure 6.29 : Comparison between the experimental and the simulated crack aspect ratio evolution 251
Figure 6.30 : Comparison between the experimental and the simulated fatigue crack propagation lives 252
Figure 6.31 : Illustration of the crack aspect ratio simulation data with and without residual stress relaxation effects 254
Figure 6.32 : Illustration of the fatigue crack propagation prediction data with and without residual stress relaxation effects 254

NOMENCLATURE

a	Crack depth
a'	Non-dimensional strain relaxation calibration coefficient
A	Area
A	Almen Intensity
A	Dimensionless calibration coefficient for hole-drilling residual stress analysis
A	Deepest point of a semi-elliptical surface crack
$A(H,h)$	Strain relaxation function
ACPD	Alternating Current Potential Difference
b	Plate half-width
b'	Non-dimensional strain relaxation calibration coefficient
B	Dimensionless calibration coefficient for hole-drilling residual stress analysis
B	Surface point of a semi-elliptical crack
B	Sub-block duration
c	Crack half-length
C	Empirical material constant in Paris Equation
C	Thermal expansion dependent material constant
C	Almen Intensity
CA	Constant amplitude
CLI	INDUSTEEL Creusot-Loire Industrie, France
CNC	Computer Numerical Control
COLOS	Common Load Sequence for the European Coal and Steel Community Research Programme
CP	Cathodic protection
CT	Compact Tension
d	Crystallographic planes separation in Bragg Equation
da/dN	Fatigue crack growth rate
D_m	Mean strain gauge grid centreline diameter
E	Young's Modulus of material
EUS	Equivalent Uniform Stress
E_1	Welding heat input rate
ESR	Equivalent stress range

f	Wave frequency
FE	Finite Element
FEA	Finite Element Analysis
FFT	Fast Fourier Transformation
h	Vector of a weight function
h	Non-dimensional hole-depth, z/r_m
H	Wave height
H	Non-dimensional depth from surface, Z/r_m
H_s	Significant wave height
HAZ	Heat Affected Zone
HSE	Health and Safety Executive (UK)
HSS	High Strength Steel
ICHD	Incremental centre-hole-drilling
IFT	Inverse Fourier Transformation
JOSH	Jack-up Offshore Standard load History
K	Stress intensity factor
K_1	Constant in *S-N* design curves
K_{appl}	Applied stress intensity factor
K_c	Fracture toughness
K_{eff}	Effective stress intensity factor
K_t	Stress concentration factor
l	Non-shot peened half-length
L	Markov-Chain/Monte Carlo feedback loop numerical parameter
L_1	Markov-Chain/Monte Carlo feedback loop numerical parameter
LEFM	Linear elastic fracture mechanics
LLCF	Long life corrosion fatigue
m	The slope of *S-N* curves
m	Empirical material constant in Paris Equation
m_0	Moment of power spectrum
m	Meyer's hardness exponent
M	Bending moment
M	Markov-Chain/Monte Carlo feedback loop numerical parameter
M_1	Markov-Chain/Monte Carlo feedback loop numerical parameter
$m(a,x)$	SIF weight function
MIC	Metal Improvement Company
MRS	Multiple Reference State
n	Integer (order of deflection) in Bragg's Equation

N	Number of fatigue cycles to failure in *S-N* approach
N	Number of fatigue cycles in linear elastic fracture mechanics
N	Almen Intensity
N	Number of stress cycles in the residual stress relaxation models
N_i	Fatigue crack initiation life
N_p	Fatigue crack propagation life
N_t	Total fatigue life
N_{t50}	S355 mean fatigue life
NDE	Non-Destructive Evaluation
NDT	Non-Destructive Testing
NPL	National Physics Laboratory
OTR	Offshore Technology Report
P	Probability in the Monte Carlo Method
PoD	Probability of Detection
PRBS	Pseudo-Random Binary Shift
PSD	Power spectrum density
$p(\Delta S)$	Probability density of the stress range, ΔS
q	Thickness exponent factor in *S-N* curve
q	Welding heat input
QB	Quick Basic®
r	Relaxation exponent in Landgraf Residual Stress Decay Equation
r_m	Strain gauge grid-centreline radius
r,θ	Polar co-ordinate systems
R	Stress-ratio
R_{max}	Maximum local stress-ratio
RMC	Root mean cube
RMS	Root mean square
S_B	Applied stress range
S355	BS EN 10025 Grade S355J2G3
SCC	Stress corrosion cracking
SCF	Stress concentration factor
SE 702	SUPERELSO 702
SIF	Stress intensity factor
S-N	Stress-life
T	Plate thickness
T	Stress vector
t	Plate thickness

t_B	Reference thickness of material in *S-N* curve
T_D	Sea state's dominant period
T_z	Sea state's zero crossing period
TSC	Technical Software Consultants
u	Displacement vector
$u(x,a)$	Crack opening displacement
U	Crack tip displacement
UEG	Underwater Engineering Group
UKOSRP	United Kingdom Offshore Steels Research Program
V	Voltage
VA	Variable amplitude
VACF	Variable amplitude corrosion fatigue
VMG	Vishay Micro-Measurements Group
w	Non-cold rolled length
W	Strain energy density
WASH	Wave Action Standard load History
WASR	Weighted average stress range
x	Distance
x	Through-thickness direction
x	Normal direction with respect to weldment
x	Rectangular co-ordinate of crack front
x_0	Size of yielded zone in weldment
y	Transverse direction with respect to weldment
y	Rectangular co-ordinate of crack front
Y	Geometry correction factor/Normalised stress intensity factor
z	Longitudinal direction with respect to weldment
Z	Hole-depth in the hole-drilling method
ΔK	Stress intensity factor range
ΔK_{th}	Threshold stress intensity factor range
ΔS	Applied stress range
$\Delta\varepsilon_{th}$	Threshold strain range in Landgraf residual stress decay model
Δ	ACPD probe spacing
α	Angle
θ	Angle
θ_0	Original angular position of the Bragg's deflection
ε	Elastic strain
ε_1	Strain relaxation reading obtained from gauge 1

ε_2	Strain relaxation reading obtained from gauge 2
ε_3	Strain relaxation reading obtained from gauge 3
η	Welding process efficiency
λ	Wavelength of incident beam in Bragg's Equation
μ	permeability of the material
ν	Poisson ratio
ρ	Weld toe radius
σ	Stress
σ_0	Reference stress magnitude
σ_m	Mean stress
σ_{max}	Maximum stress
σ_{max}	Maximum principal stress
σ_{min}	Minimum principal stress
σ_{nom}	Nominal stress
σ_R	Residual stress
σ_{Res}	Residual stress
$\sigma^{Re}{}_N$	Residual stress after *N*th cycle
$\sigma_{y0.2}$	0.2% proof stress of material
φ	Crack angle (radians)

CHAPTER 1

1.0 Introduction and Background

1.1 Introduction

Fatigue has been the archrival of engineers since its recognition during 1840s. Most material failures are caused by fatigue or at least intensely influenced by it [1.1] and it is said that fatigue causes at least 90 percent of failures in modern engineering components. Material fatigue costs the industry millions billions of pounds annually and many studies have been carried out to gain further understanding on this highly unfavourable phenomenon. Since Wöhler's famous systematic investigation of fatigue in rail axles, engineers and scientists have rigorously conducted research to characterise fatigue in engineering materials. In the last few decades the knowledge of fatigue has been extended considerably, owing to the advent of computer aided engineering. However, the lack of understanding as well as the poor management and practical application of knowledge on the prevention of material fatigue are still signified by disasters that could possibly be avoided. For example the Eschede ICE high-speed train disaster that killed 101 people in Germany (1998) and the catastrophic failure of NASA's Columbia space shuttle in 2003 clearly demonstrated that there is still room for improvement in tackling problems caused by material fatigue.

In depth knowledge of the fatigue crack growth behaviour and the characteristics of residual stresses present in structural components is a prerequisite in the fatigue life assessment of structures. Fatigue crack initiation and crack propagation behaviour in metallic materials have been extensively studied and the use of fatigue and fracture mechanics analysis has enabled engineers to generate accurate fatigue life assessments and prediction models. The integration of newly developed measurement techniques and theoretical damage models has facilitated the determination and investigation of residual stresses induced by manufacturing and fabrication processes, such as welding and shot peening. The incorporation of residual stresses into fatigue and fracture mechanics analysis is vital and will in turn lead to more realistic damage models. Although residual stress measurement in components has been a common topic for research, there is still limited data on the influence of residual stress on fatigue crack growth behaviour. Moreover, crack shape evolution, which has a profound effect on the fatigue crack growth behaviour in components, is often overlooked by researchers. It is surprising that with the vast

amount of residual stress studies conducted to date, the influence of residual stress on fatigue crack shape evolution has been comparatively ignored. In the present study, the author investigates the effect of damaging surface tensile residual stress and beneficial surface compressive residual stress on the fatigue crack growth in structural components.

It is generally known that structural components experience variable amplitude (VA) loading and are exposed to environmental conditions during their service life. The fatigue performance of materials is very sensitive to the characteristics of loading conditions and hence the use of a representative load-time sequence and suitable simulation of environmental conditions are of immense importance while evaluating the fatigue endurance of structural components through fatigue testing. Although fatigue testing using standardised load-time sequence has been developed for more than three decades, little attention has been given to the statistical nature and the suitability of the generated load history. The first part of the thesis reports the analytical development and modification work conducted on Jack-up Offshore Standard load History (JOSH), which is a standardised variable amplitude load-time sequence generator. Emphasis is given to the long term statistical nature of the generated load-time sequence and the significance on the convergence of the sequence parameters. The verified load-time sequence was employed in the investigation of the long-life corrosion fatigue performance of SE 702, a weldable high strength jack-up steel. Even though High Strength Steels (HSS) have been extensively used in the fabrication of offshore structures, especially in jack-up platforms, there is still a lack of data on the corrosion fatigue behaviour of welded components made from such steels, particularly in the long-life region. The fatigue resistance of HSS under cathodic protection and its susceptibility to hydrogen embrittlement is still an ongoing investigation area. In addition, the knowledge of the residual stresses arising from the welding process is still limited due to the relatively complex metallurgy of HSS. Through the fatigue testing and residual stress measurement of the SE 702 specimens, the fatigue crack growth behaviour of HSS welded joints in tensile residual stress field is investigated.

For decades, engineers have been 'hunting' for fatigue cracks in flawed structures by using various state-of-the-art crack inspection and measurement techniques. Operators from various industries spend enormous amounts of money annually in fatigue crack inspection and repairing works. Since fatigue cracks will inevitably grow in large structures, it would be highly beneficial if the crack initiation or path can be confirmed by the promotion of a localised non-catastrophic failure. Chapters 4 to 6 present the experimental and analytical work on the development of a 'designer crack' by the manipulation of surface residual stress. Two preferential cold working techniques termed *stitch cold rolling* and *stitch shot peening* were employed to introduce surface compressive residual stress on mild steel fatigue test specimens. The unique features of the

preferential cold working techniques were used to promote a leak-before-break crack by controlling the fatigue crack shape. The characteristics and relaxation behaviour of surface compressive residual stress due to cyclic loading is also investigated. A novel fatigue crack growth model, which is capable of modelling crack shape evolution in residual stress fields, was developed based on the robust stress intensity factor weight function method.

This chapter reviews the concepts and literature in the public domain thought to be relevant to the work presented in this Ph.D. study. Emphasis is placed on the Stress-Life approach and the Fracture Mechanics approach, particularly the Linear Elastic Fracture Mechanics approach. The sources of residual stress and the widely used measurement techniques are also discussed in detail.

1.2 Stress-Life (*S-N*) Approach

In a metal fatigue study on railway axles under rotating bending, Wöhler [1.2] observed that the components failed when subjected to many stress repetitions and all the applied stresses were lower than the static strength of the material. Further testing of various components under bending and torsional load led to the introduction of the characterisation of metal fatigue using the Wöhler curves, or better known as the stress-life (*S-N*) curves. In addition, Wöhler commented that tensile mean stress has a detrimental effect on the fatigue endurance. Since then, several empirical models based on the stress-life method had been developed for fatigue life estimation, with Gerber (Germany, 1874), Goodman (England, 1899), Soderberg (USA, 1930) and Morrow (USA 1960s) being the most widely accepted methods. These methods in general relate the mean stress, yield stress, ultimate tensile stress and endurance limit to the alternating stress range using different empirical formulae. For variable amplitude fatigue life prediction using the *S-N* approach, the Linear Damage Rule proposed by Palmgren [1.3] and Miner [1.4] is considered to be one of the most established methods.

In the present study, the stress-life (*S-N*) method was adopted for the assessment on the fatigue performance of T-butt welded joints and hence the discussion in this section will focus on offshore welded structures. The *S-N* approach has been widely used for assessing offshore structures as it is a simple but effective method to explain and quantify metal fatigue. The *S-N* method is generally based on fatigue test data and has the advantage of providing an assessment methodology which is based on a single parameter, the stress range, ΔS. Conventionally, the stress range is taken as the hot spot stress range for tubular joints and nominal stress range for welded plates and N is the number of fatigue cycles to failure. In this method, curves of applied stress range (ΔS) versus cycles to fatigue failure (N), which are known as *S-N* curves are plotted

on logarithmic scales, representing the fatigue resistance of a particular component. *S-N* curves are usually formulated for specific geometry and loading conditions, and hence lacking generality that they are only applicable to particular components cycled under particular loading sequences. In addition, *S-N* plots automatically include external effects such as complex geometry, geometric discontinuities, surface finishes, residual stresses and complex metallurgy, for example, weldments. One of the main drawbacks of the *S-N* method is that it assumes that all strains are elastic, and hence ignores the true stress-strain behaviour. This may be significant since the initiation of fatigue cracks is generally known to be caused by plastic deformation. Therefore, one can say that the *S-N* method is valid only if the plastic strains are small or negligible.

The basic design of *S-N* curves employed for offshore structures published by the Health and Safety Executive (HSE) Guidance Notes [1.5], are usually based on BS EN 10025 Grade S355J2G3 steels (formerly known as Grade 50D steel) [1.6]. These curves consist of linear relationships between $Log_{10}(S_B)$ and $Log_{10}(N)$ and are based upon a statistical analysis of appropriate experimental data. A best-fit line will be drawn through the experimental fatigue data obtained and the standard deviation is calculated from the scatter of the data. For safety reasons, the recommended *S-N* curves are two standard deviations below the mean line. The basic design *S-N* curves are of the form [1.5]:

$$Log_{10}(N) = Log_{10}(K_1) - mLog_{10}(S_B) \qquad - (1.1)$$

where N is the predicted number of cycles to failure
S_B is the applied stress range
K_1 is a constant
m is the slope of the *S-N* curve

Different welded joints are stratified into various classifications. Generally, welded joints can be categorised into nodal joints (e.g. tubular joints) and non-nodal joints. For non-nodal joints (e.g. butt joints), like the T-Butt welded specimens examined in the present study, an appropriate classification factor needs to be used in conjunction with the *S-N* curve. A plate-to-plate with transverse weldment structure is classified as a P Class welded joint and the applied nominal stress with a corresponding stress factor (Class F and F2 for P factor) should be incorporated with the design *S-N* curve. In general, the classification factor is considered to include the SCF associated with the local weld details but not any geometric stress concentrations. The details of the classifications and the correction factors can be found in the HSE Guidance Notes.

As previously stated, high strength steel was used as the material for the fatigue analysis of welded structures in this research. Hence, the design *S-N* curve from the HSE Guidance Notes must be applied with great caution since the data are based on medium strength steel (BS EN 10025 Grade S355J2G3), with yield strength circa 400MPa. In addition, the *S-N* data were obtained through constant amplitude (CA) testing, which may not be representative of the variable amplitude (VA) fatigue tests conducted in the present study. The resulting *S-N* curve from constant amplitude tests is a fundamental measure of a material's resistance to fatigue for the specified testing conditions, as the stress range applied and the endurance are measured at a single point on the curve. However, in variable amplitude loading, the fatigue performance of a material is dependent on the spectrum loading, which contains random loading frequencies and stress ranges. This is believed to have a detrimental effect on the fatigue limit of the material. According to the HSE 2000 OTR (Offshore Technology Report) [1.7], which based on a wide range of constant amplitude and variable amplitude fatigue testing of welded joints from various projects, suggested that the conventional Class F and F2 design curves (1.34P and 1.54P) relevant to the welded detail were suitable for both CA and VA loading. However, relevant authorities [1.8-1.10] have stated that more emphasis should be made towards realistic loading testing since there is limited fatigue life data available for structures tested under these conditions. Due to the difference in loading sequence parameters, fatigue data obtained from variable amplitude tests are considered difficult for comparison. Load-time sequence standardisation is considered as an effective method to overcome this problem and the analytical and experimental work presented in the succeeding chapters will demonstrate significance of a standardised load-time history. Furthermore, the methods employed for evaluating the equivalent (CA) stress range in VA amplitude loading varies among authors. For example, some older work adopted the root mean square (RMS) stress range method while more recent research utilised the root mean cube (RMC) stress range method. Although variable amplitude loading fatigue studies by Gurney [1.11] and Tilly et al [1.12] have shown differences between the results obtained by using RMS and RMC methods, none of the authors conclusively stated an advantage of one over the other. However, it is shown that for cumulative fatigue damage calculations, the root mean cube method provides a better fit for the slope of the design curve of welded joints [1.13].

1.2.1 The Implication of Other Factors on Fatigue Endurance

As stated in the preceding section, the design curves (P curve) given in the HSE Guidance Notes are for standard plate-to-plate T-butt welded joints under constant amplitude loading. The reference plate is quoted as a 16mm thick plate, which is the conventional wall thickness employed in most offshore standards. Hence, one must consider other relevant factors which have a profound effect on the fatigue life of the specimen. In general, fatigue life of a structure can be affected by factors such as the microstructure, mean stress, residual stress (tensile or

compressive), dimensions of the structure, geometric discontinuities, material properties and environmental conditions. In the following sections, only the thickness effect and environmental effect will be discussed.

1.2.1.1 Thickness Effects

Considerable research into the effect of wall thickness on the fatigue life of a structure, particularly welded components, has been carried out and documented. Since the significance of the thickness effect on the fatigue resistance of tubular joints and T-butt welded plates was demonstrated by the United Kingdom Offshore Steels Research Project [1.14], a vast number of studies have been carried out [1.15-1.18]. The findings of these studies suggest that the reduction in fatigue life of the welded joints is not only related to plate thickness but also other parameters such as the weld toe and the associated size of the local notch zone. This is confirmed by Webster et al [1.19] as they observed an increase in the weld toe stress concentration factors for thicker joints. Based on these observations, it is believed that the size effect was due to a combination of increased weld toe local stresses and the difference in stress gradient. In welded structures, where crack propagation controls the high proportion of the fatigue life, the stress gradient is lower for a thicker specimen. This is illustrated in Fig. 1.1 where the fatigue crack of a given size will be subjected to a higher stress level for a larger region in a thicker specimen. Hence, while comparing the fatigue endurance of any structure, the dimensions must be taken into account.

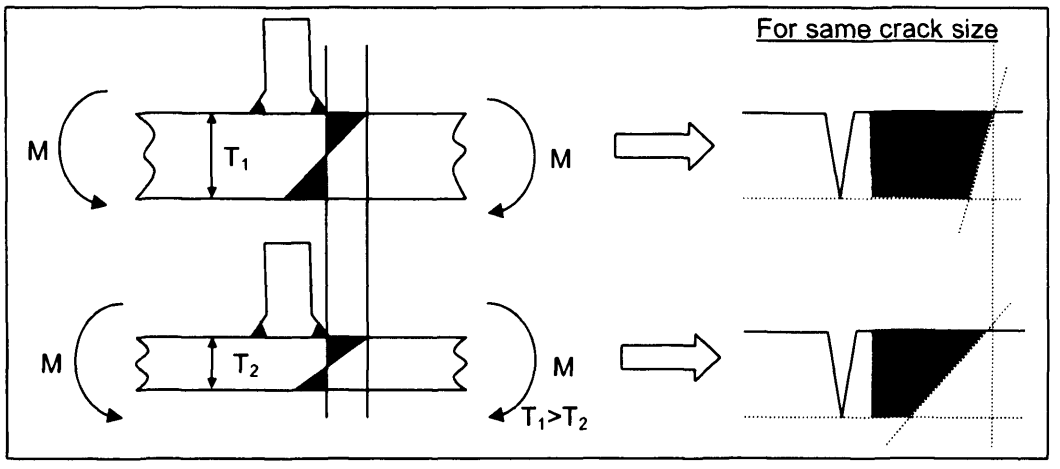

Figure 1.1: Stress gradient in a T-butt welded joint for different plate thickness

After a comprehensive review of studies, it is widely accepted for welded joints that the fatigue performance is dependant on member thickness, as performance decreasing with increasing thickness for the same nominal stress range. According to the HSE Guidance Notes, the basic design *S-N* curves are applicable to thickness less than the basic thickness, t_B, which is 16mm for

Class P. However, for members of greater thickness, a modified *S-N* relationship applies as follows [1.5]:

$$Log_{10}(N) = Log_{10}(K_1) - mLog_{10}\left(\frac{S_B}{\left(\frac{t_B}{t}\right)^q}\right) \quad \text{- (1.2)}$$

where q is the thickness exponent factor; equal to 0.3 for welded joints

t is the thickness of the member under consideration

t_B is the reference thickness (16mm for P curves)

Although a vast amount of variable amplitude loading tests have been carried out, there is no specific thickness correction factor for fatigue lives proposed. However, the OTR [1.7] published by HSE stated that "there is no fundamental reason why" the thickness correction factor employed under constant amplitude would not be applicable to variable amplitude loading data.

1.2.1.2 Environmental Effects

It is well documented that the in service environment of an offshore structure is different to that of the ambient air laboratory conditions and therefore, environmental effects have been extensively investigated by researchers. In offshore operating conditions, the air contains relatively higher levels of moisture and salt. In addition, many of these components will be subjected to repeated or constant immersion in sea water. Hence, the environmental effects will depend on whether the component is in the splash zone, fully immersed and on the level of any cathodic protection used.

Generally, concerns are focused on the leg members since they are constantly exposed to extreme marine environment throughout their service life. The joints which are located in the tidal zone, splash zone or below the mean tide level, are constantly subjected to the sea waves pounding. According to the HSE Guidance Notes, these welded joints can be stratified into two categories; unprotected joints in seawater and protected joints in seawater. For plates and tubular joints exposed to seawater, but without adequate corrosion protection, a penalty factor of 3 is introduced to the design fatigue life. A penalty factor of 2 is also adopted for protected joints as previous welded joints fatigue tested under adequate cathodic protection levels did not show trends in fatigue lives comparable to air tests. Corrosion fatigue under cathodic protection is influenced by many factors, some of which have been demonstrated to be different from material to material. The degree of endurance of a particular structure will largely depend on the complex chemical interaction in the vicinity of the crack tip and the stress concentration factor, which varies for different grades of steel. Meanwhile, the HSE OTR [1.7] on variable amplitude loading tests

suggested that the basic design curves for protected joints in seawater, which were constructed based on medium strength steels, are suitable to be adopted for high strength steels.

Fig. 1.2 below shows the welded joints *S-N* design P curves in an air environment, unprotected joints and protected joints respectively. The corresponding *S-N* curves equations are given below:

For welded joints in air environment (P curves):

$$Log_{10}(N) = 12.182 - 3Log_{10}(S_B) \quad \text{(for } N < 10^7\text{)} \quad \text{- (1.3)}$$

$$Log_{10}(N) = 15.637 - 5Log_{10}(S_B) \quad \text{(for } N > 10^7\text{)} \quad \text{- (1.4)}$$

For unprotected joints in seawater under free corrosion (P curves):

$$Log_{10}(N) = 11.705 - 3Log_{10}(S_B) \quad \text{(for } N < 10^7\text{)} \quad \text{- (1.5)}$$

For protected joints in seawater (P curves):

$$Log_{10}(N) = 11.784 - 3Log_{10}(S_B) \quad \text{(for } N < 10^7\text{)} \quad \text{- (1.6)}$$

$$Log_{10}(N) = 15.637 - 5Log_{10}(S_B) \quad \text{(for } N > 10^7\text{)} \quad \text{- (1.7)}$$

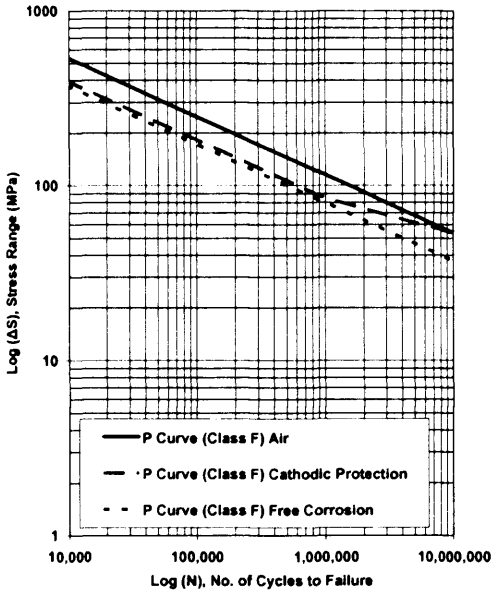

Figure 1.2: *S-N* design curves for T-butt welded plates in different environmental conditions

1.3 Fracture Mechanics Approach

Although the *S-N* approach has been extensively used in the design stages in various industries, the fracture mechanics approach is widely recognised to be a more powerful tool in terms of fatigue analysis. This is due to the fact that the robust nature of fracture mechanics enables one to overcome the most significant short comings of the *S-N* approach, which is the prediction and modelling of the structural integrity of a cracked structure. Following the pioneering period, about four decades ago, fracture mechanics has been the subject of rapid development and it is regarded as an indispensable ingredient in the safety analysis.

Unlike most traditional approaches which consider the design stress and yield stress of the material, a fracture mechanics approach involves the three variables of design stress, flaw size and the material property of fracture toughness when assessing structural integrity. It is the main concern of those practising fracture mechanics to assess cracked structures and ascertain a state of safe operation without catastrophic failure. Hence, the nature of the analysis enables the determination of the residual strength of a structure as a function of crack size, the critical crack size tolerance, crack growth rates between two specified durations and appropriate inspection schedules for cracked components. The advancement of computer technology and Non-Destructive Testing (NDT) techniques has seen the effective implementation of a defect tolerance design philosophy through fracture mechanics analysis.

The practical use of fracture mechanics has been established for use on large turbine and electric generator rotor components, the automotive industry, ship designs and in the aircraft industry. Due to its versatile approach, fracture mechanics has been extensively used in the offshore industry for which examples can be found in the literature [1.20-1.23]. In the present study, linear elastic fracture mechanics (LEFM) was adopted as the major approach in analysing the fatigue test results reported in succeeding chapters. The fundamentals of LEFM and some existing models will be discussed in detail in the following sections.

1.3.1 Linear Elastic Fracture Mechanics (LEFM)

Linear elastic fracture mechanics is a very versatile approach for the evaluation of strength of a structure or component in the presence of a crack or a flaw. In LEFM, the stress distribution near to a crack tip is defined in terms of parameters such as load, crack geometry, and material property [1.24] and the crack behaviour is assumed to be governed by crack tip stress fields. Its application to fatigue crack growth involves the crack growth process, covering the range from a detectable crack or flaw to final fracture. Hence, LEFM can be summarised as a method to determine crack growth in materials under the basic assumption that material conditions are predominantly linear elastic during the fatigue process, as is suggested by its name. In a more

traditional or conventional design method, in order to determine the structural integrity of the material, the anticipated design stress and the material flow stress are emphasised. On the other hand, the LEFM approach is based on three important variables; design stress, flaw size and fracture toughness, which replaces yield strength as the relevant material property.

In LEFM, the most fundamental crack surface displacement modes, by which a crack can extend, can be categorised into three modes. Fig. 1.3 below shows all three modes of crack opening. Mode I is the opening mode, which is the most common mode, particularly in fatigue failure. Mode II is the in-plane shearing or sometimes known as sliding mode, while Mode III is the tearing or anti-plane shear mode. Mode I is the most common crack extension due to the fact cracks tend to grow normally with respect to the maximum principal stress. In this research, only Mode I crack loading will be investigated and all discussions and interpretation will be referred to this mode only.

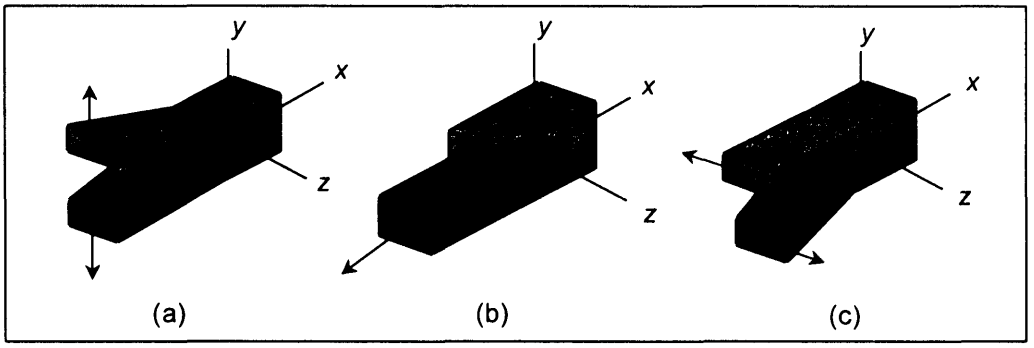

Figure 1.3: The three modes of crack opening

1.3.2 The Stress Intensity Factor (SIF)

The understanding of the stress/strain field surrounding a crack tip is a prerequisite in fracture mechanics as the crack behaviour is assumed to be governed by the crack tip stress field. The crack tip stresses in linear elastic materials are proportional to the remotely applied loading and the only length dimension common to all cracked geometries is the crack size parameter, *a*. A relationship between SIF, *K*, and the global conditions can be written as [1.24]:

$$K = f\left(\sigma, \sqrt{a}\right) \quad \text{- (1.8)}$$

This stress field relationship assumes that there is no crack tip plasticity or the region of plasticity is small compared to the overall dimensions of the crack and cracked body. For normal engineering applications, the SIF range is normally expressed in the general form:

$$\Delta K = Y\Delta\sigma\sqrt{\pi a} \quad \text{- (1.9)}$$

where ΔK is the stress intensity factor range for the corresponding applied stress range

Y is a geometry correction factor

$\Delta\sigma$ is the nominal applied stress range

a is the crack depth

The SIF range is a function of the crack size, crack shape and the applied load, as illustrated in Equation 1.9. The geometry correction factor, *Y*, which is also known as the non-dimensional SIF or normalised SIF, depends on the geometry of the component, crack geometry and loading conditions. The SIF and applied stress in Equation 1.9 are expressed in terms of ranges since in fatigue the crack growth mechanism arises due to cyclic stressing. The SIF has been proven to have a major influence on fatigue crack growth [1.25] and, that if ΔK is constant then the fatigue crack growth rate is constant in a homogeneous material.

1.3.3 Fatigue Crack Growth and The SIF

In addition to serving as an analytical tool to the static loading of cracked bodies, LEFM is also employed in the evaluation of fatigue crack growth. The derivation of SIF has enabled the mechanism of crack growth, which arises due to cyclic stressing, to be investigated. The fatigue crack propagation life of a structure is always represented by a crack depth, *a*, versus number of fatigue cycles, *N*, plot. It has to be pointed out that the notation of *N* in LEFM must not be confused with its counterpart in the *S-N* approach, where *N* denotes the number of cycles to failure. By incorporating the SIF into the fatigue crack growth data, a *da/dN* (crack growth rate) versus ΔK graph can be plotted. For most metallic materials, the fatigue crack growth rate can be expressed by the Paris Law (Equation 1.10). Subsequently, Equation 1.10 can be integrated to provide the number of cycles for a crack to propagate from an initial crack length, a_i, to a final crack length, a_f, in the form:

$$\frac{da}{dN} = C(\Delta K)^m \quad \text{- (1.10)}$$

Substituting Equation 1.9 into the equation above gives:

$$N = \int_{a_i}^{a_f} \frac{da}{C(\Delta K)^m}$$

$$N = \int_{a_i}^{a_f} \frac{da}{C\left(Y\Delta\sigma\sqrt{\pi a}\right)^m} \qquad \text{- (1.11)}$$

where C and m are empirical material coefficients (also known as Paris Law coefficients). A typical crack propagation (under constant amplitude loading) log-log plot of da/dN versus ΔK is shown schematically in Fig. 1.4 below.

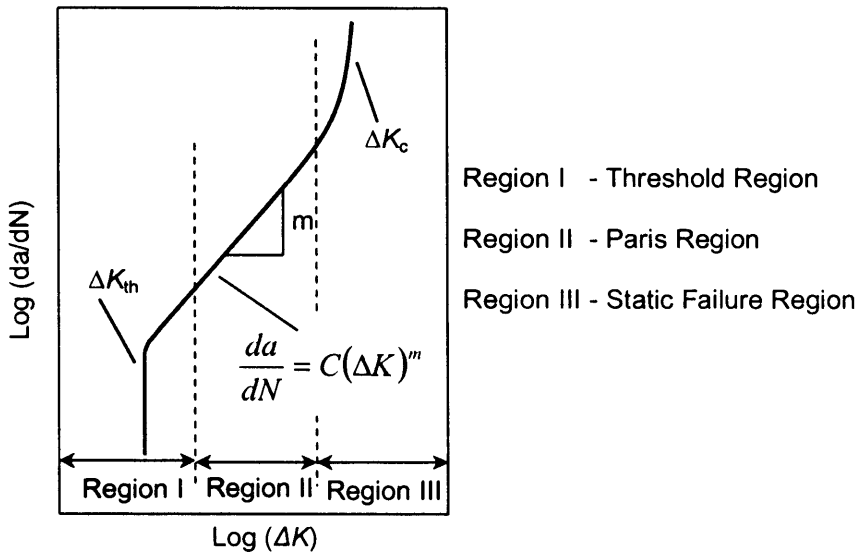

Figure 1.4: Schematic sigmoidal behaviour of fatigue crack growth rate versus ΔK

It is noteworthy that the application of LEFM to defect assessment does suffer from practical limitations, especially when applied to fatigue short-crack growth analysis. This is due to the fact that fatigue short-crack propagation is known to be dominated by the relatively large (when compared to the crack size) plastic zone at the crack tip, resulting the crack to behave inelastically. This dominance of the crack tip plasticity will significantly alter the stress field ahead of the crack tip, meaning that the stress field in the uncracked body is no longer entirely governed by the SIF. However, the approximate relations utilised in the LEFM approach do provide a robust tool for the characterisation of fatigue growth behaviour, especially when the crack size is considerably larger than the crack tip plastic zone. Moreover, in the present study, emphasis is given to the crack growth behaviour during the fatigue crack propagation phase and hence LEFM is considered to be a reliable and valid method.

1.3.4 SIF Solutions

During component residual strength or fatigue crack growth analysis, the knowledge of the SIF for the specified geometry and loading conditions is of great importance. Since the SIF can always be expressed in the form of Equation 1.9, the problem resides in the determination of the geometry correction factor, *Y*. SIF solutions for a variety of geometries can be found in published compilations of SIF solutions. The most widely used SIF compendia include Tada et al [1.26], Sih [1.27], Rooke-Cartwright [1.28] and Murakami-Tsuru [1.29-1.30]. These SIF solutions are generally presented in the normalised form and in most cases the results were obtained using analytical and numerical methods. For a specific geometry and loading conditions, the corresponding SIF solutions are usually quoted with an associated accuracy and the solutions are presented in the form of tables, charts (e.g. polynomial curve fits) or closed form parametric equations. However, published SIF solutions are often only available for simple/idealised geometries subjected to simple loading conditions, such as remotely applied uniform tension, three point bending and pure bending.

Many of the aforementioned solutions were developed in the period during the development of SIF solutions and the majority of the solutions are only available for edge cracks in two-dimensional geometries. The advent of computer systems in engineering since the 1980s saw a significant increase in the development of SIF solutions for a wider range of geometries (two-dimensional cracks in three-dimensional geometries) and components, for example flat plates [1.31], T-butt welded plates [1.32], tubular Y and K-joints [1.33, 1.34] etc. These SIF solutions are normally expressed in the form of parametric equations or empirical/semi-empirical equations and are often validated against published solutions and Finite Element (FE) models. There are several ways of plotting SIF solutions and a typical example can be found in Fig. 1.5 below, which shows the well known Newman-Raju [1.31] surface crack SIF solution in a flat plate under pure bending for a constant crack aspect ratio a/c = 0.2 (crack depth/half crack length). The graph is plotted as the normalised SIF against crack angle along the crack front. For clarification, the typical notation of a semi-elliptical surface crack can be found in Appendix A. Newman-Raju surface crack SIF empirical equations are considered to be one of the most widely used SIF solutions and they are often adopted as a basis for the formulation of fracture mechanics surface crack growth models. An example of the SIF solutions for a structural component is illustrated in Fig. 1.6 below. The figure shows the normalised SIFs for a surface crack emanating from the weld toe of a T-butt welded plate calculated from parametric equations published by Brennan et al [1.32]. In this graph, the normalised SIF is plotted as a function of the normalised crack depth, a/T (crack depth/plate thickness), and the variation of the SIFs for a crack with different crack aspect ratio is clearly illustrated.

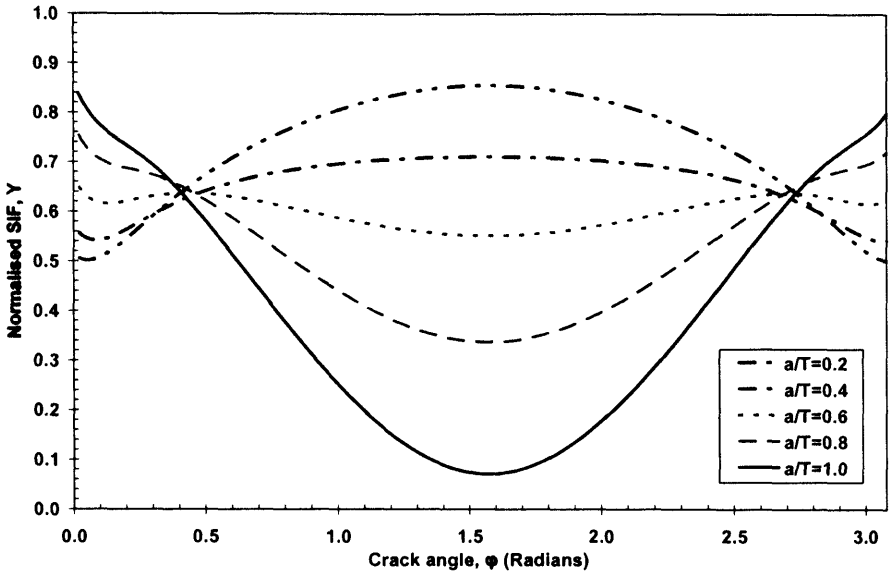

Figure 1.5: Newman-Raju normalised SIFs under bending for *a/c* = 0.2

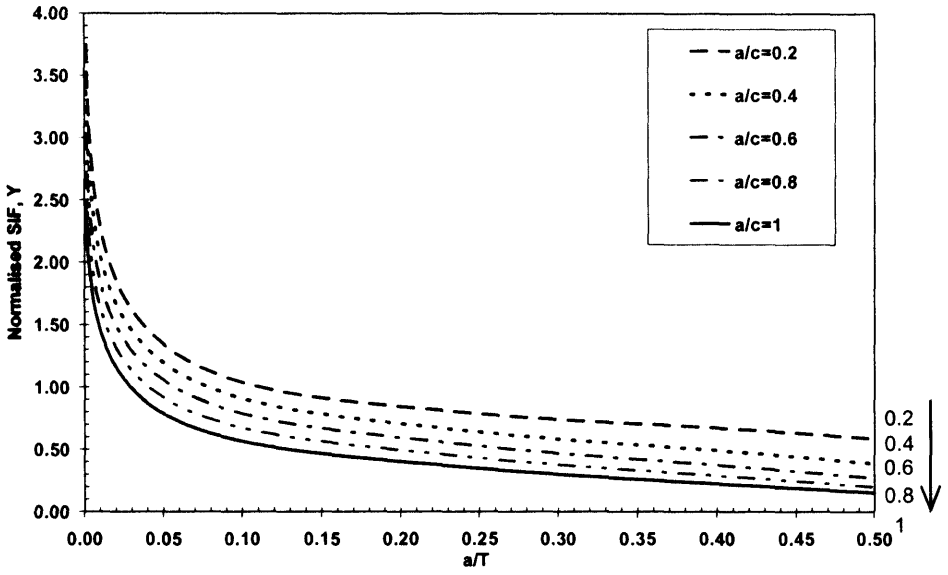

Figure 1.6: Normalised weld toe SIFs under bending obtained using Brennan et al [1.32] parametric equations

As can be seen from the figures above, the evolution of the SIFs for structural components can be determined using various published SIF solutions and these can be incorporated into the Paris Law for the specified component fatigue life or residual life prediction. Although these solutions provide a rapid calculation of SIFs, their applications are limited to simple loading conditions geometries and the approximated solutions are often not representative of real engineering components where the cracks normally reside in residual stress fields or geometrical

discontinuities. Section 1.3.5 below presents the utilisation of SIF weight functions, which allows the SIF in a component subjected to complex loading to be determined.

1.3.5 Calculation of SIFs Using Weight Functions

Most methods developed for the determination of stress intensity factors require calculation of the SIF for each stress distribution and crack depth/length. Hence, there is a need for the development of a method which involves minimum computational effort, yet provides an accurate way of evaluating SIF. Bueckner [1.35] simplified the determination of stress intensity factor considerably by introducing the weight function method.

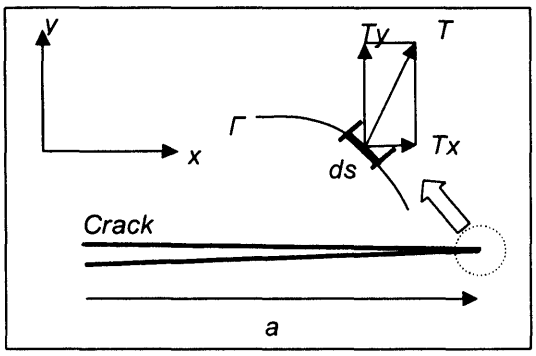

Figure 1.7: Crack loaded by body tractions

Fig. 1.7 above shows that a crack of length, a, in a cracked body may be loaded by tractions $T(s) = (T_y, T_x)^T$, which are responsible for a stress field at the crack tip, acting normal to a curve Γ [1.36]. Buekner proposed that the stress intensity factor can be expressed as:

$$K^T = \int_{\Gamma} T.h\,ds \qquad \text{- (1.12)}$$

where h is the vector of the weight function $h = (h_y, h_x)^T$. Following Bueckner's work, Rice [1.37] correlated the weight function, $m(a,x)$, to the displacement field, $u=(u_y, u_x)^T$, under an arbitrary load system:

$$m(a,x) = \frac{H}{K_r}\frac{\partial u_r(a,x)}{\partial a} \qquad \text{- (1.13)}$$

where H is the generalised modulus of elasticity, which corresponds to E for plane stress and $E/(1-\upsilon^2)$ for plane strain. The subscript, r, denotes the reference cases. Hence, presuming that the crack opening displacement (COD) field, u_r, and the corresponding reference SIF, K_r, are known, the weight function can be calculated. Consider a Mode I crack in a component subjected

to a stress distribution indicated in Fig. 1.8 below. The SIF may be simply evaluated from the integral over the crack length of the product of the weight function and the stress distribution in the crack plane of the unflawed body:

$$K = \int_0^a \sigma(x) m(a,x) dx \qquad \text{- (1.14)}$$

It is worth noting that although only Mode I loading is discussed in this section, the weight function method is a very robust and powerful tool for the analysis of cracks subjected to complex loading conditions.

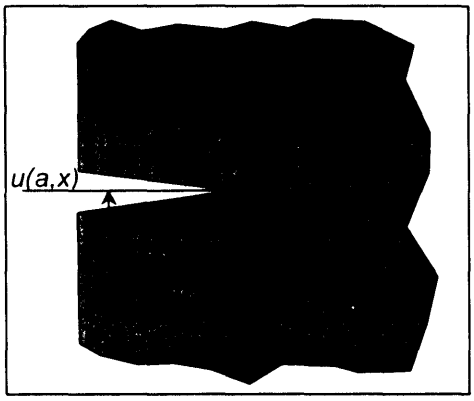

Figure 1.8: Stress distribution along a crack

It is generally known that COD data are rarely presented with the corresponding SIF solutions. Hence, early weight function solutions required extensive preliminary analysis, such as finite element analysis, to establish the crack opening displacement. Petroski-Achenbach [1.38] proposed an approximate COD function, $u_r(x,a)$ as a series of two terms, based on the principle of energy balance or also known as self-consistency, for plane problems:

$$u_r(x,a) = \frac{\sigma}{H\sqrt{2}}\left[4F(a/t)\sqrt{a(a-x)} + \frac{G(a/t)(a-x)^{\frac{3}{2}}}{\sqrt{a}}\right] \qquad \text{- (1.15)}$$

The crack face displacement is calculated from a reference stress intensity factor and several geometric conditions. The approximate COD needs to be differentiated in order to obtain the weight function (Equation 1.13) and the proposed function must meet three criteria. It must obey limiting behaviour near the crack tip, it must demonstrate consistency for small crack behaviour and finally the process must be relatively simple to enable the evaluation of unknown variables from the reference solutions. Initially, Petroski and Achenbach implemented the proposed

method to generate SIF solutions for radial cracks, edge cracks and cracked rings, which compared well with published solutions.

Fett et al [1.39] later showed that the approximate COD provided good accuracy solutions using known stress intensity factors and corresponding load states. They proposed an arithmetic series representation of COD and the series truncated at a point dependent upon the number of reference states available:

$$u_r(x,a) = \frac{2\sigma}{H}\sqrt{2}aF(a/t)\sum_{j=0}^{\infty} c_j \left(1-\frac{a}{x}\right)^{j+\frac{1}{2}} \qquad \text{- (1.16)}$$

It can be observed from Equation 1.16 that as the number of terms of the COD increases, additional conditions are required to define the unknown coefficients. Hence, the formulation of a weight function by differentiation of a crack opening displacement function is an extremely tedious process, which was described by Brennan [1.40]. An alternative approach which eliminates cumbersome mathematical differentiation involved was proposed by Ojdrovic-Petroski [1.41]. The multiple reference states (MRS) weight function approach, which defines the crack opening displacement function as it is to be implemented to form a weight function, requires at least two reference stress intensity factors solutions:

$$\frac{\partial u_r(a,x)}{\partial a} = \frac{2\sigma}{H}\sqrt{2}\sum_{j=0}^{n} c_j \left(1-\frac{a}{x}\right)^{j-\frac{1}{2}} \qquad \text{- (1.17)}$$

The use of the direct description of the derivative of COD proposed by Ojdrovic-Petroski (Equation 1.17) means that the tedious numerical differentiation of the COD field can be avoided. As previously stated, the weight function is a unique property of the component geometry. It has been demonstrated by many studies that the geometric influences on the weight function can be isolated and combined. This is made possible by the implementation of a composition technique, which enables the determination of SIF in components containing complex geometries and stress distributions. The composition technique has been successfully employed by Impellizzeri-Rich [1.42], Mattheck et al [1.43] and Niu-Glinka [1.44]. Niu-Glinka performed a closed form weight function solution for an edge crack emanating from the weld toe in a T-butt welded joint, based on the composition principle. The concept is illustrated in Fig. 1.9 below.

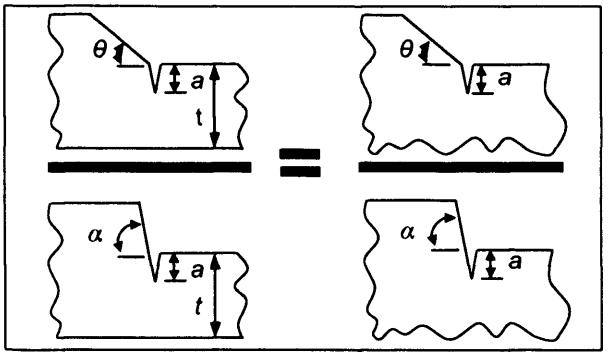

Figure 1.9: Principle of the Niu-Glinka weight function composition technique

It shows that the solutions for the geometry with the protrusion angle, θ, normalised to the geometry with protrusion, α, being equal for both finite and semi-infinite cases [1.44]:

$$\frac{K_1^{\theta}}{K_1^{\alpha}} = \frac{K_2^{\theta}}{K_2^{\alpha}} \qquad \text{- (1.18)}$$

Assuming a remote stress field, σ, is constant for both cases,

$$K_2^{\theta} = \frac{Y_1^{\theta} K_2^{\alpha}}{Y_1^{\alpha}}, \text{ where } Y = \frac{K}{\sigma\sqrt{\pi a}} \qquad \text{- (1.19)}$$

Substituting Equation 1.14 into Equation 1.19 gives

$$\int_0^a \sigma_2^a(x) m_{\theta}(a,x,\theta) dx = \frac{Y_1^{\theta}}{Y_1^{\alpha}} \int_0^a \sigma_2^a(x) m_{\alpha}(a,x,\alpha) dx \qquad \text{- (1.20)}$$

and expressing in terms of weight function gives

$$m_{\theta}(a,x,\theta) = \frac{Y_1^{\theta}}{Y_1^{\alpha}} m_{\alpha}(a,x,\alpha) \qquad \text{- (1.21)}$$

Essentially, the intrinsic normalisation nature of the composition technique eliminates the geometric influences of the component. However, Equation 1.21 will only be true if the stress distribution for both cases (θ and α) are identical, which is impossible in practice as the local stress fields in the uncracked plane will be different for different geometries [1.45]. In addition, the inclusion of the geometry correction factor also means that the weight function can only be applied to particular loading conditions. More recently, Brennan et al [1.45] extended the MRS

approach, termed the SIF weight function composition technique, which composes the constitutive SIFs geometrically by isolating the effect of stresses. The mathematical expression of weight function composition is given as:

$$\frac{m(a,x)_f^{\theta}}{m(a,x)_f} = \frac{m(a,x)_s^{\theta}}{m(a,x)_s} \qquad \text{- (1.22)}$$

where the subscripts *f* and *s* represent finite-thickness and infinite-thickness respectively. Details of this method can be found in Reference 1.45. The advantage of this method is that only one reference solution is needed in order to obtain the weight function for an edge crack emanating from a semi-infinite case and the stress fields in the uncracked plane are universally identical for all cases. This means that the weight function composed can be applied to the same geometry under any loading condition. Teh [1.46] successfully developed a library of simple case reference solutions for two-dimensional bodies by using the composition method. Currently, the composition method is being extended by Brennan et al for the generation of SIF solutions for three-dimensional cases.

1.4 Residual Stress

Residual Stress can be defined as a stress existing in a material without application or existence of external load or other sources of stress. Hence, residual stress is regarded as in a self-equilibrium state since the resultant force produced is equal to zero. Various technical terms have been used to refer to residual stresses, such as internal stresses, initial stresses, inherent stresses, reaction stresses and locked-in stresses. It can be produced by heterogeneous plastic deformations, thermal contractions and phase transformations induced by the manufacturing process. Residual stress can be classified into three categories. These are macroscopic, structural microstress and microscopic residual stress. Macroscopic residual stress is long-range in nature, and usually extending over at least several grains of the material. In contrast, structural microstress only covers a distance of one grain or a portion of a grain. Microscopic residual stress, also known as sub-microscopic stress, has a range of over several atomic distances within a grain, and its equilibrium is achieved over a small part of the grain.

Generally, residual stress can have a significant influence on the fatigue life of engineering components. It is known that near surface tensile residual stresses tend to accelerate the initiation and growth phases of the fatigue process while compressive residual stresses close to a surface may prolong fatigue life. This is due to the fact that the compressive stresses in the surface of a component must be overcome by the applied load for crack initiation to take place. In

metals, tensile residual stress on the contrary, reduces the mechanical performance of materials. Residual stress is often treated as a mean stress and can be superimposed onto the applied stress and this can be explained by using Fig. 1.10 below. Fig. 1.10a shows a metal bar that is subjected to a bending load and the applied stress gradient is shown by the black dotted line. As can be seen from the figure, the upper surface layer of the metal bar experiences high tensile stress and hence fatigue crack initiation will eventually take place if the applied stress is sufficiently high. If compressive residual stress is to be introduced onto the upper surface of the metal bar, for example by shot peening, the typical residual stress profile will take the form of the red dotted line (Fig. 1.10b). In the elastic range, the residual stress can be added to the applied stress as a static load. The resultant stress profile is shown in Fig. 1.10c. It is evident from the figure that even though the upper surface layer of the metal is subjected to a high level of applied tensile stress, the total stress remains safely in the compressive zone and this in turn will lead to an increase in the fatigue resistance. Hence, various manufacturing and fabrication techniques have been developed to deliberately introduce compressive residual stress onto the surface of components in order to improve the material mechanical properties.

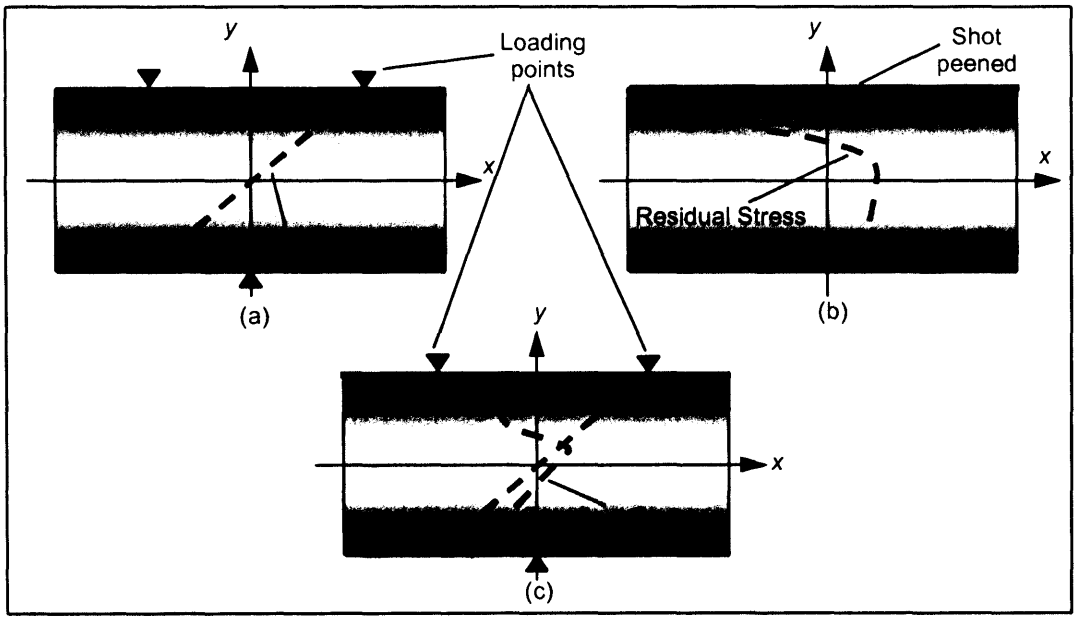

Figure 1.10: Superimposition of residual stress

The study of residual stress is not a new idea in manufacturing processes. Many research studies concerned with residual stress have been carried out on various components and predictive models for crack initiation and propagation. For example, authors in References 1.47-1.50 have successfully shown the effects and significance of residual stress in the improvement of the fatigue life of certain materials. Accordingly, the study of residual stress is an important criterion and pertinent in component performance analysis as well as in parts manufacture.

1.4.1 Sources of Residual Stress

Residual stress can be introduced directly or indirectly, by various forms of mechanical or manufacturing processes. Generally, residual stress can be induced through mechanical methods or thermal methods. Mechanical methods of inducing residual stresses rely on applying external loads that produce localised inelastic deformation [1.51]. Some examples of mechanical methods include rolling, shot peening, drawing, forging, extruding and bending. Recently, the laser shock peening technique, which is capable of introducing surface compressive residual stress onto metallic components up to a depth of 10mm has been developed [1.52]. Alternatively, thermal methods utilise inhomogeneous plastic deformation resultant of thermal load, volumetric changes and mismatches in the coefficients of thermal expansion/contraction. Quenching, injection moulding, welding, tempering, hot rolling, temper stress relief and nitriding are some common examples of residual stress induction by thermal methods. The following sections discuss further the main sources of residual stress emphasised in this study and these include cold rolling, shot peening and welding.

1.4.1.1 Welding

Many of today's steel structures are fabricated by welding techniques and the stresses arising from welding is one of the major thermal sources of residual stress. Similar to other methods, the residual stresses induced by welding are balanced within the material, which contains tensile and compressive components of stress. In general, residual stresses arise in welded structures as a consequence of the fact that during the weld heating and cooling cycle, the natural expansion and contraction of material close to the heat source is inhibited by the restraining effect of the adjacent material at a lower temperature. This can be illustrated by using Fig. 1.11 below, where the weld has had to accommodate its 'unnatural' length by plastic strain and, when cold, is subjected to longitudinal tensile stress [1.51]. In a welded structure, longitudinal residual stress and transverse residual stress distributions with respect to the direction of welding co-exist in the material. Fig. 1.12 shows that for equilibrium, the tensile stress in the weld zone is counterbalanced by compressive stresses farther out in the plate. In some cases, stress levels of yield magnitude will exist. The damaging tensile residual stress at the surface layer is an unfavourable quantity and this has a deleterious effect on the fatigue behaviour of welded structures.

In order to decrease the magnitude of residual stresses induced, post weld heat treatment has been adopted as the primary stress relief method. However, as-welded joints are complicated by various factors such as the heat input energy, the welding process, geometry of the weld, temperature distribution, formation of inelastic strain and changes in material property. In addition, other factors for example weld toe grinding or partial weld penetration also play a vital role in determining the fatigue behaviour of welded joints. Considerable amount of research has

been conducted to further understand the distortion and residual stresses generated during welding processes. Analytically or experimentally, these investigations normally consist of analysis of heat flow, analysis of transient thermal stresses, determination of incompatible strains and analysis of residual stress. In the current study, residual stresses in T-butt welded joints fabricated from HSS are studied and their influence on fatigue crack growth is investigated through fracture mechanics analysis.

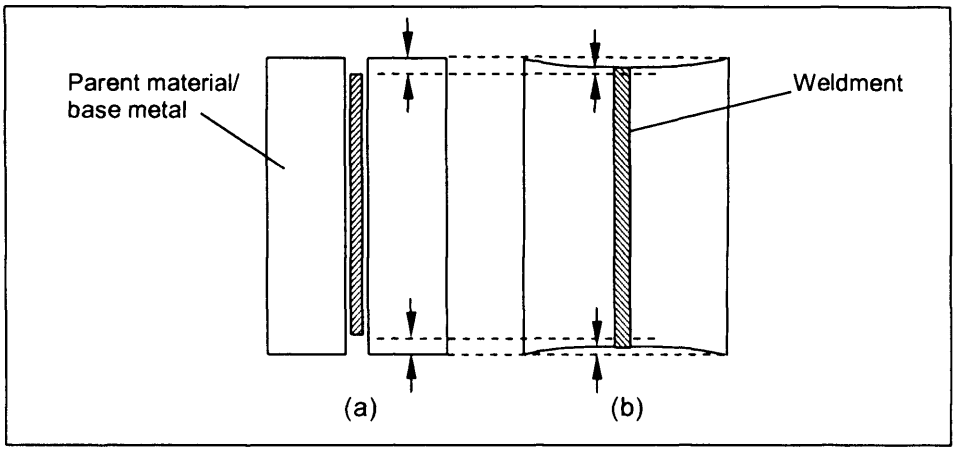

Figure 1.11: Formation of residual stress as a result of welding: (a) Natural longitudinal shrinkage of unrestrained (unattached) weld; (b) Longitudinal shrinkage of restrained weld

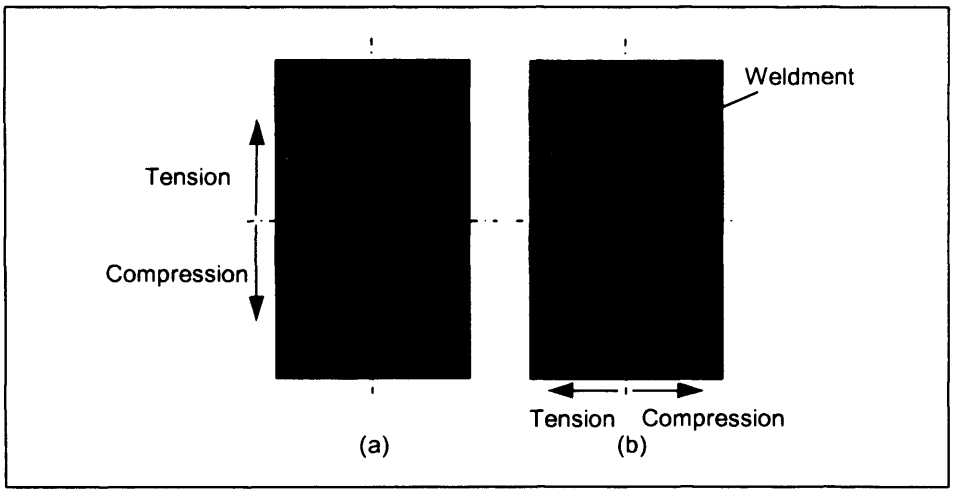

Figure 1.12: Induced residual stress in welded joint: (a) Longitudinal residual stress; (b) Transverse residual stress

1.4.1.2 Cold Rolling

Cold rolling has been adopted as a method of reducing the thickness of material for over a century and is a type of mechanical cold working process. Cold working can be defined as plastic

deformation produced on a material at a temperature below its recrystallisation temperature. The term work hardening is frequently linked with cold rolling since cold rolling introduces beneficial compressive residual stresses that often increase the material's hardness.

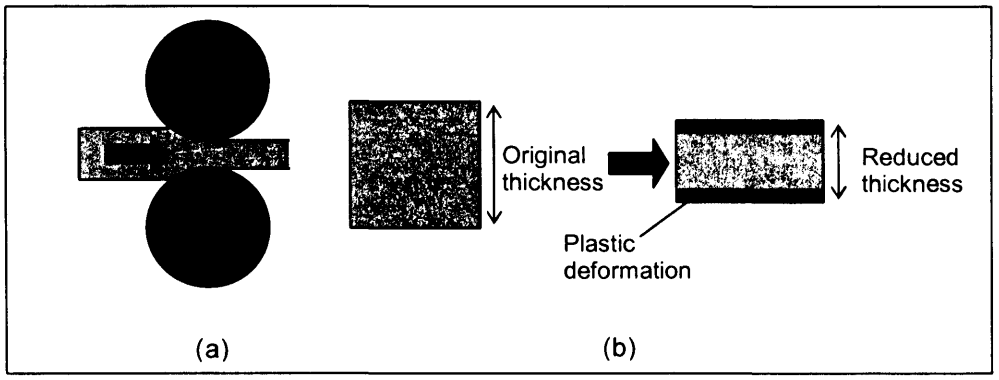

Figure 1.13: (a) Cold rolling process (b) Material thickness reduction after cold rolling

Most fatigue cracks or flaws are surface breaking. Hence, various surface treatments that introduce compressive residual stress are adopted to improve the mechanical characteristics of the surface layer. The most widely used mechanical surface treatment processes for introducing compressive surface residual stress are shot peening and cold rolling. Cold rolling, being a relatively simple and inexpensive process, has attracted the attention of many researchers [1.49, 1.50, 1.53, 1.54]. Basically, cold rolling utilises local plastic deformation by applying pressure onto the component by using rollers. Fig. 1.13 above shows the conventional cold rolling process widely used for the reduction of material thickness. As illustrated in Fig. 1.13b, both surface layers of the material are subjected to higher compressive stress than its core. Hence, it can be said that most of the plastic deformation in the longitudinal direction exists in the outer layers of the material while its core is only subjected to relatively small amount of plastic deformation or just elastic deformation. The existence of inhomogeneous plastic deformation in the structure of the material contributes to the resultant residual stress. When the applied pressure to the surfaces returns to zero (unloading), the deformed region will structurally restore itself until a self-equilibrium state is reached. Fig. 1.14 below can be used to illustrate the residual stress generation mechanism during cold rolling [1.49]. The stress distribution induced during cold rolling is indicated by the line *aoa'* while line *bob'* indicates the stress distribution during unloading. By using Wöhler concept [1.55], the residual stress can be calculated. The residual stress induced onto the material can be determined by subtracting the unloading stress distribution *bob'* from the inelastic stress distribution *aoa'*. The resultant stress distribution will be the induced residual stress distribution, indicated by line *coc'* in Fig. 1.14. The work hardening effect on the material surface will in turn lead to an increase in hardness and yield strength but the

increase must be controlled to produce optimum strength and formability. Hence, it is often that a material is annealed after underwent cold rolling process and before subsequent forming can be carried out.

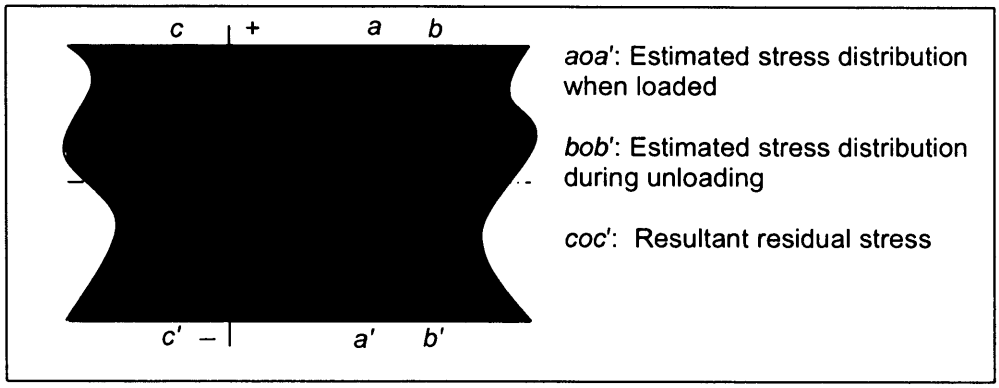

Figure 1.14: Residual stress generation mechanism during cold rolling

A localised cold rolling process was adopted in this research to introduce surface compressive residual stress onto mild steel fatigue test specimens. Fatigue crack growth behaviour under the induced residual stress field and the feasibility of controlling the crack shape using the newly developed stitch cold rolling technique is investigated. Details of the experimental study can be found in Chapter 4.

1.4.1.3 Shot Peening

Shot peening is considered to be one of the most widely used surface treatment methods for introducing beneficial residual stress in materials. Similar to cold rolling, shot peening is a cold working process in which the surface of a component is bombarded with small spherical media known as shot. The most widely used form of shot media are spherical round shots and cut wire, which are normally made from cast iron, carbon steel, stainless steel or ceramic. Each piece of shot striking the material acts as a tiny peening hammer, imparting to the surface a small indentation or dimple, as shown in Fig. 1.15 below. In order for the dimple to be created, the surface fibres of the material must yield in tension. Beneath the surface, the compressed grains try to restore the surface to its original shape, thereby producing below the dimple, a hemisphere of cold worked material highly stressed in compression. In other words, during the process of shot peening, high velocity shot causes local plastic yielding in the surface, which is thereby extended relative to the interior. The interior of the material will act to constrict the surface, resulting in high, local, compressive residual stresses in the surface balanced by the tensile stresses within the core (Fig 1.15b) and the overlapping of dimples will provide a uniform layer of beneficial compressive residual stress on the surface of the material. However, it must be noted

that in certain cases of overpeening or the use of inadequate high peening velocity can cause damage at the surface. Hence, shot peening parameters have to be varied from material to material in order to achieve optimum fatigue strength enhancement.

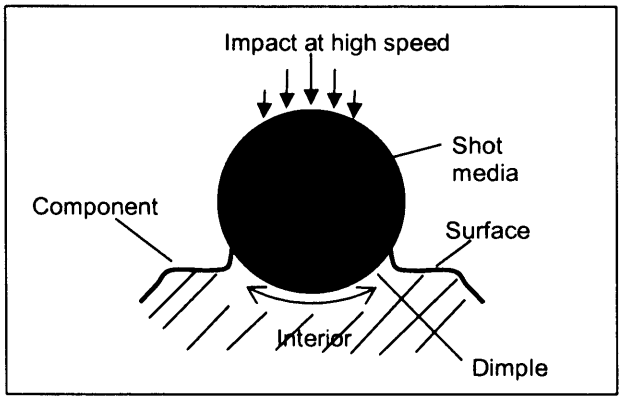

Figure 1.15: Simple illustration of the mechanism of shot peening

Shot peening intensity can be varied by using different shot media size, shot media, impingement angle and shot stream velocity. The shot peening intensity, or sometimes known as the energy of the shot stream, is measured by using Almen Intensity [1.56]. J. O. Almen introduced the Almen Strips/Blocks to characterise shot peening intensity in an effort to achieve process repeatability and standardisation. During shot peening, the induced residual stress will cause the Almen Strip to bend and Almen found that the deflection of the Almen Strip is a function of the shot peening intensity. Almen Strips are classified into "N", "A" and "C" Strip according to their corresponding thickness with "N" strip being the thinnest. Generally, shot peening process with "N" Almen Intensity is regarded as mild peening while "C" Almen Intensity is used for heavy peening. Coverage control (percentage of surface being peened) during shot peening is important in order to ascertain the introduction of a uniform distribution of surface residual stress onto the component. For metallic surfaces, the common coverage used is between 100% to 200% and it is commonly known in the shot peening industry that a coverage of 200% is sufficient for peening saturation to take place for most structural steels.

During its introduction to manufacturing processes in the 1940s, shot peening was regarded as a "specialised" technique and its application was only available or used in the aviation and automotive industries. However, significant development have been achieved during the last two decades, making shot peening a considerably less expensive surface treatment method and it has been successfully employed in various industries such as offshore, construction, shipping etc. Shot peening is extensively employed in manufacturing processes due to its advantage to be able to provide surface treatment to small and complex components. From aircraft landing gear to

engine crank shaft, offshore structures to gas turbine rotor components, shot peening has been the leading surface treatment method. Since the recognition and utilisation of shot peening, many studies have been conducted to evaluate optimum shot peening conditions and its effect on metal fatigue [1.57–1.60]. Farrahi et al [1.58] stated that the three main factors that effect the mechanical properties of the shot peened parts are:

- Strain hardening of surface layers which increases the yield stress of the shot peened material
- Compressive residual stress induced in surface layers
- Quality of the final surface finish

As stated previously, compressive residual stress is beneficial to the fatigue endurance of a material since it is widely known that cracks will not initiate or propagate in a compressed stress zone. The following presents an incomplete list of studies which demonstrate the effect of shot peening residual stress on the fatigue performance of structural components. A Norwegian research programme [1.61] concluded that the combination of weld toe grinding and shot peening contributed to a significant improvement in the fatigue life of offshore steel welded joints. As-weld toe grinding only gave a 30% increase in the fatigue life, the combination of weld toe grinding and shot peening was shown to provide more than 100% increase in the as-welded strength at one million cycles. A fatigue study on cracked aluminium and steel plates to control crack growth was conducted by NASA engineers by using the shot peening technique. One of their major findings include that crack growth was significantly delayed in the shot peened specimens. In addition, the benefits of shot peening also demonstrated 81 to 217% increase in fatigue endurance of the specimens [1.62]. In a stress corrosion cracking study of A212B steel [1.63], a fatigue enhancement of up to 15 to 30 fold could be observed when compared to as welded test specimens.

1.4.2 Measurement of Residual Stress

Determination of induced residual stress distribution is important in investigating the fatigue performance of a component since residual stresses are widely recognised to have a profound effect on the fatigue resistance of structural components. Extensive amount of quantitative and qualitative residual stress measurement techniques have been developed, in parallel with the advancement of computer and NDT technology. Fig. 1.16 below illustrates the popularity of residual stress measurement techniques among one of the leading institutions in the field. The data is obtained from a round-robin survey recently conducted by the National Physics Laboratory (NPL, UK) [1.64]. As can be seen from the figure, the hole-drilling technique is the most widely

used method followed by X-ray diffraction and neutron diffraction techniques. Comparison of the major residual stress measurement techniques can be found in Table 1.1 on page 29.

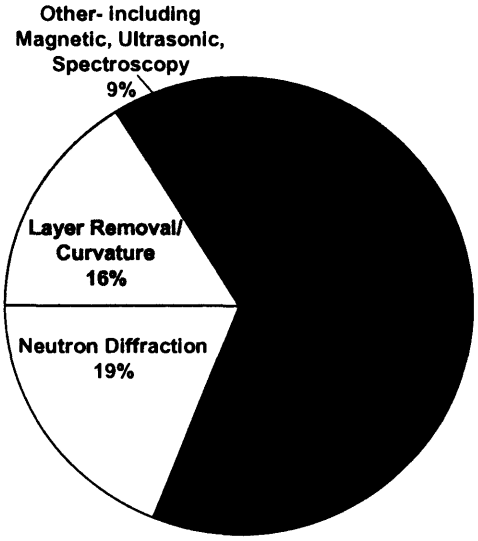

Figure 1.16: Popularity of residual stress measurement techniques [1.64]

In general, residual stress measurement can be classified into destructive or non-destructive techniques. The destructive methods are based on destruction of the state of equilibrium of the residual stress in a component and in these methods, such as the stress-relaxation technique, residual stress is determined by measuring the elastic-strain release that takes place when a particular region in the specimen is cut or removed. This means that one assumes the strains created during unloading are elastic even when the material has undergone plastic deformation. In most cases, electric resistance or mechanical strain gauges are used for measuring the strain change. The data obtained needs to be evaluated to derive the residual stress as a function of strain by using an analytical elastic theory approach or finite element method. An inherent drawback of these techniques is that they are destructive and the process might cause undesired stress distortion. However, the stress-relaxation techniques provide reliable quantitative data and are widely employed for residual stress measurement in weldments. This technique is also used in the study of stress in plates, cylinders, tubes and other three-dimensional components. Some examples of destructive techniques are sectioning, hole-drilling, machining, boring-out and photo-electric coating/drilling.

Method	Contact or Non-contact	Destructive?	In-situ measurement?	Speed	Penetration	Cost	Comment
Hole-Drilling	Contact	Semi	Yes	Medium	Up to 4mm*	Low	*Up to 100mm depth can be achieved using deep hole-drilling
X-ray Diffraction	Non-contact	No*	No	Medium	<50μm for metallic materials	Medium	*Destructive if used for depth profiling Sensitive to surface preparation
Neutron Diffraction	Non-contact	No*	No	Slow	Up to 25mm for steel	High**	*Non-destructive only if specimen is small and portable **Beam time extremely scarce and expensive
Magnetic	Non-contact	No	Yes	Fast*	Up to 10mm	Medium	*Normally requires calibration Sensitive to microstructure and magnetic properties
Ultrasonic	Contact	No	Yes	Fast	>10mm	Medium	Very sensitive to microstructure
Layer Removal/ Curvature	Contact	Yes	No	Medium*	Up to half thickness**	Low	*Depends on specimen preparation **Depth profiling is only available if used incrementally

Table 1.1: Comparison of the residual stress measurement techniques
(Data predominantly obtained from References 1.64-1.66)

The intrinsic nature of non-destructive methods has made them the preferred methods in modern day residual stress measurement. The non-destructive techniques are based upon the relationships between the physical or crystallographic parameters and residual stresses [1.65]. This is the main advantage of the non-destructive method since it does not tamper with the state of equilibrium of the material, which may cause stress distortion, redistribution or relaxation prior to measurement. Some of the prime examples of non-destructive residual stress measurement techniques are X-ray diffraction, neutron diffraction, magnetic and ultrasonic methods. The X-ray and neutron diffraction methods are applied in metals that have crystalline structures, where elastic strains can be determined by measuring the lattice parameter. Before the mapping of the residual stress distribution can be performed, the lattice parameter of the material in the unstressed state must be determined. The X-ray technique in particular is one of the rare and reliable methods available for the measurement of residual stress in complex components like gear teeth [1.67] and ball bearings [1.68].

The two major ultrasonic methods developed are the polarised ultrasonic wave technique and the ultrasonic attenuation technique [1.65]. The former makes use of a stress-induced change in the angle of polarisation of polarised ultrasonic waves, while the latter employs stress-induced change in the rate of absorption of ultrasonic waves. The variations in the flight time difference and velocity shift recorded is used to correlate with the residual stress state. Finally, the magnetic method is based on the interaction between magnetisation behaviour and elastic strain in ferromagnetic materials.

The following sections discuss several residual stress measurement techniques. For clarity, only the methods relevant to the present study are reported. These include the neutron diffraction technique and the hole-drilling methods.

1.4.2.1 Neutron Diffraction Methods

Neutrons are fundamental subatomic elementary particles in atomic nuclei which have no electrical charge. The neutron sources, like any synchrotron sources, provide a white beam without sharp peaks of characteristic radiation, which necessitates the use of a monochromator to obtain a monochromatic beam suitable for use in residual stress measurement [1.64]. Hence, in many ways, neutron diffraction technique for measuring residual stress functions is similar to the X-ray methods.

When a neutron beam with wavelength, λ, impinges on a specimen, a diffraction pattern with sharp maxima can be observed [1.69]. The diffraction angle and the wavelength of the maxima can be expressed using Bragg's equation:

$$2d\sin\theta = n\lambda \qquad \text{- (1.23)}$$

where d is the crystallographic planes separation/interplanar spacing
n is an integer (order of deflection)
λ is the wavelength of incident beam
θ is the diffraction angle between incident/reflected beam and surface of reflecting planes

The lattice spacing for a material is a constant in its unstressed state. However, the lattice spacing will vary accordingly to the applied stress, due to elastic deformation. For a monochromatic beam with a constant wavelength, by Bragg's law, the relation between the lattice elastic strain and lattice spacing can be determined as follows [1.65]:

$$\varepsilon = \frac{\Delta d}{d_0} = -\Delta\theta\cot\theta_0 \qquad \text{- (1.24)}$$

where ε is the elastic strain
Δd is the change in lattice spacing
d_0 is the lattice spacing in the unstressed state
$\Delta\theta$ is the shift in the angular position of the Bragg deflection
θ_0 is the original angular position of the Bragg deflection

Equation 1.23 shows that if the wavelength of the incident beam is known, the interplanar spacing, d, can be determined by measuring the diffraction angle. Subsequently, the elastic strain change in the material during the introduction of residual stresses can be evaluated using Equation 1.24. It is worth mentioning that the X-ray method only provides accurate stress distributions at shallow layers of materials (refer to Table 1.1) while the neutron diffraction technique is able to provide results at much greater depth. However, the X-ray method is normally preferred when only near-surface residual stress data is required due to its higher spatial resolution and considerably lower measurement time.

A typical set-up of residual stress measurement by using neutron diffraction method is shown in Fig. 1.17 below [1.69]. According to Webster et al, a typical acceptable minimum volume size is about 8mm^3, which can be in the form of 2 x 2 x 2 or 1 x 10 x 1 mm^3 'match-stick' shape if stress variation along one of the axis of the specimen is negligible.

The utilisation of neutron diffraction in residual stress measurement is growing rapidly due to its reliability and robustness. The accuracy of diffraction peaks are reported to be within 0.01 degree

and positioning accuracy of ±0.1mm can be achieved by using modern technology [1.64, 1.65]. The development of neutron diffraction technique has enabled residual stresses measurement at complex structures or geometric discontinuity such as weld toe, to be obtained at high accuracy. This level of accuracy, which can be achieved non-destructively, has made it the preferred method compared to conventional stress relaxation or ultrasonic/magnetic methods. However, this technique is widely considered to be expensive and time-consuming. For example, residual stress profiling in the depth direction for a 50mm-thick steel plate will usually take 24 hours (refer Section 3.3.2) and the facility rental can typically cost up to 2000 GBP per day [1.64]. Neutron diffraction is generally regarded as a non-destructive technique due to its measurement procedure but in practice this is only true if the specimen being measured is considerably small. Since the neutron diffraction technique is a fully laboratory-based method, very often samples are to be extracted from the original component for measurement purposes, due to logistical issues or the location of interest on the component might prevent the application of the technique.

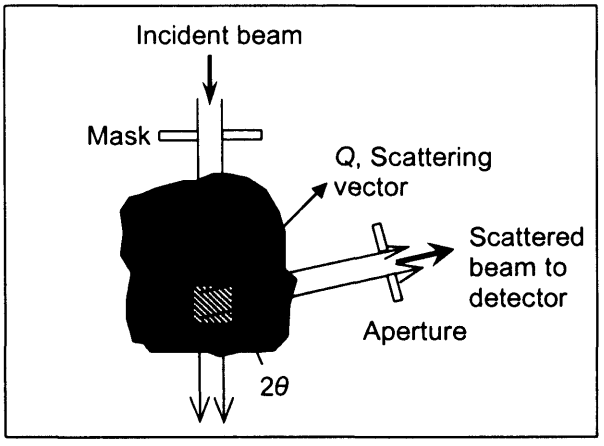

Figure 1.17: Typical set-up of a neutron diffractometer

1.4.2.2 Hole-Drilling Methods

The hole-drilling method of measuring residual stress was first proposed and used by Mathar [1.70] and was later developed by Soete [1.71] and Suppiger et al [1.72]. There are two different types of hole-drilling techniques; the centre-hole-drilling and ring core methods. Both techniques are semi-destructive since the material being removed is normally considerably small compared to the parent component. In the centre-hole-drilling method, a small circular hole (typically 1-4mm) is drilled in the specimen and the residual stresses in areas outside the hole are measured by using strain gauges (Fig. 1.18a). The residual stresses that existed in the drilled area are determined by measuring the amount of stress relaxation that occurs in the vicinity of the drilled hole. Strain relaxation/relief readings obtained from the strain gauge rosette are used to calculate the magnitude of the principal stress components. In contrast, in the ring core method, a ring

core, typically 15 - 50mm, is machined and the relieved strain is measured on the surface inside the ring using strain gauges (Fig. 1.18b). Since only the centre-hole-drilling method is to be employed in this study, the ring core method will not be discussed further.

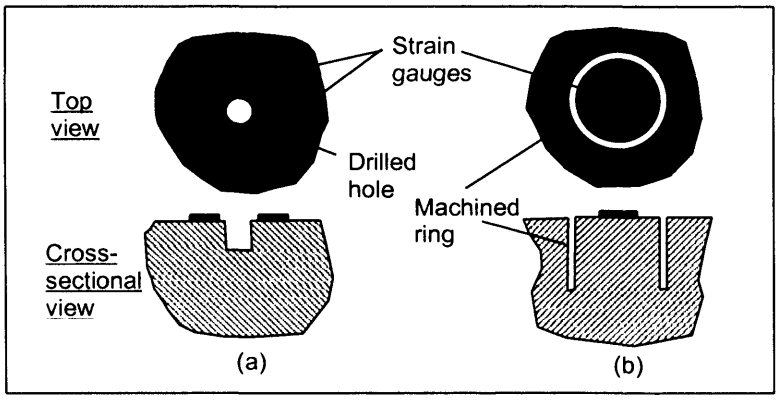

Figure 1.18: (a) Centre-hole-drilling technique (b) Ring-core technique

The hole-drilling technique is usually the preferred method over the ring core technique as the material destruction involved is minimal. In addition, it provides more localised residual stress measurements. It has been reported that the loss of sensitivity due to the distance between the gauges and the hole can be problematic while the relatively small dimension of the hole means that any error or eccentricity will lead to significant errors in the residual stress measurement. However, newly developed strain gauges and advance strain data analysis have greatly reduced these shortcomings. Despite these disadvantages, the hole-drilling method, being relatively inexpensive and simple, is the most widely used semi-destructive residual stress measurement technique. Consistent application of the technique has proven to yield good measurement results.

The centre-hole-drilling method can be stratified into the through-hole and the blind-hole technique. The through-hole technique is used where the specimen's thickness is sufficiently thin for a through-thickness-hole to be drilled. Since ordinary machine parts or structural components requiring residual stress analysis may be of any shape or size, and are rarely thin, the blind-hole-drilling is more widely used [1.73]. In the blind-hole technique, the strain relief measurement is taken at a hole-depth of approximately its diameter. The incremental centre-hole drilling (ICHD) technique is a variant of the blind-hole technique and it is implemented for residual stress profiling in the depth direction of a relatively thick specimen. This involves drilling a small hole in a series of steps using a high-speed pneumatic drill (drilling speed = 400,000rpm) until the depth of interest is reached and the corresponding strain relaxations at each depth increment are recorded using a strain recorder. The strain relaxation measurement data can be analysed using various

theoretical models with the Incremental Strain, Equivalent Uniform Stress, Integral or Power Series method being the most established. The ICHD technique coupled with the Equivalent Uniform Stress and the Integral Method were employed in the present study. The specialised hole-drilling equipment can be seen in Fig. 1.19 [1.73] below. The hole-drilling procedures will be further discussed in Chapter 5 while the analyses of the hole-drilling data are presented in Chapter 6.

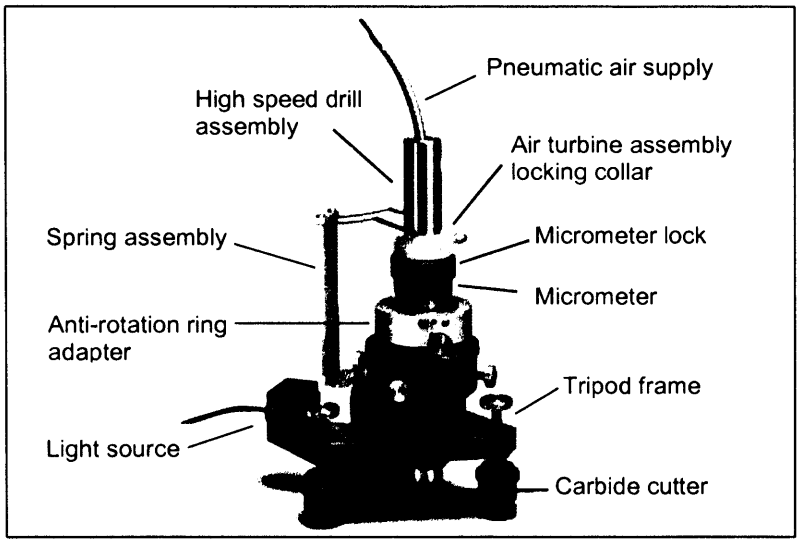

Figure 1.19: The RS-200 Milling guide used in the ICHD technique

Since its recognition in the 1930's, the hole-drilling technique has gone through phases of changes. Recently, Smith et al [1.74] developed the deep-hole-drilling technique that enables one to perform full-depth residual stress measurement of components with thickness up to 100mm. The hole was introduced by electrodischarge trepanning and the strain relaxation is based on the change in the drilled hole diameter measured by using an Air Probe. In order to eliminate the limitation caused by the usage of strain gauges in measuring the strain relaxation, new techniques have been developed to combine with the hole-drilling technique. For example, Nelson et al [1.75] developed the holographic-hole-drilling method for residual stress determination. The strain changes caused by localised stress relief are measured by real time holographic interferometry. The use of optical methods in measuring the strain changes is explored in depths by various research studies [1.76, 1.77]. The combination of optical methods with hole-drilling technique has enabled the "actual" localised residual stress relaxation at the prescribed area to be measured.

1.4.3 Residual Stress Relaxation Due to Cyclic Loading

Residual stresses can relieve or redistribute during thermal or mechanical loading and the relaxation process is widely seen as a result of cyclic plastic strain. The following discussion will concentrate on the relaxation of compressive residual stress due to cyclic loading. Surface compressive residual stresses have been proven to be beneficial since fatigue cracking normally initiates at the surface. Hence, any cyclic residual stress relaxation during operations is unfavourable and the resistance to relaxation of the induced residual stress is pertinent for the structural integrity assessment of any surface-treated components. During cyclic loading, it is generally regarded that if the sum of the residual stress and the maximum or minimum applied stress exceeds the yield strength of the material, the resulting residual stress will be equal to the yield strength minus the maximum or minimum applied stress. This concept assumes that the strain hardening effect is negligible.

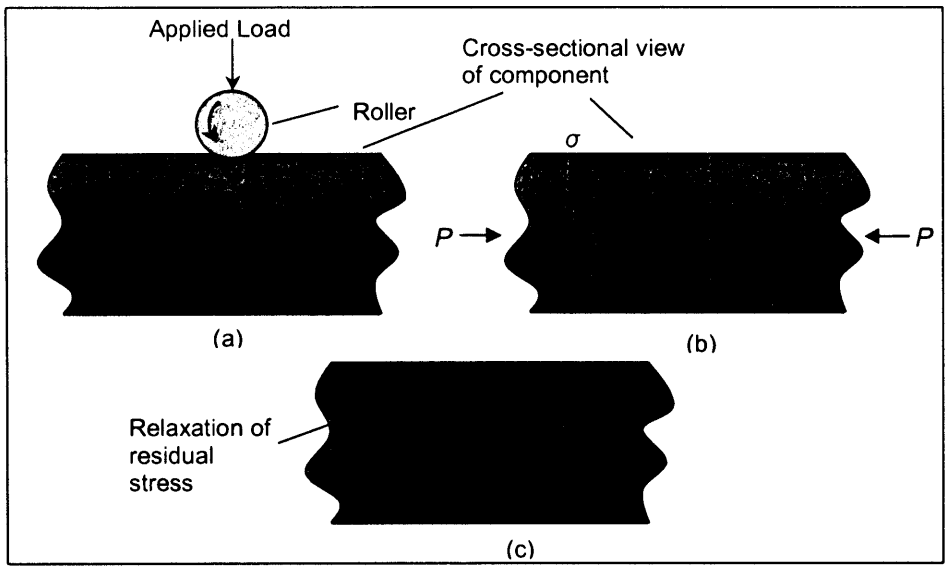

Figure 1.20: (a) Induction of residual stress by cold rolling; (b) Proof loading; (c) Relaxation of residual stress

For clarity, the aforementioned mechanism is elaborated with the aid of Fig. 1.20 above. Let us assume that the initial residual stress distribution introduced onto the surface of the component by localised cold rolling is indicated by σ_R (Fig. 1.20a). When a compressive load, P, is applied to the component, the resultant residual stress distribution will be as indicated by σ_{R1}. Consider that the yield strength of the material is indicated by σ_y and according to the Proof Loading theory the maximum resultant residual stress distribution will be unable to 'grow' beyond the shaded line and the stress distribution takes the shape shown in Fig. 1.20b. When the structure is unloaded, the estimated residual stress distribution will be σ_{R2}, as illustrated in Fig. 1.20c.

Many studies have been carried out investigating the behaviour of residual stress during fatigue cycling. However, the phenomenon and mechanism of stress relaxation are still not clear, and only a few predictive models have been proposed to estimate the degree of residual stress decay during cyclic loading. Several combinations of load and material have been investigated and some relaxation models have been put forward. It is impossible for this thesis to include all the models proposed, and hence only the major ones are reported. One of the earliest research studies on prediction of residual stress relaxation was conducted by Morrow-Sinclair [1.78]. They conducted strain-controlled axial fatigue tests on surface-treated SAE 4340 steel specimens and obtained mean stress relaxation data as a function of the number of strain repetitions. Based on the data obtained, a relationship between mean stress and number of fatigue cycles was proposed:

$$\frac{\sigma_{mN}}{\sigma_{m1}} = \frac{\sigma_y - \sigma_a}{\sigma_{m1}} - \left(\frac{\sigma_a}{\sigma_y}\right)^b \log N \qquad \text{- (1.25)}$$

where σ_{mN} is the mean stress at the Nth cycle
σ_{m1} is the mean stress at the first cycle
σ_a is the alternating stress amplitude
σ_y is the material yield strength
b is a constant dependent on material softening and applied strain range, $\Delta\varepsilon$
N is the number of stress cycles

Following Morrow's work, Jhansale-Topper [1.79] demonstrated how residual stress varies as an exponential decay function towards zero, or to an asymptotic non-zero value. They observed a linear relationship between the remaining residual stress magnitude with the number of fatigue cycles when plotted in logarithmic scale and a residual stress decay model which enables the remaining residual stress to be calculated easily was put forward. Equation 1.26 below shows the Jhansale-Topper residual stress decay equation:

$$\sigma_{rN} = \sigma_{r0}(N)^r \qquad \text{- (1.26)}$$

where $\sigma^e{}_N$ is the surface residual stress after N stress cycles
σ_{r0} is the initial residual stress
r is the relaxation exponent as a function of the applied strain amplitude, $\Delta\varepsilon$

Landgraf [1.80, 1.81] confirmed the trend observed by Jhansale-Topper but he found that there was a certain strain/stress range where the relaxation was virtually zero in the shot peened SAE 1045 spring steel specimens subjected to fatigue cycling. The surface residual stress measurement data was obtained by using the X-ray diffraction technique. He popularised the above equation by introducing a threshold strain amplitude, $\Delta\varepsilon_{th}$, into the relaxation exponent, below which residual stress relaxation will not be expected to occur. Landgraf suggested that the relaxation exponent, r, can be related to $\Delta\varepsilon_{th}$ using Equations 1.27 and 1.28 below:

$$r = 8.5\times10^{-2}\left(1-\frac{\Delta\varepsilon}{\Delta\varepsilon_{th}}\right) \quad \text{- (1.27)}$$

$$\Delta\varepsilon = 2\cdot\exp\left[-8.41+5.36\times10^{-3}\times HB\right] \quad \text{- (1.28)}$$

where HB is the material's hardness in Brinell Hardness

Landgraf showed that the above equations are valid for a wide range of carbon steels. In addition to the validation of the model in a series of his own research studies, comparison was made with an earlier study by Mattson-Coleman [1.82] conducted on SAE 5160 specimens and very good agreement between the X-ray residual stress measurement data and the residual stress decay model was reported.

Kodama [1.83] studied the relaxation of residual stress on annealed mild steel specimens. The X-ray diffraction technique was employed for the measurement of surface compressive residual stresses induced by shot peening. He concluded that the degree of relaxation was governed by the stress range applied and a logarithmic relationship between the remaining residual stress and the number of stress cycles could be observed. However, Kodoma stated that the logarithmic relationship should not include the remaining compressive residual stress at the first cycle as a considerably more drastic relaxation was observed (≈50%) when compared with the subsequent values. The residual stress relaxation prediction model proposed by Kodoma can be written as:

$$\sigma_N^{re} = A + m\log N \quad \text{- (1.29)}$$

where A is a material constant depending on the applied stress range
m is a material constant depending on the applied stress range

The residual stress relaxation relationship proposed by Kodoma was observed by Holzapfel [1.84] et al in a recent study on AISI 4140 steel. However, Castex [1.85] found that Equation 1.29 is

only true if the applied stress amplitude is above the endurance limit, otherwise the residual stress in the mild steel specimens being studied remained unchanged up to 10^5 fatigue cycles. In other words, this observation actually further supports Landgraf's proposal of introducing a threshold strain amplitude into the Jhansale-Topper model. This is contrasted by a study of relaxation of residual stresses on cold-expanded fastener holes conducted by Özdemir-Edwards [1.86]. They concluded that relaxation of the compressive residual stress field around a cold expanded hole occurs even when the applied stress range is below the endurance limit and the rate of relaxation is mainly governed by the propagation of fatigue short cracks (if present). In a study recently conducted on shot peened 60SC7 spring steel by Farrahi et al [1.58], a logarithmic residual stress decay can also be observed. They concluded that fatigue cycling produces a decrease in residual stresses and in micro-strain and the reductions are a function of the applied stress amplitude and the depth of the plastically deformed layer. However, no residual stress relief model is derived due to the lack of data. One of the most recent proposed models is the analytical residual stress relaxation model by Zhuang et al [1.87]. The proposed model incorporates the initial cold work effect and also takes into account a local reversed flow strength function, which are detailed in Reference 1.87. The analytical model derived was further validated using Finite Element Analysis. Based on the cold work relaxation concept and the Bauschinger effect, the prediction of residual stress relaxation is proposed as:

$$\frac{\sigma_N^{re}}{\sigma_0^{re}} = A\left(\frac{2\sigma_a^2}{(1-R)(C_w\sigma_y)^2}\right)^m (N-1)^B - 1 \qquad \text{- (1.30)}$$

where σ_0^{re} is the initial residual stress

A is a material constant dependent on cyclic stress and strain response

σ_a is the cyclic stress amplitude

R is the stress ratio

C_w is a parameter which accounts for the degree of cold working

m is a material constant

B is a constant that controls the relaxation rate versus loading cycles

Equations 1.26-1.28 (often known as the Landgraf Residual Stress Decay Model) above are considered to be one of the most extensively used relaxation model due to the fact that the exponential residual stress decay can be observed in various studies. In addition, the model contains parameters which can be easily determined experimentally or found in many published papers and standards. On the contrary, some of the parameters in other models, for example Equations 1.29 and 1.30, are not clearly defined or are difficult to be evaluated. Due to its

simplicity and the availability of material data, the residual stress monitoring data obtained in the present study will be compared to Landgraf's residual stress decay model and the results can be found in Chapter 6.

1.5 Summary and Overview of Thesis

This chapter presented a review of the pertinent issues related to the investigation of the influence of surface residual stress on fatigue crack growth. The fundamentals of the stress-life approach and the fracture mechanics approach were briefly discussed. The sources of residual stresses and the current most-adopted residual stress measurement techniques were discussed in detail. The comparison of the available residual stress measurement techniques has enabled the most suitable methods for the present study to be identified. Review of the published residual stress relaxation models clearly shows that residual stress decay due to cyclic loading is an extremely challenging topic and further work is needed to better understand this phenomenon.

The primary objectives of this Ph.D. research study can be summarised as follows:

1. The development of a stationary standardised load-time sequence for variable amplitude corrosion fatigue testing of jack-up structural components in parallel with the experimental investigation of the long-life corrosion fatigue performance of SE 702 steel.

2. The investigation of the characteristics of residual stresses present in T-butt welded joints induced by welding and its influence on fatigue crack growth.

3. The development and implementation of stitch cold rolling and stitch shot peening techniques in fatigue crack shape control.

4. A quantitative understanding of residual stress and its effect on fatigue crack shape evolution through residual stress monitoring.

Chapter 2 reports the modification work conducted on Jack-up Offshore Standard load History (JOSH). This enabled the development of a stationary load-time sequence representative of the loading conditions of a North Sea jack-up structure. The significance of the stationary aspect of the load-time sequence parameters is shown using relevant sequence analyses.

Chapter 3 presents the fatigue testing of SE 702 high strength steel. The variable amplitude load-time sequence developed in Chapter 2 was employed in the long-life corrosion fatigue tests. The

residual stresses arising from welding were measured and its influence on the fatigue crack growth in the test specimens was analysed using LEFM crack growth models. The effect of cathodic protection on the variable amplitude corrosion fatigue performance of SE 702 is investigated and rigorously compared to previous studies.

Chapter 4 concerns the application and feasibility of preferential cold working in controlling fatigue crack growth. The newly developed stitch cold rolling technique was successfully employed in introducing surface compressive residual stress onto the mild steel specimens being fatigue tested and its influence on the fatigue crack shape evolution is studied.

Chapter 5 illustrates the extension of the preferential cold working technique by using stitch shot peening. Large scale fatigue testing of axial mild steel specimens has enabled the fatigue crack growth behaviour in surface compressive residual stress field to be investigated. A unique residual stress monitoring programme was conducted to better understand the residual stress relaxation due to cyclic loading and its effect on fatigue crack growth.

Chapter 6 presents the analytical work conducted on the experimental results obtained from the fatigue tests described in Chapter 5. The residual stress monitoring data were analysed using the Equivalent Uniform Stress Method and the Integral Method. The results illustrate the difference between the methods and its significance on the measured residual stress profile. A detailed error analysis on the strain hardening effect induced by shot peening is also included. This chapter also demonstrates how the residual stress measurement data were utilised to develop a residual stress decay model. This model was successfully incorporated into the SIF weight function for the fatigue life prediction and simulation of crack shape evolution of the stitch peened specimens.

Chapter 7 reviews the research work conducted and draws conclusions based on the present findings. Future work is discussed and several recommendations are put forward for further understanding of fatigue crack growth in residual stress field.

1.6 References

[1.1] Schütz W., "A History of Fatigue", *Engng Fract Mech*, Vol. 54, No. 2, 1996, pp. 263-300.

[1.2] Wöhler A., "Versuche zur Ermittlung der auf die Eisenbahnwagenachsen einwirkenden Kräfte und die Widerstandsfähigkeit der Wagen-Achsen", *Zeitschrit für Bauwesen*, X, 1860, pp. 583-616.

[1.3] Palmgren A., "Durability of Ball Bearings", *Z Ver Deut Ing*, Vol. 68, 1923, pp. 339-341.

[1.4] Miner M. A., "Cumulative Damage in Fatigue", *J Appl Mech*, Vol. 12, 1945, pp. A159-A164.

[1.5] Health and Safety Executive (UK), "Steel", Offshore Technology Report 2001/015, Health and Safety Executive (UK), United Kingdom, 2002.

[1.6] British Standards Institute, "BS EN 10025:2004 – Hot Rolled Products of Non-Alloy Structural Steels", British Standards Institute, 2004.

[1.7] Health and Safety Executive (UK), "Fatigue Design Curves for Welded Joints in Air and Seawater Under Variable Amplitude Loading", Offshore Technology Report - OTO 1999 058, Health and Safety Executive (UK), 2000.

[1.8] Barke J. C., "Data Surveys of Hydrogen Assisted Cracking in High-Strength Jack-up Steels", Offshore Technology Report - OTO 97 072, Health and Safety Executive (UK), 1998.

[1.9] Abernethy K., Fowler C. M., Jacob R. and Dvey V. S., "Hydrogen Cracking of Legs and Spudcans on Jack-up Drilling Rigs- A Summary of Results of An Investigation", HSE Report - OTO 91 351, Health and Safety Executive (UK), 1992.

[1.10] Sharp J. V., Billingham J. and Robinson M. J., "The Risk Management of High-Strength Steels in Jack-ups in Seawater", *Marine Struct*, Vol. 14, 2001, pp. 537-551.

[1.11] Gurney T. R., "Fatigue Tests on Fillet Welded Joints Under Variable Amplitude Loading", TWI Report 293/1985, November 1985.

[1.12] Tilly G. P. and Nunn D. E., "Variable Amplitude Fatigue in Relation to Highway Bridges", In: *Proc Institute Mechanical Engng*, Vol. 194, 1980, pp. 259.

[1.13] Gibstein M. B. and Moe E. T., "Fatigue of Tubular Joints", In: Fatigue Handbook of Offshore Steel Structures, Ed: Almar-Naess A., Tapir Academic Press, 1985, pp. 313-370.

[1.14] United Kingdom Offshore Steels Research Project - Phase I: Final Report, Ed: Peckover R., Health and Safety Executive Report OTH 88 282, Her Majesty's Stationary Office, London, 1988.

[1.15] Wylde J. G. and Mcdonald A., "The Influence of Joint Dimensions on Fatigue Strength of Welded Tubular Joints", In: *Proc Int Conf Behaviour of Offshore Struct*, 1979, Paper 42.

[1.16] Berge S., "On the Effect of Plate Thickness in Weldments", *Engng Fract Mech*, Vol. 21, No. 2, 1985, pp. 423-435.

[1.17] Gurney T. R., "The Influence of Thickness on Fatigue of Welded Joints – 10 Years On", In: *Proc 8th Int Conf Offshore Mech Artic Engng*, 1989.

[1.18] Gurney T. R., "Thickness Effect in 'Relatively Thin' Welded Joints", The Welding Institute and Health & Safety Executive (UK), Offshore Technology Report OTH 91 358. 1995.

[1.19] Webster S. E. and Walker E. F., "The Effect of Section Thickness on the Fatigue Performance of Welded and Cast Steel Joints", In: *Proc 2nd Intl Conf Fat & Fat Threshold*, Ed: Beevers C. J., 1984.

[1.20] Rhee H. C. and Salama M. M., "Opportunities for Application of Fracture Mechanics for Offshore Structures", *Fract Mech Offshore Industry*, Reprinted from Applied Mechanics Reviews, ASME Book No. AMR032, Vol. 41, No. 2, 1998.

[1.21] Dharmavasan S. and Dover W. D., "Nondestructive Evaluation of Offshore Structures Using Fracture Mechanics", *Fract Mech Offshore Industry*, Reprinted from Applied Mechanics Reviews, ASME Book No. AMR032, Vol. 41, No. 2, 1998.

[1.22] Etube L. S., "Fatigue and Fracture Mechanics of Offshore Structures", Engineering Research Series - ERS-4, Professional Engineering Publishing Ltd., ISBN 1 86058 312 1, 2001.

[1.23] Hsu T. M., Carter E. W., Fu S. L. and Mitchell J. S., "Application of Fracture Mechanics Methodology to Assessment of Weld Defects in Offshore Platforms", In: *Proc 5th Int Conf Civil Engng Oceans*, 1992, pp. 733-749.

[1.24] Anderson T. L., "Fracture Mechanics- Second Edition", CRC Press, ISBN 0 84934260 0, 1995.

[1.25] Pook L. P., "Linear Elastic Fracture Mechanics for Engineers - Theory and Application", WIT Press, ISBN 1 85321 703 5, 2000.

[1.26] Tada H., Paris P. C. and Irwin G. R., "The Stress Analysis of Cracks Handbook", Del Research Corporation, Pennsylvania, 1973.

[1.27] Sih G. C., "Handbook of Stress Intensity Factors", Institute of Fracture and Solid Mechanics, Lehigh University, Pennsylvania,1973.

[1.28] Rooke D. P. and Cartwright D. J., "Compendium of Stress Intensity Factors", Her Majesty's Stationary Office, London, 1976.

[1.29] Murakami Y. and Tsuru H., "Stress Intensity Factors Handbook", Vol. I-II, Pergamon Press, ISBN: 0 08 034809 2, 1987.

[1.30] Murakami Y. and Tsuru H., "Stress Intensity Factors Handbook", Vol. III, Pergamon Press, ISBN: 0 08 034809 2, 1991.

[1.31] Newman J. C. Jr. and Raju I. S., "Empirical Stress-Intensity Factor Equation for The Surface Crack", *Engng Fract Mech*, Vol. 15, No. 1-2, 1981, pp. 185-192.

[1.32] Brennan F. P., Dover W. D., Kare R. F. and Hellier A. K., "Parametric Equations for T-Butt Weld Toe Stress Intensity Factors", *Int J Fat*, Vol. 21, 1999, pp. 1051-1062.

[1.33] Etube L. S., Brennan F. P. and Dover W. D., "New Method for Predicting Stress Intensity Factors in Cracked Welded Tubular Joint", *Int J Fat*, Vol. 22, No. 6, 2000, pp. 447-456.

[1.34] Shao Y. B. and Tjhen L .S., "Parametric Equation of Stress Intensity Factor for Tubular K-Joint Under Balanced Axial Loads", *Int J Fat*, Vol. 27, No. 6, 2005, pp. 666-679.

[1.35] Bueckner H. F., "A Novel Principle for the Computation of Stress Intensity Factors", *Z Angew Math Mech*, Vol. 50, 1970, pp. 529-546.

[1.36] Fett T. and Munz D., "Stress Intensity Factors and Weight Functions", *Advances in Fract Series*, Computational Mechanics Publications, ISBN 1 831 497 4, 1997.

[1.37] Rice J. R., "Some Remarks on Elastic Crack-tip Stress Fields", *Int J Solids Struct*, Vol. 8, 1972, pp. 751-758.

[1.38] Petroski H. J. and Achenbach J. D., "Computation of the Weight Function from a Stress Intensity Factor", *Engng Fract Mech*, Vol. 10, 1978, pp. 257-266.

[1.39] Fett T., Mattheck C. and Munz D., "On the Calculation of Crack Opening Displacement from the Stress Intensity Factor", *Engng Fract Mech*, Vol. 27, 1987, pp. 697-715.

[1.40] Brennan F. P., "Evaluation of Stress Intensity Factors by M.R.S. Weight Function Approach", *Theoretical Appl Fract Mech*, Vol. 20, 1994, pp. 249-256.

[1.41] Ojdrovic P. R. and Petroski H. J., "Weight Functions from Multiple Reference States and Crack Profile Derivatives", *Engng Fract Mech*, Vol. 39, 1991, pp. 105-111.

[1.42] Impellizzeri L. F. and Rich D. L., "Spectrum Fatigue Crack Growth in Lugs", American Society for Testing and Materials, ASTM STP 595, 1976, pp. 320-336.

[1.43] Mattheck C., Munz D. and Stamm H., "Stress Intensity Factors for Semi-Elliptical Surface Cracks Loaded by Stress Gradients", *Engng Fract Mech*, Vol. 18, No. 3, 1983, pp. 633-641.

[1.44] Niu X. and Glinka G., "The Weld Profile Effect on Stress Intensity Factors in Weldments", Vol. 35, 1987, pp. 3-20.

[1.45] Brennan F. P. and Teh L. S., "Determination of Crack-Tip Stress Intensity Factors in Complex Geometries by the Composition of Constituent Weight Function Solutions", *Fat Fract Engng Mater and Struct*, Vol. 27, No. 1, 2004, pp. 1-7.

[1.46] Teh L. S., "Library of Geometric Influences for Stress Intensity Factor Weight Functions", Ph.D. Thesis, University of London, 2002.

[1.47] Burrell N. K., "Controlled Shot Peening to Produce Residual Compressive Stress and Improved Fatigue Life", *Residual Stress for Designers and Metallurgists*, Materials/Metals Working Technology Series, American Society for Metals, 1980, pp. 139-150.

[1.48] Okamoto A. and Nakamura H., "Influence of Residual Stress on Fatigue Cracking", *J Pressure Vessel Technol, Transaction of the ASME*, Vol. 112, No. 3, 1990, pp. 199-203.

[1.49] Han S. K., "Fatigue and Fracture Mechanics Analysis of Components Containing Residual Stress Fields", Ph.D. Thesis, University of London, 2002.

[1.50] Knight M. J., Brennan F. P. and Dover W. D., "Fatigue Improvement of Threaded Connections by Cold Rolling", *J Strain Analysis Engng Design*, 2005, pp. 83-93.

[1.51] Maddox S. J., "Fatigue Strength of Welded Structure - Second Edition", Abington Publishing, ISBN 185573 013 8, 1991.

[1.52] Hammersley G., Hackel L. A. and Harris F., "Surface Prestressing to Improve Fatigue Stength of Components by Laser Shot Peening", *Optics Lasers Engng*, Vol. 34, 2000, pp. 327-337.

[1.53] Mackinnon J. A. and Pook L. P., "Residual Stress Measurement in Cold-Rolled Mild Steel", *Exper Techniq*, Vol. 11, No. 9, 1987, pp. 15-17.

[1.54] Benamar A., Inglebert G., Lu J., Flavenot J. F. and Barbarin P., "Study of Strengthening of An Austenitic Stainless Steel by Cold Rolling (Theoretical and Experimental Approach", In: *Proc 2006 SEM Conf Expo Exper Appl Mech*, 2006, pp. 1510-1517.

[1.55] Timoshenko S. P., "History of Strength of Materials", McGraw Hill Book Company Inc., ISBN 0486611876, 1953.

[1.56] Almen J. O. and Black P. H., "Residual Stress and Fatigue in Metals", McGraw Hill Book Company Inc., ISBN 0486611876, 1963.

[1.57] Misumi M., Ohhashi T. and Ohkubo M., "Effect of Shot-Peening on Surface Propagation in Plane-bending Fatigue", *Advances in Surface Treatment*, Vol. 3, Pergamon Books Ltd., ISBN 0 08 033464 4, 1986, pp. 55-74.

[1.58] Farrahi G. H., Lebrun J. L. and Courtain D., "Effect of Shot Peening on Residual Stress and Fatigue Life of a Spring Steel", *Fat Fract Engng Mater Struct*, Vol. 18, No. 2, 1995, pp. 211-220.

[1.59] Wang S. P., Li Y., Yao M. and R. Wang, "Fatigue Limit of Shot-Peened Metals", *J Mater Processing Technol*, Vo. 73, 1998, pp. 57-63.

[1.60] Gao Y. K., Yao M., Shao P.G. and Zhao Y. H., "Another Mechanism for Fatigue Strength Improvement of Metallic Parts by Shot Peening", *J Mater Engng Performance*, Vol. 12, 2003, pp. 507-511.

[1.61] Haagensen, "Prediction of the Improvement in Fatigue Life of Welded Joints Due to Grinding", TIG Dressing, *Weld Shape Control and Shot Peening*, The Norwegian Institute off Technology, Trondheim, 1993.

[1.62] Dubberly, Everett, Matthews, Prabhakaran and Newman, "The Effects of Shot and Laser Peening on Crack Growth and Fatigue Life in 2004 Aluminium Alloy and 4340 Steel", US Air Force Structural Integrity Conference, 2000.

[1.63] Gillespie B., "Controlled Shot Peening Can Help Prevent Stress Corrosion", In: *3rd Int Conf Shot Peening*, Garmisch-Partenkirchen, 1987, pp. 149-156.

[1.64] Kandil F. A., Lord J. D., Fry A. T. and Grant P. V., "A Review of Residual Stress Measurement Methods – A Guide to Technique Selection", NPL Report MATC(A)04, National Physics Laboratory (UK), 2004.

[1.65] Withers P. J. and Bhadeshia H. K. D. H., "Residual Stress Part 1 – Measurement Techniques", *Mater Sci Technol*, Vol. 17, 2001, pp. 355-365.

[1.66] Flavenot J. F., "Handbook of Measurement of Residual Stresses", Ed.: Lu. J., Society for Experimental Mechanics, Pennsylvania, 2001, pp. 35-48.

[1.67] Gurova T., Teodosio J. R. and Monine V., "Analysis of Residual Stress State in Speed Gears for Automotive Vehicles", In: *Proc SPIE- Int Society Optical Engng*, Vol. 4348, 2001, pp. 308-311.

[1.68] Oquri T., Murata K., Mizutani K. and Uegami K., "Application of X-ray Stress Measuring Technique to Curved Surfaces- Residual Stress on Spherical Surfaces", *Mater Science Research Int*, Vol. 8, No. 2, 2002, pp. 74-81.

[1.69] Webster G. A. and Wimpory R. C., "Non-destructive Measurement of Residual Stress by Neutron Diffraction", *J Mater Processing Technol*, Vol. 117, 2001, pp. 395-399.

[1.70] Mathar J., "Determination of Metal Stress by Measuring the Deformation Around Drill Holes", Transactions of the American Society of Mechanical Engineers, Vol. 86, 1934, pp. 249-254.

[1.71] Soete W., "Measurement and Relaxation of Residual Stresses", *Welding J*, Vol. 28, No. 8, 1949, pp. 354-364.

[1.72] Suppiger E. W., Riparbelli C. and Ward E. R., "The Determination of Initial Stresses and Results of Tests on Steel Plates", *Welding J*, Vol. 30, No. 2, 1951, pp. 91-104.

[1.73] Vishay Micro-Measurements Group Inc., "Measurements of Residual Stresses by the Hole-Drilling Strain Gage Method", Tech Note TN-503-6, Revision 25-01-05, USA, 2005.

[1.74] Smith D. J., Bouchard P. J. and George D. "Measurement and Prediction of Residual Stresses in Thick Section Steel Welds", *J Strain Analysis*, Vol. 39, No. 2, 200, pp. 117-124.

[1.75] Nelson D. V. and Makino A., "The Holographic-Hole Drilling Method for Residual Stress Determination", *Optics Lasers Engng*, Vol. 27, 1997, pp. 3-23.

[1.76] Viotti M. R. and Kaufmann G. H., "Accuracy and Sensitivity of a Hole Drilling and Digital Speckle Pattern Interferometry Combined Technique to Measure Residual Stresses Optics and Lasers in Engineering", Vol. 41, No. 2, 2004, pp. 297-305.

[1.77] Pisarev V. S., Balalov V. V., Aistov V. S., Bondarenko M. M. and Yustus M. G., "Reflection Hologram Interferometry Combined with Hole Drilling Technique as an Effective Tool for Residual Stresses Fields Investigation in Thin-Walled Structures", *Optics Lasers Engng*, Vol. 36, No. 6, 2001, pp. 551-597.

[1.78] Morrow J. and Sinclair G. M., "Cycle-dependant Stress Relaxation", In: *Sympo Basic Mechanisms Fat*, ASTM STP 237, American Society for Testing and Materials, 1958, pp. 83-109.

[1.79] Jhansale H. R. and Topper T. H., "Cyclic Stress-Strain Behaviour – Analysis, Experimentation and Failure Predieciton", ASTM STP 519, American Society for Testing and Materials, 1973, pp. 246-270.

[1.80] Landgraf R. W., "Cyclic Deformation Behavior of Engineering Alloys", In: *Proc Fatigue-Fundamental Applied Aspects*, Sweden, 1977.

[1.81] Landgraf R. W. and Chernenkoff R. A., "Residual Stress Effects on Fatigue of Surface Processed Steels", In: *Analytical Methods for Residual Stress Effects in Fatigue*, ASTM STP 1004, Ed.: Champoux R. L., Underwood J. H. and Kapp J. A., American Society for Testing and Materials, 1988, pp. 1-12.

[1.82] Mattson R. L. and Coleman W. S., "Residual Stress Effects on Fatigue of Surface Processed Steels", In: *Analytical Methods for Residual Stress Effects in Fatigue*, ASTM STP 1004, Ed.: Champoux R. L., Underwood J. H. and Kapp J. A., American Society for Testing and Materials, 1988, pp. 1-12.

[1.83] Kodoma S., "The Behavior of Residual Stress During fatigue Stress Cycles", In: *Proc 2nd Int Conf Mechanical Behavior of Metals*, Society of Material Science, Vol. 2, 1972, pp. 111-118.

[1.84] Holzapfel H., Schulze V., Vöhringer O. and Macherauch E., "Residual Stress Relaxation in an AISI 4140 Steel Due to Quasistatic and Cyclic Loading at High Temperatures", *Mater Sci Engng*, Vol. A248, 1998, pp. 9-18.

[1.85] Castex L., "Evolution of Prestresses Due to Shot Peening During an Alternating Torsion Test", In: *Conf Groupement français pour l'analyse des contraintes par diffractometrie X*, Besancon, France, 1982, pp. 89-98.

[1.86] Özdemir A. T. and Edwards L., "Relaxation of Residual Stresses at Cold-Worked Fastener Holes Due to Fatigue Loading", *Fat Fract Engng Mater Struct*, Vol. 20, No. 10, 1997, pp. 1443-1451.

[1.87] Zhuang W. Z. and Halford G. R., "Investigation of Residual Stress Relaxation Under Cyclic Load", *Int J Fat*, Vol. 23, 2001, pp. S31-S37.

CHAPTER 2

2.0 Variable Amplitude Load-Time History Generation

2.1 Introduction

Generally the basic fatigue behaviour of materials and structures is determined adopting constant amplitude loading resulting in various characteristic quantities and relationships such as S-N curves, cyclic stress-strain curve, fatigue crack growth rates and threshold values and etc. Constant amplitude (CA) loading is fully described by several parameters such as maximum/minimum or range/mean and number of load cycles. However, most structures experience in-service loading environments with variable amplitude applied, mean loads and frequencies. Hence, over the entire service life, materials or structures could be subjected to variable amplitude (VA) loading beyond what is expected under normal operating conditions of CA loading.

To ensure design safety, engineers need to be able to model or predict service life and fatigue crack growth behaviour of structural components accurately. Neglecting the effect of in-service loading conditions as well as environmental factors in fatigue life assessment can lead to non-conservative life predictions. Therefore, in addition to CA testing, tests with realistic load sequences are often required in order to investigate any susceptibility to the characteristics of VA loading and to assess the in-service integrity for given materials and components. After the pioneering work of Palmgren [2.1] and Miner [2.2] on cumulative fatigue damage in the 1950s and 1960s, fatigue tests under random loading [2.3, 2.4] and programmed loading [2.5, 2.6] were actively conducted. Based on these studies, standardised load-time histories have been subsequently developed so that the in-service loading conditions can be replicated in laboratory tests.

Although many models, including those described in the following sections, are able to simulate realistic load sequences, the validity and suitability of the generated sequence are often overlooked. This chapter gives an insight to a stationary standardised load-time sequence, generated using the Jack-up Offshore Standard load History (JOSH) model, for variable amplitude corrosion fatigue testing of jack-up structures. A brief review of existing service load simulation models for offshore structures is included since the JOSH model was retrospectively

developed based on the early wave models. This is followed by the background work required for a wave loading design and the main components of the JOSH framework. Great emphasis is placed on the statistical aspect and analysis of the load sequence. The generated load sequence was employed in fatigue testing of high strength jack-up steel programme, which will be fully discussed in Chapter 3.

2.2 Service Load Simulation for Fatigue Testing

The earliest standardised load-time history work recorded was by Ernest Gassner [2.7] in 1941. Gassner stressed the importance of the cumulative frequency distribution of load amplitudes corresponds to that of a stationary Gaussian process and the overall load intensities had to be specifically selected such that the block sequence had to be repeated several times until component failure was observed. The load sequence employed was an approximation of VA loading by a sequence of load blocks with varying sizes and hence technically speaking it cannot be classified as a standardised load-time history. However, it was the underlying idea of Gassner's approach that paved the foundation for the development of realistic service load simulations.

Standardised load histories have been developed for more than 30 years since the advantages of a more generic nature and practical applications have been recognised. The advent of servo-hydraulic actuators and computers has enabled fatigue testing to be conducted under increasingly complex fatigue loads. With the need for optimum light-weight design, originally the aircraft industry was the main driver for the development of standard load histories and some of the most well-known models include TWIST [2.8] and FALSTAFF [2.9]. Load sequences generated from TWIST and FALSTAFF were applied for transport and fighter aircraft respectively, and they are still being used in numerous studies on materials, joints and structural elements. Further examples from aerospace field include HELIX/FELIX [2.10] and TURBISTAN [2.11].

2.2.1 Parameters in a Wave Loading Model

Before further discussing the generation of standardised load history for fatigue testing of offshore structures, the parameters employed in VA loading and wave loading are elaborated in this section. Ocean wave motions are considered to be a random process, and hence wave data can be represented by certain statistical parameters. The basic parameters presented in this section are based on Reference 2.12, which were used by most wave loading designs discussed earlier.

Fundamentally, most wave loading theories are modelled and designed based on three major parameters, namely water depth, wave height and wave period. Wave height H, can be defined

as the vertical distance between a crest and the adjacent trough of the wave, and this is the primary parameter describing the sea states. On the other hand, wave period is the total time elapsed during the wave elevation, after it crossed an arbitrary reference level. Being a random process, the ocean waves can be categorised into different sea states according to the different wave heights. Conventionally in wave modelling, a sea state is defined as the condition of the ocean surface, characterising the wave spectrum. In modern days, the term sea state is used to denote the water surface elevation and the resultant loading condition on a structure, and this definition is adopted in this study. In a multi-sea state model, each individual sea state is normally expressed in terms of significant wave height, H_s and mean zero crossing wave period, T_z. Significant wave height is defined as the mean of one-third of the largest waves from the recorded wave height of the sea state. However, this can be a time consuming and expensive process for long term wave modelling, and hence approximate methods have been proposed. The most widely-used approximation is shown in Equation 2.1, where the significant wave height can be calculated from m_0, the spectral moment:

$$H_s = 4\sqrt{m_0} \qquad \text{- (2.1)}$$

The sea state is usually presented in the form of the normalised power spectral density (PSD) against the cyclic frequency. A typical wave loading power spectrum is shown in Fig. 2.1 below.

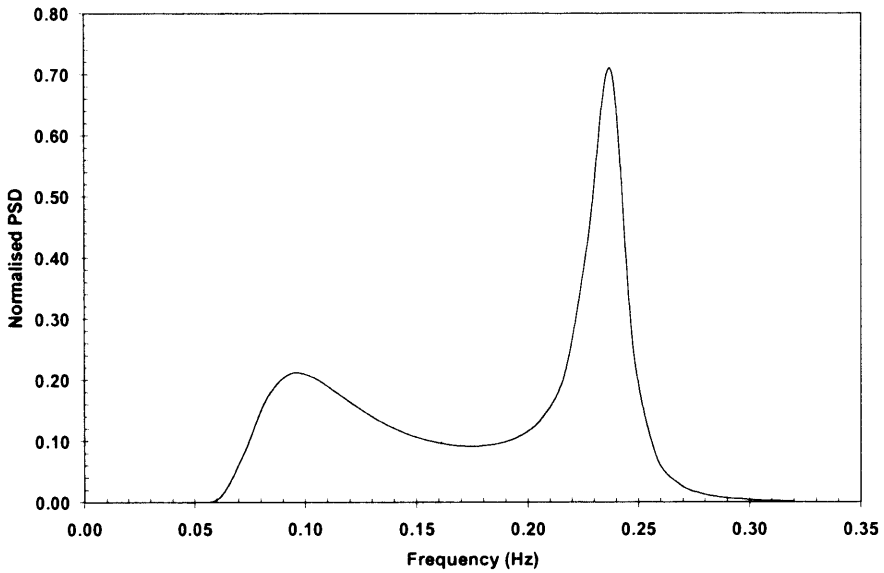

Figure 2.1: A typical wave loading power spectrum

As can be seen from the figure, the dominant wave frequency of the wave spectrum is approximately 0.24Hz and the area under the curve gives the total energy of the wave system.

2.2.2 Standardised Load-Time Histories for Offshore Structures

The development of standardised load histories for offshore structures was considered to be relatively slow compared to the aerospace industry. During the early 80s and through into the 90s, when the offshore industry was booming, attention was given to the performance of offshore structures, especially tubular elements. Schütz et al [2.13] developed The Common Load Sequence for fatigue evaluation of Offshore Structures (COLOS) for the European Coal and Steel Community Research Programme. The overall spectrum consisted of seven stationary Gaussian spectra of different Root Mean Square (RMS) values, representing a single narrow band stress spectrum. Due to the fact that COLOS was one of the earliest standardised load history developed, there were several main drawbacks with the sequence used. The load history ignored the dynamic and resonance effects of offshore structures, and the frequency control was far from accurate. Hence, it was later found that the load sequence was not realistic for the evaluation of the performance of offshore structures.

The UKOSRP II double peaked spectrum [2.14], which is similar to the COLOS sequences, did not model the realistic load history since it was only based on a single stormy sea state. The double peak spectrum adopted was recorded from the Forties Bravo platform. The main drawback of this model is that it did not monitor the long term variation in sea state RMS and this means that some features in the multi-sea state spectrum might be missing. However, the resulting load history had the advantage of being pseudo-random since the UKOSRP II spectrum utilised a suitable pseudo-random binary shift register developed at UCL.

Wirsching [2.15] proposed a long term stress history of deep water structures, which modelled the long term variation in sea state RMS. The study focused on welded offshore structures and was mainly based on the Palmgren-Miner rule, S-N curves, rainflow counting method and probabilistic fatigue failure. The statistical and fatigue damage data is shown in Table 2.1 below. One of the most significant developments of the Wirsching Algorithm is that the sea state spectrum incorporated the dynamic amplification effects, which is expressed in the form of stress spectral density function. The long term load history was simulated with the use of a discrete Markov Chain model that enables one to model the sequence of sea states. However, Wirsching's Algorithm assumed that the transfer function from surface water elevation to stress was linear and modelled the structure as a simple resonant system. Hence, this oversimplification makes the model inadequate for the use of spectral density function measured at North Sea [2.16]. In order to reduce the testing time for laboratory tests, Hart and Lin [2.17] proposed a modified Wirsching's load spectrum, which the three lowest sea states were omitted while the three highest sea states were combined into one sea state. The overall appearance of the long term stress history was maintained by controlling the stress level and the same Markov Chain model was employed to

simulate the multi-sea state sequence. The main deficient features of this model are that the generation algorithm is machine dependent and the frequency control is poor.

Significant wave height H_s (m)	Mean zero crossing period T_Z (S)	Fraction of time in sea state $\tilde{a}_i$	Rate of peaks n_i (Hz)	Zero Crossing Rate F_i (Hz)	Spectral width parameter	Process RMS stress σ_i (MPa)
16.0	17.3	0.0000368	0.209	0.0976	0.884	47.3
14.5	16.5	0.0000932	0.213	0.104	0.872	41.2
13.0	15.8	0.00037	0.216	0.109	0.863	35.2
11.4	14.7	0.0022	0.223	0.120	0.842	29.7
9.9	13.6	0.0073	0.229	0.133	0.814	24.6
8.4	12.7	0.0135	0.234	0.144	0.788	19.9
6.9	11.6	0.0265	0.240	0.160	0.745	15.5
5.3	10.3	0.060	0.247	0.178	0.693	11.5
3.8	9.1	0.210	0.253	0.199	0.617	7.72
2.3	7.7	0.490	0.261	0.223	0.519	4.27
0.8	4.4	0.190	0.280	0.271	0.251	1.65

Table 2.1: Statistic and fatigue damage data for simulated North Sea condition proposed by Wirsching [2.14]

Sea state number	Significant wave height *Hs* (m)	Corresponding range of *Hs* (m)	Zero crossing period *Tz* (s)	Zero crossing rate *Fi* (Hz)	Fraction of time %
0	1.75	0.00-1.95	5.9	0.169	38.5
1	2.55	1.95-2.85	6.4	0.156	28.5
2	3.40	2.85-3.80	6.9	0.145	17.5
3	4.15	3.80-4.50	7.3	0.137	7.18
4	4.80	4.50-5.10	7.7	0.130	3.40
5	5.45	5.10-5.75	8.0	0.125	2.16
6	6.15	5.75-6.55	8.4	0.119	1.31
7	6.90	6.55-7.35	8.7	0.115	0.678
8	7.80	7.35-8.30	9.1	0.110	0.334
9	8.80	8.30-9.40	9.5	0.105	0.154
10	10.35	9.40-12.55	10.2	0.098	0.0797
11	13.60	>12.55	11.5	0.087	0.0043

Table 2.2: Sea state data proposed by WASH

Wave Action Standard History (WASH) [2.18-2.21] was developed based on the approach proposed by Lin and Hart, for fatigue testing of offshore structures in the North Sea. The fundamental WASH model is similar to the Lin and Hart proposal but there are several unique features that WASH incorporated. First of all, the signal generation mechanisms in WASH have been designed as a 'standard' and hence it is machine independent. The algorithm is reproducible and this was made possible by using a suitable Pseudo-Random Binary Shift (PRBS) technique [2.22]. In addition, the WASH sequence utilised realistic sea states obtained from monitored offshore structure service data (Table 2.2 above). As can be seen from the table,

a significant wave height range (third column) is assigned to each sea state and the corresponding H_S is evaluated from the mean of one-third of the largest waves from the recorded wave height of the sea state. As presented in the sixth column, the cumulative percentage of occurrence of each sea state was recorded so that the actual probabilistic nature of the wave loading can be modelled using a Markov Chain process. Basically, WASH can be broken down into two major components, which enable the simulation of random multi-sea state load sequence. The first component is the random load history for each sea state and the second component is the selection of the proceeding sea states for the entire sequence. The unique and reliable features of the WASH model were then implemented in the development of JOSH. The JOSH model, together with its major components is further discussed in the following sections.

2.3 Jack-up Offshore Standard load History (JOSH)

The growing trend of utilising jack-ups as production platform as well as mobile exploration rig, since in the 80s, have spurred the demand for the fatigue performance of jack-up structures. A typical jack-up platform is shown in Fig. 2.2.

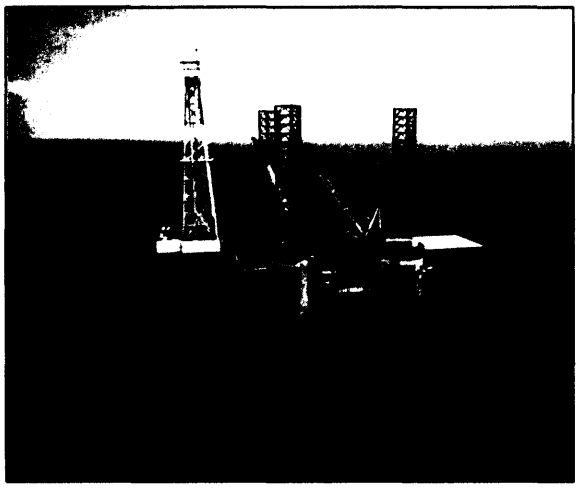

Figure 2.2: A typical jack-up platform (Texas Pride, Gulf of Mexico, USA)

Although WASH is a powerful and reliable model for generating standardised multi-sea state load histories, it cannot be applied to Jack-ups since resonance and dynamic effects dominate the power density functions for typical Jack-up platforms [2.23]. Etube et al [2.24, 2.25] developed the JOSH model, which takes into account the dynamic response of Jack-up by using the transfer function approach. The structural response data employed were based on the in-service data monitored on two typical Jack-up platforms (Ekofisk and Silver Pit) in the North Sea. The data was obtained through extensive oceanographic modelling over a long period of time in order to

take into account the long term sea states variation. The modified Pierson-Moskowitz (PM Spectrum) [2.26] wave spectra model was adopted for the spectrum modelling in JOSH. A conventional PM model will express the wave power spectral density, $S_{yy}(f)$ as:

$$S_{yy}(f) = \frac{H_s^2 T_z}{8\pi^2}(fT_z)^{-5} \exp\left[-\frac{1}{\pi}(fT_z)^{-4}\right] \quad \text{- (2.2)}$$

where H_s is the significant wave height
T_z is the mean zero crossing period
f is the wave frequency

By using this approach, a site-independent transfer function can be determined, which can then be used to obtain the corresponding response spectrum before generating the complete load history. However, it was found that the wave energy measured at typical jack-up sites was concentrated at frequencies slightly higher than predicted by Equation 2.2. In order to rectify the frequency shifting, the modified Pierson Moskovitz spectrum model was proposed:

$$S_{yy}(f) = \frac{H_s^2 T_z}{8\pi^2}((f-\beta)T_z)^{-5} \exp\left[-\frac{1}{\pi}((f-\beta)T_z)^{-4}\right] \quad \text{- (2.3)}$$

As can be seen from the above equation, the frequency content was modified with a frequency correction parameter β, which is dependent on jack-up site and wave height. Etube [2.24] demonstrated that Equation 2.3 yielded a more accurate wave energy spectrum, validated by the comparison with two jack-up sites in the North Sea. In the mathematical modelling of the dynamic structural response of jack-ups, a simplified two-dimensional model (Fig. 2.3) was proposed, represented by the general structural vibration equation:

$$M\ddot{X} + C\dot{X} + KX = F(t) \quad \text{- (2.4)}$$

where $F(t)$ is the excitation force
M is the mass of the system being modelled
C is damping coefficient
K is the stiffness matrices
X is the displacement

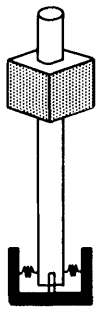

Figure 2.3: A simplified two-dimensional model of jack-up platform

The structural response predicted using the simplified 2-D model will then be incorporated into the wave loading spectrum to generate the realistic jack-up platform sea state spectra. Then, the Markov Chain-Monte Carlo and Pseudo-Random Binary Shift (PRBS) techniques (Appendix B), which were an integral part in the WASH framework, were implemented to generate a standardised multi-sea state load-time history according to the input parameters. Once the load-time history is generated, the number of sequence cycles is determined using rainflow cycle counting technique (Appendix C). Hence, it can be seen that the fundamental load history generation mechanism of JOSH is almost identical to WASH, and the only differences are the incorporation of structural dynamic response and different number of sea states used.

2.3.1 Operation of JOSH Sequence Generator

The preceding sections discussed the main components and features of the JOSH framework. It is worth mentioning that the original JOSH model was coded using Fortran 95® and under the current study, the entire model was re-coded in Digital Visual Fortran®. New sub-routines and functions were introduced in order to improve the efficiency and user-interface of the sequence generator. As previously stated, since the current study emphasised on the modification rather than the development of the JOSH model, only the main features are discussed. However, it is worthwhile to briefly describe the overall operation and procedures involved during the generation of the variable amplitude loading sequence. The load history generation process for JOSH can be summarised in the following steps and Fig. 2.4 below:

1. The dynamic response of the structure is modelled analytically by using a simplified model of the jack-up platform. The resultant structural response data is then combined with the sea wave dynamics recorded to produce realistic sea states for jack-up structure.
2. In the current JOSH model, eight sea states were proposed and each of them is described by the significant wave height and the mean zero crossing period. The Pierson-Moskovitz spectral dynamic response model (for North Sea wave modelling) is used to generate the power density spectrum for each of the sea states.

3. By entering the relevant sea states data and the fixed sub-block duration, the Markovian transition probabilities matrix is constructed. These probabilities are also stored as cumulative probabilities, which will be used in the Pseudo-Random Binary Shift (PRBS) register generator. It must be noted that in order to generate a statistically stable and reproducible sequence, the combination of the number of shift register elements, return period, resolution and the number of pre-shifts, must be adequately implemented in both the PRBS technique and Markov Chain method.
4. Prior to the load history generation, the user has to input the starting sea state, scale of the sequence, sub-block duration, total length of sequence and the relevant numerical parameters.
5. During the first stage of generation, an Inverse Fourier Transform (IFT) is performed on each sea state spectrum to form a variable amplitude time series according to the prescribed sub-block duration. These amplitude time series are then stored.
6. In the final stage, the PRBS technique is implemented to generate a series of random numbers. These numbers are then used in conjunction with the Monte Carlo simulation and Markovian cumulative probabilities to select the next sea state. When the next sea state is determined (up, down or remain), the corresponding time series is retrieved and stored.
7. Step 5 and 6 will repeat until the sequence has reached its prescribed length. The resultant will be the complete variable amplitude loading sequence.

2.4 Analysis of Generated Sequences

Although JOSH has been verified to be a standardised load-time history generator, it is important that the relevant analysis is carried out in order to ascertain that the sequence generated is appropriate for fatigue testing purposes. Unfortunately, very often little attention is given to the validity of the generated sequence. For example, although in many wave models (including those discussed earlier) the random sea-state behaviour was successfully modelled using a Markov Chain process, they were all based on the assumption that the Markovian process is a statistical stationary one. However, none has demonstrated proof to support this assumption and very often over-simplification will lead to erroneous results. Hence, the assessment of the long term statistical nature of the complete load-time sequence is a prerequisite if realistic and representative loading conditions are to be achieved.

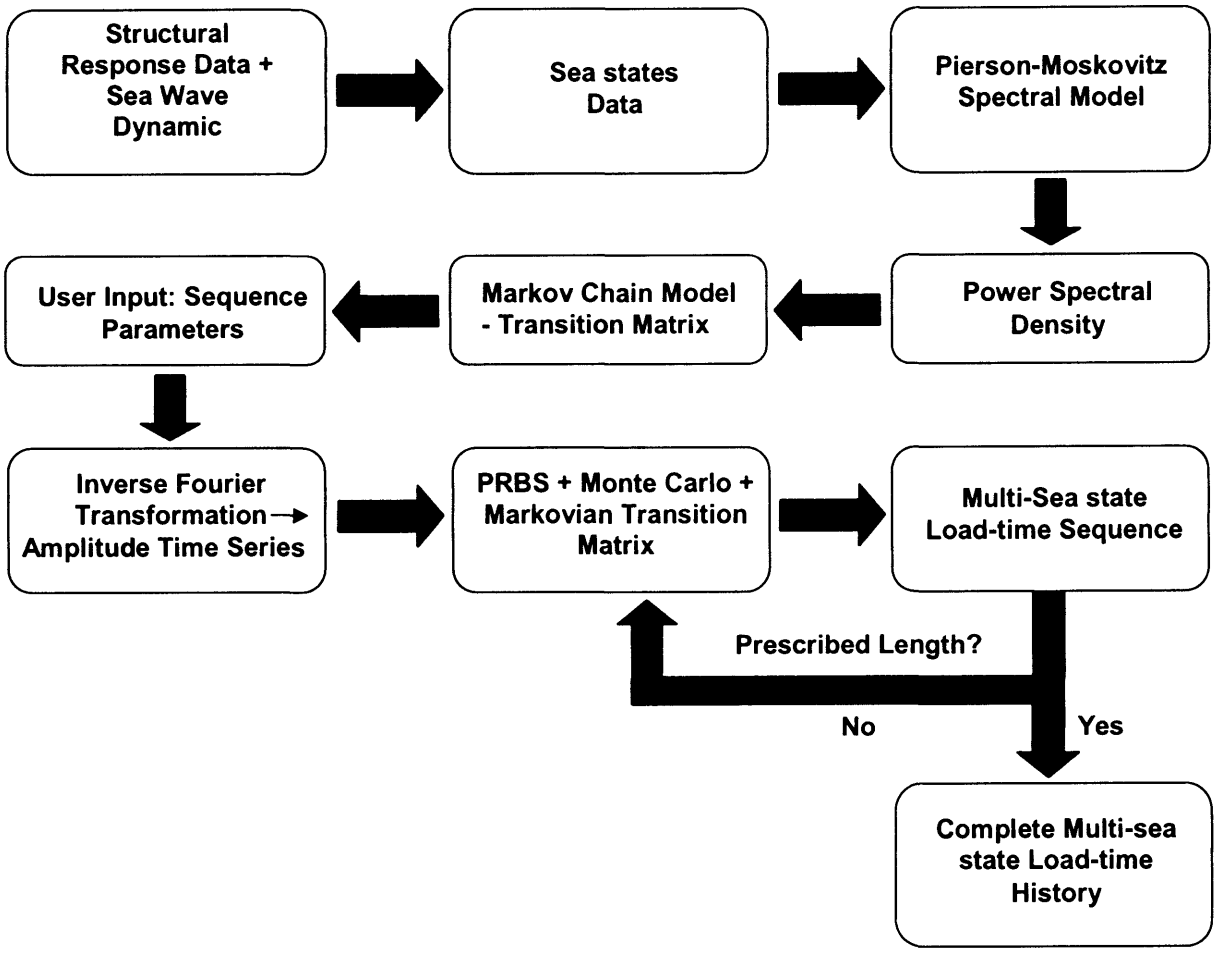

Figure 2.4: Summary of the load-time history generation mechanism of JOSH

In a previous study on the corrosion fatigue performance of HSSs using the JOSH model, Tantbirojn [2.27] addressed the non-stationary effects observed in the generated load-time sequence. These effects were demonstrated to have a profound effect on the fatigue crack growth behaviour in the specimens being studied. These observations will be further discussed in the following sections. The primary parameters considered are the stationary points, the equivalent stress range (ESR) (Appendix D) and the power spectral density. Other influential factors such as sub-block duration and starting sea state are also briefly discussed. Since the JOSH model implemented in this study was modified and developed under the original framework [2.24, 2.25, 2.27], the statistical aspects of the current sequence [2.28] will be constantly compared with the authors' results.

2.4.1 Basic Parameters of the JOSH Sequence

Table 2.3 below shows the sea states data used in the initial JOSH generator while the corresponding Markov Chain transition matrix is illustrated in Table 2.4. The values presented in Table 2.4 represent the probability for each sea state to move to the adjacent sea state (up or down) or to stay in the current sea state. Sea states 1 to 4 are generally considered to be calm sea states while sea states 8 to 12 are defined as storm load conditions. Although the original dataset proposed by the JOSH model contains 12 sea states, only the first 8 sea states were used in this study by omitting the last four sea states. This is due to the fact that the overall contribution of the last four sea states is insignificant and a shorter stationary point can be achieved by decreasing the number of sea states used, as proposed by Lin and Hart [2.17], Kam [2.18] and Tantbirojn [2.27]. These features will be further discussed in the following sections.

Sea State Number	*Hs* (m)	*Tz* (s)	% of Occurrence
1	1.25	5.5	38.5000
2	1.75	5.9	28.5000
3	2.25	6.2	17.5000
4	2.75	6.5	7.1800
5	3.25	6.8	3.4000
6	3.75	7.1	2.1600
7	4.25	7.4	1.3100
8	4.75	7.7	0.6780
9	5.25	7.9	0.3340
10	6.25	8.4	0.1540
11	7.25	8.9	0.0797
12	8.00	9.2	0.0043

Table 2.3: Sea states data employed in JOSH

The power spectra for the 8 sea states used are shown in Fig. 2.5 below. The number of points chosen to represent a power spectrum determines the resolution of the final load-time history. Previous studies [2.18, 2.24] have shown that a 32-point-spectrum gives adequate resolution for a

typical double peak offshore power spectrum and this was adopted in the current JOSH sequence (Fig. 2.6). The spectra were inputted into Procedure No.5 of the sequence generation mechanism described in Section 2.3.1.

	Probability		
Sea state	**Up**	**Stay**	**Down**
1	0.0000	0.9965	0.0035
2	0.0047	0.9893	0.0060
3	0.0097	0.9848	0.0055
4	0.0134	0.9782	0.0084
5	0.0177	0.9689	0.0135
6	0.0218	0.9555	0.0227
7	0.0364	0.9365	0.0272
8	0.0525	0.9092	0.0380
9	0.0777	0.8990	0.0233
10	0.0510	0.8788	0.0706
11	0.1364	0.8546	0.0090
12	0.1667	0.8333	0.0000

Table 2.4: Sea states transition matrix for 10 minutes sub-block duration

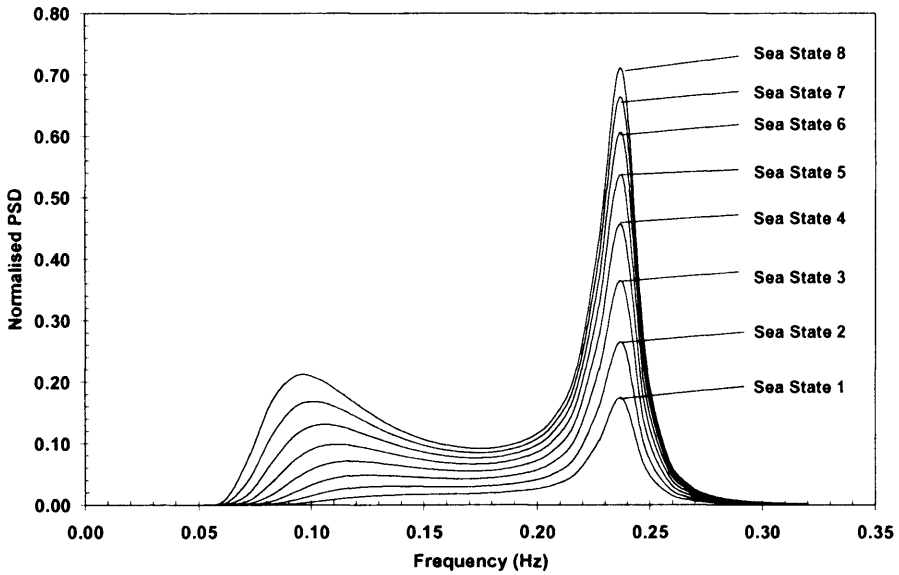

Figure 2.5: Power spectra for the 8 sea states used in JOSH

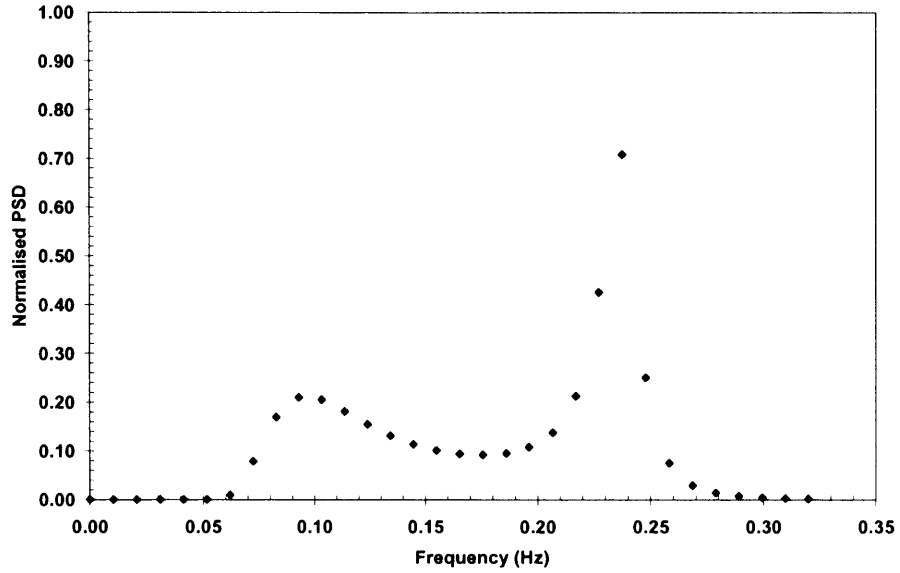

Figure 2.6: A 32-point power spectrum used in JOSH

As described in Appendix B, the PRBS technique was employed in both load-time history generation and random number generation for sea-states transitions. Before the PRBS register can be used, it must be pre-shifted to eliminate the transient behaviour. The number of pre-shifts required will depend on the return period length of the feedback loop. As stated in the appendix, a four way feedback loop was used in the shift register and the elements values (M, L, M_1 and L_1) used must be appropriate. A list of valid M, L, M1 and L1 values can be found in Reference 2.29. Based on the required return periods of the applications, the feed back loops chosen for the PRBS register technique in the load-time history generation and Markov Chain-Monte Carlo sea-states transition were M = 100, L = 8, M_1 = 7 and L_1 = 2 and M = 14, L = 5, M_1 = 3 and L_1 = 1 respectively. The minimum required pre-shifts were 27 and 14 respectively, according to the procedures outlined by Press et al [2.28] and Kam [2.18].

2.4.2 Stationary Point

Statistically, a process is defined to be stationary if the probability characteristics of the process are independent of time. In this case, the ESR and the power spectrum for the entire sequence should converge once the stationary point is achieved. For WASH, the recommended minimum sequence length was forty thousand seconds or ten thousand cycles. The length proposed was relatively short in order to speed up the convergence of the statistical parameters. The sequence used in this study has approximately 230,000 cycles, which is equivalent to a length of 20,000 minutes. The sequence was seen to be sufficient in representing a two-year round service loading of a jack-up structure. Fig. 2.7 shows the generated variable amplitude load sequence JOSH while Fig. 2.8 shows the sea states distribution for the complete sequence.

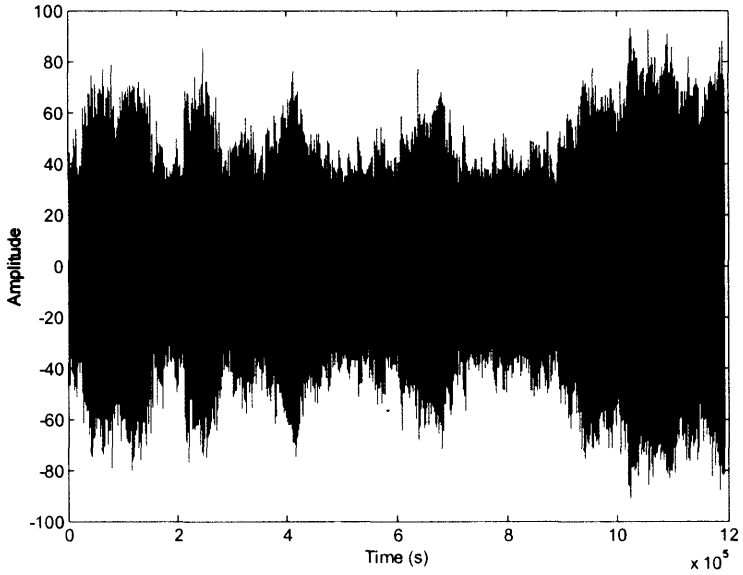

Figure 2.7: Variable amplitude load-time sequence generated using JOSH

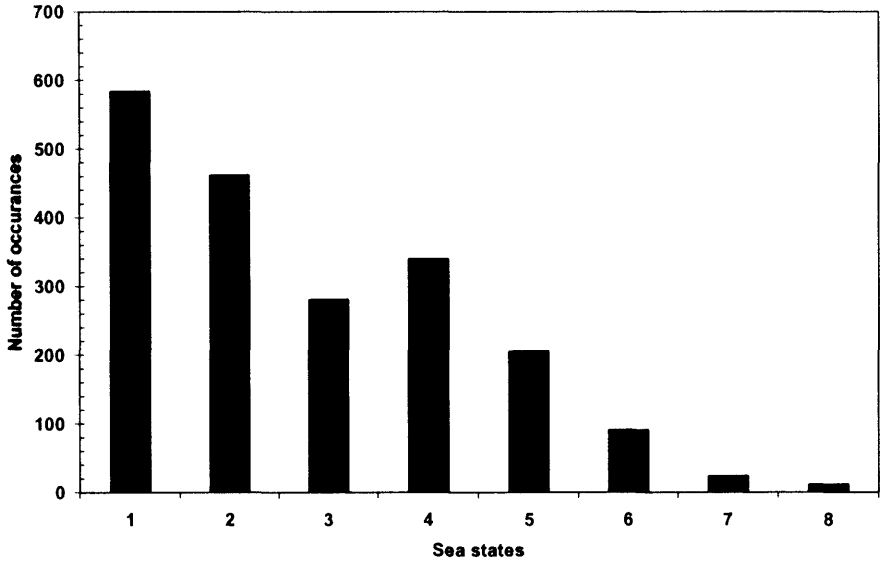

Figure 2.8: Sea state distribution for the entire sequence

2.4.3 Equivalent Stress Range (ESR)

As can be seen from Fig. 2.7, the JOSH10 sequence was generated as a series of turning points on a scale between -100 and +100. By using the rainflow cycle counting technique, the individual stress ranges were identified and the occurrence of different stress ranges was recorded. The load history was then scaled accordingly in order to achieve the ESR required. Fig. 2.9 shows the resultant stress range distribution obtained by using the rainflow counting method. In order to ensure that the load history is statistically ergodic and stationary, cycle counting was performed on

various durations of the sequence considered. Subsequently, the ESRs were calculated and compared with the prescribed value.

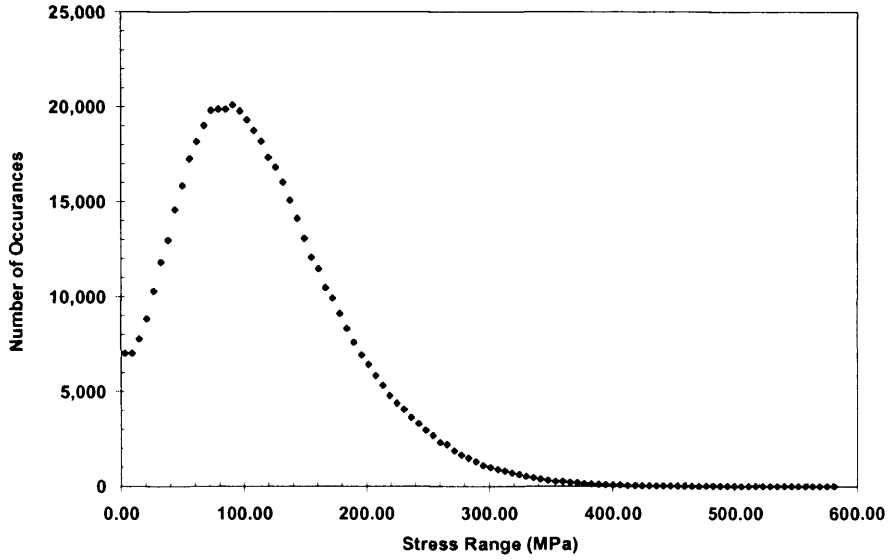

Figure 2.9: Stress range distribution obtained using rainflow cycle counting

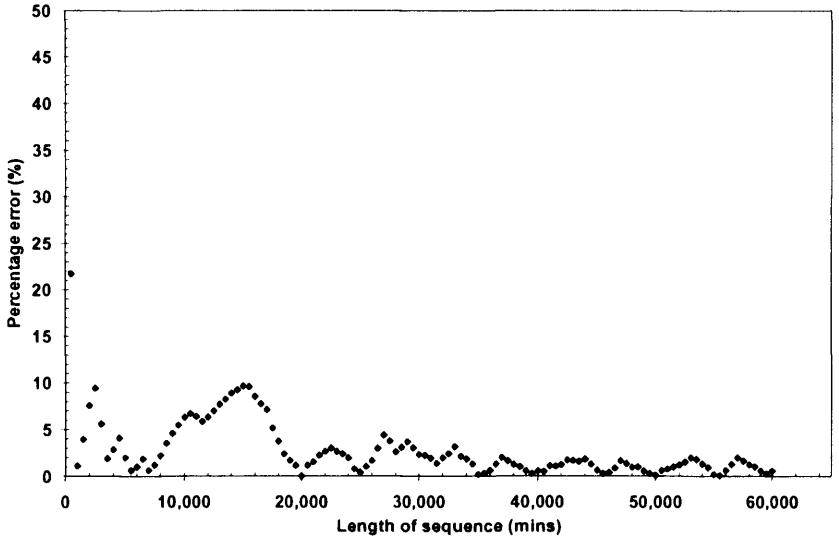

Figure 2.10: Convergence of the ESR

Fig. 2.10 above illustrates the percentage error when compared to the prescribed ESR for one complete sequence and this was repeated for three sequential load histories. As can be observed from the figure, the percentage errors converged well below 5% of the prescribed value once the length has reached one complete sequence. Hence, it has been shown that the generated sequence is statistically stationary and ergodic.

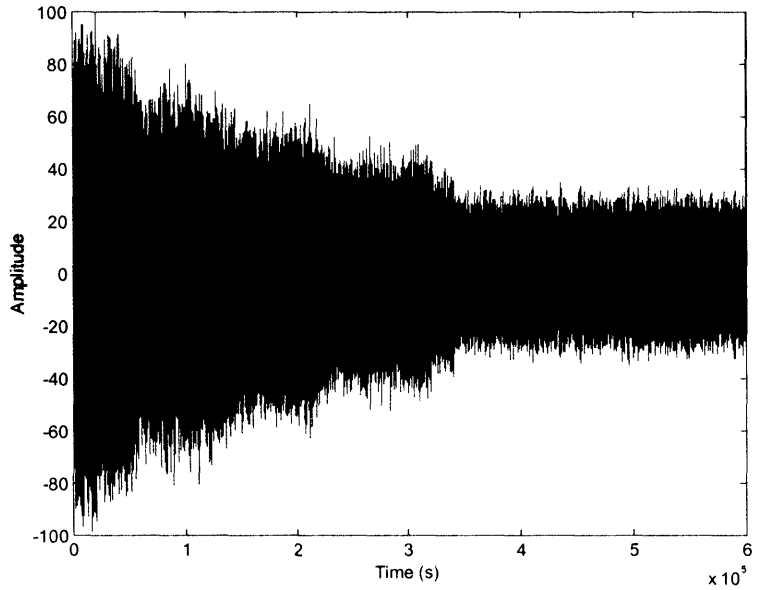

Figure 2.11: Load-time history plot of the JOSH sequence used in Reference 2.27

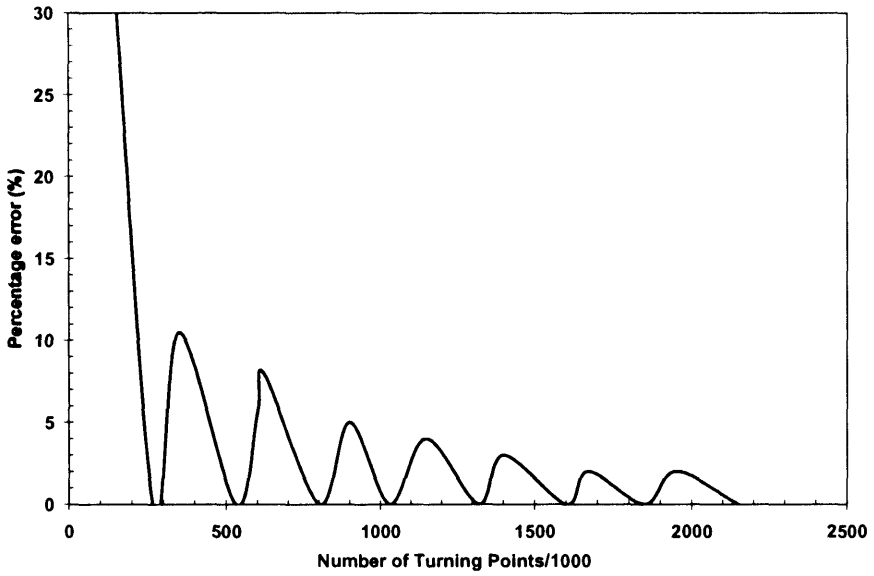

Figure 2.12: Percentage error in ESR of JOSH sequence for different sequence duration [2.27]

The current sequence is compared with the sequence obtained from References 2.25 and 2.27 in order to show the significance of a stationary system. Fig. 2.11 above shows the load-time history generated using JOSH by Etube and Tantbirojn while Fig. 2.12 illustrates the corresponding percentage error of ESR for different duration of the sequence. The sequence consisted of approximately 200,000 turning points and a sub-block duration of 20 minutes was employed. As can be seen from Fig. 2.11, the amplitude decreases over time (from stormy sea states to calm sea

states) and this shows that the sea states were not adequately mixed for a multi-sea state load-time sequence. In addition, the ESR does not achieve a stationary point even after numerous repeats of the sequence, as illustrated in Fig. 2.12. These unfavourable characteristics were later found to have caused discrepancies in the variable amplitude fatigue data [2.27] obtained, which will be further discussed in Chapter 3.

It is noteworthy that the sequence generated in References 2.25 and 2.27 is considered to be erroneous since it was employed in medium-high cycle fatigue testing. However, the sequence might be deemed to be suitable in specialised tests, such as fatigue testing of components in stormy sea state loading conditions. It must be noted that prudent consideration must be given to the fatigue life prediction of the specimens since problems will arise if the fatigue test is shorter than the stationary point of the sequence. In other words, if the fatigue life of any particular specimen is shorter than the stationary point (one complete sequence), there will be a large variation in the actual equivalent stress range experienced. Hence in the fatigue test data presented in Chapter 3, the actual ESRs were calculated for each individual test.

2.4.4 Power Spectrum Density (PSD)

In CA loading, the stress range and the mean stress are sufficient to define the required fatigue test parameters. However, for VA fatigue tests, the two governing parameters are the ESR and the power density spectrum. In fatigue analysis, any load-time history can be characterised as frequency against the corresponding power density, by converting the loading sequence into a power spectrum. In many cases, especially in multi-sea state modelling, power spectrum is the preferred comparison method for different time series as the plot displays distinctive characteristics. This is highly important as even though the sequence is stationary in the aspect of equivalent stress range, the frequency content in the spectrum might be different. For example, Fig. 2.13 shows the percentage change in the normalised power spectrum density for one frequency in the sequence employed in the study by Tantbirojn [2.27]. As can be seen from the figure, the percentage error only falls below 5% after approximately six complete sequences but the dominant spectrum density shows no clear sign of convergence. In the present study, this discrepancy was rectified by employing the appropriate Markovian transition matrix and numerical parameters.

Similar to the ESR, the power spectrum plot will converge once the stationary point is reached. A Fast Fourier Transformation (FFT) [2.30] is used to convert the time series into power spectrum and in this study, a custom written MATLAB® program was used. MATLAB FFT provides a robust and fast algorithm to perform Discrete Fourier Transform (DFT) on the sequence (with length N) considered, by reducing the amount of data from N^2 to $NLog_2N$. The 32-point power density

spectrum of one complete sequence is shown in Fig. 2.14 below, having a dominant frequency of approximately 0.24Hz.

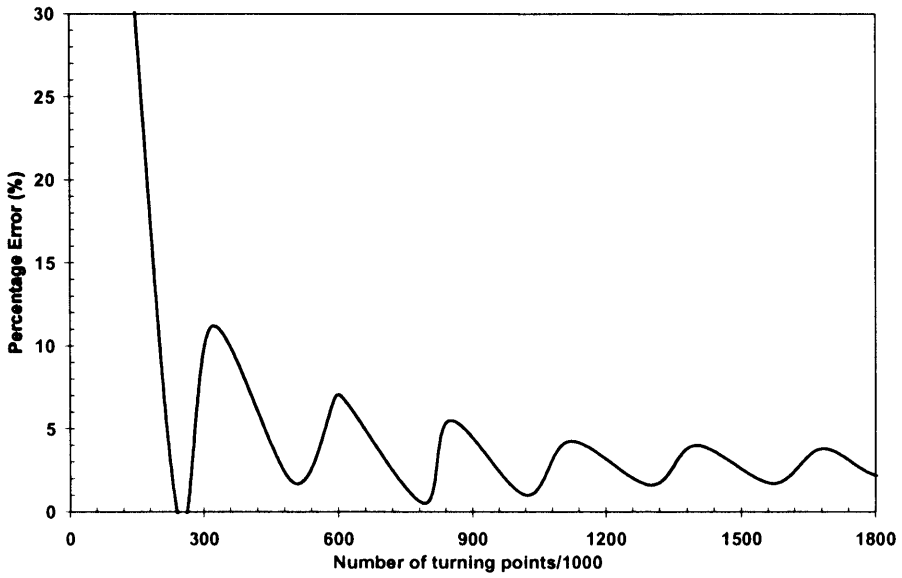

Figure 2.13: Percentage error in the normalised power density for the dominant frequency of the sequence [2.27]

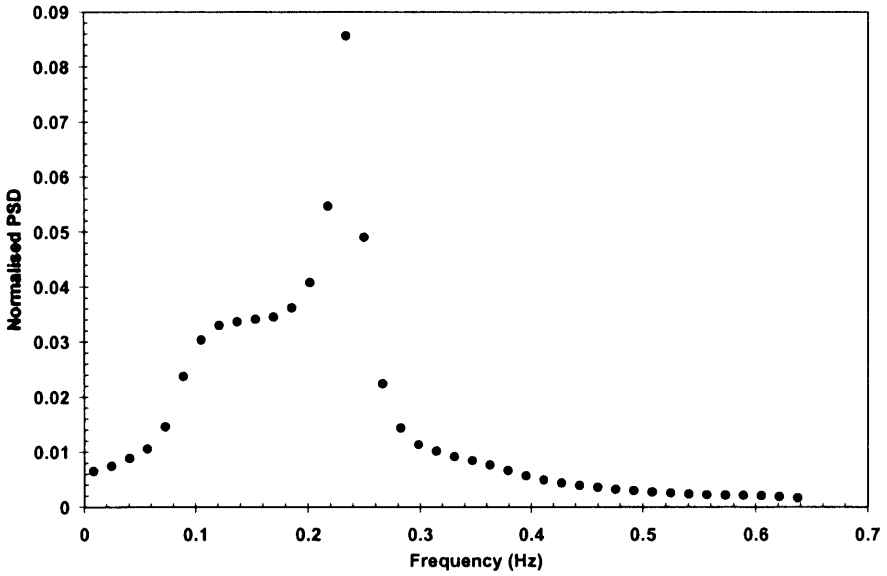

Figure 2.14: Power spectral density for one complete JOSH sequence

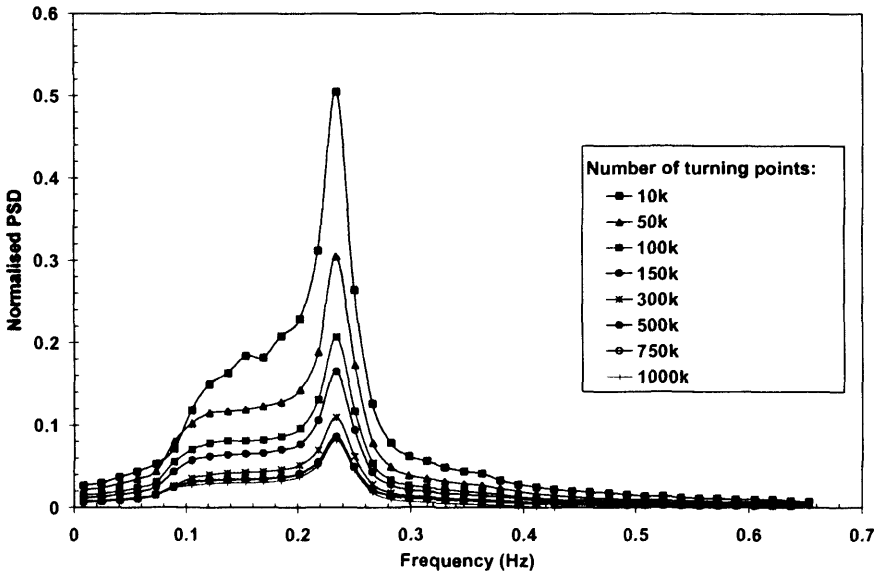

Figure 2.15: Convergence of the JOSH power spectrum

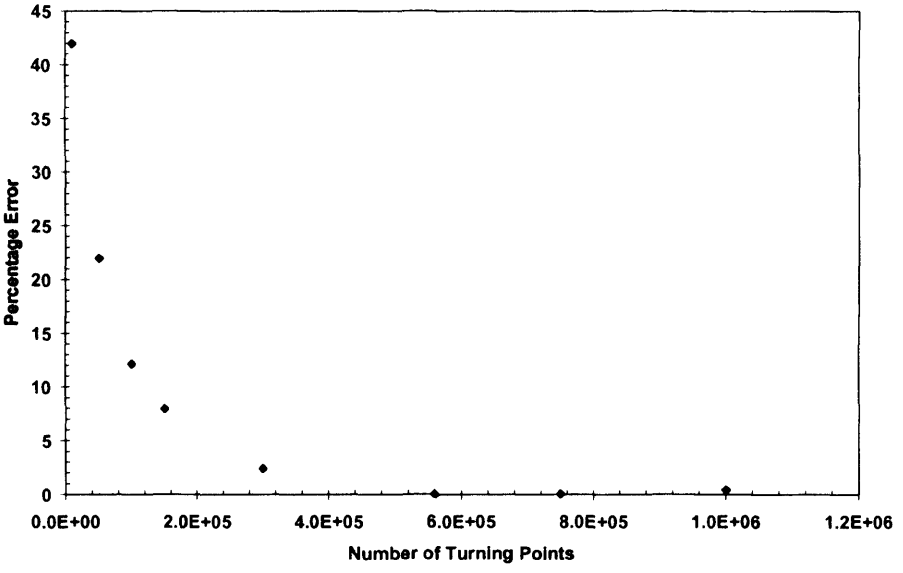

Figure 2.16: Percentage error in normalized PSD of the dominant frequency in the JOSH sequence

By performing FFT on different sequence lengths, the convergence of the power spectrum can be investigated (Fig. 2.15). It can be seen from the figure that all the points on the PSD plot converge after a complete sequence (550,000 turning points) and the shape of the spectrum is conserved. Fig. 2.16 above shows the corresponding percentage error in the normalised PSD of the dominant frequency (0.24Hz). Again, it can be observed that the percentage error in the normalised PSD decreases to virtually zero after one complete sequence. Since the FFT on the load sequence is an extremely time-consuming process, the results of up to two sequential load histories are included. However, it is expected these are sufficient to confirm the convergence of the spectrum,

and hence it can be said that the power density function of the load history is stationary after one complete sequence length.

2.4.5 Sub-Block Duration

The total duration and sub-block duration adopted for the sequence is 20,000 and 10 minutes respectively. Tantbirojn claimed that by using different total sequence durations, there will be variations in both the distribution of sea states and ESR in the complete sequence. Recently, after performing some relevant analysis, it is found that the usage of inadequate numerical parameters and the Markovian transition matrix in that particular study [2.25, 2.27] during the sequence generation led to erroneous conclusions. As can be seen from Fig. 2.17 below, the stress range distributions for both 20,000-minute (2000 transitions) and 40,000-minute (4000 transitions) total sequence duration is almost identical. The only differences are the number of transitions and the number of occurrences for the individual stress ranges is halved when the total duration is doubled. However, it is shown that the ESR was conserved since the proportions of individual occurrences were unchanged while applying the equivalent stress range approach.

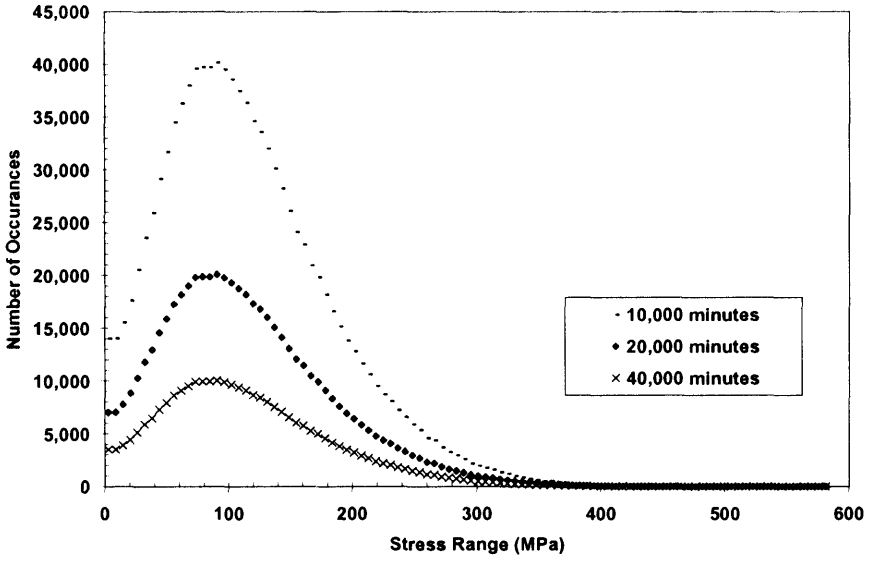

Figure 2.17: Stress range distribution for different sequence length

In practice, the sea state sub-block duration varies with wave height. However, realistic sub-block duration is not practical for laboratory testing as variable sub-block duration will lead to more statistical uncertainties in the generated sequence. In addition, the cumulative time spent in any particular sea state might not match the actual data if realistic sub-block duration is used. Olagnon et al [2.31] proposed the fixed length sub-block, which was widely considered to be a logical proposal for offshore load generator. The transition matrix used in the JOSH sequence was

obtained by implementing Olagnon's proposal, which based on the PRBS and Markov Chain-Monte Carlo method. The details are discussed in Appendix B. Table 2.5 below shows the sea states distribution for different sub-block durations together with the actual data. As can be seen from the table, only the sea states distribution obtained using the 10 minutes sub-block resembles the actual distribution. In addition, it is the only distribution that contains the 8 sea states proposed. In general practice, 10 minutes is recommended as the sub-block duration as in which the wave properties are measured every three hours [2.18, 2.21] and this duration was also employed by the WASH framework. It is also worthwhile to mention that the sequence stationary point (Section 2.4.2) will be achieved in a shorter period if a shorter sub-block duration is used.

	Percentage of Occurrence, %			
Sea State	**10 min**	**20 min**	**30 min**	**Actual**
1	29.2000	32.3400	45.8500	38.5000
2	23.1000	28.500	36.6000	28.5000
3	14.0500	26.0600	16.3681	17.5000
4	17.0000	9.8000	1.2319	7.1800
5	10.3000	0.6230	0.0000	3.4000
6	4.5500	0.1770	0.0000	2.1600
7	1.2000	0.0000	0.0000	1.3100
8	0.6000	0.0000	0.0000	0.6780

Table 2.5: Percentage of occurrence of sea states for different sub-block durations

2.4.6 Starting Sea States

By using the transition matrix correction proposal by Kam [2.18], the finalised transition matrix for the 8 sea states is evaluated (Fig. 2.18 below). The real time sea state occurrences of the JOSH sequence are illustrated in Fig. 2.19. This feature, which was not in the original JOSH model, was added so that the sea states occurrences can be monitored. As can be observed from Fig. 2.19, Sea State 1 is designated as both the starting and ending sea state, as recommended by Kam [2.18] and Tantbirojn [2.27].

According to the Markov Chain technique, the starting sea state will not affect the overall distribution of the sequence. However, this will only be true if the adequate Markovian transition matrix and numerical parameters are used. In order to verify that the Markovian transition matrix evaluated using Olagnon's proposal [2.31] was correct, the VA sequence for 8 different starting sea states were generated. Fig. 2.20 illustrates the load-time history plots of the JOSH sequence for 8 different starting sea states and the sea states distribution is tabulated in Table 2.6. On the other

hand, Fig. 2.21 shows the same plots for 12 different starting sea states obtained from Tantbirojn's [2.27] variable amplitude corrosion fatigue tests and the sea state occurrences are tabulated in Table 2.7.

$$T = \begin{bmatrix} 0.0000 & 0.9965 & 0.0035 \\ 0.0047 & 0.9893 & 0.0060 \\ 0.0097 & 0.9848 & 0.0055 \\ 0.0134 & 0.9782 & 0.0084 \\ 0.0177 & 0.9689 & 0.0135 \\ 0.0218 & 0.9555 & 0.0227 \\ 0.0364 & 0.9365 & 0.0272 \\ 0.0525 & 0.9475 & 0.0000 \end{bmatrix}$$

Figure 2.18: Finalised transition matrix for the 8 sea states used in the JOSH sequence

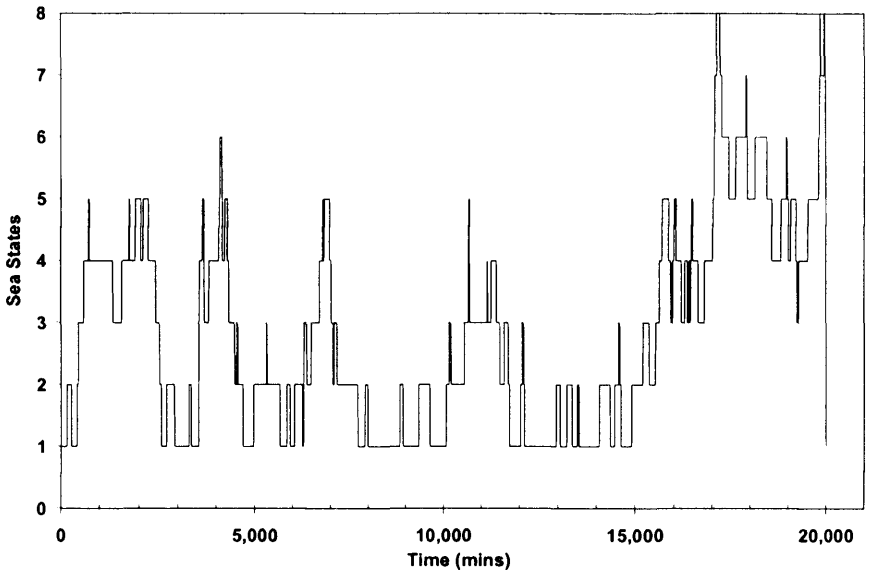

Figure 2.19: Real-time sea state occurrences for the JOSH sequence

As can be seen from Fig. 2.20, the difference in the general shape of the sequence is insignificant and this is further confirmed by the values obtained in Table 2.6. However, the sea states distribution obtained from Tantbirojn's study was inconsistent and this can be observed from the general shape of the time history plots in Fig. 2.21. Furthermore, the sea states distribution obtained using sea state 1 as the starting sea state only contains the first two sea states (Table 2.7). The stationary effect of the load-time sequence used in the present study can be appreciated by comparing the load-time sequences presented in Figs. 2.20 and 2.21.

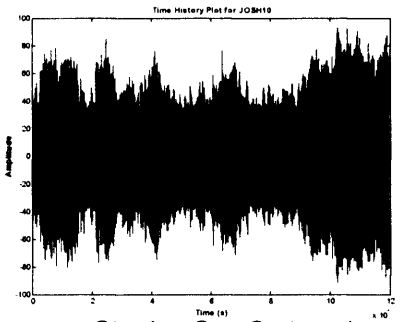

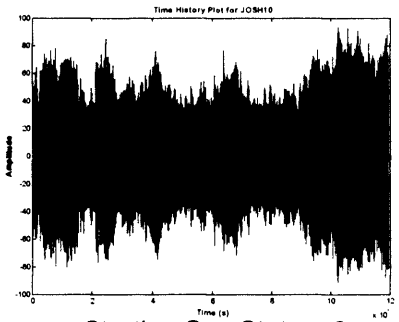

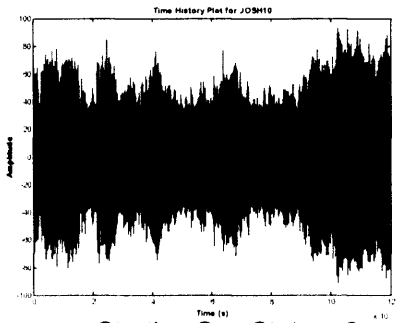

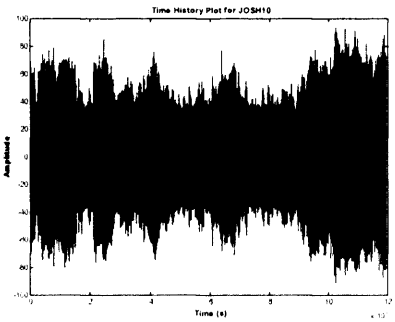

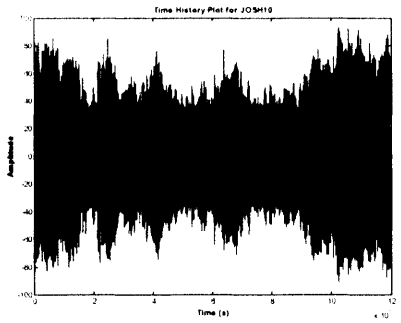

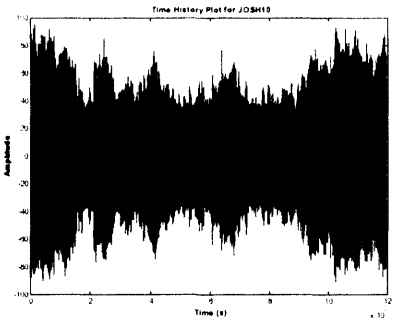

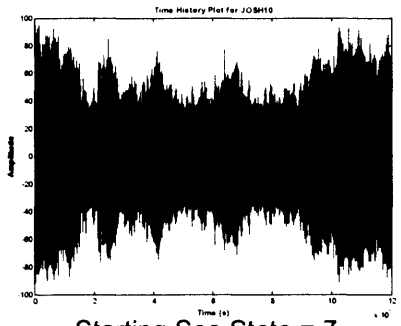

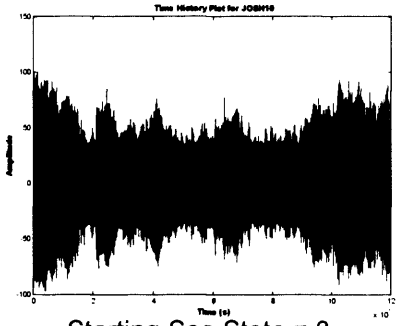

Figure 2.20: Load-time history plots of the JOSH sequence with 8 different starting sea state

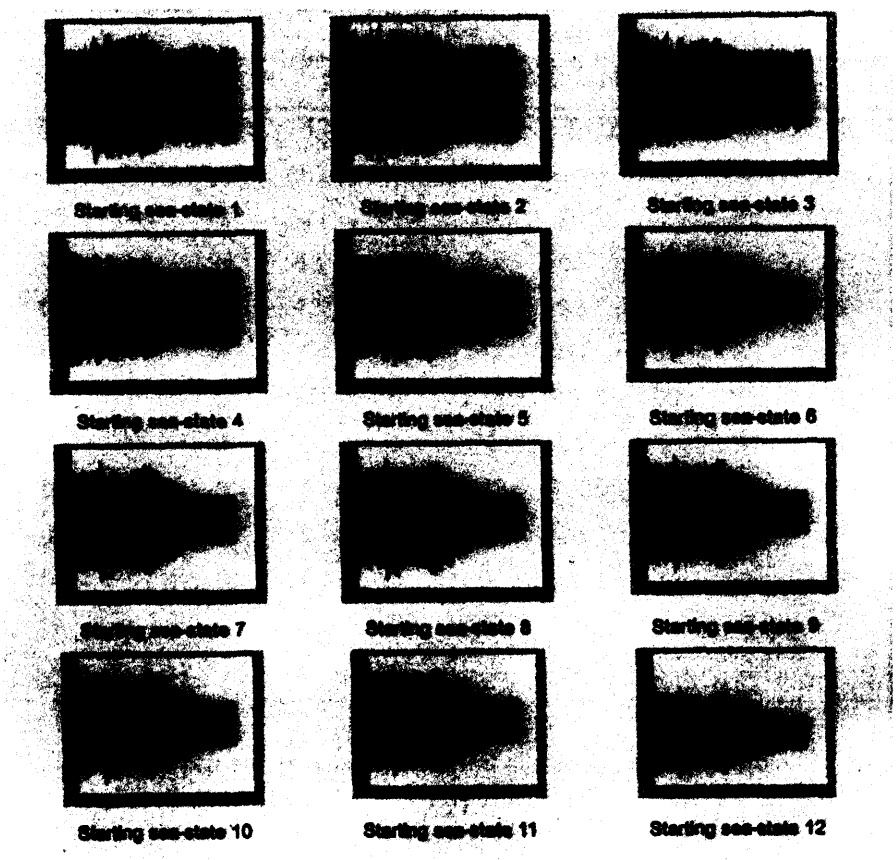

Figure 2.21: Load-time history plots of the JOSH sequence for 12 different starting sea state obtained from Tantbirojn's study [2.27]

	Number of occurrences							
	Starting Sea States							
Sea State	1	2	3	4	5	6	7	8
1	584	565	565	553	553	553	553	553
2	462	470	455	463	448	448	448	448
3	281	292	307	285	278	244	244	244
4	340	340	340	366	284	257	257	253
5	206	206	206	206	302	246	246	235
6	91	91	91	91	99	184	173	145
7	24	24	24	24	24	56	67	55
8	12	12	12	12	12	12	12	67

Table 2.6: Distribution of sea state of the JOSH sequence with different starting sea state

	Number of occurrence											
	Starting Sea State											
Sea State	1	2	3	4	5	6	7	8	9	10	11	12
1	668	497	497	497	237	237	237	237	237	237	237	237
2	329	488	407	407	224	76	76	76	76	76	76	76
3	0	15	96	83	165	35	35	35	35	35	35	35
4	0	0	0	13	351	93	93	93	93	93	93	93
5	0	0	0	0	23	112	112	106	89	89	89	89
6	0	0	0	0	0	214	204	199	170	170	170	170
7	0	0	0	0	0	71	81	82	94	94	94	57
8	0	0	0	0	0	133	133	143	165	165	165	173
9	0	0	0	0	0	0	26	26	28	28	28	46
10	0	0	0	0	0	0	3	3	3	13	4	14
11	0	0	0	0	0	0	0	0	0	0	9	1
12	0	0	0	0	0	0	0	0	0	0	0	9

Table 2.7: Distribution of sea states with 12 different starting sea state obtained from Reference 2.27

In order to ascertain that the overall distribution is independent of the starting sea state, the ESR for all cases was evaluated and compared. Figs. 2.22 and 2.23 below show the ESR and the corresponding percentage error of the JOSH10 sequence with different starting sea states. As can be seen from both figures, the percentage error of ESR for all cases was well within 5%, which is considered to be insignificant. This is further confirmed in Fig. 2.24, which shows that there is virtually no difference in the stress range distribution for the JOSH sequence with different starting sea states. Hence, the Markovian transition matrix evaluated is confirmed to be adequate for the generation of the load sequence and the statistical nature of the actual sea state distribution has shown to be conserved. This is of utmost importance in order to ensure that the sea states are properly mixed.

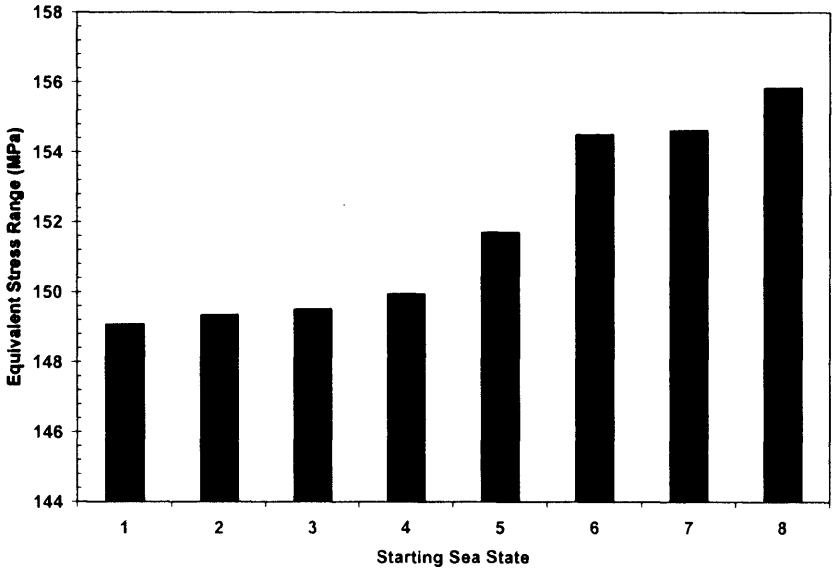

Figure 2.22: ESR of the JOSH sequence with different starting sea state

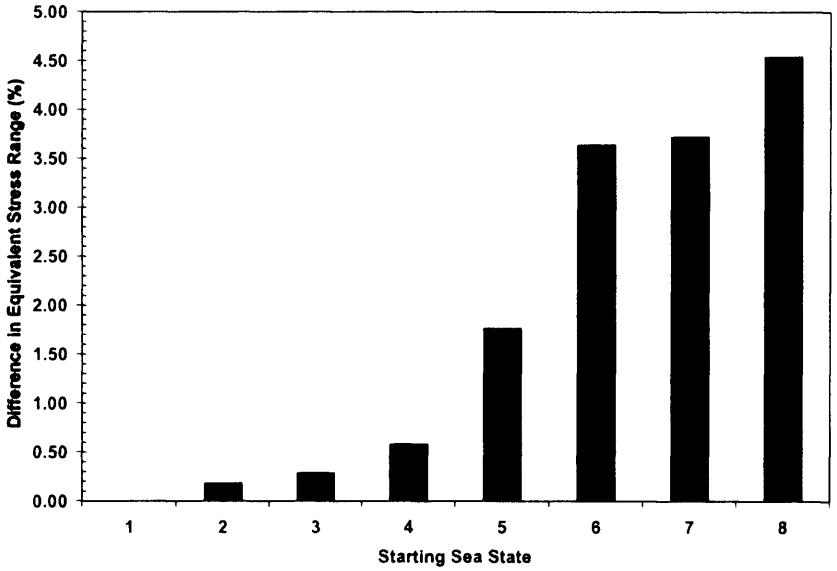

Figure 2.23: Percentage difference in ESR of the JOSH sequence with different starting sea state

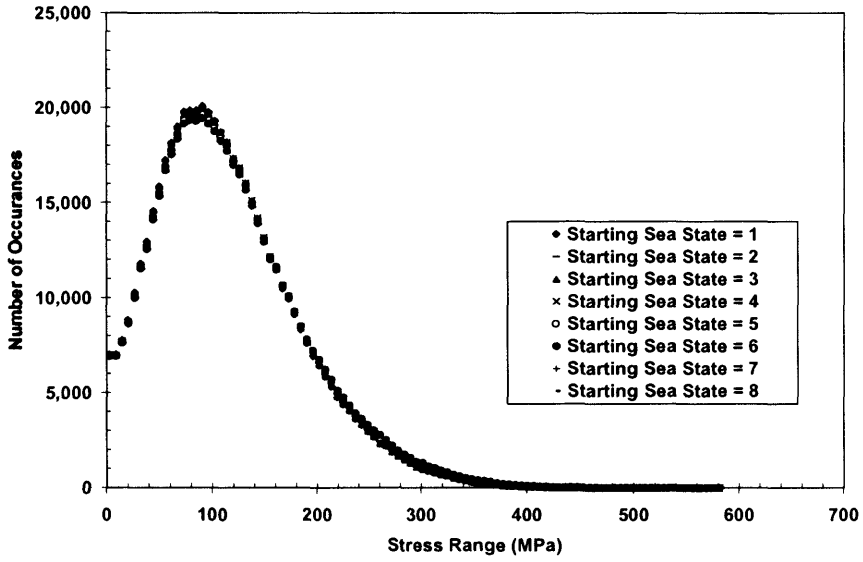

Figure 2.24: Stress range distributions of the JOSH sequence with different starting sea state

2.5 Summary

The importance of realistic loading conditions in fatigue testing was discussed in this chapter. Although there are various models that can generate VA load-time histories, very few studies were carried out on assessing the suitability of the generated sequences. As shown in the preceding sections, the JOSH model utilises advanced simulation techniques to generate the VA load-time history. The statistical stationary aspect of the JOSH load sequence is clearly demonstrated in the above sections, by using the relevant analyses. The analyses clearly highlighted the importance of an ergodic and stationary load-time history and it has been shown that erroneous parameters used in the JOSH model can lead to an inadequately mixed sequence. A non-stationary load sequence will have varying equivalent stress range, frequency content and power density spectrum. A standardised stationary load sequence is vital since the statistical nature of the load sequence is known to have a detrimental effect on the fatigue crack growth. This is highly important as non-uniform fatigue crack growth will cause problems during fatigue analysis and can lead to erroneous results. The stationary load sequence generated using the JOSH model described earlier was employed in the fatigue testing of high strength jack up steel detailed in Chapter 3.

2.6 References

[2.1] Palmgren A., "Durability of Ball Bearings", *Z Ver Deut Ing*, Vol. 68, 1923, pp. 339-341.

[2.2] Miner M. A., "Cumulative Damage in Fatigue", *J Appl Mech*, Vol. 12, 1945, pp. A159-A164.

[2.3] Head A.K. and Hooke F.H., "Random Noise Fatigue Testing", *Proc Int Conf Fat Metals, Institute Mech Engng,* 1956, pp. 301–303.

[2.4] Kowalewski J., "On the Relation between Fatigue Lives under Random Loading and under Corresponding Program Loading", In: Full-Scale Fatigue Testing of Aircraft Structures, Ed: Plantema F. J. and Schijve J., Oxford: Pergamon Press, 1961, p. 60–75.

[2.5] Gassner E., "Effect of Variable Load and Cumulative Damage on Fatigue in Vehicle and Airplane Structures", *Proc Int Conf Fat Metals, Institute Mech Engng,* 1956, pp. 304-316.

[2.6] Schijve J., "The Endurance under Program-Fatigue Test", In: Full-Scale Fatigue Testing of Aircraft Structures, Ed: Plantema F. J. and Schijve J., Oxford: Pergamon Press; 1961, p. 41–59.

[2.7] Gassner E., "der deutschen Luftfahrtforschung", Jahrbuch, 1941, Vol. I, p. 472.

[2.8] Schütz D. , Lowak L., de Jonge J. B. and Schijve J., "A Standardised Load Sequence for Flight Simulation Tests on Transport Aircraft Wing Structures", LBF-Report FB-106, NLR-Report TR 73, 1973.

[2.9] Aicher W., Branger J., van Dijk G. M., Ertelt J., HÜck M., de Jonge J. B., Lowak H., Rhomberg H., SchÜtz D. and Schütz W., "Description of a Fighter Aircraft Loading Standard for Fatigue Evaluation FALSTAFF", Common Report of F+ W Emmen, LBF, NLR, IABG, 1976.

[2.10] Edwards P. R. and Darts J., "Standardised Fatigue Loading Sequences for Helicopter Rotors (HELIX and FELIX)", RAE- Report TR 84084 and TR 84085, Royal Aircraft Establishment, 1984.

[2.11] Breitkopf G. E., "Basic Approach in the Development of TURBISTAN, a Loading Standard for Fighter Aircraft Engine Disk", IN: Development of Fatigue Loading Spectra, Ed: Potter J. M. and Watanabe P. T., American Society for Testing and Materials, *ASTM-STP 1006*, 1989, pp. 65-78.

[2.12] Department of Energy, "Offshore Installations: Guidance on Design, Construction and Certification", 4th Edition, HMSO, Consolidated Edition, 1993.

[2.13] Pook L. P., "Spectral Density Functions and The Development of Wave Action Standard History (WASH) Load Histories", Int J Fat, TF-1892, 1985.

[2.13] Shutz W., Bergmann, Hruler and Huck, "The Common Load Sequence for Fatigue Evaluation of Offshore Structures- Background and Generation", IABG Report, TF-1892, 1985.

[2.14] United Kingdom Offshore Steels Research Project-Phase II: Final Summary Report, Ed. R. Peckover, Health and Safety Executive Report OTH 87 265, Her Majesty's Stationary Office, 1987.

[2.15] Wirsching P. W., "Probability-Based Fatigue Design Criteria for Offshore Structures", *Int J Fat*, Vol. 2, 1980, pp. 77-83.

[2.16] Pook L. P., "Spectral Density Function and the Development of Wave Action Standard History (WASH) Load Histories", *Int J Fat*, Vol. 11, No. 4, 1989, pp. 221-232.

[2.17] Lin N. K. and Hart W. H., "Time Series Simulation of Wide-Band Spectra for Fatigue Tests of Offshore Structures", *J Energy Resources Technol*, Vol. 106, 1984, pp. 466-472.

[2.18] Kam J. C. P., "Wave Action Standard History (WASH) for Fatigue Testing Offshore Structures", *Applied Ocean Research*, Vol. 14, Issue 1, 1992, pp.1-10.

[2.19] Pook L. P., "Spectral Density Function and the Development of Wave Action Standard History (WASH) Load Histories", *Int J Fat*, Vol. 11, No. 4, 1989, pp. 221-232.

[2.20] Pook L. P. and Dover W. D., "Progress in the Development of a Wave Action Standard History (WASH) for Fatigue Testing Relevant to Tubular Structures in the North Sea", American Society for Testing and Materials, Symposium on the Development of Standard Load Spectra, 29 April 1987.

[2.21] Schütz W. and Pook L. P., "WASH (Wave Action Standard History) A Standardised Stress-Time History for Offshore Structures", Development in Marine Technology 3, Steel in Marine Structures, Ed: Noordhoek C. and Back J., Elsevier, 1987, pp. 161-178.

[2.22] Kam J. C. P. and Dover W. D., "The Procedures to Generate the Wave Action Standardised History (WASH) - The Manual", UCL Report to the WASH Committee, 1988.

[2.23] Brekke J. N., Campbell R. B., Lamb W. C. and Murff J. D., "Calibration of a Jack-up Structural Analysis Procedure Using Field Measurements from a North Sea Jack-up", *Proc Offshore Technol Conf*, OTC 6465, 1990.

[2.24] Etube L. S., Brennan F. P. and Dover W. D., "Modelling of Jack-up Response for Fatigue under Simulated Service Conditions", *Marine Struct*, Vol. 12, 1999, pp. 327-348.

[2.25] Etube L. S., "Fatigue and Fracture Mechanics of Offshore Structures", Engineering Research Series- ERS-4, Professional Engineering Publishing Ltd., ISBN 1-86058-312-1, 2001.

[2.26] Pierson W. J. and Moskowitz L., "A Proposed Spectral Form for Fully Developed Wind Seas Based on the Similarity Theory of SA Kitaigorodsjii", *J Geophys Res*, Vol. 69, No. 24, 1964, pp. 5181-5190.

[2.27] Tantbirojn N., "Fatigue Testing of Weldable High Strength Steels Under Simulated Service Condition, Ph.D. Thesis, University College London, 2002.

[2.28] Ngiam S. S., Brennan F. P., Dover W. D. and Stacey A., "A Stationary Standardised Load Sequence for Variable Amplitude Corrosion Fatigue Testing of Jack-Up Structural Components", Tenth International Conference- The Jack-Up Platform, September, 2005.

[2.29] Press W. H., Flannery B. P., Teukolsky S. A. and Vetterling W. T., "Numerical Recipes in C: The Art of Scientific Computing- 2nd Edition", Cambridge University Press, ISBN 0521431085, 1992.

[2.30] Newland D. E., "Introduction to Random Vibrations, Spectral and Wavelet Analysis- 3rd Edition", Addison-Wesley Publishing Co., ISBN 0582215846, 1996.

[2.31] Olagnon M., Lebas G. and Thebault J., "Characterisation of Sea-States for Fatigue Testing Purposes", *Proc of 7th Int Symposium of Offshore Mech and Artic Engng*, ASME, Houston, 1988.

CHAPTER 3

3.0 Variable Amplitude Corrosion Fatigue (VACF) Testing of High Strength Steel

3.1 Introduction

In recent years there has been considerable interest in the offshore industry in using High Strength Steels (HSS) in the construction of offshore structures. This growing trend has seen HSS widely used in the fabrication of Jack-up platforms for production purposes, largely due to the optimisation of light weight design. This is particularly important due the competitive Oil & Gas industry, as considerable reduction in weight can lead to a significant saving in both manufacturing and operation costs. Jack-up platforms are conventionally designed to operate in a water depth of 100 meters with an intended service life of 35 years [3.1]. In the early days, they were used extensively as short term mobile drilling rigs and for other maintenance operations. This however is now changing as jack-ups are increasingly being used as long term production platforms for production and exploration. The use of jack-ups for production and marginal field development means long term deployment, which significantly increases the risk of deterioration from long term problems such as corrosion fatigue. Hence, for production purposes, the service life of these structures must be assessed.

HSS with nominal yield strength of circa 450 to 700MPa have been commonly used in the fabrication of jack-ups, especially in the leg structures. Early realistic loading fatigue studies conducted on the offshore structures in the North Sea reported in Chapter 2 have provided the foundation of standard load histories for VA fatigue testing but these studies focused only at fixed platforms and medium strength steels. The load histories are not appropriate for jack-up structures as they are subjected to different loading conditions due to the inherent dynamic response of these structures. In this study, the modified JOSH framework described in the previous chapter is used as the standard load history generator for the fatigue testing of HSS.

Previous HSS projects [3.2-3.4] have concentrated mainly on establishing the influence of cathodic protection (CP), and over-protection, on the fatigue life of welded joints as the HSE Guidance [3.5] has proposed the need for CP limiters when using HSS. A major finding from the early studies was that at least some of the newer steels were not very susceptible to over-

protection in a corrosive environment at modest lives. The impetus for this research programme stems from concerns over the lack of data for fatigue of HSS in the long life region, the effect of cathodic protection and its susceptibility to hydrogen embrittlement. In addition, guidance on the residual stresses in welded joints for structural health assessment is only available for medium-strength steels. Hence, fatigue data under realistic loading and the behaviour of residual stresses arise from the welding procedures for HSS are still limited. Residual stresses induced during welding are known to have a deleterious effect on the fatigue resistance of welded components. Therefore, the current investigation aims to strengthen the understanding of such steels.

This chapter reports the experimental work conducted to investigate the medium-to-long life corrosion fatigue performance of SUPERELSO 702 (SE 702), a widely used high strength weldable jack-up steel (made by INDUSTEEL Creusot-Loire Industrie, France as an equivalent to A517 Grade Q steel). For clarity, some of the aspects of corrosion fatigue of offshore structures are included. Neutron diffraction residual stress measurement data are presented and compared to various standards and literature. The fatigue results presented include the measured fatigue life, fatigue crack growth rate and crack shape evolution. Stress life (*S-N*) and linear elastic fracture mechanics are the major approaches adopted for the analysis of the T-butt specimens tested. Experimental data is compared with data obtained from previous HSS studies. The influence of residual stress on fatigue crack growth is demonstrated by using a novel SIF weight function-based crack growth analyses.

3.2 Corrosion Fatigue of Offshore Structures

Corrosion is defined as the reaction of a material with its surroundings that produces measurable changes and the possibility of leading to damage. In metals, corrosion is a destructive process that will result in gradual deterioration of the material in a chemical oxidation-reduction reaction. Many researchers have demonstrated that the combined presence of water vapour and oxygen is the main cause of the atmospheric effect on the fatigue endurance of materials. Most metallic corrosion processes involve transfer of electronic charge in an aqueous or corrosive environment. In the offshore environment, seawater is known as the main source of corrosive media. The interaction of combined action of an alternating stress and a corrosive environment is termed corrosion fatigue, which is a type of environmental induced cracking phenomenon. It is worth mentioning that stress corrosion cracking (SCC), which is normally associated with static tensile stresses, is a completely different process compared to corrosion fatigue cracking although there are some distinctive similarities. Environment assisted fatigue has been a major concern for engineers especially in the offshore industry.

3.2.1 Hydrogen Embrittlement in HSSs

Hydrogen embrittlement, or sometimes known as hydrogen induced cracking, is a brittle mechanical failure caused by penetration and diffusion of atomic hydrogen into the crystal structure of an alloy [3.6]. Recent studies have shown that the presence of hydrogen in the aqueous environment plays a more significant role in the embrittlement of HSS [3.7-3.9]. Although the processes of corrosion fatigue and hydrogen embrittlement of HSS involve complex environmental conditions and electrochemical reactions, the overall process can be summarised as follows:

Anodic reaction:

$$Fe \rightarrow Fe^{2+} + 2e^{-} \quad \text{- (3.1)}$$

Cathodic reaction:

$$2H^{+} + 2e^{-} \rightarrow H_2 \quad \text{- (3.2)}$$

Overall reaction:

$$Fe + 2H^{+} \rightarrow Fe^{2+} + H_2 \quad \text{- (3.3)}$$

Due to the nature and complexity of hydrogen embrittlement in HSS, there is no definitive explanation of the phenomenon. Several models have been proposed to explain the basic embrittling mechanism during the crack initiation and propagation stage [3.9-3.12]. Generally, the most common hydrogen embrittlement mechanisms are the high-pressure bubble formation, reduction in surface energy (adsorption mechanism), reduction in the lattice cohesion force (decohesion mechanism), hydrogen interaction with dislocations, and hybride formation [3.9]. In HSSs, the effect of internal hydrogen super-saturation is significant, as a result, they are more susceptible to hydrogen embrittlement.

Since corrosion is a highly unfavourable phenomenon, many measures have been taken in order to prevent such a damaging process. Cathodic protection is one of the most widely used methods of corrosion prevention and mitigation. With an adequate cathodic protection system, the corrosion rate can be reduced to virtually zero and it can be used to reduce the corrosion of any metallic alloy exposed to any aqueous electrolyte. However, cathodic over-protection is to be avoided since the more negative the protection level, the more aggressive the cathodic reaction will be. It can be observed from Equation 3.2 that a more active cathodic reaction will increase the hydrogen content in the vicinity of the structure, resulting in higher susceptibility of hydrogen embrittlement especially in HSSs. The optimisation between corrosion control and susceptibility

of hydrogen diffusion in HSS is an ongoing research topic and hence it would be beneficial to investigate the VACF performance of HSS in such conditions.

3.2.2 Effect of Cathodic Protection on Fatigue Crack Growth

Cathodic protection is an electrochemical means of corrosion control in which the oxidation reaction in a galvanic cell is concentrated at the anode and suppresses corrosion of the cathode in the same cell [3.13]. It must be noted that although the mechanism of anodic protection is similar to cathodic protection, they are two different techniques. In cathodic protection, the object to be protected is the cathode while the anode is protected in anodic protection. In general, there two types of cathodic protection: sacrificial anode (passive) systems or impressed-current (active) systems.

In this study, emphasis is given to the impressed-current method, which requires the application of a cathodic potential or current to the structure to be protected by the use of an auxiliary power supply. In fatigue tests, cathodic protection can be stratified into three categories; under-protection (free corrosion), adequate protection and over-protection. These categories are a function of the relative magnitudes of the protection potential and the equilibrium potential for the free corrosion of bare steel in sea water [3.14]. The equilibrium basic potential for free corrosion of bare steel in seawater is approximately -650mV [3.13] with respect to Ag/AgCl reference electrode and adequate protection is said to be achieved if the cathodic potential applied to the structure virtually stops the dissolution of iron ions into the aqueous solution. A series of tests from the UKOSRP programme [3.15] have identified the adequate CP level on offshore structures in seawater environment to be around -850mV. Most of the fatigue design guidance for offshore structures are based on the medium strength steels such as BS EN 10025 Grade S355J2G3 [3.16] with yield strength circa 350MPa. The fatigue performance of HSSs under environmental loading and cathodic protection is not widely available. The concern of such limitation of data on a widely used material in the offshore industry, especially in the fabrication of jack-up structures, is noted by Sharp et al [3.17].

Extensive corrosion fatigue testing has been carried out in the past decade on offshore structures. Austin et al [3.18] and Vinas-Pich et al [3.19] concluded that overprotection of BS EN 10025 Grade S355J2G3 tubular joints showed a significantly shorter life compared to air and adequate CP. In these tests, the cathodic over-protection level used was -1050mV and the joints were tested under environmental loading. In addition, tests on API-X65 (yield strength circa 590MPa) have shown that cathodic over-protection can result in accelerated crack growth rates compared to free corrosion and air fatigue crack growth data [3.19, 3.20]. However, the results obtained were too few to statistically compare their performance with BS EN 10025 Grade S355J2G3.

One of the earliest studies confirming the detrimental effect of cathodic over-protection on HSSs was conducted under slow strain rate tests [3.21]. However, the tests conducted did not consider the effect of hydrogen embrittlement in HSSs under realistic loading and hence considered to be not conclusive. Since then, a newer generation of high strength jack-up steels with improved performance have been widely used in the offshore industry for better strength-to-weight ratio. Myers and Etube [3.22, 3.23] conducted a series of corrosion fatigue tests of tubular joints fabricated from SE 702 (yield strength circa 700MPa) under CA and VA loading. They concluded that increasing the cathodic protection level from -800mV to -1050mV results in a shorter fatigue life. The fatigue data suggested that the performance of this HSS joints was not necessarily inferior to that of conventional structural steel. In addition, although over-protection led to shorter fatigue lives, they have demonstrated that it was less damaging than stated by Davey [3.21]. It is important to stress that Davey's observations were drawn based on fatigue data obtained from an older generation of jack-up steels and not of SE 702. Additional tests suggested that there is no evidence that SE 702 is any more susceptible to hydrogen embrittlement than other HSS of similar grade. However, further tests at lower stress levels were recommended in order to investigate the effect of over-protection in multi-state variable amplitude loading corrosion fatigue.

Tantbirojn [3.4, 3.24] further investigated the corrosion fatigue of HSSs by using the JOSH framework. The specimens used were parent plates, ground welded plates and T-butt welded joints fabricated from SE 702 and DILIMAX690E-Z15, a high strength jack-up steel with a yield strength of 690MPa. Cathodic protection levels of -800mV and -1050mV were used and the specimens were tested under four point bending. The data obtained demonstrated that there is slight improvement in fatigue lives compared to BS EN 10025 Grade S355J2G3 (type 50D) steels. The results also showed that the CP level is significant and that higher CP potentials will have a detrimental effect on the fatigue performance of HSSs. It was observed that increasing the CP potentials shortened the fatigue life but the sensitivity to cathodic over-protection was greater than anticipated. Furthermore, the data were obtained only from the medium-life region and the VA load-time sequence used was not statistically stationary, as described in Chapter 2. The results were considered to be inconclusive and hence further fatigue tests using an adequate and stationary load sequence were needed to verify the observations. In this study, corrosion fatigue performance of T-butt welded joints fabricated from SE 702 is further investigated. The specimens were tested under the recently modified variable amplitude load-time sequence with cathodic protection levels of -800mV and -1050mV.

3.3 Residual Stresses in Welded Joints

Welding is widely adopted as a fabrication process in offshore structures due to its superiority over many other joining methods. Welded joints are very sensitive parts of the structure due to the metallurgical complexity and stress conditions in the vicinity of the welded region. In welded joints, for example T-butt welded plates, the residual stress field can be characterised by components of stress in the weld longitudinal and transverse directions, $\sigma_{zz}(y,x)$ and $\sigma_{yy}(y,x)$ respectively, and the spatial variation of these components in the transverse (y) and through-thickness (x) directions [3.25], as shown in Fig. 3.1 below. The stress component in the normal (x) direction is generally small and often assumed to be negligible, assuming that spatial variations of the stress in the longitudinal direction (z) of the weld are unimportant.

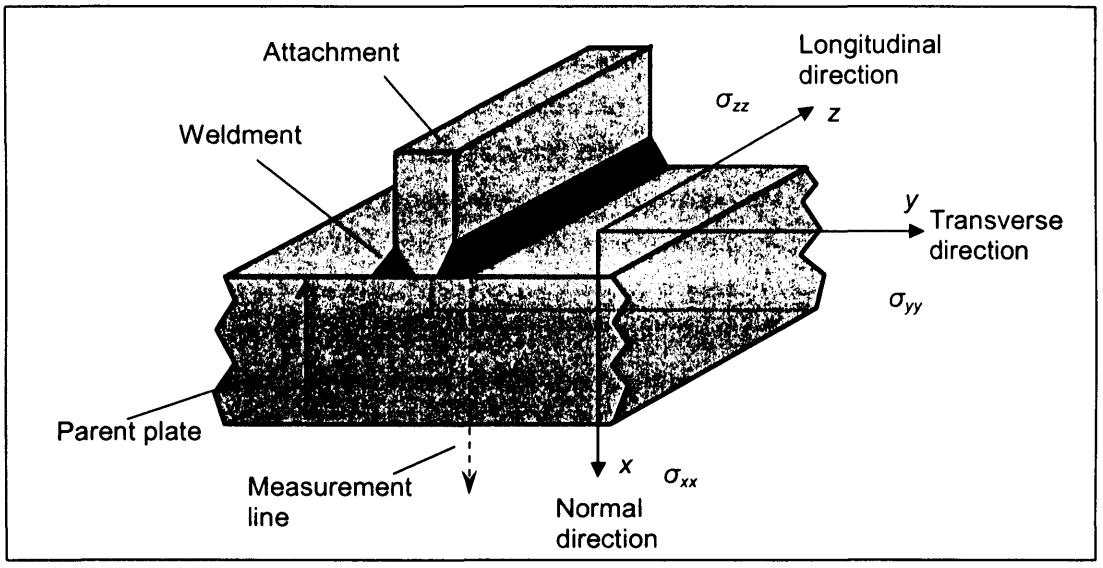

Figure 3.1: Directions of residual stresses in a T-butt welded plate

The presence of high surface tensile residual stresses at the weld toe region has a detrimental effect on the fatigue resistance of the structure, especially when the stress magnitude reaches the yield strength of the material. In addition, SCC might occur at components constantly exposed to corrosive environment if the tensile residual stress is sufficiently high. During cyclic loading the transverse tensile component (with respect to the weldment and crack faces) of the surface residual stress (Fig. 3.1) will contribute to the effective stress magnitude, in other words resulting in a higher SIF. Using the conventional approach of superposition of SIFs, the effective SIF due to the applied mechanical stress, σ_{appl} and the residual stress, σ_{res} can be written as:

$$K_{eff} = K_{appl} + K_{res} \quad - (3.4)$$

This higher effective SIFs will in turn increase the fatigue crack growth rate for cracks initiating at the weld toe. In many cases, the presence of relatively high magnitude of residual stresses in welded joints means that the fatigue behaviour is no longer governed by the applied mean stress. Hence, the understanding of residual stresses is a prerequisite in the fatigue and fracture mechanics analysis of welded joints in order to generate accurate SIF solutions and realistic life predictions.

In order to reduce the magnitude of the damaging tensile residual stresses in welded components, various procedures have been adopted in the industry with post weld heat treatment (PWHT) being the most common. Other methods include vibratory stress relief treatment, shot peening, low plasticity burnishing and others mechanical stress improvement procedures (MSIP). All PWHTs, including stress relief annealing, intermediate stress relief and dehydrogenation treatments are widely considered to be time consuming high cost operations, and significantly deters productivity. For example in a recent EU funded project, ELIXIR [3.26], it is postulated that the elimination of PWHT during fabrication would translate into 10% to 15% of cost savings in some industries. The aims of the project included the development of a standardised fast repair welding procedures without PWHT and the guidelines for the elimination of intermediate PWHT in industrial fabrication.

3.3.1 Residual Stress Distributions in Welded Joints

HSSs are generally known to have a combination of good strength and toughness but are difficult to weld without precautionary procedures such as material pre-heating. A high level of heat input is also often used in the welding of HSS structures due to its poor weldability. Due to the complex metallurgy of HSS, investigation into improving the weldability of HSS and the residual stresses arising from the welding process is still an ongoing research topic. Recognising the significance of residual stresses on fatigue crack growth in welded components, British Energy Generation Ltd. R6 [3.25], BS 7910 [3.27, 3.28] and API RP 579 [3.29] provide recommended residual stress distributions for the assessment of crack-like flaws in a variety of welded geometries. The compendia include representative through thickness longitudinal and transverse residual stress distributions based on reviews of published experimental data obtained from as-welded structures and structures subjected to PWHT. The measurement data used by R6 and BS 7910 were originally obtained from the EU funded SINTAP Project [3.30] but these data are mainly based on medium-strength steels. In this section, the recommended residual stress distributions will be compared to the experimental measurements obtained from the SE 702 T-butt welded specimens. It should be noted that only the through-thickness transverse residual stress distributions are discussed and the residual stresses referred to in this section are the long range macro residual stresses.

In R6, BS 7910:2005 and API RP 579, the transverse residual stress distribution at the weld toe in ferritic T-butt welded plates is based on the electrical energy of the largest weld run at the weld toe and the distribution is only valid for flaws emanating from the welded side. The bilinear upper bound function proposed by Leggatt [3.31] has a maximum residual stress at the weld toe and reduces linearly to zero at a distance of x_0 from the surface. The normalised transverse residual stress distribution can be written as:

If $x_0 < T$,

$$\frac{\sigma_{res}}{\sigma_Y} = 1 - \frac{x}{x_0} \quad \text{- (3.5)}$$

If $x_0 > T$,

$$\frac{\sigma_{res}}{\sigma_Y} = 1 \quad \text{- (3.6)}$$

$$x_0 = \sqrt{\frac{C}{\sigma_Y}\left(\frac{\eta q}{v}\right)} \quad \text{- (3.7)}$$

Where σ_{res} is the transverse residual stress in MPa

σ_Y is the 0.2% proof stress of the material in MPa

C is a thermal expansion dependent material constant (= 122 for ferritic materials)

η is the welding process efficiency (= 0.8 for ferritic materials)

q/v is the heat input rate in J/mm

x is the distance into the plate measured from the surface at the weld toe in mm

T is the parent plate thickness in mm

x_0 is the size of the yielded zone in mm

In BS 7910:1999, the corresponding normalised transverse residual stress distribution is an empirical polynomial upper bound fit on the experimental data and is given as:

$$\frac{\sigma_{res}}{\sigma_Y} = 0.97 + 2.3267\left(\frac{x}{T}\right) - 24.125\left(\frac{x}{T}\right)^2 + 42.485\left(\frac{x}{T}\right)^3 - 21.087\left(\frac{x}{T}\right)^4 \quad \text{- (3.8)}$$

The SE 702 HSS used in this study has a yield strength of 700MPa and the average welding electrical heat input rate used was 1.8kJ/mm. The resultant distributions recommended by the

standards discussed above are plotted in Fig. 3.2 below. The residual stresses were normalised with respect to the parent plate material yield strengths while the positions along the thickness were normalised with respect to the parent plate thickness. It must be noted that the recommended distributions are upper bound profiles to experimental data and hence they are not necessarily self-equilibrating. In R6, the as-welded residual stress distributions in ferritic T-butt welded plates are valid for thickness = 25 to 100mm, yield strength = 375 to 420MPa and welding electrical heat input per unit length = 1.4kJ/mm. No validity ranges are provided for T-butt welded plates in both revisions of BS 7910 while API RP 579 claimed that the distributions are valid for all ferritic steels. It has to be pointed out that in R6 and BS 7910, the recommended distributions are based on limited experimental data, resulting in a limited validity ranges considering the wide range of steels and welding procedures used in various industries. As can be seen from the equations above and Fig. 3.2 below, the two different revisions of BS 7910 provide distinctive transverse residual stress distributions but the ambiguity is not addressed in the current standard.

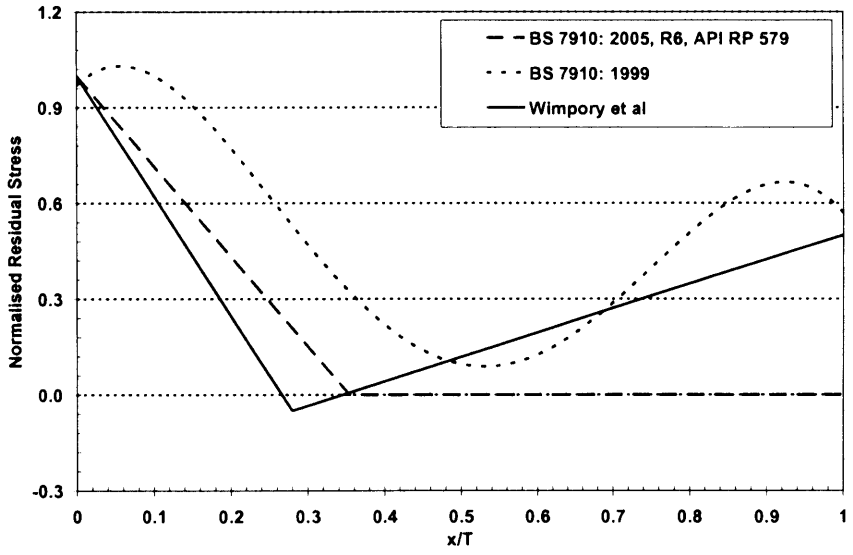

Figure 3.2: Recommended transverse residual stress distributions

Recently, Wimpory [3.32] and Hyeong et al [3.33] conducted extensive residual stress measurements in various welded geometries using neutron diffraction, X-ray diffraction and deep hole drilling techniques. The welded components investigated included T-butt welded plates, tubular T-joints, tubular Y-joints, pipe-butt welds, tube-on-plates, cold bent-pipes and repair welds fabricated from a wide range of engineering steels (including SE 702) and welding procedures. The experimental data obtained from the different measurement techniques have shown good agreement and broadly similar trends. Emphasis was given to the transverse through-thickness residual stress distributions and when the stress profiles were normalised by their respective

material yield strength, an inverse linear correlation versus the normalised depth can be observed. The experimental data obtained were compared to various literature and to data in R6 and BS 7910. A bilinear estimation of upper bounds of the experimental data was obtained following a statistical analysis. The bilinear normalised transverse residual stress distribution for T-butt welded plate joints is plotted in Fig. 3.2 above.

As can be seen from the figure, BS 7910:1999 provides the most conservative estimation followed by the distribution recommended by R6, BS 7910:2005 and API RP 579. Wimpory et al noted the over-conservatism in the distributions recommended by the standards and stated that the proposed bilinear estimation provides a more realistic estimation since it was based on a wider range of welded geometries, steels and welding procedures. However, it was reported [3.32, 3.33] that when neutron diffraction data were plotted in normalised form, the residual stresses in medium strength steels are slightly higher than those obtained from HSS. The differences were thought to be caused by possible measurement errors (±30MPa), and the different weld geometries and welding procedures. In addition, the authors stated that the proposed bilinear distribution for T-butt welded plates may be non-conservative for $x/T>0.3$ due to the extrapolation process on the membrane stress involved. This clearly suggests that further investigation is needed. The over-conservatism of the distributions recommended by the standards above has also been addressed in other literatures e.g. [3.34, 3.35]. The recommended distributions, however, do provide an insight to the residual stresses present in welded joints when actual data are not available. If necessary, the residual stress distributions can be scaled accordingly to give profiles with higher or lower conservatism, depending on the application and the safety factor required.

Although the studies described above were based on a wide range of welded geometries, distinctive differences can still be seen from the proposed distributions. Due to the various materials and welding techniques adopted in industry, it is extremely difficult to replicate the exact measurement data, if not impossible. The complex metallurgy around the welded region and the differences in the weld toe geometry as well as the welding quality have always posed a problem for engineers. Although significant advancements have been achieved in past decades, there is still a lack of reliable in-situ residual stress measurement techniques. In addition, in-situ residual stress measurement in many structural components, especially in offshore structures is extremely difficult.

It has to be pointed out that the recommended distributions for the assessment of structures containing defects did not take into account the residual stress relaxation effect. The longstanding inability to perform reliable and non-destructive in-situ measurement means

monitoring of residual stresses on installed structures can be problematic. Furthermore, it is widely known that most in-service structures experience realistic loading and environmental conditions, which will significantly alter the residual stresses. Hence, the fundamentals of the behaviour and mechanism of residual stresses, including the relaxation effect (e.g. under CA loading) have to be understood before other relevant factors are considered.

3.3.2 Residual Stress Measurements in T-butt Welded Plates using a Neutron Diffraction Technique

In order to gain a better understanding of the residual stresses present in welded joints fabricated from HSS, neutron diffraction measurements were carried out in conjunction with a collaboration project with Imperial College [3.36]. Originally, one of the main objectives of the project was to investigate the effect of welding heat input energy on the through-thickness residual stress distributions in T-butt welded joints fabricated from HSS. The measurements performed on the specimens used in the present study, which had a welding heat input rate, E_I of 1.8kJ/mm were compared to those (from Imperial College) with identical geometrical weld and global dimensions but with a welding heat input rate of 3.6kJ/mm. Both batches of specimens were provided by INDUSTEEL CLI. For comparison purposes, the measurement data from Reference 3.32 for BS EN 10025 Grade S355J2G3 [3.16] T-butt welded plates are also included. Table 3.1 below summarises the weld parameters.

Specimen	Thickness (mm)	Yield Strength (MPa)	Restraint	No. of Passes	Current (A)	Voltage (V)	Heat Input Rate, E_I (kJ/mm)
SE 702 (1)	50	700	Yes	43	550	30	1.8
SE 702 (2)	50	700	Yes	43	550	30	1.8
SE 702 (3)	50	700	Yes	30	550-560	30-31	3.6
S355J2G3	50	355	Yes	18	170-240	21-23	2.0-2.5

Table 3.1: Summary of weld parameters

Prior to testing, ≈15mm slices were extracted from all the SE 702 test specimens to carry out the measurement, as measurements on the full-width specimen will require an excessively long beam time and were logistically impractical. The neutron diffraction measurement facility was provided by the NFL facility of the University of Uppsala, Studsvik, Sweden. Strains were measured in the longitudinal (z), normal (y) and transverse (x) directions using a 2 x 2 x 2 mm^3 sampling volume along the measurement line shown in Fig. 3.1 above. The 211 Bragg reflection with a wavelength

of 12Å was chosen, which yielded a reflection at approximately $2\theta = 93.5^{\circ}$ [3.36]. The average time taken for the measurement in each direction was approximately 24 hours. It has to be pointed out that the strain measurements in all three directions (i.e. *z*, y, and *x*) allowed the component of stress in these directions to be determined but they may not necessarily be the principal stresses.

Figs. 3.3 to 3.5 below show the neutron diffraction measurement data for SE 702 T-butt welded plates. The uncertainty in the stress measurements is ±30MPa. Due to time restrictions and scarcity of beam time, measurements were only performed on two of the specimens used in the present study. However, the measurement data show very good agreement in terms of profile and magnitude. It can be seen from Fig. 3.3 that the longitudinal residual stresses in all three specimens have comparable magnitudes. In the normal direction, the tensile zone for the specimens with lower heat input rate is smaller (Fig. 3.4). The magnitude of the stresses in the normal direction is relatively low compared to the stresses in other directions. Generally, the transverse residual stresses measured in the lower heat input specimens are relatively low. It may be seen from Fig. 3.5 that the peak transverse residual stress for SE 702 (1) and SE 702 (2) are much lower (less than half) compared to the value of the specimen with a higher heat input rate. However, the profiles are very similar in trend and the tensile residual stresses reduce to zero at approximately 7mm~8mm from the weld toe.

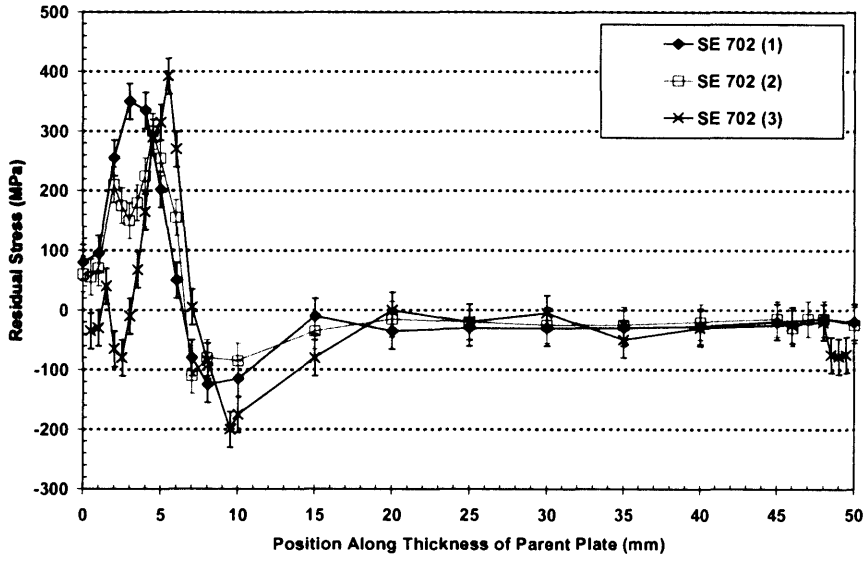

Figure 3.3: Longitudinal through-thickness residual stress distributions

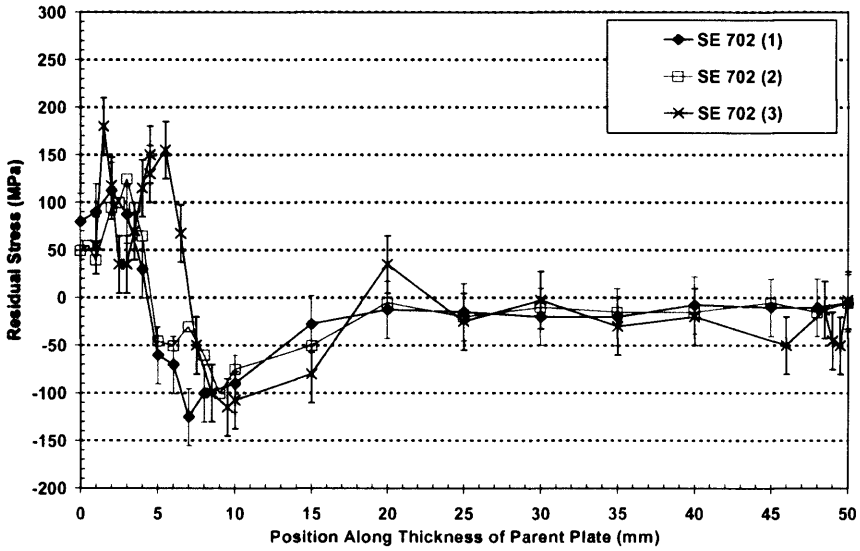

Figure 3.4: Normal through-thickness residual stress distributions

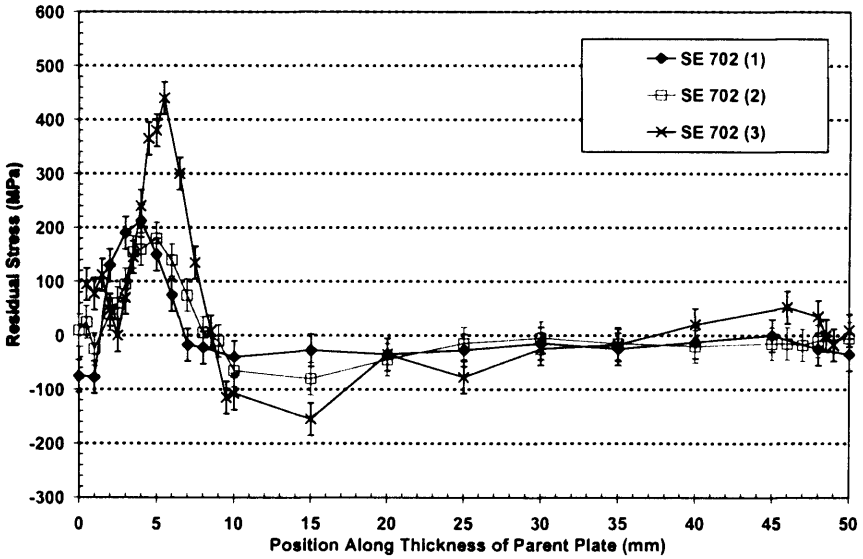

Figure 3.5: Transverse through-thickness residual stress distributions

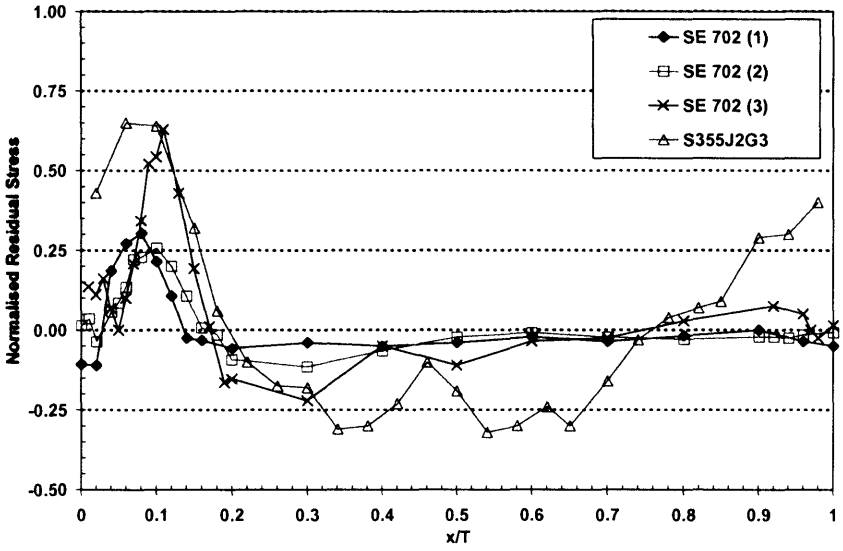

Figure 3.6: Normalised transverse residual stress distributions of SE 702 and S355J2G3

Fig. 3.6 above shows the comparison of the normalised transverse residual stress distributions between SE 702 and S355J2G3. From the figure, it can be seen that the high heat input rate measurement data of the SE 702 specimen compares well with the S355J2G3 measurement in terms of the magnitude and profile. The residual stresses in SE 702 (1) and SE 702 (2) on the other hand are observed to be much lower. The significant reduction in the peak transverse residual stresses may be related to the heat input rate to yield strength ratio (E_I/σ_Y). SE 702 (3) and S355J2G3 have comparable E_I/σ_Y ratios of 5.1 x 10^{-3} m^2 and 5.6 – 7.0 x 10^{-3} m^2 respectively. SE 702 (1) and SE 702 (2) have a E_I/σ_Y ratio of 2.6 x 10^{-3} m^2, which is approximately half of the value obtained from SE 702 (3) and S355J2G3. From Fig. 3.6 above, a reduction by a factor of 2 can also be observed in the peak transverse residual stresses in SE 702 (1) and (2).

The residual stress distributions presented above are reproduced in Fig. 3.7 below for comparison. It can be seen from the figure that all the measurement data are within the recommended upper bound estimations provided by the standards. The peak stress of SE 702 (3) is slightly higher than the upper bound estimation proposed by Wimpory et al but this could be due to measurement error. The over-conservatism of the distributions recommended by R6, BS 7910 and API RP 579 is evident from the graph. However, the experimental data used by the standards are mostly based on medium-strength steels and hence more tests are required to verify and expand the validity of these distributions.

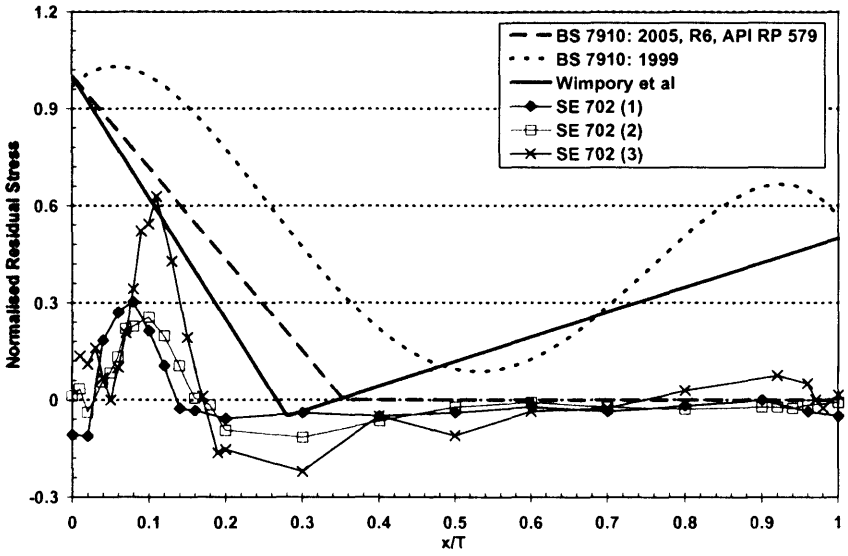

Figure 3.7: Comparison of normalised transverse residual stress distributions

The detailed comparison of the residual stress distributions presented above clearly show the applicability and limitations of the existing standards on the issue of residual stresses in welded joints. It is evident that there is a lack of residual stress data for welded joints fabricated from some newly developed steels. Furthermore, the influence of welding procedures on the induced residual stresses, especially in HSS, has not been widely investigated. Hence, further work is very much needed in order to better understand the generation and behaviour of residual stresses in welded joints fabricated from HSS. While conservatism is often seen as a practical option, it must be noted that over-conservatism in structural integrity assessment can lead to unwarranted repair or maintenance and unnecessary decommissioning of structures.

3.4 Experimental Test Details

3.4.1 Test Specimens

A total of five SE 702 T-butt welded specimens were supplied by INDUSTEEL CLI. The quoted mechanical and chemical properties of SE 702 are shown in Tables 3.2. The full-penetration welded T-butt specimens were fabricated from 50mm thick plates. The welding consumable used was Oerlikon Fluxofil and the average welding heat input energy employed was 1.8kJ/mm. Fig. 3.8 below shows the detailed dimensions of the test specimens and the welding procedures can be found in Fig. E1 in Appendix E.

Chemical composition of SUPERELSO 702 (wt%)					
C	**S**	**P**	**Si**	**Mn**	**Ni**
0.130	0.001	0.007	0.260	1.050	1.400
Cr	**Mo**	**Cu**	**Sn**	**Al**	**B**
0.410	0.470	0.190	0.002	0.020	0.001
Mechanical properties of SUPERELSO 702					
Ultimate tensile strength (MPa)			790-940		
Yield Stress (MPa)			700 min.		

Table 3.2: Quoted chemical composition and mechanical properties of SE 702

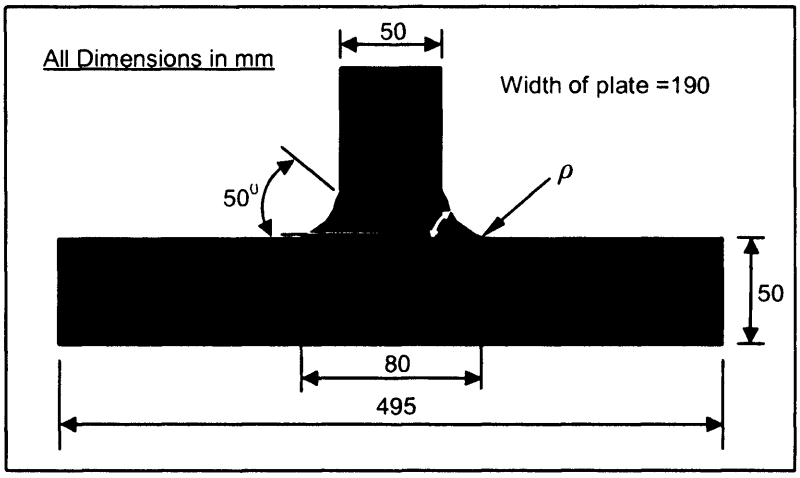

Figure 3.8: Dimensions of T-butt welded specimens

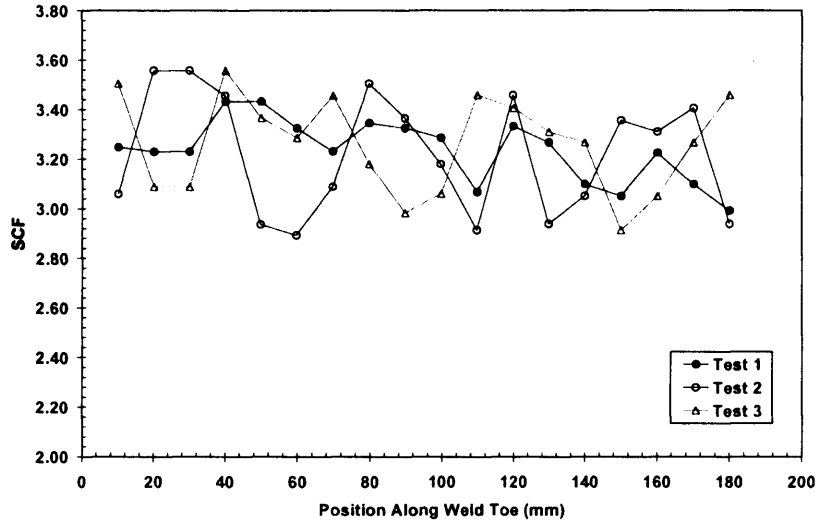

Figure 3.9: Samples of weld toe SCFs

Prior to testing, the weld toe root radius for all the test specimens were experimentally determined using the shadowgraph technique. The results were then analysed using published parametric equations for the evaluation of weld toe SCF [3.37]. The average SCF was calculated to be approximately 3.24. Samples of the weld toe SCFs are shown in Fig. 3.9 below.

3.4.2 Fatigue Test Set-up

All the tests were carried out under VA loading. The test programme consisted of one air test and four corrosion fatigue tests. Two of the corrosion test specimens were tested under medium life fatigue loading while the remaining two underwent long life fatigue testing. The fatigue tests were conducted under pure bending and the test set-up on an Instron 1000kN servo-hydraulic fatigue test machine can be seen in Fig. 3.10 below. The complete JOSH sequence was generated using 2000 sea state blocks of 10 minutes sub-block duration. Sea state 1 was set as the starting sea state for the sequence and one complete sequence consists of 536,657 turning points, which is equivalent to 268,326cycles. Table 3.3 below tabulates the details for one complete JOSH sequence while Table 3.4 summarises the fatigue test parameters. In order to minimise load interaction effects during VA loading, it is common practice to introduce a clipping ratio (maximum stress/RMS stress), i.e. limiting the peak stress of the load-time sequence. Despite that, over peak-clipping must be avoided in order to ensure that the modified stress history will have sufficient damaging stress ranges to be representative of the originally sequence. Previous studies [3.4, 3.23, 3.24] have shown that a clipping ratio of no more than 5 is optimum for the wave loading on jack-up platforms in the North Sea. In the present study, a clipping ratio of approximately 4.5 was adopted.

Parameter	Value
Sea states used	1-8
Mean stress(MPa)	321/216
Maximum stress(MPa)	613.42/415
Minimum stress(MPa)	29/17
RMS(based on rain flow ranges) (MPa)	133/90
Clipping ratio	4.61/4.59
Equivalent stress range (MPa)	149/101
Total number of cycles (Rain flow)	268,326
Average frequency (Hz)	0.24

Table 3.3: JOSH sequence parameters

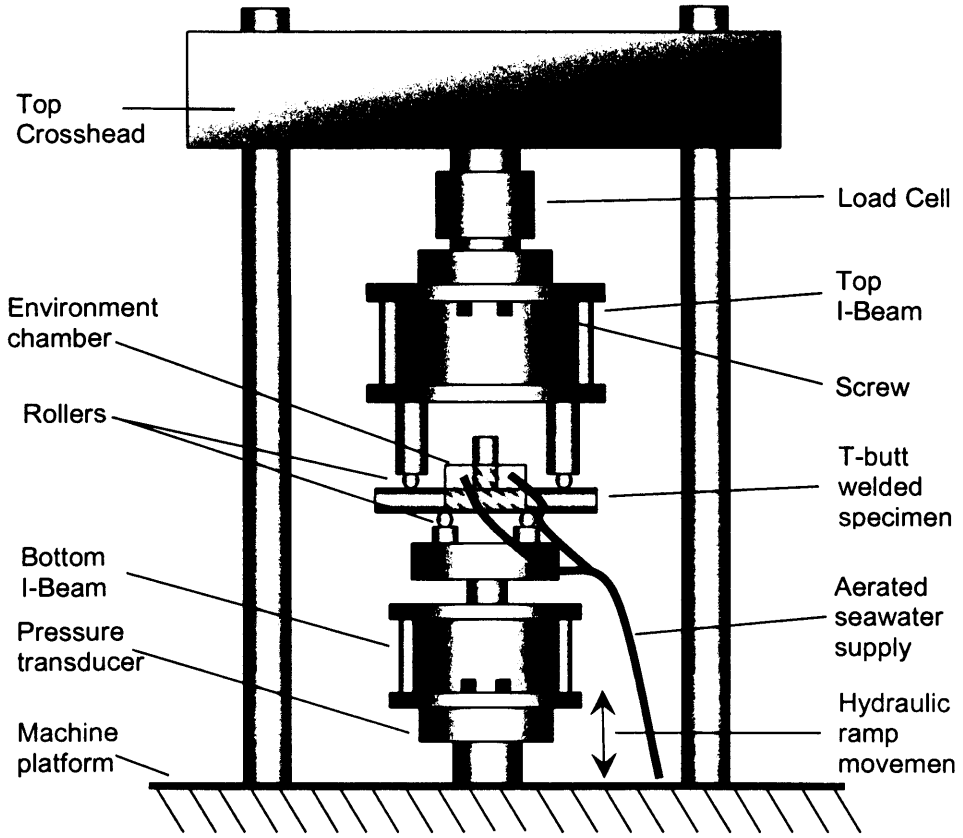

Figure 3.10: Test set-up on the Instron 1000kN fatigue test machine

Specimen	Type of loading	Environment	ESR (MPa)
Test 1	Variable Amplitude (VA)	Air	149
Test 2	Variable Amplitude (VA)	Seawater (CP -800mV)	149
Test 3	Variable Amplitude (VA)	Seawater (CP -1050mV)	149
Test 4	Variable Amplitude (VA)	Seawater (CP -800mV)	101
Test 5	Variable Amplitude (VA)	Seawater (CP -1050mV)	101

Table 3.4: Summary of fatigue test parameters

3.4.3 Test Control and Data Acquisition

The hydraulic actuator on the Instron fatigue test machine was connected to a digital Dartec 9600 System B controller, which was used to produce the absolute ramp motion corresponding to the VA loading sequence, by using load control mode [3.38]. A dedicated computer was connected

to the digital controller, where the generated JOSH sequence was played back. The generated sequence is in the form of turning points in the range of ±100 (Fig. 2.7), which can be scaled accordingly using a customary software (written in Quick Basic™) before being played back into the digital controller. The synchronisation between the computer and the Dartec 9600 digital controller enables the hydraulic actuator to respond correspondingly to the generated VA sequence in absolute mode.

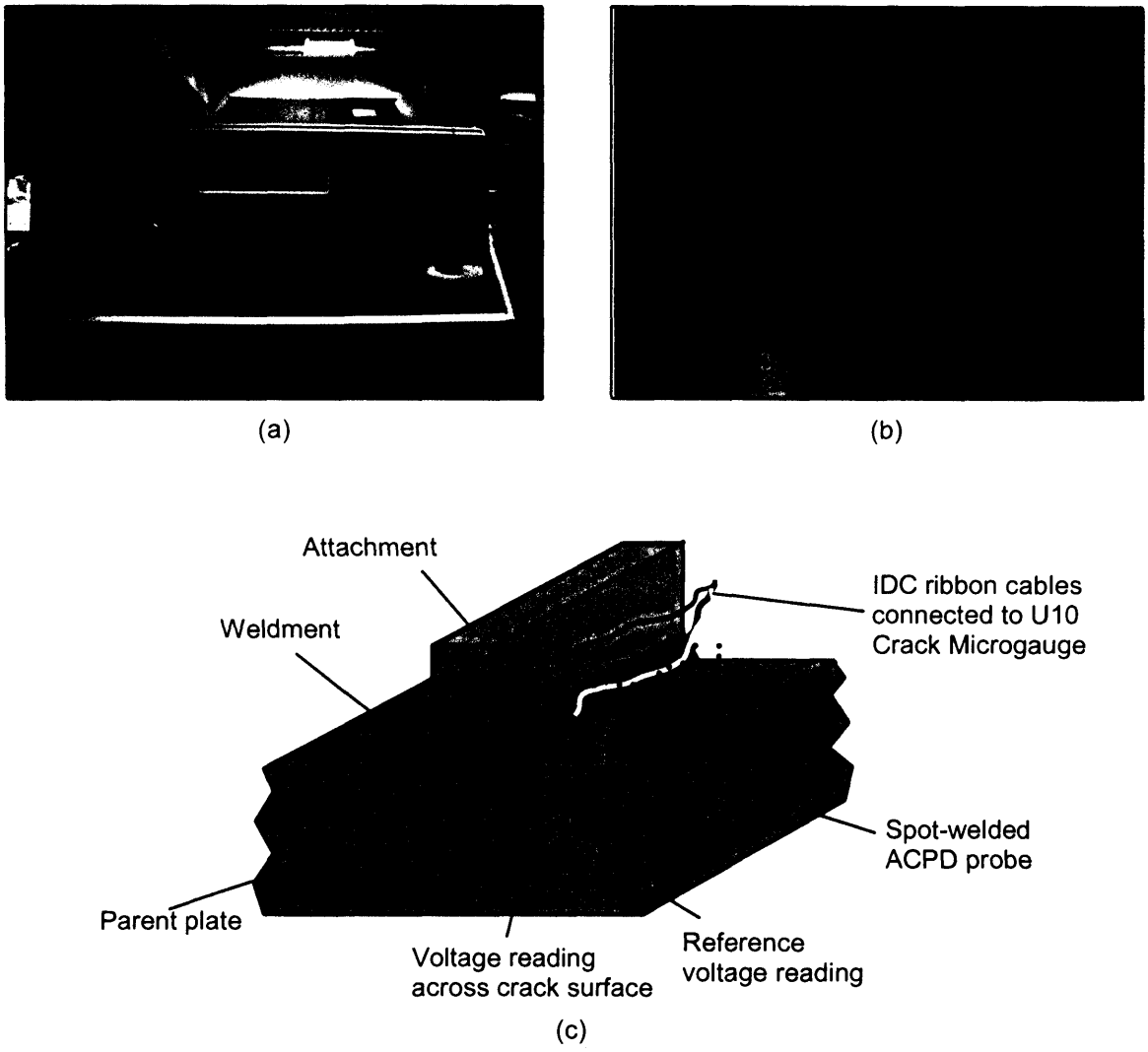

Figure 3.11: (a) U10 Crack Microgauge; (b) Spot-welded ACPD probes and (c) Figure showing an array of spot welded ACPD probes on a T-butt test specimen

In addition, the QB™ software also has the facility for obtaining crack growth data in the course of a fatigue test. The data acquisition was based on the Alternating Current Potential Difference (ACPD) technique [3.40] (Appendix E). Automated multi-channel ACPD measurements were

used to determine the crack growth profile along the weld toe using a U10 Microgauge [3.40]. This was made possible by using spot-welded probes, which were connected to the U10 Microgauge (Fig. 3.11a above) using IDC ribbon cables, as shown in Fig. 3.11b. Fig. 3.11c shows an array of spot-welded ACPD probes on a T-butt test specimen.

3.4.4 Simulation of Environmental Conditions

The effect of environmental conditions on the fatigue behaviour of welded joints has been discussed in previous sections. Hence, the appropriate simulated conditions must be achieved in order to obtain representative results.

The welded joint was immersed in artificial seawater made to ASTM D1141 standard [3.41]. The environment chamber around the parent plate and welded section was constructed from 10mm Perspex sheets and silicon sealant, which provided the required flexibility during the fatigue test. The fully aerated seawater was pumped from an insulated reservoir through a closed loop circulation into the environment chamber (Fig. 3.12a below). The seawater temperature range was maintained between 8°C and 10°C using an auxiliary refrigeration system and the pH level was also monitored constantly in the course of the test and maintained between 7.8 and 8.2. Two CP levels (-800mV and -1050mV) with respect to Ag/AgCl reference electrode, were used in this study. All CP potentials were based on the impressed current method, applied and maintained by using a Wenking CP Potentiostat per weld toe, as shown in Fig. 3.12b below.

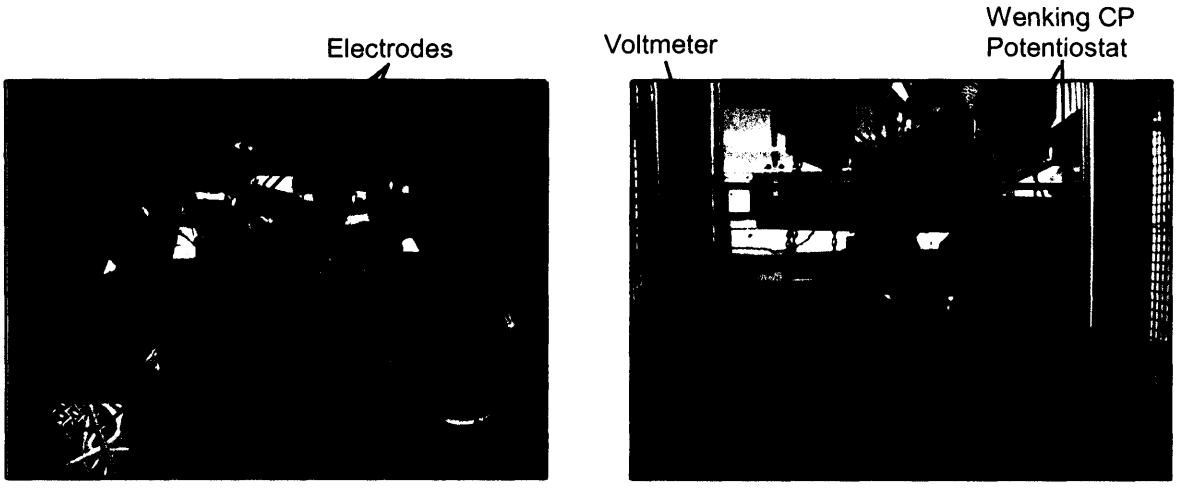

Figure 3.12: Environment chamber and impressed current cathodic protection set-up for corrosion fatigue tests

Prior to the fatigue test, the welded section was submerged in the artificial seawater with the adequate cathodic protection level. Pre-charging of specimens prior to testing is considered

essential to replicate the hydrogen concentrations profiles that develop in cathodically protected steels over many years in service. A soak time of two weeks was adopted in order to achieve uniform polarization of the specimen and allow hydrogen to diffuse through the steel. The soak time implemented was based on previous studies [3.4, 3.23, 3.24, 3.42, 3.43], which concluded that a minimum soak time of two weeks is sufficient for uniform hydrogen diffusion into the specimen.

3.5 Fatigue Test Results

The results obtained from the fatigue tests are presented in this section. They are presented in the form of initiation data, crack shape evolution curves, crack growth curves and the fatigue life of each specimen presented in *S-N* format. The average time taken for the tests with an ESR of 149MPa was approximately six weeks while the high cycle fatigue tests (ESR = 101MPa) lasted between four and five months.

3.5.1 *S-N* Data

The fatigue lives of the specimens are presented in the *S-N* format. Since the fatigue tests were conducted under VA loading conditions, the stress range used is the ESR for the VA sequence used while the life represents the number of fatigue cycles to failure. It must be noted that the correction factor to 16mm plate thickness (Section 1.2.1.1) was applied to the all the ESRs in the plots. The experimental fatigue life of each specimen is given in Table 3.5 below, with the corresponding actual equivalent stress range. The ESR shown was derived from the rainflow cycle counting technique, on the specific sequence duration for each test. The end of each test was defined as the attainment of a half plate thickness crack. The fatigue initiation data are also presented as a ratio of the initiation life, N_i, to the total fatigue life, N_t. It is important to note that Tests 1 to 3 had considerably different ESR during the fatigue crack initiation stage since all of the tests had initiation life shorter than the stationary point of the sequence. Fig. 3.13 below shows the *S-N* plot of the experimental results obtained, together with the Class P (Class F) design curves [3.44]. The fatigue lives predicted by the P Design Curves for Air and Sea environments of the 16mm BS EN 10025 S355J2G3 T-plate welded joint data are included in Table 3.6 for comparison. The stress ranges shown in the second column were corrected to a 16mm plate thickness so that the test results are comparative to the Design Curves.

Specimen	Effective ESR (MPa)	Duration	Initiation Life, N_i	Propagation Life, N_p	Total Life, N_t	N_i / N_t
Test 1	150	6 weeks	170,297	321,778	492,075	0.346
Test 2	152	6 weeks	222,309	213,691	436,000	0.510
Test 3	140	4 weeks	18,638	212,649	231,287	0.081
Test 4	101	19 weeks	1,810,000	780,000	2,590,000	0.70
Test 5	101	16 weeks	1,495,000	507,197	2,020,197	0.74

Table 3.5: Summary of fatigue test results and durations

Specimen	Corrected Stress Range (MPa)	Environment	Experimental Life, N_t	S355 Mean Life, N_{t50}	N_t / N_{t50}
Test 1	211	Air	492,075	161,570	3.05
Test 2	214	CP = -800mV	436,000	62,100	7.02
Test 3	197	CP = -1050mV	231,287	79,500	2.91
Test 4	142	CP = -800mV	2,590,000	211,676	12.23
Test 5	142	CP= -1050mV	2,002,197	211,676	9.46

Table 3.6: Comparison of fatigue life with BS EN 10025 Grade S355J2G3

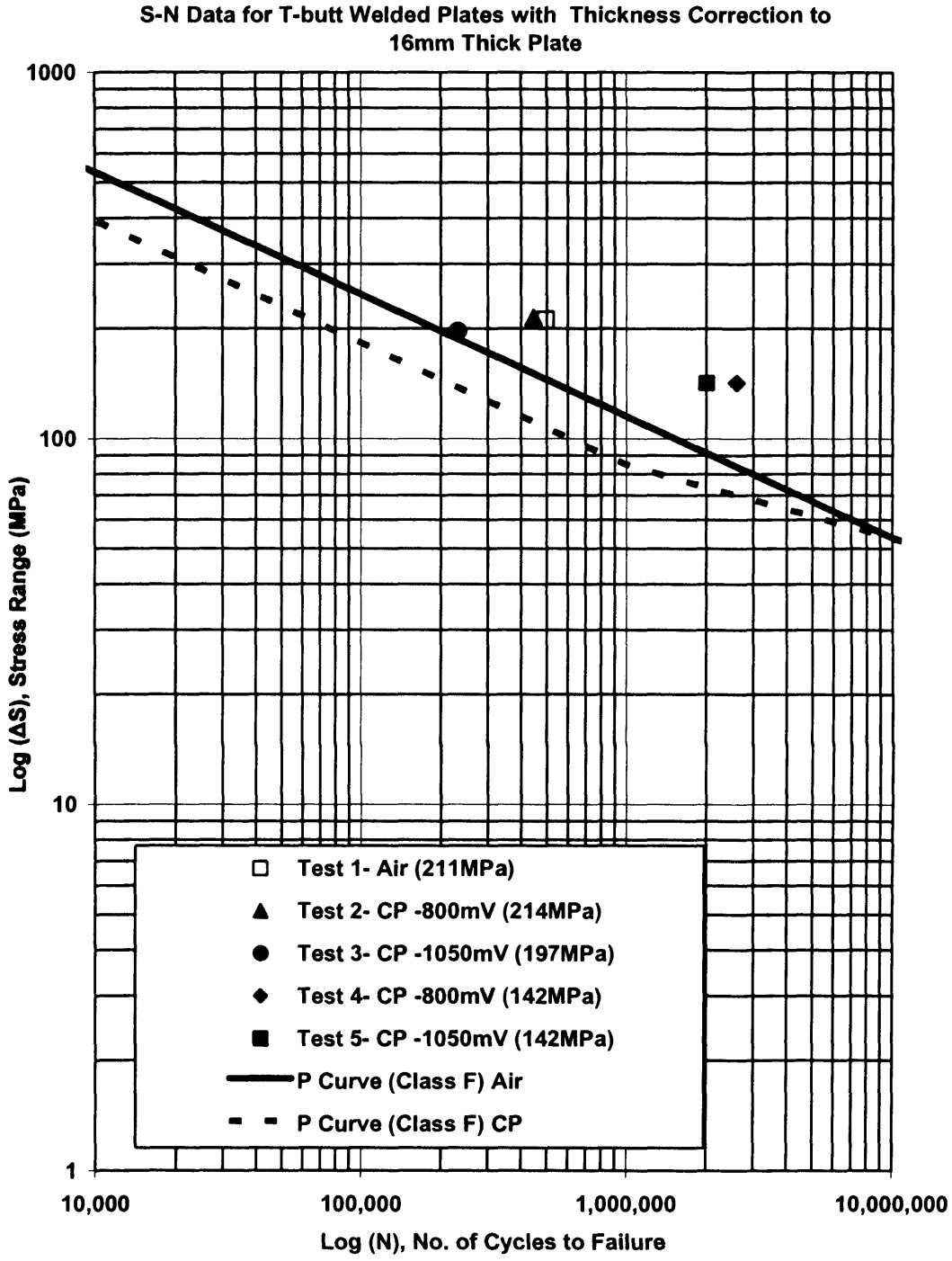

Figure 3.13: *S-N* plots of the experimental data and the Class P Design Curves

3.5.2 Fatigue Crack Growth Data

The crack growth curves for all the tests are shown in Figs. 3.14 to 3.19 below. The progress of the deepest point of the crack is plotted in these curves. The results obtained for the air test (Test 1) are shown in Fig. 3.14 while the results obtained from the corrosion tests are shown in Figs. 3.14 to 3.18 respectively. For comparison, the fatigue crack growth data for all the tests are reproduced in Fig. 3.19.

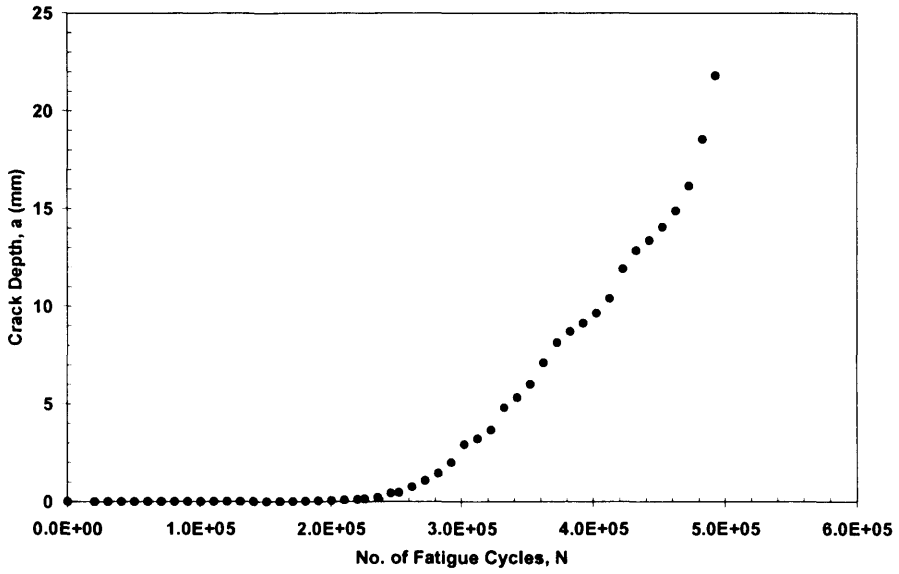

Figure 3.14: Fatigue crack growth data for Test 1

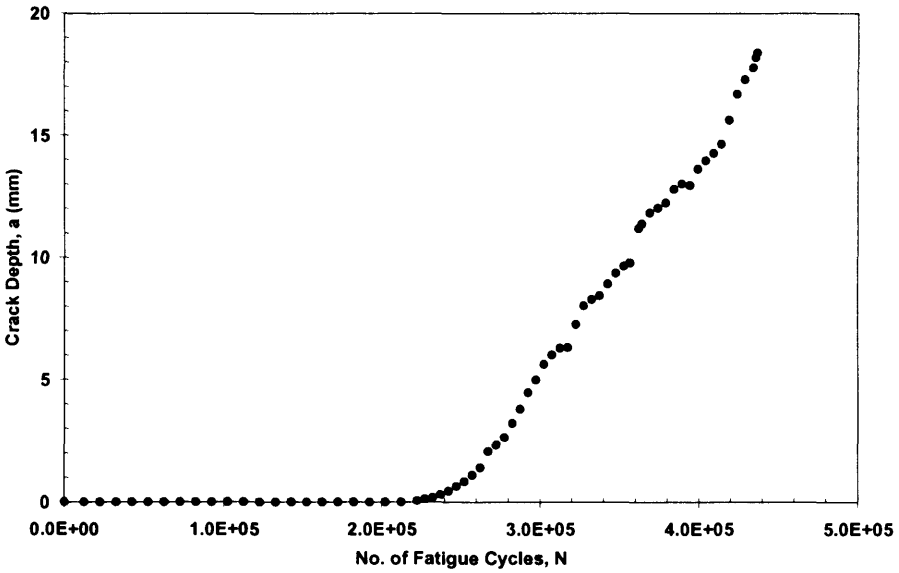

Figure 3.15: Fatigue crack growth data for Test 2

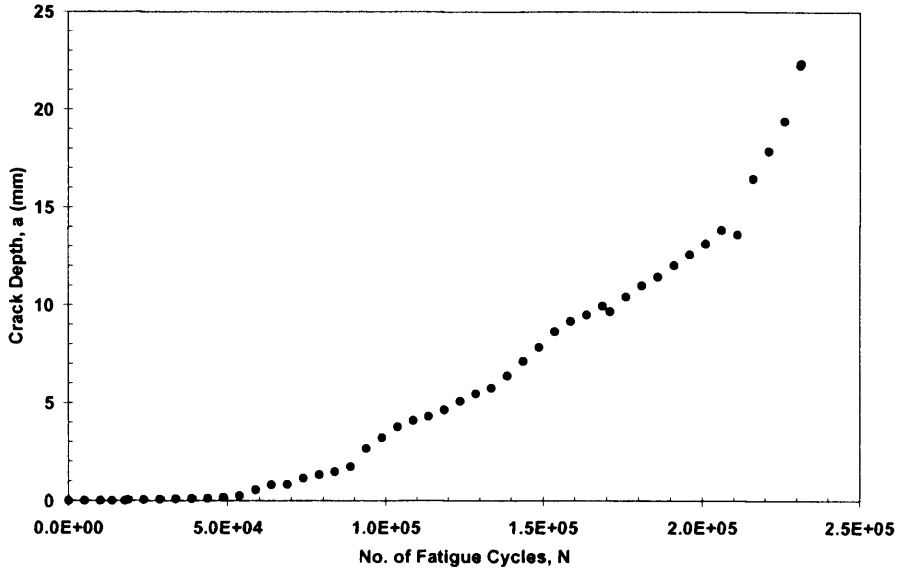

Figure 3.16: Fatigue crack growth data for Test 3

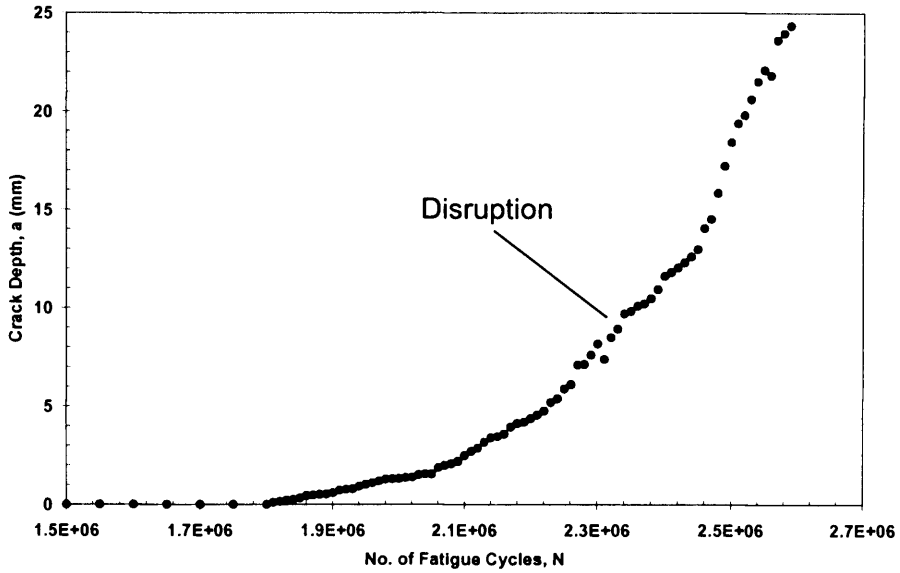

Figure 3.17: Fatigue crack growth data for Test 4

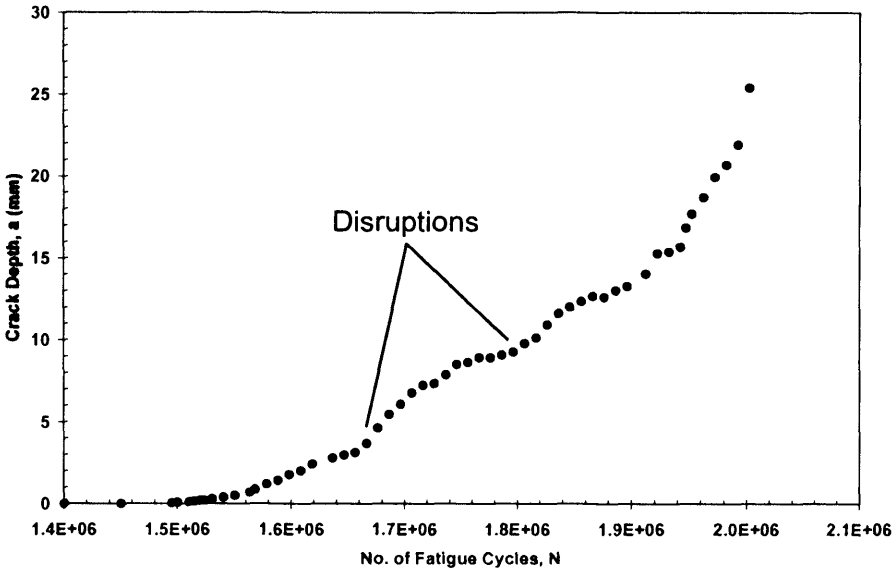

Figure 3.18: Fatigue crack growth data for Test 5

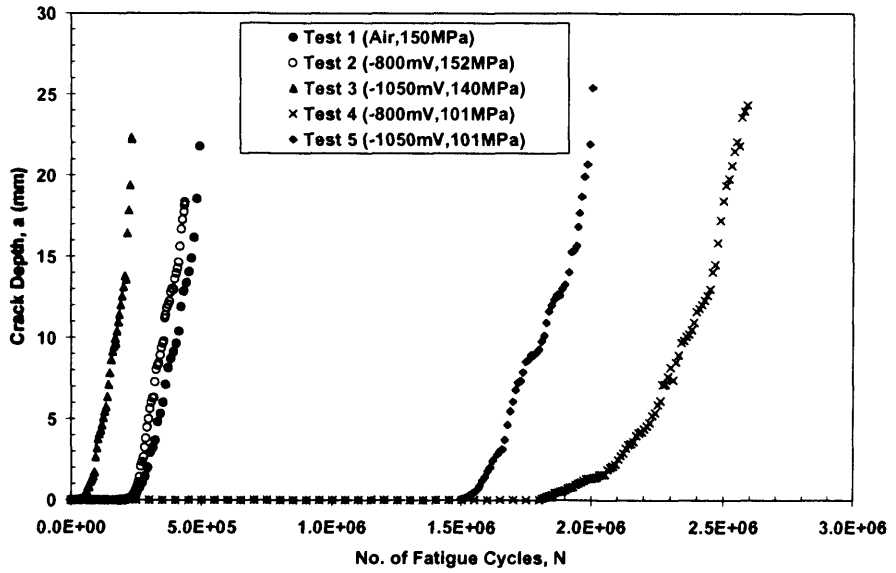

Figure 3.19: Fatigue crack growth data for all tests

For Test 1, final inspection was performed after the specimen had undergone 321,778 of crack propagation cycles (total fatigue life of 492,075) and the maximum crack depth recorded was 21.87mm. Test 2 had a propagation life of 213,691 cycles and a maximum crack depth of 18.38mm was recorded from the final inspection. Although the crack depth had not reached half of the plate thickness, the test was terminated prematurely due to a severe leakage on the environment chamber. It is believed that the decreasing rigidity of the specimen had caused the silicon sealant to break down. As can be seen from Fig. 3.16 above, fatigue testing of Test 3 was terminated at 231,287 cycles, after having undergone approximately 213,000 fatigue crack

propagation cycles. A maximum crack depth of 23.20mm was recorded from the final inspection. On the other hand, Test 4 had a fatigue crack propagation life of approximately 1,000,000 cycles, as shown in Fig. 3.17 above. Finally, Test 5 had undergone 507,197 of crack propagation cycles (total fatigue life of 2,020,197 cycles) and the maximum crack depth recorded was 25.40mm.

3.5.3 Crack Shape Evolution Data

The ACPD probes (10mm spacing) spot welded along the length of the weld toe enabled the crack shape evolution to be monitored. Crack shape evolution data show crack front profile and how this front advanced as the number of fatigue cycles was increased. This is obtained from measurements taken along the entire length of the weld toe at appropriately defined ACPD inspection intervals and about eighteen positions were monitored on each weld toe (it varied slightly from test to test).

Examples of early crack shape evolution data can be seen in Figs. 3.20 and 3.21 below. The crack shape evolution data obtained on completion of the tests are shown in Figs. 3.22 to 3.26 for the respective tests. Each plot represents only the failed side of the weld but in most cases, there were cracks on both sides of the parent plate. In some specimens, two crack initiation sites were detected. For example in Fig. 3.20 and 3.23, there were two crack initiation sites (position 100mm and 140mm) detected. The cracks coalesced after approximately 30,000 crack propagation cycles. This is similar for Test 3, where the cracks initiated at position 50mm and 100mm coalesced after about 58,500 fatigue crack growth cycles. Two crack initiation sites were also detected in Test 4 and the cracks coalesced after about 200,000 crack propagation cycles, as can be seen in Fig. 3.25. As for Test 5, crack initiations were detected at position 50mm and 100mm (Fig. 3.26) and the cracks coalesced after approximately 310,000 cycles. From the figures below, it is evident that semi-elliptical cracks were recorded during early fatigue crack growth in all the test specimens. The multiple cracks coalesced considerable early in the crack propagation life to form a long edge crack. This is not evident in Fig. 3.25 below as the spot welded ACPD probes at both of the edges of Test 4 detached during the course of the fatigue test, resulting in the loss of measurement data.

In some specimens, unconventional crack shape can be observed from the data collected. For example for Test 2 in Fig. 3.23, an unusual "trough" on the crack profile can be observed at the 110mm position, where the two initiated cracks coalesced. These could well be due to line contacts interfering with the ACPD measurements of crack depth. In the ACPD technique, this effect is called "line-contact effect", which occasionally occurs when multiple crack initiation exists and the final links are not served. This phenomenon can also be observed in Test 4 and Test 5.

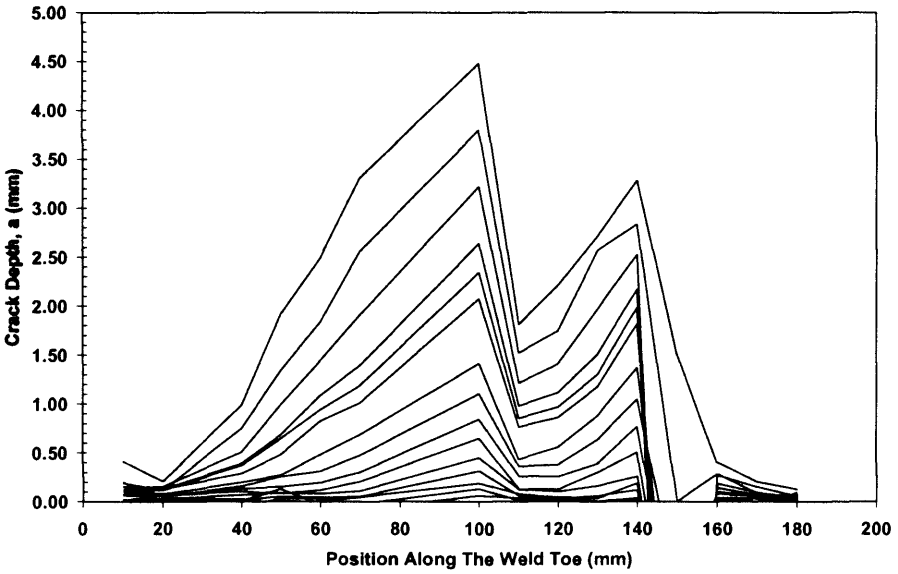

Figure 3.20: Early crack shape evolution data for Test 2

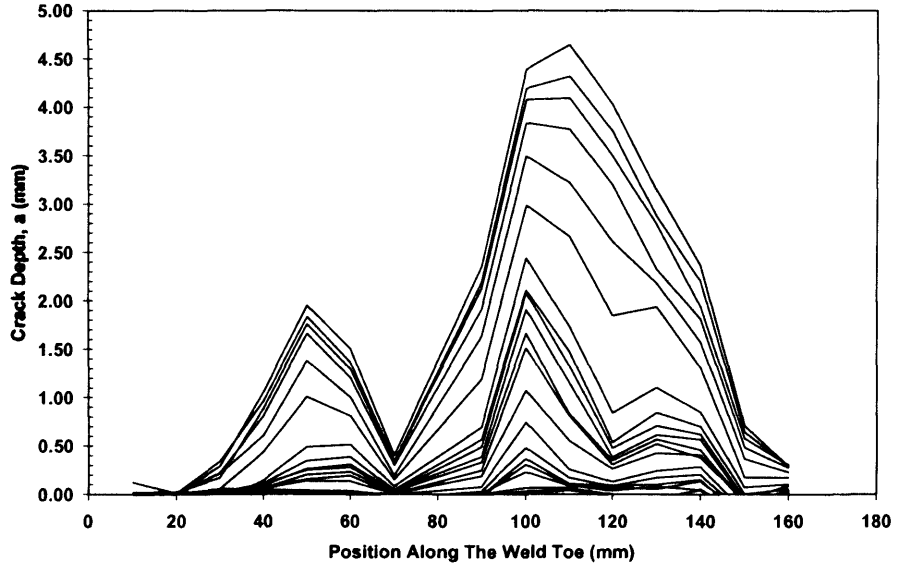

Figure 3.21: Early crack shape evolution data for Test 3

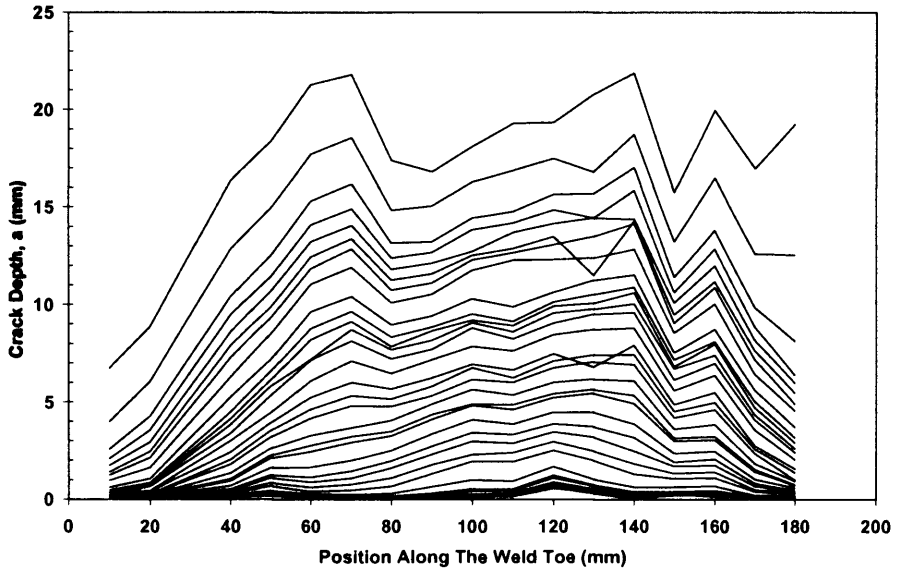

Figure 3.22: Crack shape evolution data for Test 1

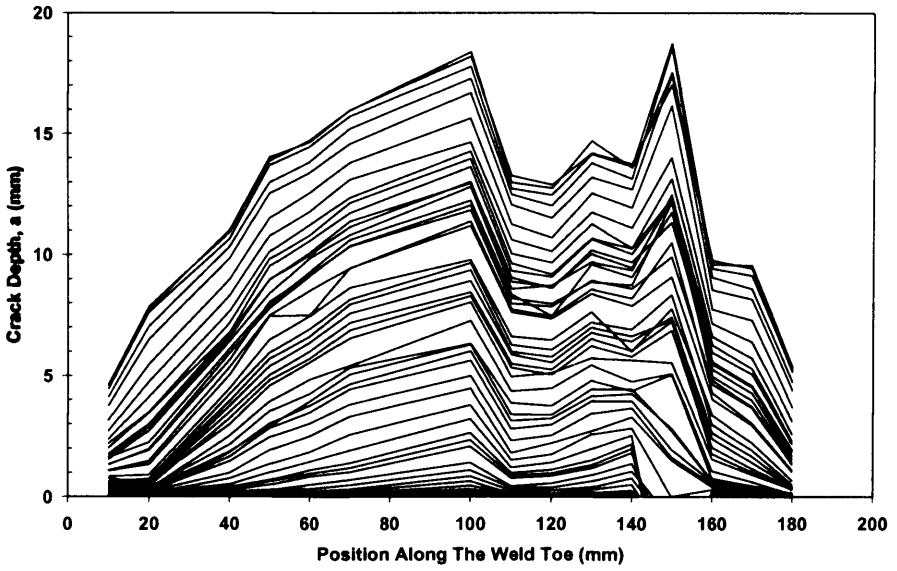

Figure 3.23: Crack shape evolution data for Test 2

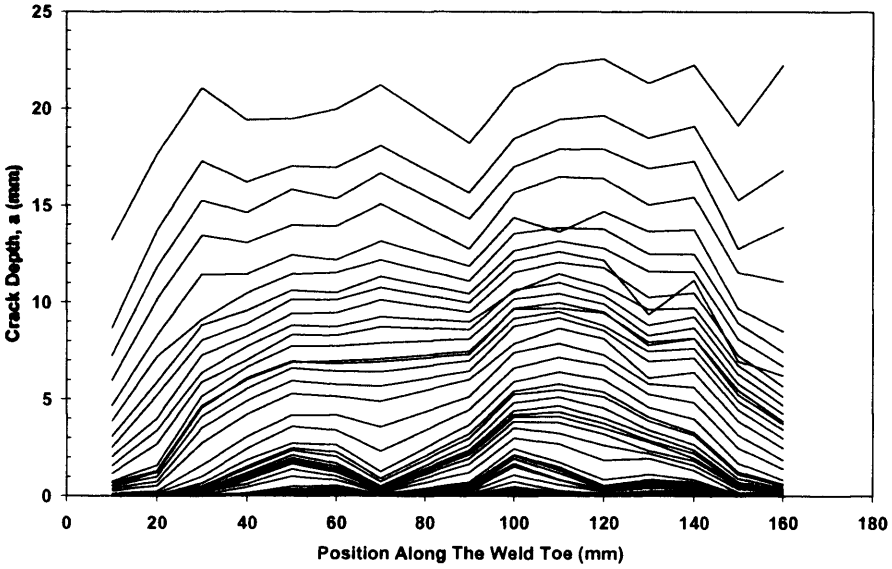

Figure 3.24: Crack shape evolution data for Test 3

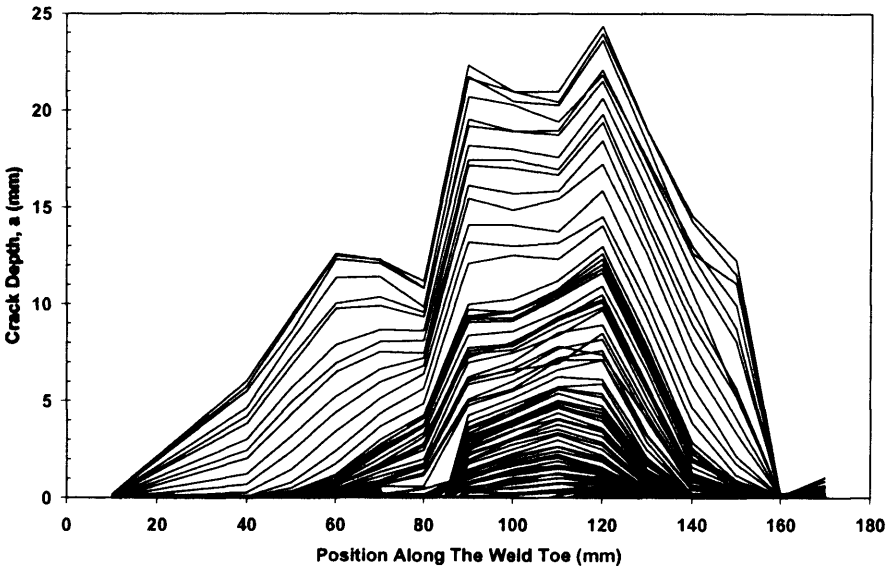

Figure 3.25: Crack shape evolution data for Test 4

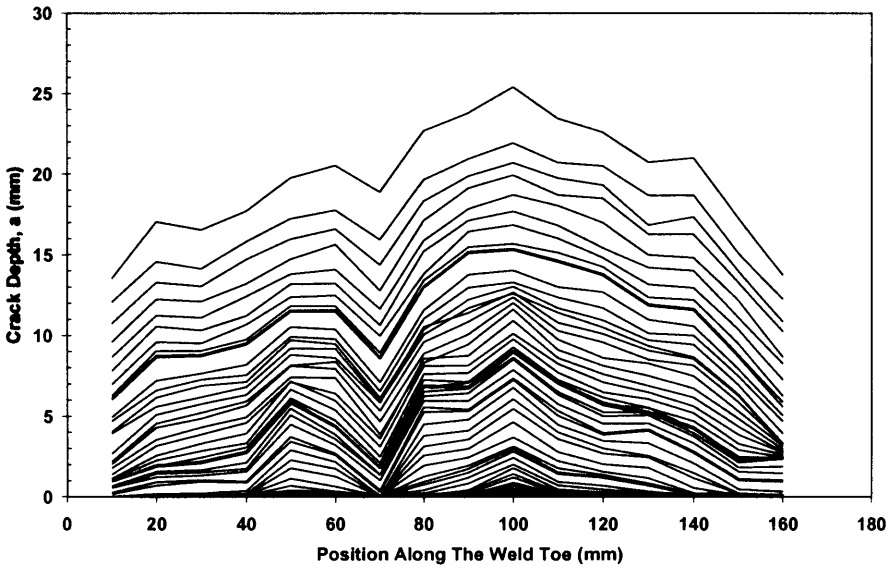

Figure 3.26: Crack shape evolution data for Test 5

3.6 Discussion of Fatigue Test Results

3.6.1 Fatigue Life

The fatigue crack initiation data shows that Test 1 and Test 2 have similar initiation cycles. However, there is a 90% reduction in the crack initiation cycles for Test 3, as shown in Table 3.5 and Fig. 3.19 above. On the other hand, Test 4 and Test 5, which were tested under an ESR of 101MPa, undergone fatigue initiation life of approximately 1,850,000 and 1,500,000 cycles respectively. Although the initiation cycles are significantly different between Test 2 and Test 3, the fatigue crack propagation cycles for both corrosion tests are very similar. For the long life corrosion tests, only 17% reduction in the crack initiation cycles was observed in Test 5 compared to Test 4. As can be seen from Table 3.5, the fatigue crack propagation lives for Test 2 and Test 3 are similar while a 35% reduction was recorded in Test 5 compared to Test 4. From the data obtained, it cannot be concluded that the data clearly shows the susceptibility of hydrogen embrittlement in HSS subjected to cathodic over-protection and it is believed that the significant reduction in initiation life of Test 3 is an isolated case. Visual inspection on the weld toe following the completion of Test 3 revealed welding imperfections in the vicinity of crack initiation site, which might have acted as additional stress raisers. If the reduction in initiation life is solely caused by cathodic over-protection, a similar reduction in fatigue crack initiation life should be observed in Tests 5. In addition, both Tests 3 and 5 show comparable fatigue crack propagation lives when compared to Tests 2 and 4 respectively.

The total fatigue life of Tests 1, Test 2, Test 4 and Test 5 is about 490,000, 436,000, 2,600,000 and 2,000,000 cycles respectively. The fatigue lives of Tests 4 and 5 are sufficient in representing a twenty-year round service loading of a jack-up structure. As can be seen from the *S-N* plot in Fig. 3.13 above, the experimental fatigue lives for Test 2 and Test 4 are well above the P curve (Class F) CP line and also the Class F Air line. Hence, it can be said that cathodic protection level of -800mV with respect to Ag/AgCl, as proposed by UK HSE Offshore Guidance Notes [3.44, 3.45], is adequate for the application to HSS. The mean line for the test specimens tested in corrosive environment clearly suggests that the Class F Design curves might be over-conservative for the application of HSS, especially in the long life regime. The most significant reduction in life (≈50%) is observed in Test 3, having a total fatigue life of just over 230,000 cycles. For Test 5, there is a reduction of 22% in the total fatigue life. In general, the shorter fatigue life of the corrosion tests is believed to be mainly caused by the hydrogen embrittlement effect. Furthermore, with cathodic over-protection, the effect of internal hydrogen super-saturation is more significant in HSS due to the accelerated formation of hydrogen content on the material. The mechanism of hydrogen embrittlement is known to increase the crack propagation rate possibly through enhanced grain boundary attack.

Although the results obtained have shown that cathodic over-protection has a detrimental effect on the fatigue performance of high strength steel, it is not as damaging as suggested in some literatures [3.21]. As can be seen from Fig. 3.13, the fatigue results have shown that the effect of cathodic over-protection is less detrimental in the low stress regime. Furthermore, SE 702 show far superiority in fatigue performance when compared to the corresponding predicted fatigue lives of BS EN 10025 S355 steel although an improvement is very much expected. The degree of improvement, especially for the fatigue lives in corrosive environment, is just remarkable (Table 3.6 above). Overall, the results obtained are consistent with previous high strength steels corrosion fatigue studies [3.4, 3.23], where a reduction factor of 30 – 50% was observed for cases where the CP level was increased from -800mV to -1050mV.

Fig. 3.27 below shows the comparison of the fatigue lives between the experimental results obtained in this study with previously conducted long life corrosion fatigue (LLCF) study by Tantbirojn [3.4, 3.24]. In the study, a total of 12 T-butt welded plates were fatigue tested using identical CP levels and similar ESRs adopted in the present study. As can be seen from the figure, there is a significant improvement in the fatigue lives of the SE 702 specimens. The fatigue lives of Test 1, Test 2, Test 4 and Test 5 are well above all the mean lines. Although Test 3 has a relatively shorter fatigue crack initiation life, its fatigue life is above the -1050mV (over-protection) mean line presented by Tantbirojn. It is believed that the LLCF test data obtained in this study is more representative and adequate due to several reasons.

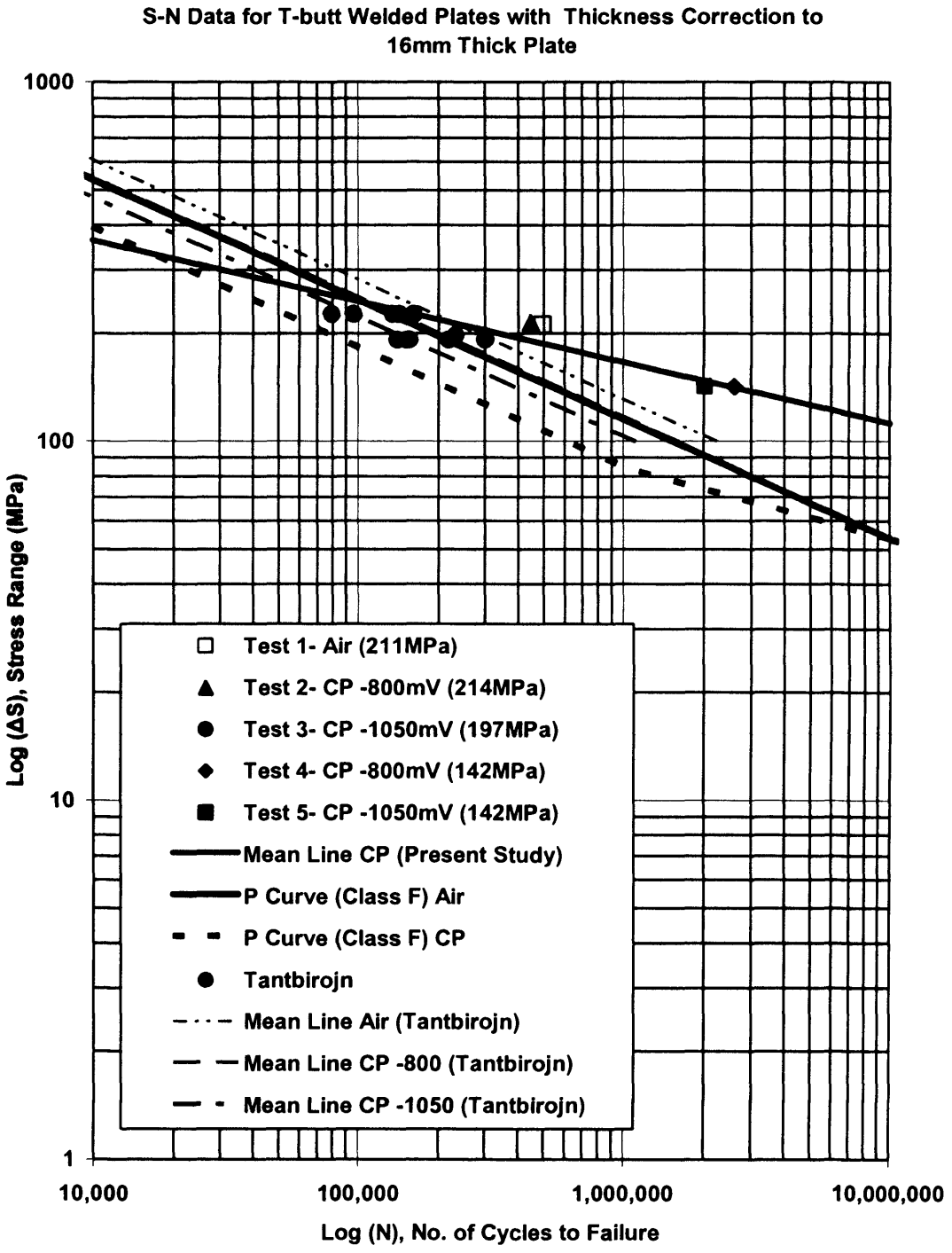

Figure 3.27: Comparison of experimental fatigue lives with results obtained from the study conducted by Tantbirojn [3.24]

The average fatigue life of the specimens tested by Tantbirojn was well under 170,000 cycles. The considerably short fatigue lives and the susceptibility of cathodic over-protection are significantly more severe than anticipated. As can be seen from Fig. 3.27, most of the results are close to and below the Class F design curve and the mean line for the present study. It is believed that the variable amplitude load sequence generator used was inadequate for the evaluation of long life fatigue performance of HSS. The VA load-time sequence used by Tantbirojn was found to have a decreasing amplitude against time [3.24], as shown in Fig. 2.11 presented in Chapter 2. This is mainly caused by the inadequate mixing of the sea states during the generation of the load history. In addition, the use of inappropriate wave modelling parameters is also believed to have contributed to the undesired characteristic in the load sequence. The relatively high stress ranges at the beginning of the sequence is found to have significantly accelerated the fatigue crack initiation rate of the specimens, resulting in considerably shorter fatigue lives.

3.6.2 Fatigue Crack Growth

As can be observed from the figures, the fatigue crack growth under VA loading conditions is considered to be steady although the JOSH variable amplitude load-time sequence consists of multi-sea states with varying stress intensity. However, this has been anticipated since the relevant analysis performed have shown that the JOSH sequence is stationary and the sea states are adequate mixed by using the appropriate Markov Chain-Monte Carlo technique. This becomes more evident when the results are compared with the fatigue data obtained by Etube [3.23] and Tantbirojn [3.24], as shown in Figs. 3.28 and 3.29 below respectively. Both the authors have used JOSH as the standard load history generator for fatigue testing but the sequence parameters were different from those used in the present study. As can be seen from the figures, there is a high crack growth rate at the beginning of each sequence repetition followed by almost constant growth rate and subsequent fall. The characteristic "stair case" type and non-uniform crack growth curves can be observed from both the figures, which is not seen in the results obtained in the current study. It is worth mentioning that a less significant "stair case" phenomenon can be observed in Test 4 (circa 2.4 million cycles) and Test 5 (circa 1.65 and 1.8 million cycles), but these points coincide with the disruptions caused during the fatigue test. Hence, it is not unreasonable to conclude that the unconventional fatigue crack growth pattern is not caused by the multi-sea states load sequence.

From the results presented above, the statistical nature of the load sequence is shown to have a detrimental effect on the corrosion fatigue crack growth. The convergence of the load-time sequence parameters is highly important as non-uniform fatigue crack growth will cause problems during fatigue analysis and can lead to erroneous results. It has to be pointed out that the

sequences used by the authors reported earlier are deemed to be inappropriate only for long life fatigue tests. This is due to the fact that in practice, a structure may be subjected to relatively higher loads (storm) immediately after installation. However, the current load sequence is more adequate in the present study since the emphasis is on the fatigue performance of high strength steel in the long life region.

Figure 3.28: Fatigue crack growth data obtained from Reference 3.23

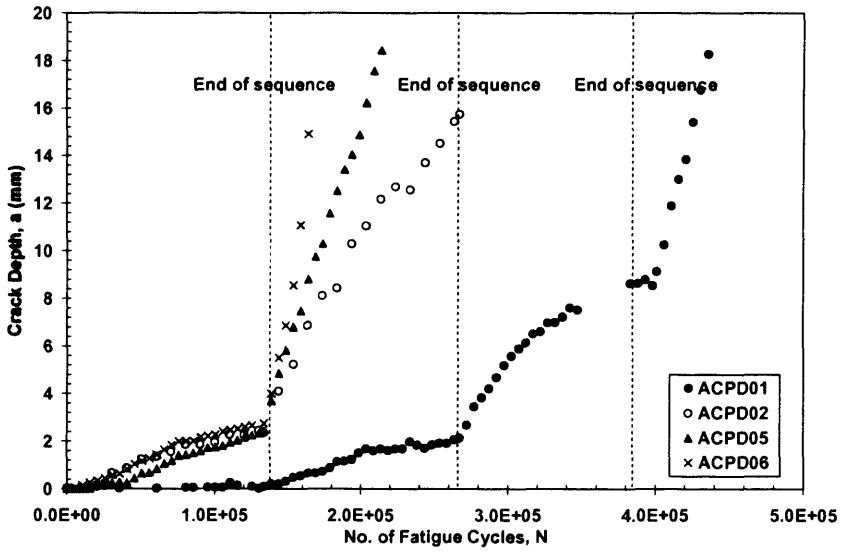

Figure 3.29: Fatigue crack growth data obtained from Reference 3.24

3.7 Fracture Mechanics Analysis of Fatigue Test Results

3.7.1 Fatigue Crack Growth Rate in VA Loading

It is widely known that most welded structures, especially those used in offshore structures contain flaws or imperfections. However, these flaws may not necessarily affect the overall structural integrity or service performance of the structure to a degree that might call for decommissioning. When cracks are discovered in-service, the current practice is to repair whenever possible. The economic constraints of offshore production, however, are now encouraging a more rational and cost-effective strategy to be established. The *S-N* approach is a very useful tool during the design stages but it provides little information on the assessment of structures containing crack like flaws. Before maintenance strategies can be rationalised, it is important to develop the ability to assess crack growth and this requires the application of fracture mechanics.

Generally, the fatigue crack growth rate of a material is assessed on a logarithmic crack growth rate against SIF range plot, i.e. Log *da/dN* vs. Log ΔK, as shown in Fig. 1.5 in Section 1.3.3. From the crack depth measurement data collected using ACPD, the crack growth rate (per cycle), *da/dN*, for the deepest point of the crack in all the specimens can be determined. The instantaneous crack growth rates were evaluated by fitting a second-order seven-element polynomial to the fatigue crack growth data, as recommended in ASTM 647 [3.46]. The procedures outlined in ASTM 647 are for the evaluation of crack growth rate under CA loading but since there is no published standard for the case of VA loading, this widely adopted method was used. The fatigue data reduction process was carried out using a program written in Digital Visual Fortran®.

As previously stated, a crack of depth, *'a'*, propagating in a body subjected to a remote stress range, $\Delta\sigma$, has a SIF range, ΔK that can be written as:

$$\Delta K = Y\Delta\sigma\sqrt{\pi a} \qquad \text{- (3.9)}$$

Before the experimental SIFs can be determined, the corresponding applied stress ranges and geometry correction factors *Y* must be known. The evaluation of SIFs under VA loading has always been a relatively difficult task since the stress history contains random load/stress ranges. Load interaction effects, e.g. over-loading/under-loading, which is known to cause crack retardation/acceleration, are often associated with irregular crack propagation behaviour in VA loading. In addition, crack retardation effects have been previously observed in many corrosion

fatigue tests, a phenomenon usually attributed to wedging/crack closure effect. The general explanation is that corrosion product could be deposited on the surfaces of the crack during a period of low stress cycles. When there is a high proportion of small stress cycles in the stress history it is possible for deposits to form a wedge in the crack and thus reducing the effect of both mechanical stressing and corrosion. There are various proposed models that take into account the sequence effects and crack closure but these involve extremely tedious analysis and the use of these methods in the prediction of fatigue crack growth is outside the scope of the work presented in this thesis. In the present study, the equivalent stress range concept outlined in Appendix D was adopted. The load interaction effects (if any) are considered to be minimal judging from the considerably smooth crack growth data collected, which show no clear sign of crack retardation effects. In addition, the use of the adequately mixed sea states and stationary load-time sequence coupled with an appropriate clipping ratio is believed to have minimised any artificial load interaction effects.

The following sections present the determination of the T-butt welded plate weld toe SIF by using a SIF weight function method. The versatile nature of the weight function method enables the accommodation of complex stress fields and BS7910: 2005 [3.27] has identified the weight function method as a valid tool in the determination of SIFs for cracks propagating in residual stress fields. In order to obtain representative experimental crack growth rate data, the neutron diffraction tensile residual stress data described in Section 3.3.2 were incorporated into the crack growth models presented in this section.

3.7.2 Experimental Stress Intensity Factors

3.7.2.1 SIF Prediction for a Surface Crack in a T-butt Welded Plate

For comparative purposes, two different crack models were adopted during the evaluation of the SIF for cracks propagating from the weld toe of the T-butt specimens. The first model utilised the Niu-Glinka [3.47] weight function for the deepest point of a semi-elliptical surface crack emanating from the weld toe of a T-butt welded joint. As described in Section 1.3.5, the weight function method is a powerful and robust tool in the evaluation of SIFs in complex geometries and loading conditions. The main advantages of the Niu-Glinka weight function over other SIF solutions are that it provides a rapid SIF calculation and it takes into account the geometrical effect of the weld angle and toe radius of the welded joint. The weight function is based on the composition technique described in Section 1.3.5 and it is valid for a wide range of geometric parameters. Based on the weight function composition technique, Niu-Glinka postulated that the ratio of the SIF for an edge crack in a flat plate to that of an edge crack in a weldment is the same as the analogous ratio for semi-elliptical cracks of the same depth and under the same stress system [3.47]:

$$\frac{K_e^p}{K_e^w} = \frac{K_s^p}{K_s^w} \quad \text{- (3.10)}$$

Hence, the SIF for the deepest point of a semi-elliptical crack in a weldment, K_s^w, can be written as:

$$K_s^w = \frac{K_e^w}{K_e^p} \cdot K_s^p \quad \text{- (3.11)}$$

where the superscripts *w* and *p* denote weldment and plate respectively, while the subscripts *s* and *e* denote surface crack and edge crack respectively. A graphical illustration of Niu-Glinka's SIF weight function composition method (Equation 3.10) is shown in Fig. 3.30 below.

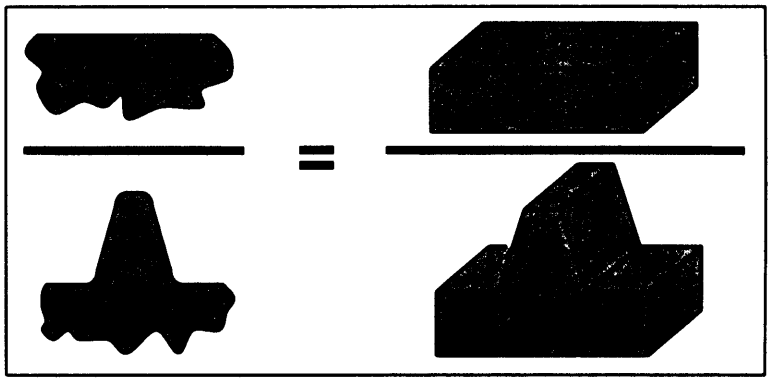

Figure 3.30: A graphical illustration of Niu-Glinka's SIF weight function composition method

The numerical calculation of K_s^w can be summarised as follows:

1. Calculation of K_e^w using Niu-Glinka's [3.48] weight function for an edge crack emanating from the weld toe of a T-butt welded plate under stress system $\sigma(x)$.

   $$K_e^w = \int_0^a m_e^w(x,a,\alpha) \cdot \sigma(x) dx \quad \text{- (3.12)}$$

2. Calculation of K_e^p using Bueckner's [3.49] weight function for an edge crack in a flat plate under stress system $\sigma(x)$.

   $$K_e^p = \int_0^a m_e^p(x,a) \cdot \sigma(x) dx \quad \text{- (3.13)}$$

3. Calculation of K_s^p using Shen-Glinka's [3.50] weight function for the deepest point of a semi-elliptical surface crack in a flat plate under stress system $\sigma(x)$.

$$K_s^p = \int_0^a m_s^p(x,a,c)\cdot\sigma(x)dx \qquad \text{- (3.14)}$$

4. Calculation of K_s^w using Equation 3.11 under stress system $\sigma(x)$.

The reference SIF solutions presented above are an established set of weight functions, which were validated against numerous published solutions and finite element results, and proven to be consistent and accurate over the validity ranges. It is noteworthy that Niu-Glinka actually used Newman-Raju's [3.51] empirical equations for the evaluation of K_s^p instead of a weight function. However, using this solution will only allow the determination of K_s^w under either pure bending or uniform tension and the SIFs have to be calculated individually for different *a/T* and *a/c*. In the present study, the Shen-Glinka [3.50] weight function (Section 6.3.3) was used for K_s^p since it provides a closed form solution and it has the advantage of accommodating any complex stress system. Before generating the T-butt semi-elliptical surface crack SIFs, each individual reference SIF solution was validated against published solutions. The SIF weight functions were computed using MATLAB®.

In order to accurately calculate the T-butt surface crack SIFs using the weight function method, the stress distribution in the prospective plane of the uncracked body must be known. The stress field near the weld toe is distinctly different from a pure bending stress distribution in a flat plate and Schijve [3.52] and Glinka [3.53] showed that a notch tip stress field is strongly dependent on the SCF and the notch tip radius (weld toe radius in this case). For the plane of maximum stress (normal to crack face/weldment), where the plane of potential crack initiation and propagation is usually expected, Glinka [3.53] derived the following expression for the transverse stress field (Fig. 3.1) ahead of the weld toe:

$$\sigma_{yy} = \frac{K_t\sigma_0}{2\sqrt{2}}\left[\left(\frac{x}{\rho}+\frac{1}{2}\right)^{-1/2} + \frac{1}{2}\left(\frac{x}{\rho}+\frac{1}{2}\right)^{-3/2} + \sum_{i=0}^{i=1} C_i\left(\frac{x}{x_0\rho}\right)^{1/2+i}\right]\left(1-\frac{x}{x_0\rho}\right) \qquad \text{- (3.15)}$$

where K_t is the weld toe stress concentration factor and σ_0 is the reference stress magnitude

$x_0 = \frac{\chi}{\rho}$, χ = neutral axis and ρ is the weld toe radius

$C_0 = 1.459\alpha^2 - 3.056\alpha + 2.4$ for $\frac{\pi}{6} \leq \alpha \leq \frac{\pi}{3}$, $C_1 = 1$ and α is the weld angle

The higher terms in Equation 3.15 allow the stress field far away from the weld toe to be calculated. The normalised full-field stress distribution for the 50mm-thick T-butt welded plate is illustrated in Fig. 3.31 below. Niu-Glinka claimed that the proposed transverse stress field polynomial expression has an accuracy of 3 percent when compared with the corresponding finite element results. In a T-butt welded plate, its intrinsic geometries have an influential effect on the SIF during the early crack propagation stage. However, when the crack propagates to a certain depth, the effect is believed to diminish, resulting in the corresponding SIF to resemble a flat plate solution. In the case of a surface crack, Brennan et al demonstrated that the effect of the weldment decays rapidly as *a/T* (crack depth to plate thickness ratio) increases from zero and at *a/T*≈0.15, the weld toe SIFs for a T-butt plate are almost identical to that of a flat plate for all crack aspect ratios and this can be clearly seen in Fig. 3.32 below. The figure shows the predicted normalised weld toe SIF for the T-butt welded plates used in this study. The solutions are for a T-butt plate under bending and the normalised SIFs are plotted for surface cracks with different crack aspect ratios.

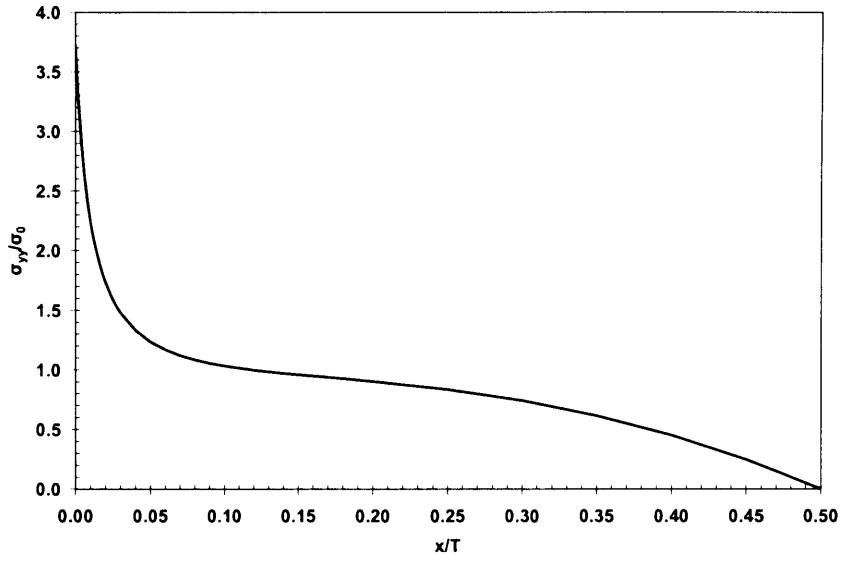

Figure 3.31: Normalised full-field stress distribution ahead of the weld toe in a T-butt welded plate under bending

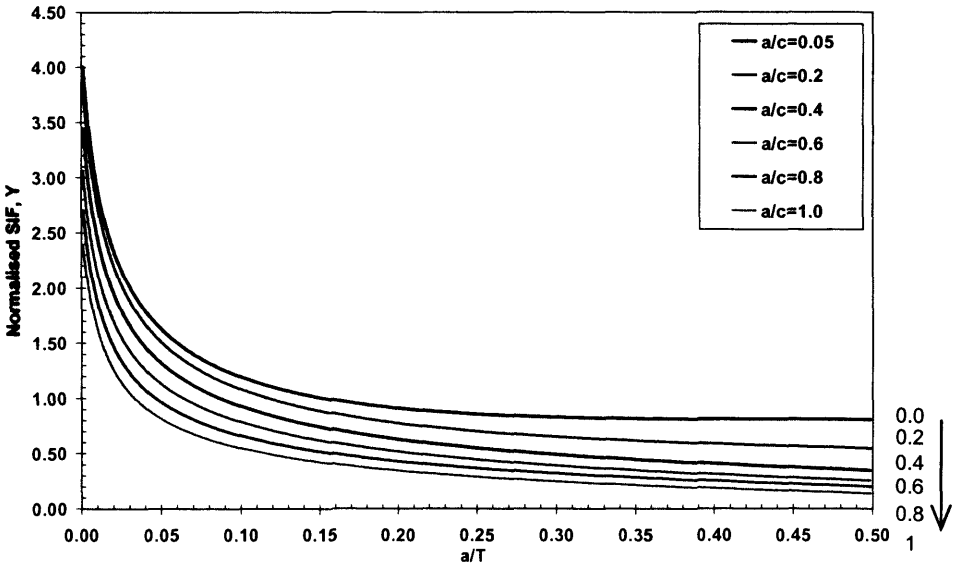

Figure 3.32: Normalised T-butt surface crack SIF prediction using Niu-Glinka's [3.47] weight function under bending

3.7.2.2 SIF Prediction for an Edge Crack in a T-butt Welded Plate

As can be seen from the fatigue crack shape evolution data presented (Figs. 3.20 to 3.26 above), the surface cracks coalesced to form a long edge crack at very early stage of crack propagation. As such, the SIF solution obtained above, which was developed for semi-elliptical cracks, might not be appropriate for the SIF predictions. Hence, a second method, which involves the calculation of the SIFs using Niu-Glinka's [3.48] weight function for an edge crack emanating from the weld toe of a T-butt welded plate was adopted. The weight function was derived by using Petroski-Achenbach's COD approximation presented in Section 1.3.5. Similar to the aforementioned composition technique, Niu-Glinka proposed that the ratio of the SIF of an edge crack in a finite-thickness strip with corner angle, α, to that of an edge crack in a finite-thickness strip with right angle corner is the same as the analogous ratio for semi-finite strips of the same crack depth and stress system:

$$\frac{K_f^{\alpha}}{K_f^{90}} = \frac{K_s^{\alpha}}{K_s^{90}} \quad \text{- (3.16)}$$

Hence, the SIF for an edge crack propagating from the weld toe of a finite-thickness T-butt welded plate, K_f^{α}, can be written as:

$$K_f^{\alpha} = \frac{K_s^{\alpha}}{K_s^{90}} K_f^{90} \qquad \text{- (3.17)}$$

The reference SIF solutions K_s^{α} and K_s^{90} were obtained from Hasabe et al [3.54, 3.55] and the Niu-Glinka weight function is valid for T-butt welded plates with weld angle, α, from 30° to 60° and normalised weld toe radius, ρ/T, from 1/50 to 1/15. Fig. 3.33 below shows the normalised SIF prediction for an edge crack propagating at the weld toe of the T-butt welded plates (under pure bending) used in the present fatigue tests. The SIF solutions obtained using the two different weight functions are reproduced in Fig. 3.34 for comparison. This shows difference between the generated SIF solutions. From the figure, it can be observed that the difference becomes less significant for surface cracks with lower aspect ratio (long shallow crack). However, a difference will always present due to the fact that for a surface crack (under bending) that propagates sufficiently deep into the plate, the crack length (surface point) will advance at a much faster growth rate due to the considerably higher SIF when compared to the deepest point value.

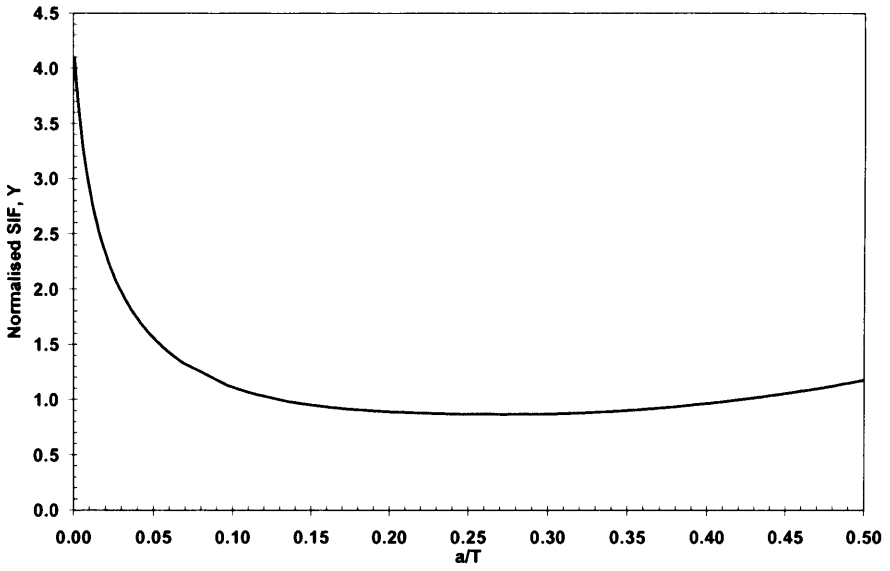

Figure 3.33: Normalised T-butt edge crack SIF prediction under bending using Niu-Glinka's [3.48] weight function

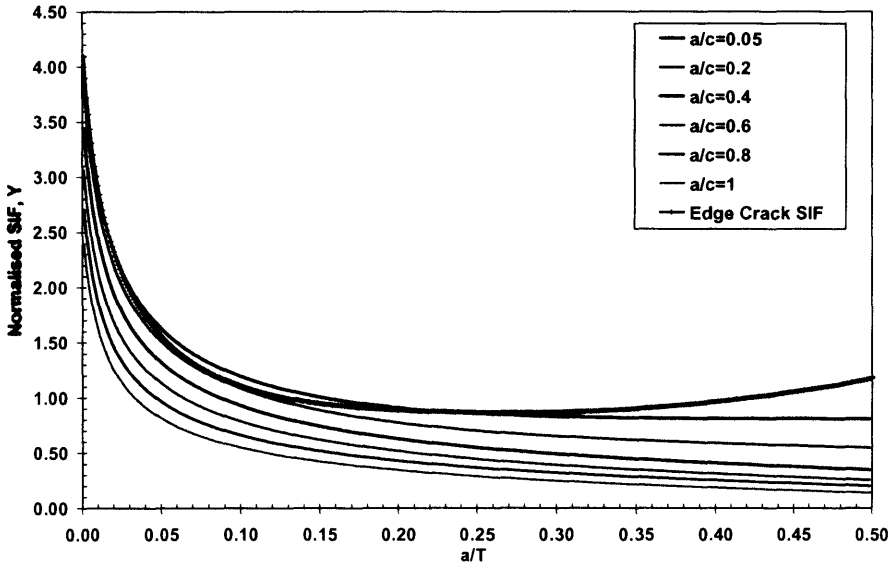

Figure 3.34: Comparison of the T-butt weld toe normalised SIFs under bending

3.7.2.3 Inclusion of Surface Tensile Residual Stress Fields into the SIF Prediction

The normalised SIFs calculated above provide crucial information on the crack propagation behaviour in the T-butt specimens but they do not take into account the residual stress present in the vicinity of the weldment. The exclusion of surface tensile residual stress in the crack growth analysis of welded joints could lead to non-conservative fatigue life predictions. This section will present the analytical work conducted to incorporate the surface residual stress data into the SIF predictions. Fig. 3.35 below shows the reproduction of the transverse residual stress data first presented in Section 3.3.2. The residual stress distributions in the longitudinal and normal directions are not considered in this analysis as they do not contribute towards the Mode I crack opening. Since the non-linearity of the measured data will pose a problem in the numerical simulation of the SIFs, a tri-linear upper bound residual stress distribution is proposed. In addition, the usage of an upper bound distribution will also lead to a more conservative SIF prediction.

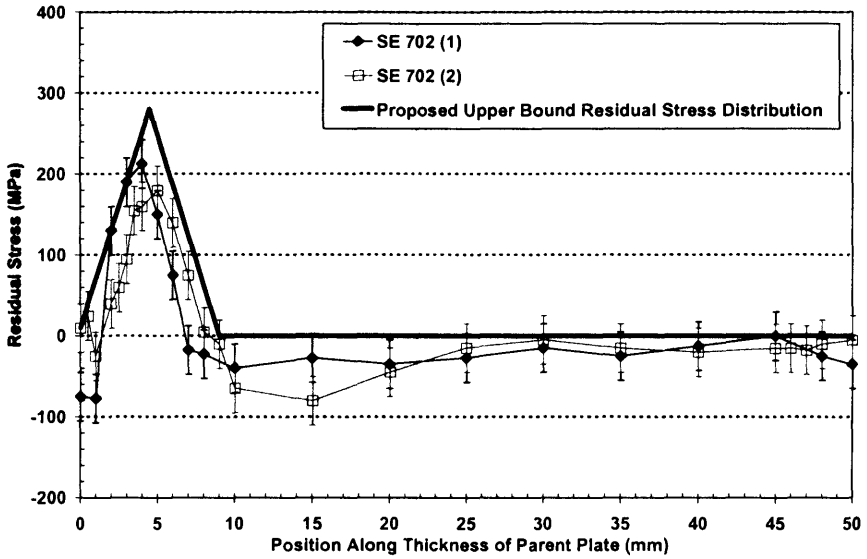

Figure 3.35: Proposed tri-linear upper bound transverse residual stress distribution

Assuming linear elastic conditions, the residual stress was treated as a mean stress and was added to the applied stress distribution during the SIFs calculation. As can be seen from Equation 1.14 (Section 1.3.5), calculation of SIFs using a weight function method involves the integration of the stress distribution in the crack plane of the unflawed body and this procedure can be problematic in this case since the tri-linear upper bound residual stress distribution takes the form of a continuous piecewise linear function. The difficulty can be resolved by introducing intervals to the stress distribution and this can be explained with the aid of Fig. 3.36 and the corresponding expressions below.

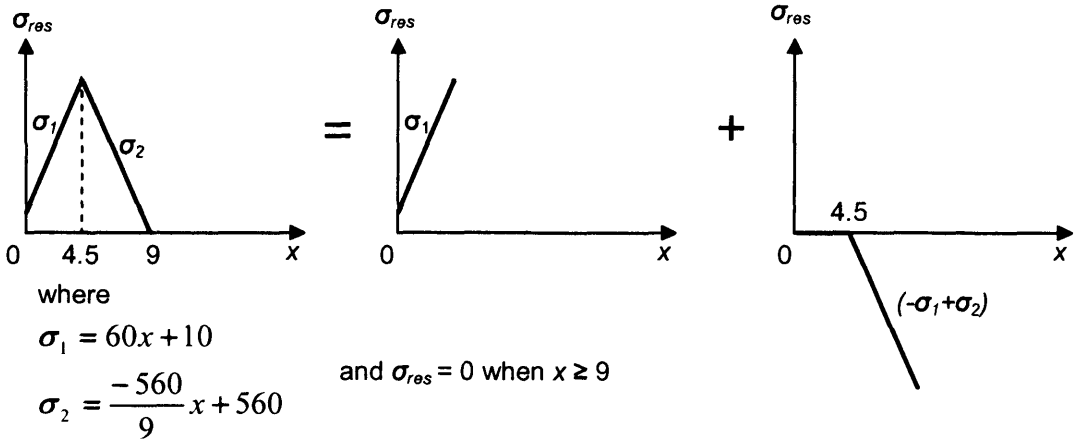

where

$\sigma_1 = 60x + 10$

$\sigma_2 = \frac{-560}{9}x + 560$

and $\sigma_{res} = 0$ when $x \geq 9$

Figure 3.36: Expression of the transverse residual stress distribution using piecewise continuous linear function

Hence, in mathematical form, the overall residual stress distribution, $\sigma_{res}(x)$, can be expressed as:

$$\sigma_{res}(x) = (60x + 10) \cdot ((x > 0) AND (x < 4.5)) + \left(\frac{-560}{9}x + 560\right) \cdot ((x > 4.5) AND (x < 9)) \quad \text{- (3.18)}$$

And in numerical form (MATLAB®):

$$\sigma_{res}(x) = \left[60x + 10 - \left(60x + 10 + \frac{560}{9}x - 560\right) \cdot (x > 4.5)\right] \cdot (x < 9) \quad \text{- (3.19)}$$

By assigning the appropriate intervals to the piecewise continuous linear function, the SIFs can be determined by evaluating the integral over the crack length of the product of the weight function and the resultant stress distribution in the uncracked body. Figs. 3.36 and 3.38 below illustrate the normalised SIF prediction for an edge crack in a T-butt welded plate and for surface cracks in a T-butt welded plate respectively, with the inclusion of the surface tensile residual stress. The edge crack solution is also included in Fig. 3.38 for comparison. As can be seen from the figures, the SIF predictions have been significantly altered by the presence of the surface tensile residual stress. The following sections will demonstrate the significance of the inclusion of residual stresses in the fatigue crack growth analysis of welded joints.

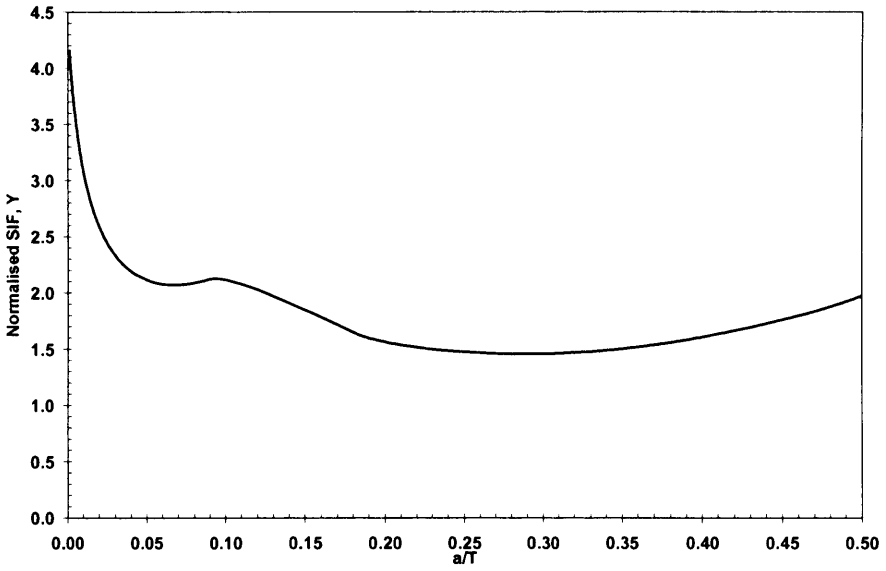

Figure 3.37: Normalised SIF prediction for an edge crack in a T-butt welded plate under bending with the inclusion of the surface tensile residual stress

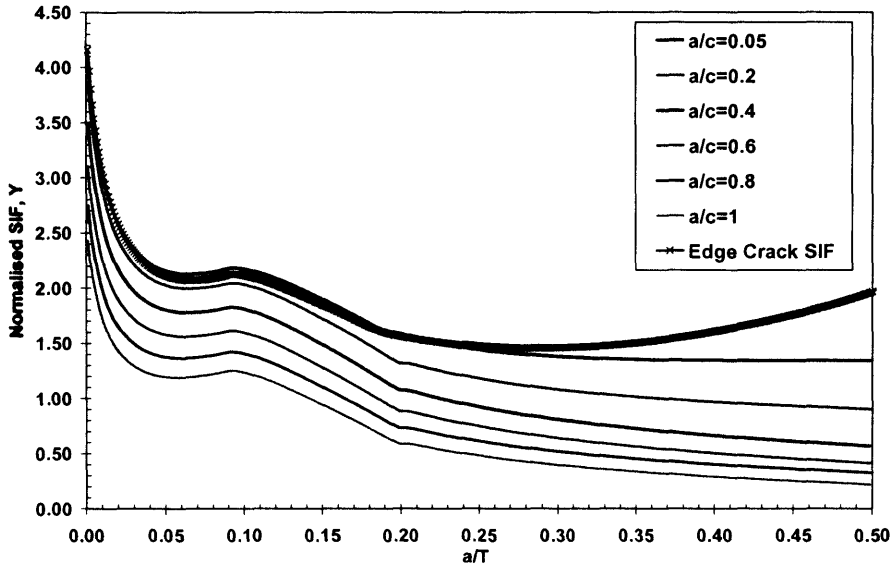

Figure 3.38: Normalised SIF predictions for semi-elliptical surface cracks in a T-butt welded plate under bending with the inclusion of the surface tensile residual stress

3.7.3 Discussion of Fatigue Crack Growth Rate Results

In this section, the experimental SIFs determined using the methods presented above are discussed in detail and compared with the results obtained from previous corrosion fatigue testing studies. Figs. 3.39 and 3.40 show the fatigue crack growth data obtained using the Niu-Glinka T-butt welded plate surface crack SIF and T-butt welded plate edge crack SIF respectively. It is important to stress that the initial crack sizes used in the analysis are identical to those obtained experimentally. The summary of the crack growth rate results, taking into account the surface residual stress, are shown in Figs. 3.41 and 3.42 for T-butt surface crack SIFs and T-butt edge crack SIFs respectively. For comparison purposes, the fatigue crack growth rate data for the individual tests are plotted in Figs. F1 to F5 in Appendix F.

The fatigue crack growth data for BS EN 10025 Grade S355J2G3 steel was obtained from Reference 3.2. King et al assessed the fatigue crack growth rate of S355 steel by using standard tensile specimens fabricated from materials cut from tubular joints. The tests were performed under air and corrosive environment (CP level -800mV). In a parallel study by Coudert et al (from CLI) [3.3], the fatigue crack growth rate of SE 702 in a corrosive environment was investigated using standard compact tension (CT) specimens fabricated from material (Base Metal and Heat Affected Zone) extracted from a welded K-joint. The corrosion fatigue tests were conducted in synthetic seawater and a CP level of -800mV was applied. Both the studies described above were conducted under CA loading and the test conditions were kept consistent so that the test

data are comparative. The data shown in the figures are the mean lines of the experimental results with their respective validity ranges. It can be seen that the SE 702 data provided by CLI generally behaves better in a corrosive environment compared to the S355 steel.

As can be observed in Figs. 3.39 and 3.40, there are only slight differences between the crack growth rate data analysed using the surface crack weight function and the edge crack weight function. This is an expected observation as the surface cracks in the T-butt welded joints propagated sufficiently deep into the parent plate, the crack aspect ratios constantly decreased ($dc/dN \gg da/dN$), resulting in the long surface cracks to behaving like edge cracks. Figs. F1 to F5 show that the SIF ranges obtained using the T-butt surface crack weight function were slightly underestimated in the early and final crack propagation stage when compared to the values obtained using an edge crack solution. However, there is good agreement between the data analysed using the two different methods in most of the SIF ranges.

Since fatigue crack growth under VA loading is a random process, relatively larger scatter is expected for the test results obtained in the present study when compared to standard CA crack growth rate investigation test data. It can be observed from Figs. 3.39 to 3.42 that the experimental SIFs evaluated with the inclusion of the residual stress provide a less conservative analysis of the crack growth rate data. The experimental SIFs evaluated with the exclusion of the surface tensile residual stress resulted in a large scatter and lower SIF range. This is particularly evident in Figs. F1 and F2, where the SIFs calculated with the inclusion of the residual stress yielded much smoother results. In general, all the experimental SIFs data resemble a conventional crack growth rate plot.

For clarity, the following discussions in this paragraph will concentrate on the experimental SIFs with the incorporation of surface residual stress field. Test 1 (air test) shows a good experimental crack growth rate data despite being tested in VA loading. It is believed that the corrosive environment and cahtodic protection contribute to the irregular fatigue crack growth rates of Tests 2 to 5. Comparing the slopes of the da/dN-ΔK curves, the SE 702 experimental data suggest superior fatigue crack growth resistance in a corrosive environment when compared to the medium strength S355 steel. As can be seen from Figs. 3.41 and 3.42, the crack growth rates for the cathodically over-protected specimens are higher, especially during the early and final crack propagation stages. However, the experimental data clearly show that the influence of cathodic over-protection and hydrogen embrittlement in the corrosion fatigue of HSS are not as significant as reported [3.4, 3.19, 3.21]. The data obtained from the corrosion tests show multiple segments in the plot and this phenomenon is generally observed in corrosive fatigue test data, especially for tests conducted under cathodic protection. However, the experimental SIFs obtained in this study

are much more stable compared to those reported by Etube [3.23] and Tantbirojn [3.24]. It can be seen in Figs. 3.39 to 3.42 that the experimental SIFs of Test 4 and 5 begin almost in the threshold region, regardless of the presence of surface tensile residual stress. The SIF ranges of Tests 4 and 5 are relatively small due to the lower ESR used. In addition, the crack growth rates for Tests 4 and 5 (Figs. F4 and F5) seem to reach a plateau at approximately 30 $MPam^{1/2}$, suggesting that the crack growth rate might be constant at higher SIF ranges in the high cycle regime.

In order to demonstrate the significance of the inclusion of surface tensile residual stress into the fatigue crack growth analysis of welded joints, the experimental SIFs analysed using the aforementioned methods for all the corrosion tests are reproduced in Fig. 3.43 in the form of mean-lines. As can be seen from the figure, introducing surface tensile residual stress into the calculation of the effective SIF range resulted in an improvement in the experimental crack growth rate data. In contrast to this observation, the exclusion of residual stress fields in a crack growth rate assessment of a welded joint will eventually lead to a non-conservative approach due to the fact that the effective SIF range will be higher due to the surface tensile residual stress. One shortcoming of the current crack growth models is that they did not incorporate the residual stress relaxation effect. In other words, the predicted SIFs will have lower magnitudes if residual stress decay is to be considered. There is currently no published standard regarding this issue and therefore a certain degree of over-conservatism is commonly associated with the fatigue and fracture mechanics analysis of welded joints with the presence of surface tensile residual stress.

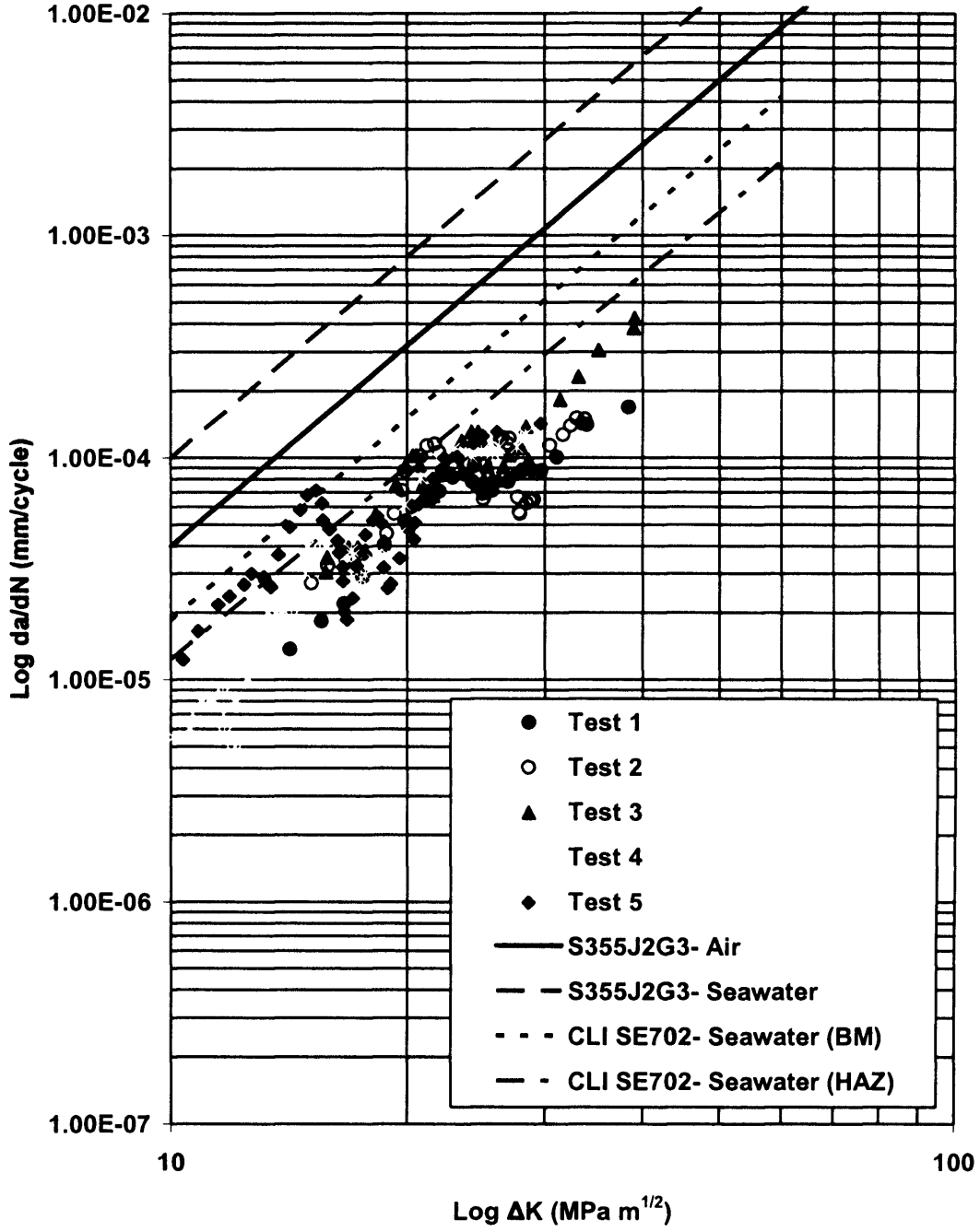

Figure 3.39: Fatigue crack growth rate data analysed using Niu-Glinka T-butt welded plate surface crack (deepest point) weight function

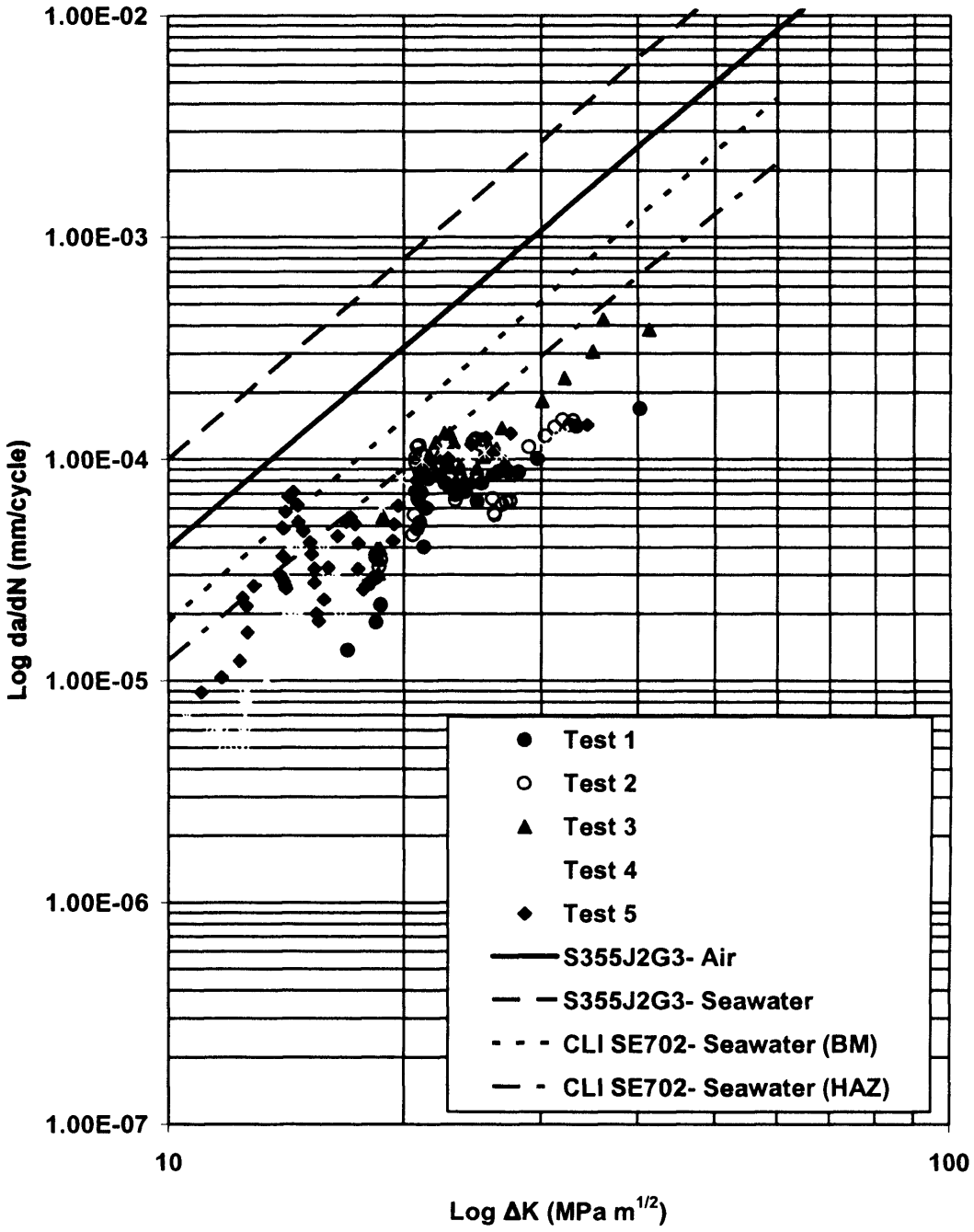

Figure 3.40: Fatigue crack growth rate data analysed using Niu-Glinka T-butt welded plate edge crack weight function

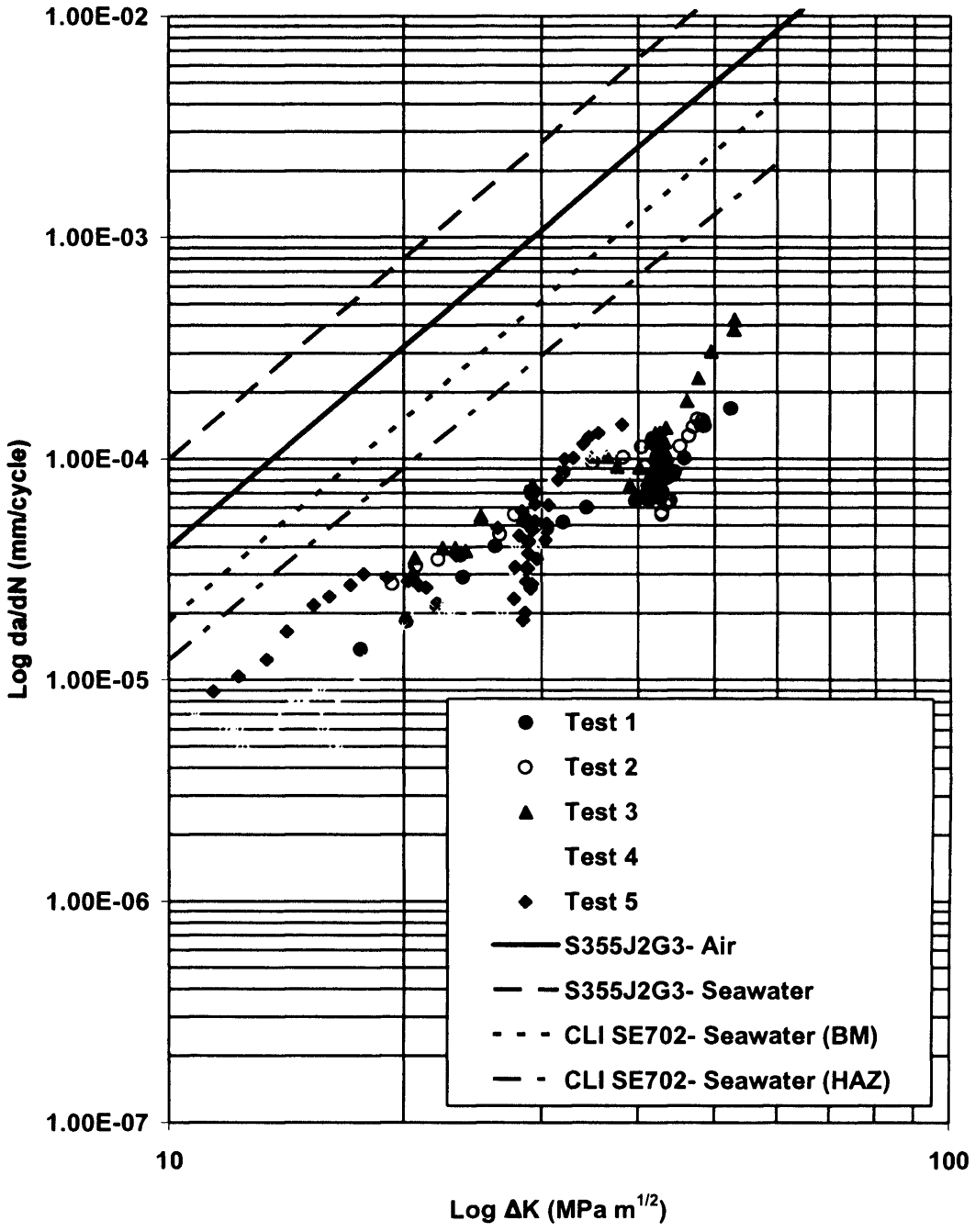

Figure 3.41: Fatigue crack growth rate data analysed using Niu-Glinka T-butt weld toe surface crack (deepest point) weight function with the incorporation of residual stress field

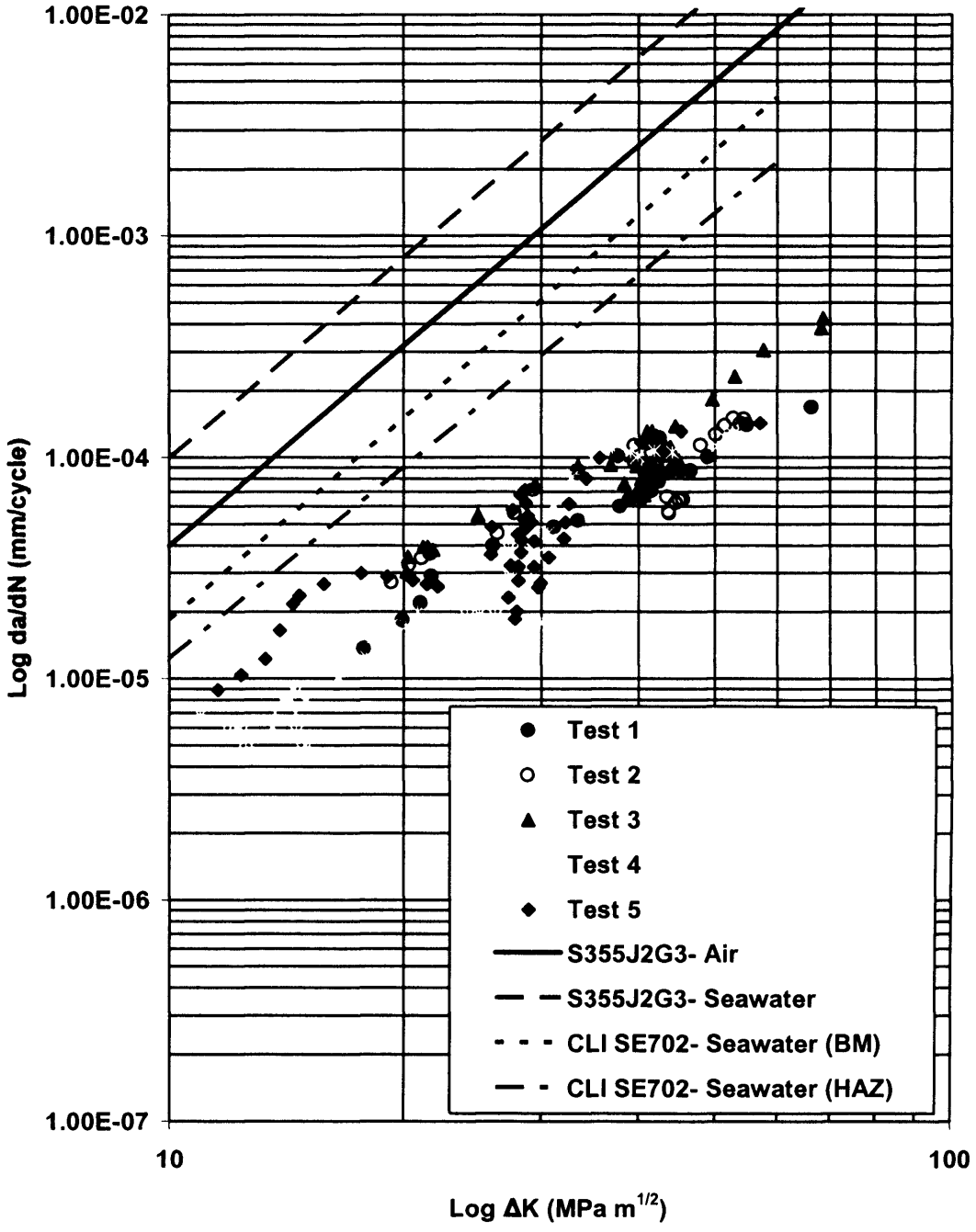

Figure 3.42: Fatigue crack growth rate data analysed using Niu-Glinka T-butt weld toe edge crack weight function with the incorporation of residual stress field

Since it is believed that this is the first study that applies surface residual stress to real crack growth data, no direct comparison can be made with literature published to date. However, the detrimental effect of surface tensile residual stress on the fatigue performance of welded joints can be demonstrated by using the fatigue life prediction of the SE 702 T-butt welded plate specimens. By implementing the Paris Law (Equations 1.10 and 1.11), the residual life of a component containing a crack can be accurately predicted if the corresponding SIF, stress range and the Paris material coefficients, *C* and *m*, are known. The Paris material coefficients for SE 702 can be obtained from Reference 3.3, which were evaluated from the CT tests performed by Coudert et al. Table 3.7 below tabulates the Paris material coefficients for SE 702, obtained under different test conditions.

Test Conditions	**C**	**m**
CT Test- Air	2.72×10^{-12}	3.53
CT Test- Base Metal; Corrosive; CP -800mV	1.73×10^{-11}	3.03
CT Test- Heat Affected Zone; Corrosive; CP -800mV	1.63×10^{-11}	2.88

Table 3.7: The Paris material coefficients for SE 702

Fig. 3.44 illustrates the fatigue crack propagation life predictions for the SE 702 T-butt welded plate specimens used in the current study. These were calculated by incorporating the T-butt welded plate edge crack SIF (Section 3.7.2.2) into the Paris Law. The fatigue crack propagation life predictions were generated for the SE 702 T-butt welded plates in both air and corrosive environment with the respective equivalent stress range so that they are comparable with the experimental data. The predicted lives for all the tests are tabulated in Table 3.8 below, together with the corresponding percentage difference with respect to the experimental crack propagation life. It is worth mentioning that the Paris material coefficients were obtained from CT tests conducted in CA loading conditions. Hence, a difference between the predicted lives and the experimental lives is expected since the SE 702 specimens were fatigue tested under VA loading in the present study. However, it can be appreciated from Fig. 3.44 and Table 3.8 that the predicted fatigue crack propagation lives with the inclusion of surface tensile residual stress are much closer to the experimental values when compared to the predicted lives without residual stress. For example in Test 1, the predicted life with residual stress is only 8% higher than the experimental value while without residual stress shows a 27% over-estimation. This over-estimation of fatigue lives (analysed without residual stress) can seen in all the tests. Relatively

higher differences in the predicted lives for the corrosion tests, in particular the long-life fatigue tests, can be observed. The large differences might be due to the hydrogen embrittlement effect, which is known to be more significant in the high cycle fatigue region. The crack propagation life predictions clearly show that the exclusion of surface tensile residual stress in the fatigue crack growth analysis of welded joints will lead to a high degree of non-conservatism. Hence, it can be concluded that the effect of surface tensile residual stress must be considered in order to generate representative and accurate component life prediction models.

Specimen	Initial *a*	Initial *c*	Experimental Crack Propagation Life	Predicted Crack Propagation Life (without residual stress)	Predicted Crack Propagation Life (with residual stress)
Test 1	0.50	10	321,778	408,902 (+27%)	346,000 (+8%)
Test 2	0.45	10	213,691	333,180 (+56%)	281,120 (+32%)
Test 3	0.43	10	212,649	333,180 (+57%)	281,120 (+32%)
Test 4	0.38	10	780,000	1,124,483 (+44%)	899,586 (+15%)
Test 5	0.40	10	507,197	1,124,483 (+121%)	899,586 (+77%)

Table 3.8: Comparison between experimental and predicted fatigue crack propagation lives

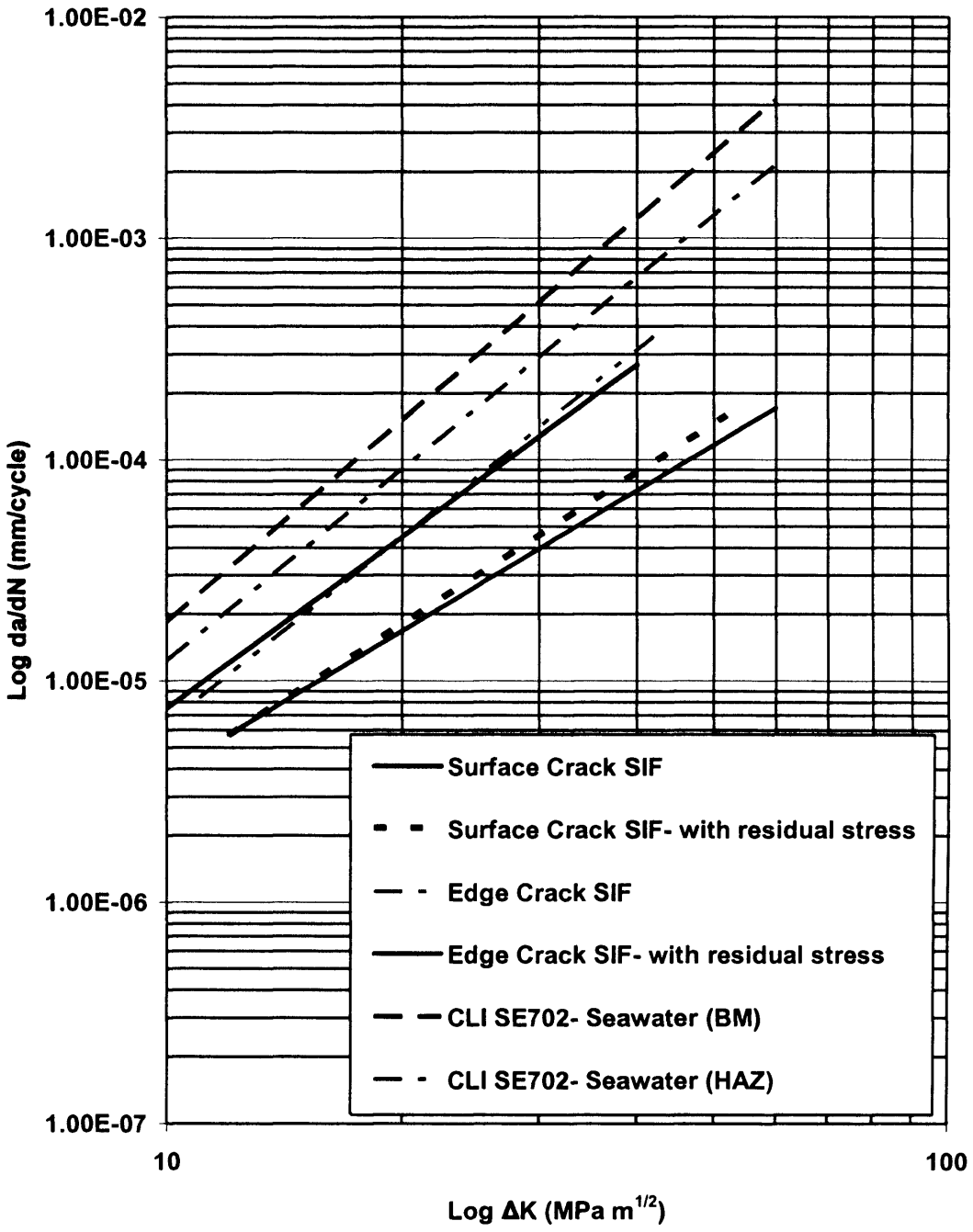

Figure 3.43: Comparison of the fatigue crack growth rates data for all tests

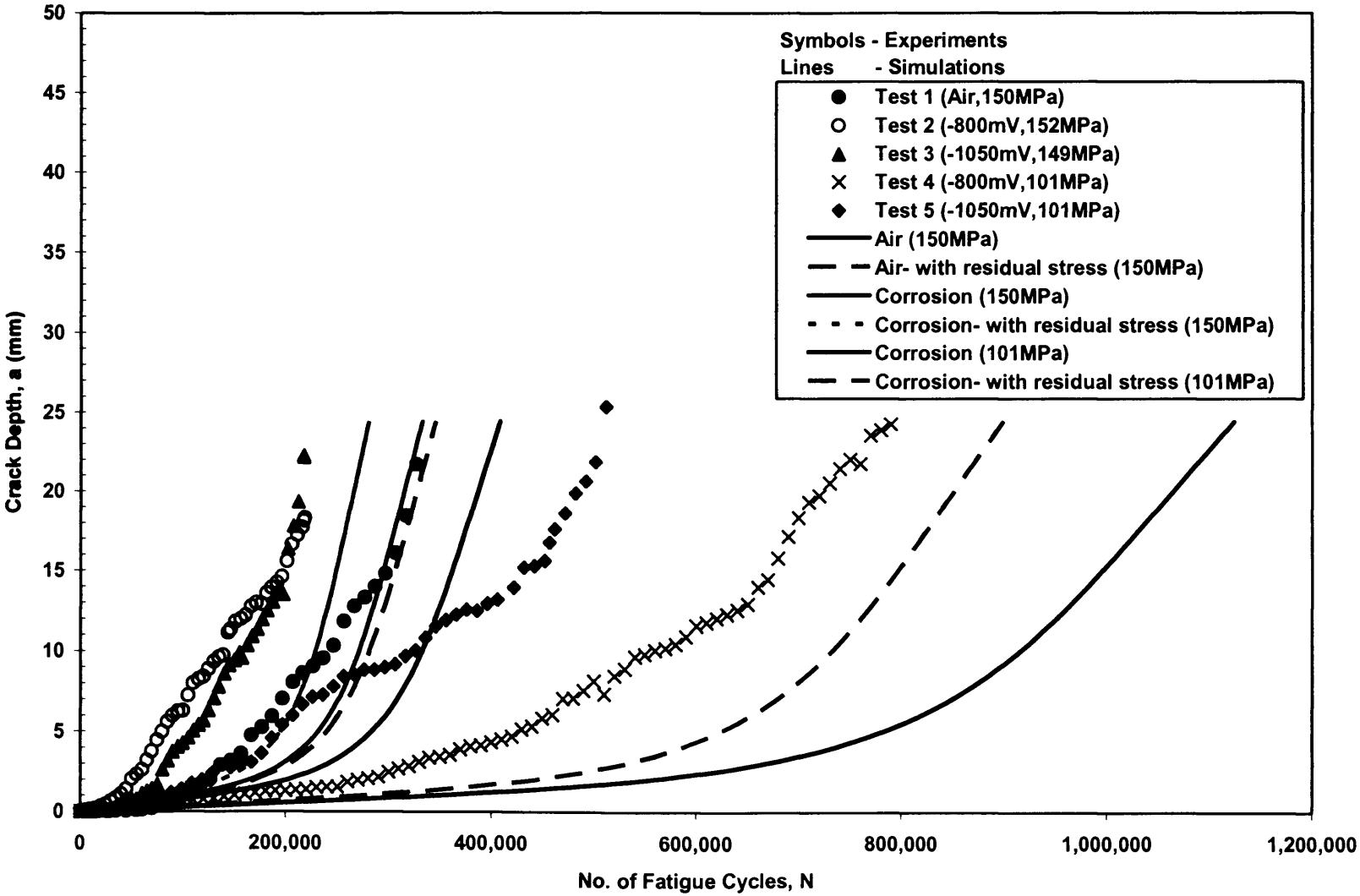

Figure 3.44: Comparison between the experimental and the predicted fatigue crack propagation lives

3.8 Summary

This chapter presented details of the variable amplitude corrosion fatigue tests conducted on T-butt welded plate specimens fabricated from SE 702, a widely used weldable high strength steel. The significance of residual stresses in welded joints is discussed and the data presented clearly show that further work is needed in order to develop an in-depth understanding of residual stresses in HSS. A total of one air test and four corrosion fatigue tests with cathodic protection were carried out under simulated environmental conditions using the Jack-up Offshore Standard load History (JOSH) generator. Fatigue crack growth during the course of the fatigue tests was monitored using periodic ACPD inspections. The statistical stationary load-time sequence used allowed the long life fatigue performance of HSS to be investigated. The results are presented in the form of fatigue crack initiation data, crack growth and crack shape evolution data. Experimental results obtained show a reduction in the fatigue life of specimens subjected to cathodic over-protection. However, the influence of cathodic over-protection and hydrogen embrittlement in HSS are not as detrimental as reported [3.4, 3.19, 3.21]. The fracture mechanics analysis performed also enabled the fatigue crack growth rate of the SE 702 specimens to be assessed. The data show that the cathodic over-protected specimens had higher fatigue crack growth rates, especially in the long-life region. In general, the long life corrosion fatigue test results obtained are satisfactory and compare well with previous corrosion fatigue studies. The significance of surface tensile residual stress on the fatigue crack growth rate data is clearly demonstrated using the weight function based crack growth analysis. The detailed fatigue crack propagation life prediction analysis further shows that residual stress has a deleterious effect on the fatigue performance of welded joints.

3.9 References

[3.1] Frieze P. A., Morandi A. C., Birkinshaw M., Smith D. and Dixon A. T., "Fixed and Jack-up Platforms: Basis for Reliability Assessment", *Marine Struct*, Vol. 10, No. 2, 1997, pp. 263-284.

[3.2] King R., Sharp J. V. and Nichols N. W., "The Influence of Sea-Water and Cathodic Protection on the Fatigue Performance of High Strength Steels for Jack-Ups", In: *Proc Conf Offshore Mech Artic Engng*, Calgary, 1997.

[3.3] Coudert E. and Renaudin C., "Variable Amplitude Corrosion Fatigue Behaviour and Hydrogen Embrittlement of High Strength Steels for Off-shore Applications", In: *Proc 8th Int Offshore Polar Engng Conf*, Vol. IV, 1998, pp.116-122.

[3.4] Tantbirojn N., Bowen R. J., Etube L. S., Dover W. D., Kilgallon P. J., Roberts T. and Spurrier J., "Variable Amplitude Corrosion Fatigue of Jack-up Steels", Health and Safety Executive Offshore Technology Report, 2001/79, ISBN 071762319X, 2001.

[3.5] Health & Safety Executive (UK), "Background to New Fatigue Guidance for Steel Joints and Connections in Offshore Structures", Offshore Technology Report- OTH 92 390, Health & Safety Executive (UK), 1992.

[3.6] Jones D. A., "Principles and Prevention of Corrosion", Macmillan Publishing Company, ISBN 0 02 361215 0, USA, 1992.

[3.7] Coudreuse L., Renaudin C. Bocquet P. and Cadiou L., "Evaluation of Hydrogen Assisted Cracking Resistance of High Strength Jack-Up Steels", *Marine Struct*, Vol. 10, 1997, pp. 85-106.

[3.8] Tiwari G. P., Bose A., Chakravartty J. K., Wadekar S. L., Totlani M. K., Arya R. N. and Fotedar R. K., "Study of Internal Hydrogen Embrittlement of Steels", *Mater Sci Engng A: Struct Mater: Properties Microstruc Processing*, Vol. 286, No. 2, 2000, pp. 269-281.

[3.9] Eliaz N., Shachar A., Tal B. and Eliezer D., "Characteristics of Hydrogen Embrittlement, Stress Corrosion Cracking and Tempered Martentsite Embrittlement in High-Strength Steels", *Engng Failure Analysis*, Vol. 9, 2002, pp. 167-184.

[3.10] Cotis R. A., "Stress Corrosion Cracking in High Strength Steels", *Corrosion*, Editor: Shrier, Jarman and Burstein, 3rd Edition, 1994.

[3.11] Nelson H. G., "Hydrogen Embrittlement", *Treatise on Mater Sci Technol*, Editor: Brian C. L. and Banerji S. K., Academic Press, Vol. 25, 1983, pp.275-359.

[3.12] Beghini M., Benamati G. and Bertini L., "Hydrogen Embrittlement Characterisation by Disk Pressure Tests: Test Analysis and Application to High Chromium Martensitic Steels", *J Engng Mater Tech*, Vol.118, No. 2, 1996, pp. 179-185.

[3.13] Uhlig H. H. and Revie R. W., "Corrosion and Corrosion Control- An Introduction to Corrosion Science and Engineering", John Wiley & Sons Inc., ISBN 0471078182, 1997.

[3.14] von Baeckmann W., Schwenk W. and Prinz W., "Handbook of Cathodic Corrosion Protection- Theory and Practice of Electrochemical Protection Processes- 3rd Edition", Gulf Publishing Company, ISBN 0 88415 056 9, 1997.

[3.15] United Kingdom Offshore Steels Research Project (UKOSRP) - Phase II: Final Summary Report, Editor: Peckover R., Health and Safety Executive Report OTH 87 265, Her Majesty's Stationary Office, 1987.

[3.16] British Standards Institute, "BS EN 10025:2004 – Hot Rolled Products of Non-Alloy Structural Steels", British Standards Institute, 2004.

[3.17] Sharp J. V., Billingham J. and Robinson M. J., "The Risk Management of High-Strength Steels in Jack-ups in Seawater", *Marine Struct*, Vol. 14, 2001, pp. 537-551.

[3.18] Austin J. A. and Dover W. D., "Variable Amplitude Corrosion Fatigue of Tubular Welded T-Joints under Axial Loading", In: *Fat Crack Growth in Offshore Struct*, Ed: Dover W. D., Dharmavasan S., Brennan F. P. and Marsh K., Vol. 1, EMAS Publishing, ISBN 0947817 78 6, 1995.

[3.19] Vinas-Pich J., Kam J. C. P. and Dover W. D., "Variable Amplitude Corrosion Fatigue of Medium Strength Steel Tubular Welded Y-Joints", In: *Fat Crack Growth in Offshore Struct*, Ed: Dover W. D., Dharmavasan S., Brennan F. P. and Marsh K., Vol. 1, EMAS Publishing, ISBN 0947817 78 6, 1995.

[3.20] Smith A. T., "The Effects of Cathodic Over-Protection on the Corrosion Fatigue Behaviour of API 5L X65 Grade Welded Tubular Joints", Ph.D. Thesis, City University, 1995.

[3.21] Davey V. S., "The Cathodic Protection of High Strength Steel in a Marine Environment", Health and Safety Executive Offshore Technology Report OTN 1999 015, 1999.

[3.22] Myers P., "Corrosion Fatigue and Fracture Mechanics of High Strength Jack Up Steels", Ph.D. Thesis, University of London, 1998.

[3.23] Etube L.S., Myers P., Brennan F. P. and Dover W. D., "Constant and Variable Amplitude Corrosion Fatigue Performance of a High Strength Jack-up Steel", In: *Proc 8th Int Offshore Polar Engng Conf*, Vol. IV, 1998, pp. 123-130.

[3.24] Tantbirojn N., "Fatigue Testing of Weldable High Strength Steels Under Simulated Service Condition", Ph.D. Thesis, University of London, 2002.

[3.25] British Energy Generation Ltd., "Assessment of the Integrity of Structures Containing Defects", R6 Rev. 4, British Energy Generation Ltd., UK, 2001.

[3.26] ELIXIR Project: Extending Plant Life through Improved Fabrication and Advanced Repair Methodology, EC Growth 5th Framework Programme, Contract no. ELIXIR-GRD1-2000-25239, 2001-2004.

[3.27] British Standards Institute, "BS 7910:2005 Guide to Methods for Assessing the Acceptability of Flaws in Metallic Structures", British Standards Institute, 2005.

[3.28] British Standards Institute, "BS 7910:1999 Guide to Methods for Assessing the Acceptability of Flaws in Metallic Structures", Amendment No. 1, British Standards Institute, 1999.

[3.29] American Petroleum Institute, "API Recommended Practice for Fitness-For-Service", API RP 579, American Petroleum Institute, 2000.

[3.30] SINTAP Project: Structural Integrity Assessment Procedure, Brite-Euram Programme, Contract no. EU-Project BE 95-1462, 1999.

[3.31] Leggatt R. H., "Welding Residual Stresses", In: *Proc 5th Int Conf Residual Stress (ICRS-5)*, Editors: Ericsson T., Oden M. and Andersson A., Vol. 1, 1997, pp. 12-25.

[3.32] Wimpory R. C., May P. S., O'Dowd N. P., Webster G. A., Smith D. J. and Kingston E., "Measurement of Residual Stresses in T-plate Weldments", *J Strain Analysis*, Vol. 38, No. 4, 2003, pp. 349-365.

[3.33] Hyeong Y. L., Kamran M. N. and O'Dowd N. P., "A Generic Approach for a Linear Elastic Fracture Mechanics Analysis of Components Containing Residual Stress", *Int J Pressure Vessels Piping*, Vol. 82, 2005, pp. 797-806.

[3.34] Stacey A., Barthelemy J. Y., Ainsworth R. A., Leggatt R. H. and Bate S. K., "Quantification of Residual Stress Effects in the SINTAP Defect Assessment Procedure

for Welded Components", In: *Proc 18th Int Conf Offshore Mech Arctic Engng*, OMAE99/MAT-2044, 1999.

[3.35] Anderson T. L. and Osage D. A., "API 579: A Comprehensive Fitness-for-purpose Guide", *Int J Pressure Vessels Piping*, Vol. 77, No. 14-15, 2000, pp. 953-963.

[3.36] Wimpory R. C., O'Dowd N. P. and Nikbin K. M., "Residual Stress Measurement in a Welded High Strength Steel: Effect of Heat Input", Report IMPBEJRC2004/01/01, October 2004.

[3.37] Brennan F. P., Peleties P. and Hellier A. K., "Predicting Weld Toe Stress Concentration Factors for T and Skewed T-joint Plate Connections", *J Strain Analysis*, Vol. 38, No. 4, 2000, pp. 573-584.

[3.38] Dartec Ltd., "Dartec 9600 Advanced Digital Controller Use Instructions", Issue No. 3, Dartec Ltd., UK, 1997.

[3.39] Dover W.D. and Collins R., "Recent Advances in the Detection and Sizing of Cracks Using Alternating Current Field Measurements (A.C.F.M.)", *British J NDT*, Vol. 22, 1980, pp. 291-295.

[3.40] Technical Software Consultants Ltd., "Crack Microgauge – Model U10 User Manual", Technical Software Consultants Ltd., Milton Keynes, UK, 1993.

[3.41] American Society for Testing and Materials, "Standard Practice for the Preparation of Substitute Ocean Water", ASTM D1141-98 (2003), American Society for Testing and Materials, 2003.

[3.42] Sharp J. V., Billingham J. and Stacey A., "Performance of High Strength Steels Used in Jack-ups in Seawater", *Marine Struct*, Vol. 12, 1999, pp. 349-369.

[3.43] Laws P., "Corrosion Fatigue Performance of Welded High Strength Low Alloy Steels for Use of Offshore", Ph.D. Thesis, Cranfield University, 1993.

[3.44] Health and Safety Executive (UK), "Steel", Offshore Technology Report 2001/015, Health and Safety Executive (UK), United Kingdom, 2002.

[3.45] Health and Safety Executive (UK), "Fatigue Design Curves for Welded Joints in Air and Seawater under Variable Amplitude Loading", OTO 1999 058, Health and Safety Executive (UK), United Kingdom, 2000.

[3.46] American Society for Testing and Materials, "Standard Test Method for Measurement of Fatigue Crack Growth Rates", ASTM E647-05, American Society for Testing and Materials, 2005.

[3.47] Niu X. and Glinka G., "Stress-Intensity Factors for Semi-Elliptical Surface Cracks in Welded Joints", *Int J Fract*, Vol. 40, 1989, pp. 255-270.

[3.48] Niu X. and Glinka G., "The Weld Profile Effect on Stress Intensity Factors in Weldments", *Int J Fract*, Vol. 35, 1987, pp. 3-20.

[3.49] Bueckner H. F., In: *Z Angew Math Mech*, Vol. 51, 1971, pp. 97-109.

[3.50] Shen G. and Glinka G., "Weight Functions for a Semi-Elliptical Crack in a Finite Thickness Plate", *Theore Applied Fract Mech*, Vol. 15, No. 3, 1991, pp. 247-255.

[3.51] Newman J. C. Jr. and Raju I. S., "Empirical Stress-Intensity Factor Equation for The Surface Crack", *Engng Fract Mech*, Vol. 15, No. 1-2, 1981, pp. 185-192.

[3.52] Schijve J., "Stress Intensity Factor of Small Cracks at Notches", *Fat Engng Mater Struct*, Vol. 5, No. 1, 1982, pp. 77-90.

[3.53] Glinka G., "Calculation of Inelastic Notch-Tip Strain-Stress Histories under Cyclic Loading", *Engng Fract Mech*, Vol. 22, No. 5, 1985, pp. 839-854.

[3.54] Hasebe N. and Ueda M., "Crack Originating from An Angular Corner of A Semi-Infinite Plate with a Step", *Bulletin of the JSME*, Vol. 24, No. 189, 1981, pp. 483-488.

[3.55] Hasebe N. Matsuura S. and Kondo N., "Stress Analysis of A Strip with A Step and A Crack", *Engng Fract Mech*, Vol. 20, No. 3, 1984, pp. 447-462.

CHAPTER 4

4.0 Experimental Investigation of Fatigue Crack Shape Evolution in Residual Stress Fields

4.1 Introduction

The lifetime of structural components is usually assessed based on the interaction between existing defects/flaws, the number of fatigue cycles and the stress history. These stresses are a combination of the applied stresses and the locked-in residual stresses. Residual stresses can arise from a number of sources and can be present in the unprocessed material, introduced during manufacturing or can arise from in-service loading conditions [4.1, 4.2]. The sources of residual stresses have been discussed in detail in Chapter 1.

It is generally known that the introduction of compressive residual stress improves the mechanical properties and hence the fatigue life, while tensile residual stress tends to reduce the fatigue endurance. Many studies have shown significant improvement in resistance to fatigue crack initiation [4.3, 4.4] and fatigue crack propagation [4.5-4.7] by cold working the exposed surface layers of metallic components. Based on an extensive literature review, it appears that very often the magnitude of residual stresses present and the resulting life have been measured, but the understanding of the mechanisms which govern the fatigue life performance have not been sufficiently addressed. In addition, although the effects of residual stresses on fatigue strength and residual stress measurement techniques have been common research topics, the influences of residual stresses on crack shape evolution have not received much attention [4.8]. If a crack propagates into a section of a material containing residual stress, the determination of the effective SIF range (ΔK) usually involves a non-uniform stress distribution. Hence, in order for engineers to accurately generate fatigue crack growth predictions, the interaction between crack shape evolution and residual stresses must be understood.

Knowing that cold working can improve the fatigue resistance of materials, it is utilised in this study to explore its characteristics. In theory, the controlled application of residual stresses can be used to influence the initiation, growth rate and shape of fatigue cracks which might develop in a structural component [4.9]. This chapter presents an experimental study of fatigue crack shape control using a recently developed technique termed controlled stitch cold working [4.4, 4.10].

The first part of the chapter will address the importance of crack shape evolution on fatigue crack growth in structural components. This is followed by a detailed description of the fatigue testing of stitch cold rolled specimens. The study reported here provided a valuable insight into the feasibility of the preferential cold working technique and paved the way for the fatigue testing programme presented in Chapter 5.

4.2 The Significance of Fatigue Crack Shape on Crack Propagation

Generally, fatigue crack shape (crack aspect ratio) is expressed as the ratio of crack depth to crack half-length (*a/c*). The knowledge of crack growth patterns is of immense importance since the SIFs around a surface crack front are very sensitive to the crack aspect ratio. This can be illustrated by using the well known Newman and Raju [4.11] flat plate surface crack stress intensity factor solutions.

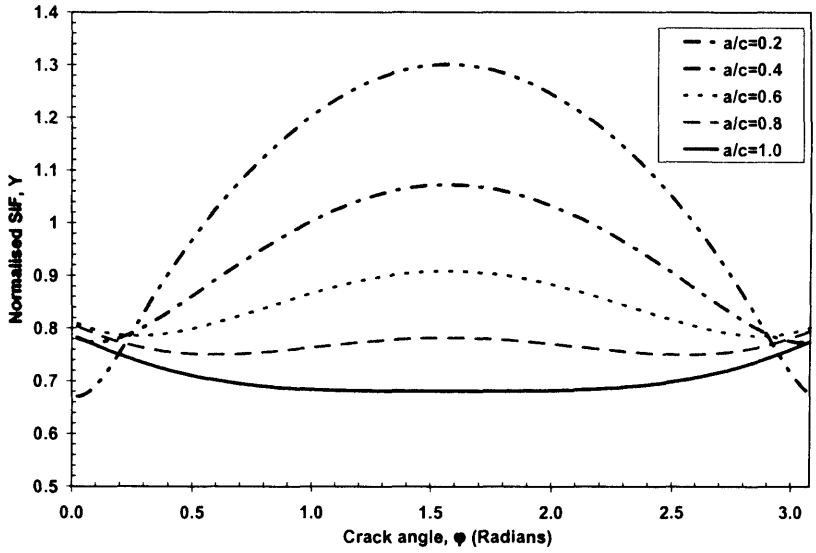

Figure 4.1: Newman & Raju [4.12] normalised surface crack SIFs under tension for $a/T = 0.4$

Fig. 4.1 above shows the normalised SIF (or *Y* Factor) versus crack angle ($0 \rightarrow 180^{\circ}$) plot for a range of crack aspect ratios under tension. It should be noted that the crack depth to plate thickness ratios for all crack aspect ratios are identical ($a/T = 0.4$ in this case). At the crack deepest point ($\pi/2$) of a long crack with an aspect ratio of $a/c = 0.2$, it can be seen that the SIF is higher than at the surface point. Since the SIF is highest at the deepest point, the crack will have a tendency to grow in the depth direction faster. In other words, the crack aspect ratio will become higher as the crack advances. For a shorter crack with an aspect ratio of $a/c = 0.6$, the SIF at the crack deepest point is much lower. However, the crack will still tend to grow in the

deepest point direction since the SIF is still higher compared to the value at the surface point. On the other hand, a very short crack with an aspect ratio of *a/c* = 1 (semi-circular crack) will have the highest SIF at the surface point meaning that the crack will tend to grow in the length direction, resulting in lower crack aspect ratio as the crack grows. Since the SIFs around the crack front are the main driving force in crack propagation, it can be appreciated that fatigue crack growth can be significantly altered if the fatigue crack shape can be controlled.

Let us now consider Figs. 4.2 and 4.3, which show the normalised surface crack SIFs for a range of crack depth to plate thickness ratios (*a/T*) under axial tension and pure bending respectively. In these plots, the crack aspect ratios are kept constant at *a/c* = 0.2. Fig. 4.3 shows that when the crack is shallow compared to the plate thickness, the maximum SIF occurs at the deepest point but as the crack advances, the maximum SIF location gradually switches from the deepest point to the surface point. By comparing Figs. 4.2 and 4.3, it is evident that for a crack with the same aspect ratio, the crack has higher SIFs at the deepest point under axial tension compared to pure bending as the crack propagates. In other words, for similar applied surface stress amplitudes, a plate containing a surface crack will fail with a higher crack aspect ratio in tension compared to bending. Hence, it is hypothesised that axial tension should be more likely to produce a leak-before-break crack (through thickness with high *a/c* ratio). This observation allows the development of a methodology for controlled failure design which will be described in the following section.

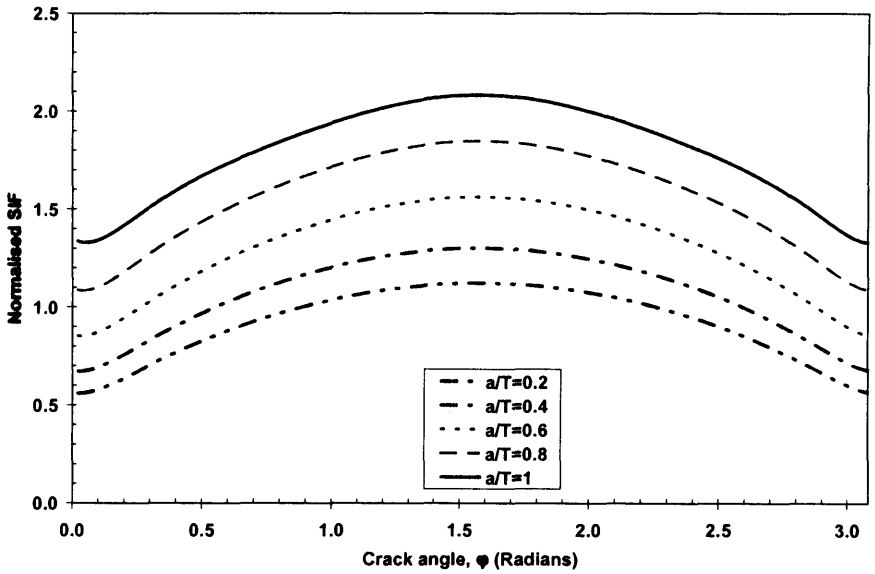

Figure 4.2: Newman & Raju [4.12] normalised SIFs under tension for *a/c* = 0.2

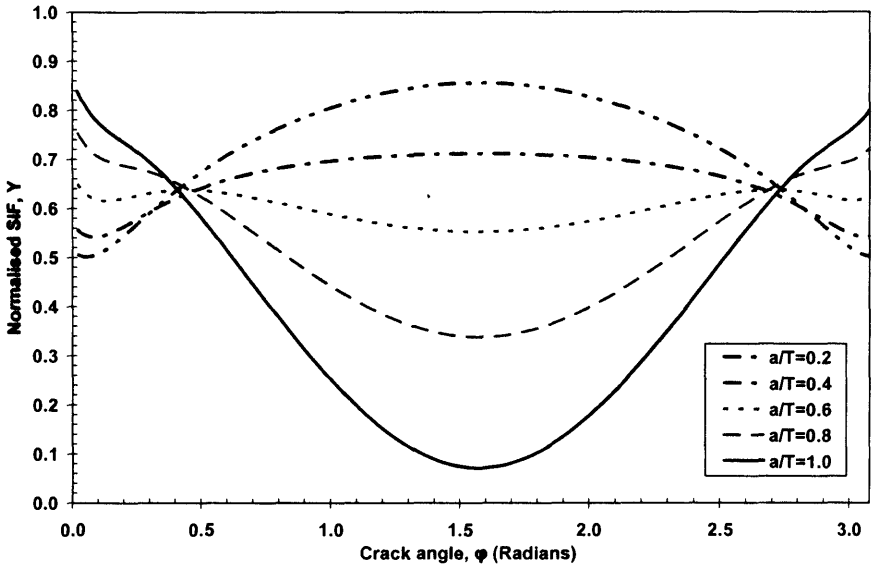

Figure 4.3: Newman & Raju [4.12] normalised SIFs under bending for a/c = 0.2

4.3 Fatigue Crack Shape Control Using Stitch Cold Rolling

The control of crack shape by introducing different levels of compressive residual stress in drillstring threaded connections was investigated by Knight et al [4.3, 4.4, 4.12]. In an attempt to use variations in the level of compressive residual stress to influence the crack length in drill string threaded connections, Knight et al developed a controlled cold rolling technique termed stitch cold rolling. The idea behind stitch rolling is to apply differing intensities of compressive residual stress at specific regions in a structural component to preferentially strengthen certain areas relative to others.

The development of stitch cold rolling is based on philosophies such as Fail Safe and Controlled Failure Design [4.13, 4.14]. In these methodologies, the aim is to control the manner in which a structure may fail, based on the concept that statistically, some failures will inevitably occur. For example in drillstring threaded connections, fatigue failures can be categorised into twist-off and wash-out. A twist-off failure is caused by a sudden fracture, occurs when the remaining circumference material ligament is unable to withstand the applied load. This is considered to be a catastrophic failure and a highly unfavourable event since the retrieval of the downhole broken connections is an extremely complex and expensive operation [4.12]. A wash-out is a detectable partial failure, which is the preferred failure mode since remedial action can be carried out before catastrophic failure occurs. Consider two simplified threaded connections containing defects shown in Fig. 4.4. By successful implementation of anisotropic material properties and introduction of a compressive residual stress field, the crack aspect ratio at failure can be altered.

High aspect ratio failure (Fig. 4.4a) giving wall penetration prior to fracture, known as leak before break, can be achieved by controlling the fatigue crack propagation path. Knight successfully demonstrated that stitch cold rolling has a significant influence on the crack growth, fatigue life and crack shape evolution in drillstrings. Following Knight's work, stitch rolling was adopted here in the study of crack shape evolution in flat plates.

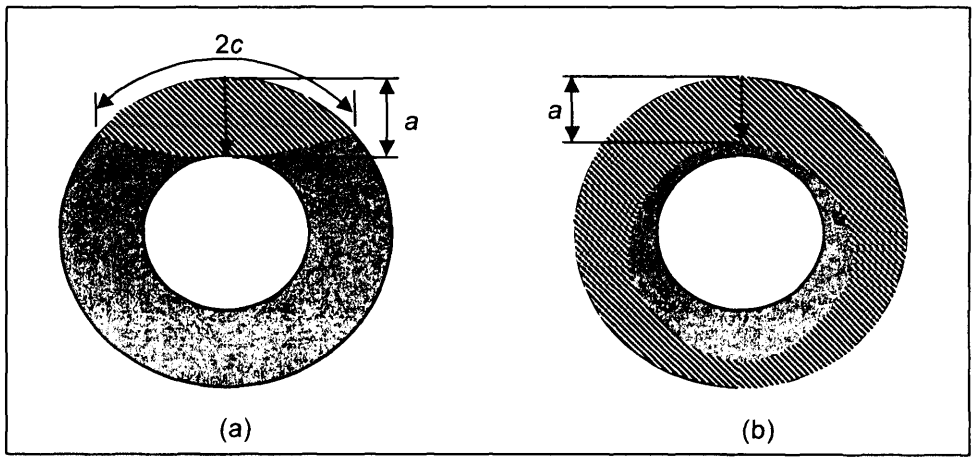

Figure 4.4: Crack aspect ratio (*a/c*) at failure (a) High aspect ratio failure (b) Low aspect ratio failure

The development of the stitch cold rolling technique is still at its infancy and hence its full potential is still to be discovered. However, it is postulated that the implementation of the controlled failure design concept using the stitch cold rolling technique is revolutionary in many engineering aspects. For example, knowing where cracks will initiate and propagate, the location of fatigue cracks or defects can be predicted before inspections are carried out. This can be a vital development since the decrease in inspection duration can lead to a considerable reduction in maintenance cost. In addition to that, with the knowledge of fatigue crack locations, additional uncertainty during inspection can be significantly reduced, which means that the probability of detection (PoD) will be greatly enhanced. In addition, the application of leak before break design and the improvement in fatigue life of components means that corrective action can be performed before catastrophic failure occurs. Consequently, engineers will be able to generate more accurate models and this will significantly improve the reliability and safety of the structures.

4.4 Experimental Test Details

4.4.1 Test Specimens

The test specimens were fabricated from BS EN 10025 Grade S275JR (formerly known as BS 4360 Grade 43A), a mild steel with a yield strength of 275MPa [4.15]. The chemical composition and mechanical properties of S275JR mild steel can be found in Table 4.1. A total of six flat plate specimens were used in this study. The plates were 790mm in length and 200mm in width, Tests CR1, CR2 and CR3 had a thickness of 40mm (Fig. 4.5) while Tests CR4 and CR5 and CR6 were 20mm thick. Test CR1 served as a control specimen for comparison purposes while Tests CR2 to CR6 were stitch cold rolled with different cold rolling parameters. All the specimens were machine-notched in the centre using a 60^{o} cutter with radius of 0.35mm. The dimensions of the machined notch are shown in Fig. 4.6 while Table 4.2 tabulates the dimensions of the original and cold rolled notch. It can be seen that the use of an over-sized roller has significantly deformed the machined-notch.

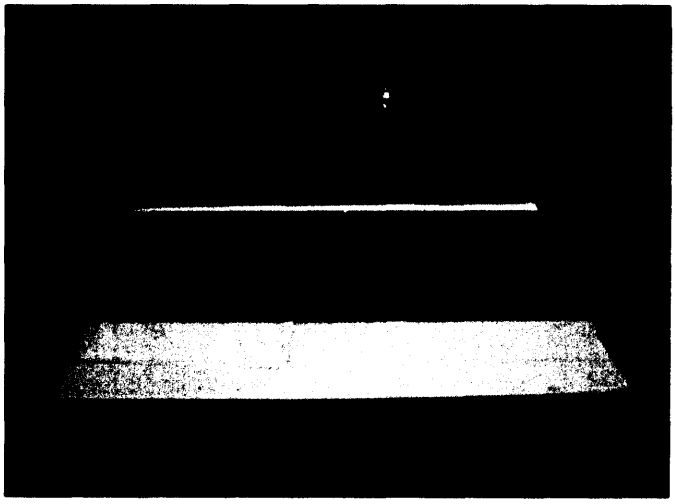

Figure 4.5: BS EN 10025 Grade 275JR mild steel plate

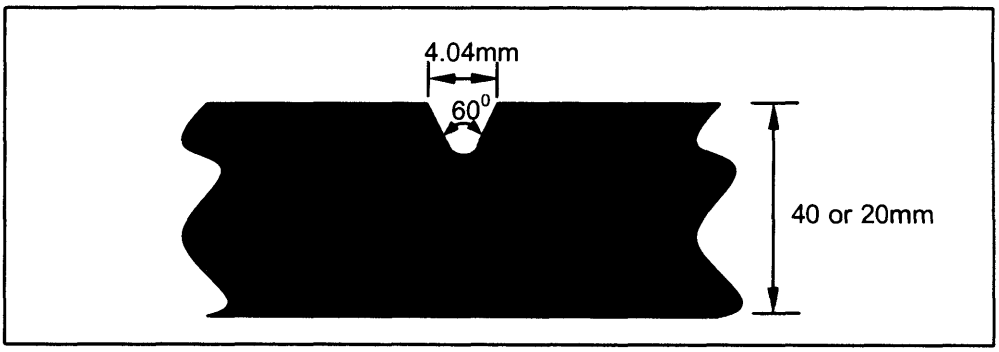

Figure 4.6: Geometry of test specimen machined notch

Chemical composition of BS EN 10025 S275JR	
Element	**WT%**
C_{max}	0.240
Mn_{max}	1.600
P_{max}	0.045
S_{max}	0.045
N_{max}	0.014
Cu_{max}	0.600
Mechanical properties of BS EN 10025 S275JR	
Ultimate Tensile Strength (MPa)	410-560
Yield Strength (MPa)	275

Table 4.1: Chemical composition and mechanical properties of BS EN 10025 S275JR steel [4.15]

Dimensions	Original	Deformed/Cold Rolled
Depth (mm)	3.50	3.97
Width (mm)	4.04	5.14
Root Radius (mm)	0.35	0.98
Inclined Surfaces (deg)	60	67.6

Table 4.2: Dimensions of original and cold rolled notch

In order to calculate the test applied load and avoid plasticising the material at the notch root, the theoretical stress concentration factor {SCF} must be known. Stress concentration factors for various types of notches in flat plates under axial tension or pure bending can usually be found in the Peterson SCF Handbook [4.16]. However, the SCF for the current notch could not be determined from the handbook as the ratios of notch depth to the thickness of the specimens were too low, resulting in the SCF values to be outside the range of the published SCF curves. Hence, it was decided to conduct a finite element analysis (FEA) for the determination of the theoretical SCF. A 2D FE model was built using the ABAQUS software [4.17]. *End Biasing* was introduced at the boundaries of mesh surfaces so that the critical region surrounding the notch would have an appropriate density of elements (Fig. 4.7). Mesh refinement and optimisation were performed by examining the convergence the SCF values. As can be seen from Fig. 4.8, the theoretical SCF values converged after a number of mesh refinements and the final value was

found to be approximately 7. Following fatigue testing, this theoretically calculated SCF value was later demonstrated to be over-conservative.

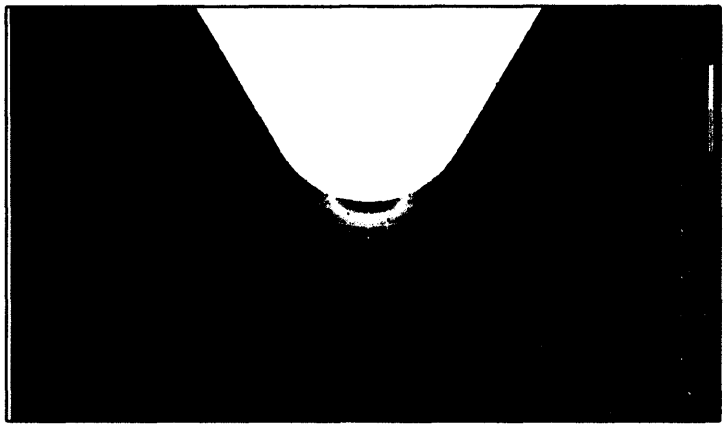

Figure 4.7: A 2D FE mesh of the notch root

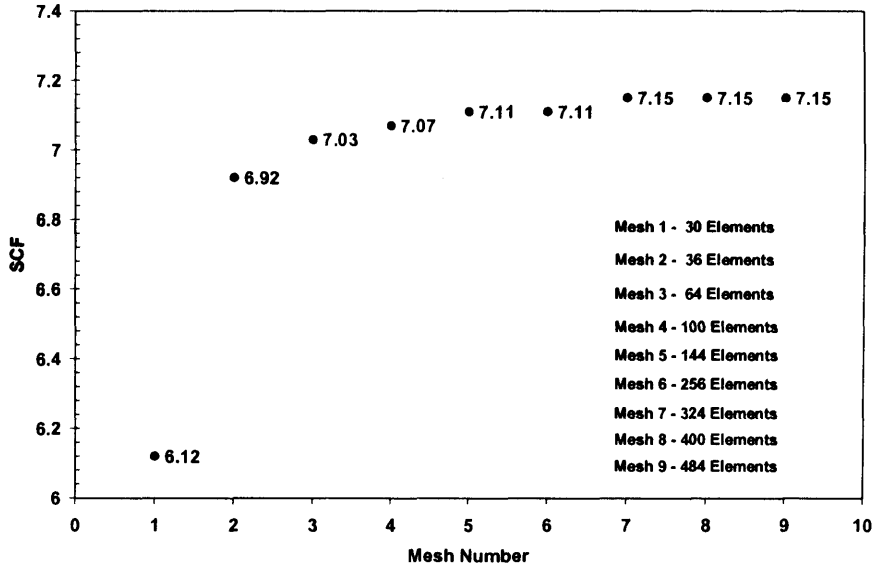

Figure 4.8: Determination of theoretical SCF using FEA

4.4.2 Stitch Cold Rolling Parameters

Fig. 4.9 illustrates the localised stitch cold rolling technique that was used in this study while Fig. 4.10 shows a compressive residual stress zone either side of an untreated zone at the root of a v-notched plate. In this example the cold rolled region was strengthened while the non-cold rolled region was left unprotected. Hence, cracks were expected to initiate in the non-cold rolled region. The unique characteristic of stitch cold rolling is believed to influence the crack shape evolution.

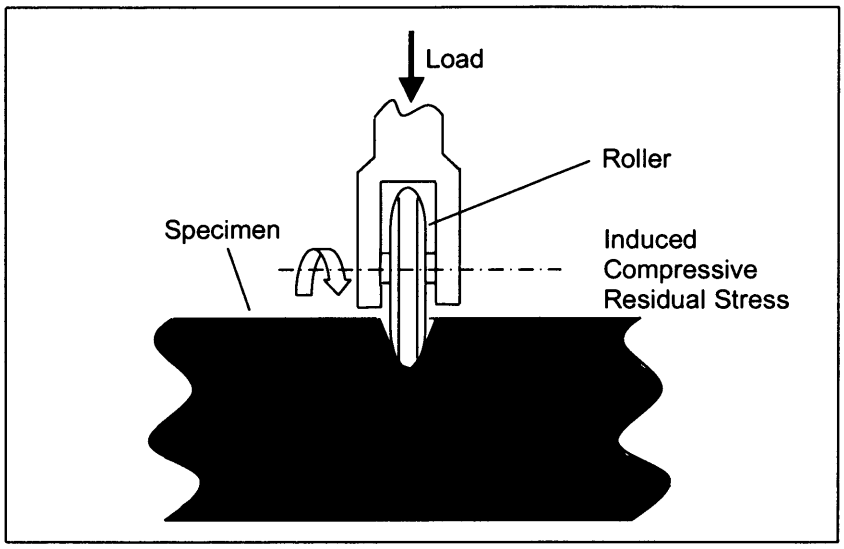

Figure 4.9: Induced compressive residual stress during cold rolling

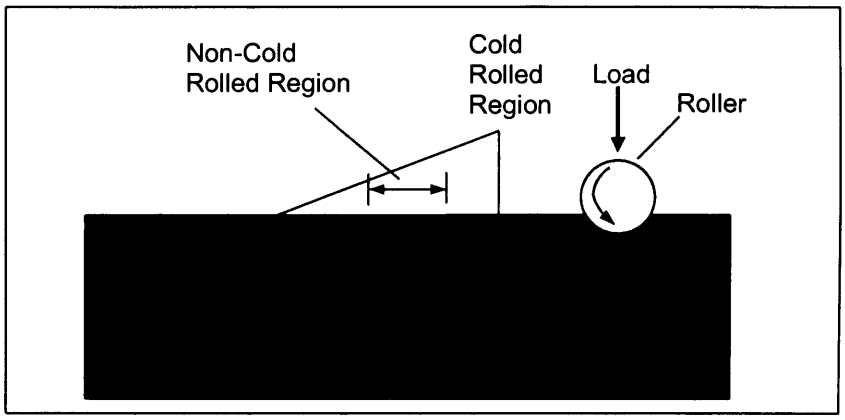

Figure 4.10: Preferential cold working

Stitch cold rolling was performed using a custom-built cold rolling rig, shown in Fig. 4.11 [4.18] below. The main cold rolling tool consists of a roller piston (Fig. 4.12) fitted into a high pressure hydraulic cylinder, which was connected to a manual hydraulic jack that provided the required rolling pressure. During the cold rolling process, a force of 11kN was applied to the roller placed in the machined notch on the flat surface and forced along the notch by using a 5 tonne bottleneck hydraulic jack, as shown in Fig. 4.11b. The applied load was constantly monitored and maintained using the manual hydraulic jack. Multi-pass stitch rolling was adopted in order to provide a more uniform distribution of residual stress, as suggested by Knight [4.12]. Table 4.3 below summarises the stitch cold rolling parameters and the test specimens, together with their respective cold rolling parameters can be found in Appendix G. A summarised flow chart of stitch cold rolling procedures can also be found in Fig. G2 in Appendix G.

(a) (b)

Figure 4.11: Stitch cold rolling set-up

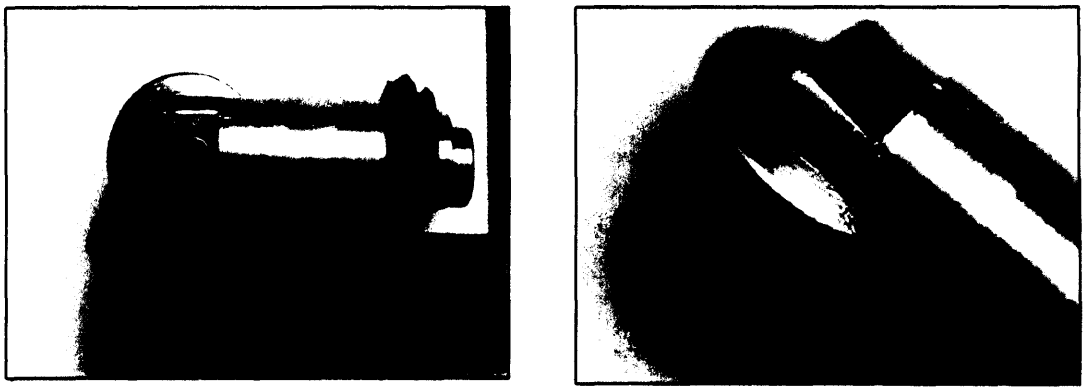

(a) (b)

Figure 4.12: Roller used for stitch cold rolling

Specimen	Plate Thickness (mm)	Cold Rolling Pressure (psi)	No. of Passes	No. of Re-rolled passes (after initiation)	Non-cold Rolled Length (mm)
Test CR1	40	6000	-	-	-
Test CR2	40	6000	3	3	20
Test CR3	40	6000	3	3	40
Test CR4	20	6000	4	0	20
Test CR5	20	6000	5	0	20
Test CR6	20	6000	5	0	40

Table 4.3: Test specimen details

Table 4.3 above shows Tests CR2, CR4 and CR5 had an non-cold rolled length of 20mm while Tests CR3 and CR6 had a longer unprotected length of 40mm. Since Tests CR2 and C3 were

the first stitched cold rolled specimens to be fatigue tested and the degree of residual stress relaxation under cyclic loading was unknown, both specimens were re-rolled following fatigue crack initiation. This was to ensure that some compressive residual stress would remain to influence the crack growth even after a relatively high number of fatigue cycles.

4.4.3 Fatigue Test Set-up

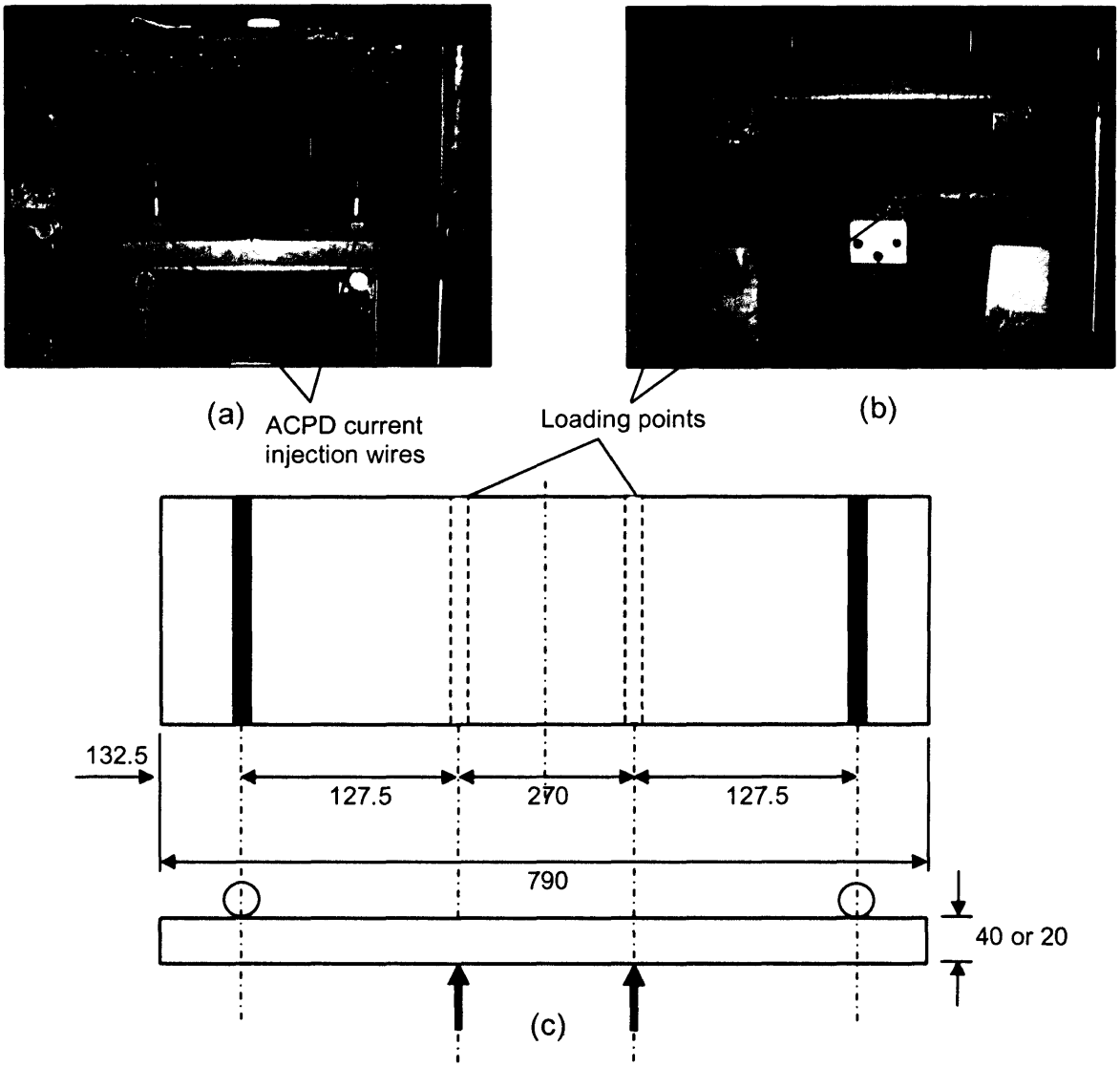

Figure 4.13: Four point bending fatigue test set-up

All the tests were conducted under four point bending in ambient air on an Instron 1000kN servo-hydraulic fatigue test machine (Fig. 4.13 above). The specimens were fatigue cycled under constant amplitude loading at a nominal stress range of approximately 120MPa. The frequency used was 4Hz and the fatigue cycling was performed under load control, meaning that the

specimens were subjected to the pre-defined load amplitude regardless of any change in the specimen stiffness.

Crack depth sizing and monitoring was by Alternating Current Potential Difference (ACPD) technique. The ACPD current injection wires are clearly visible in the fatigue test set-up shown in Figs. 4.13(a) and (b). ACPD was employed due to it being non-destructive and its ability to provide rapid crack depth measurement during the course of a fatigue test. ACPD measurements were performed using a U8 Crack Microgauge [4.19]. By performing manual ACPD measurements along the width of the plate, the depth and length of the cracks can be constantly monitored. In order to build up a comprehensive set of crack growth data, the fatigue tests were stopped at suitable intervals so that ACPD inspections can be carried out. During ACPD inspections, the test specimens were subjected to a mean load so that the crack faces would remain open. This is extremely important as closed crack faces may cause an underestimation in the crack depth measurement.

4.5 Fatigue Test Results

Table 4.4 below summarises the fatigue test parameters and results. It must be noted that except for Test CR1, none of the cracks grew through the plate thickness or width and tests were terminated due to cracks initiating at other locations (at the specimen edges) or for reasons of time and project resources. The following sections present the fatigue test results obtained in the form of fatigue crack initiation, crack growth and crack shape evolution.

Specimen	Nominal Stress Range (MPa)	Fatigue Cycling Frequency (Hz)	No. of Cycles to Crack Initiation	No. of Crack Propagation Cycles	Total Test Cycles
Test CR1	51-97	4	2,235,000	1,880,000	4,115,000
Test CR2	122	4	128,000	3,872,000	4,000,000
Test CR3	122	4	100,000	4,750,000	4,850,000
Test CR4	120	4	345,000	3,373,000	3,718,000
Test CR5	120	4	1,161,000	8,219,000	9 ,380,000
Test CR6	120	4	500,000	5,500,000	6,000,000

Table 4.4: Summary of fatigue test results

4.5.1 Fatigue Crack Initiation Data

After careful consideration, Test CR1 was fatigue cycled at an initial nominal stress range of 51MPa (corresponding to a local stress range of 357MPa based on an SCF=7). However, no crack initiation was detected after approximately 600,000 fatigue cycles and the applied nominal stress range was gradually increased up 97MPa (corresponds to a local stress range of 679MPa). Crack initiation was detected after the specimen was subjected to 875,000 fatigue cycles at a nominal stress range of 97MPa and the total crack initiation recorded was approximately 2.2 million cycles. The crack initiation data clearly suggest that the theoretical SCF value calculated was over-conservative. Two distinct crack initiation sites were detected in Test CR1. They were quarter-elliptical corner cracks developed from the edges of the specimen. The unexpected high initiation life of Test CR1 is believed to be due to the effect of coaxing [4.20, 4.21]. Coaxing refers to an increase in the fatigue strength of a susceptible metal brought about by prior cycling at a lower stress level than its fatigue limit. This is the most likely reason why Test CR1 had a considerably high fatigue crack initiation life. An example of an early crack growth plot is shown in Fig. 4.14.

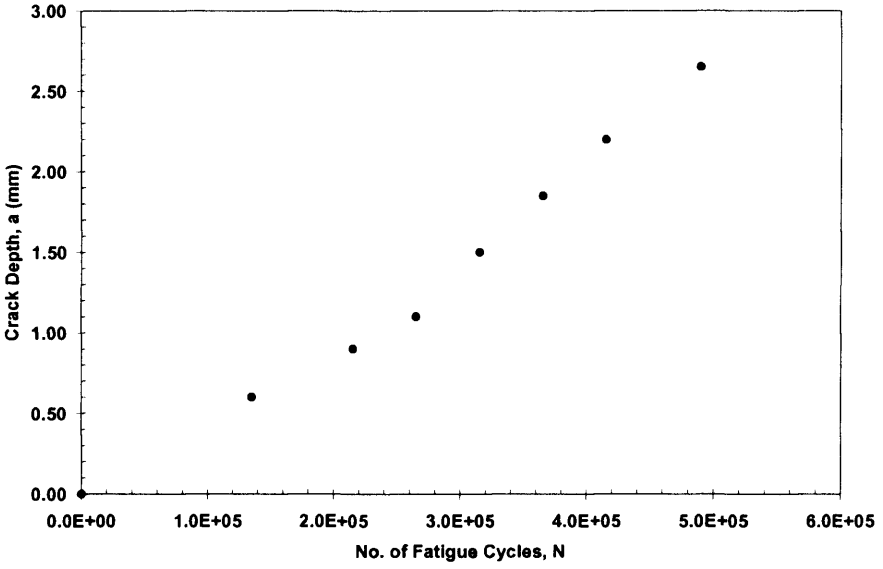

Figure 4.14: Early crack growth data for Test CR1

Crack initiation was detected in the non-cold rolled region in Tests CR2 to CR6. Based on the crack initiation data obtained from Test CR1, it was decided to fatigue cycle the subsequent specimens at a higher nominal stress range. The nominal stress range applied to Tests CR2 to CR6 was approximately 120MPa. The higher nominal stress for Tests CR2 and CR3 contributed to the relatively lower fatigue initiation life compared to Test CR1. The crack initiation life of Tests CR2 and CR3 were 128,000 cycles and 100,000 cycles respectively. For the 20mm plates, the

fatigue crack initiation life of Tests CR4, CR5 and CR6 was 345,000, 1,161,000 and 500,000 cycles respectively. Tests CR4 and CR6 had comparable crack initiation lives but the relatively high initiation life of Test CR5 was unexpected. This is because all the tests were conducted in a consistent manner and the specimens were subjected to the same nominal stress range of 122MPa.

4.5.2 Fatigue Crack Growth Data

It can be generally observed from Table 4.4 above that there is a significant improvement in fatigue crack propagation life for all stitch cold rolled specimens. The fatigue crack growth curves for all the tests are shown in Figs. 4.15 to 4.20 below and all the crack growth results are compared in Fig. 4.21. The graphs are plotted using the ACPD crack depth data for the deepest point on the crack front. The crack growth results for the 40mm-thick specimens are presented in Figs. 4.15 to 4.17 while the results for the 20mm-thick specimens are shown in Figs. 4.18 to 4.20. The crack growth data for both cracks detected in Test CR1 are shown in Fig. 4.15, together with the corresponding stress history prior to crack initiation. Final inspection was performed after the specimens had undergone 2,755,000 of crack propagation cycles and the fatigue life was approximately 4.1 million cycles. It can be seen that the crack depth data for the corner cracks were unusually high for a crack that had propagated under bending. It is believed that the edge effect [4.22] phenomenon observed in the ACPD technique had over-sized the crack depth measurement. In general terms, edge effects occur due to the fact that non-uniform magnetic fields are present at the edges of a plate as the electrical field becomes weaker further away from the field input axis.

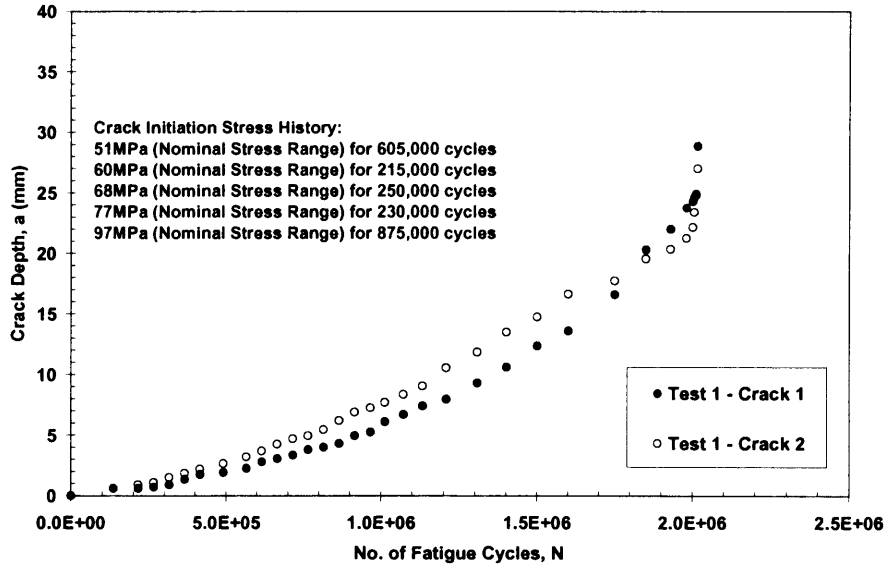

Figure 4.15: Fatigue crack growth data for Test CR1

In Test CR2, steady fatigue crack growth data was recorded until the crack advanced out of the non-cold rolled length to meet with the cold rolled region. The same can also be observed in Test CR3. Fig. 4.16 clearly shows normal crack growth in Test CR2 up to approximately 1 million cycles and the crack depth almost remained constant from 1 million to 3 million cycles. Further cycling saw a recovery of crack growth and the total fatigue life recorded was 4 million cycles. In Test CR3, normal fatigue crack growth can be observed up to 2 million cycles (Fig. 4.17 below) and the crack propagation rate had reduced significantly when the crack length reached 40mm, which is equal to the non-cold rolled length. The crack retardation resulted in growth of only 1.5mm in the next 3 million fatigue cycles. Test CR3 was terminated after it had undergone approximately 4.8 million crack propagation cycles. Tests CR4 to CR6 showed similar crack growth retardation behaviour, but to a lesser extent. Figs. 4.18 to 4.20 below show steady crack growth throughout the tests but the slow linear crack growth rate clearly differs from a conventional crack growth curve, e.g. Fig. 4.15. This is particularly evident in the crack growth data obtained from Tests CR4 and CR5, where the crack growth rate decreases with increasing number of fatigue cycles, while a typical crack will advance with an increasing crack propagation rate. The fatigue crack propagation lives of Tests CR4 to CR6 were 3.4, 8.2 and 5.5 million cycles respectively. Tests CR3 and CR6, which had the longest non-cold rolled length (40mm) clearly show deeper cracks despite these having two different plate thicknesses.

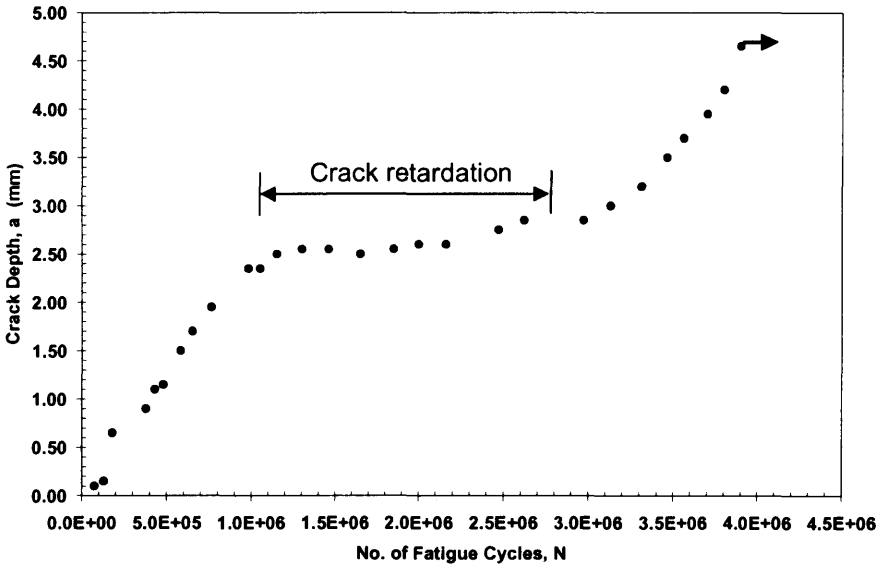

Figure 4.16: Fatigue crack growth data for Test CR2 (non-cold rolled length = 20mm)

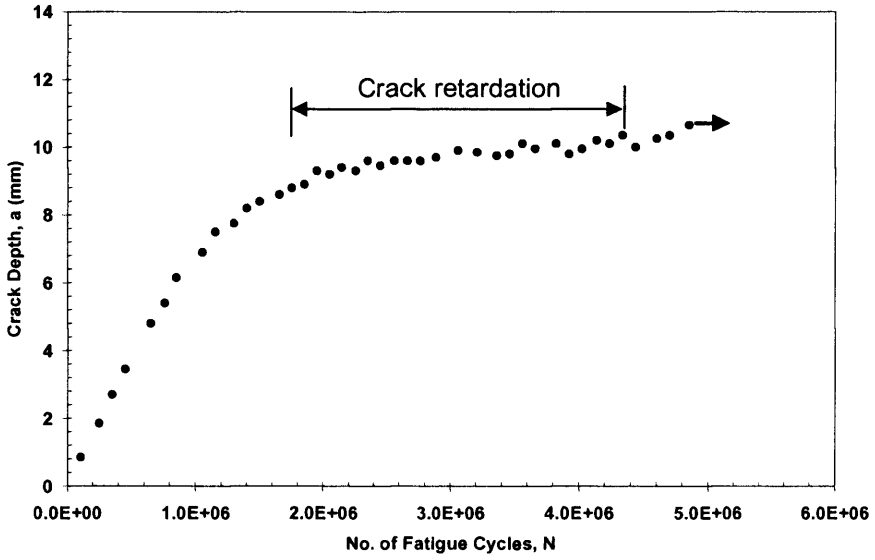

Figure 4.17: Fatigue crack growth data for Test CR3 (non-cold rolled length = 40mm)

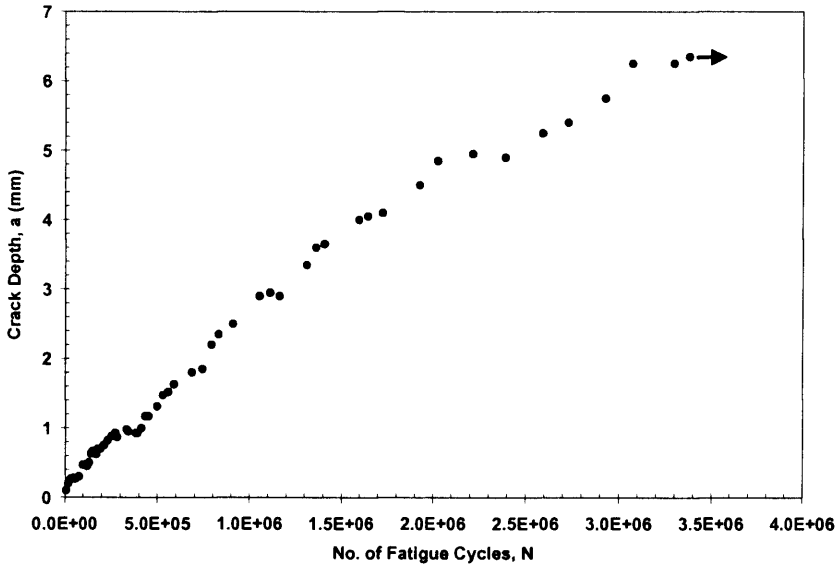

Figure 4.18: Fatigue crack growth data for Test CR4 (non-cold rolled length = 20mm)

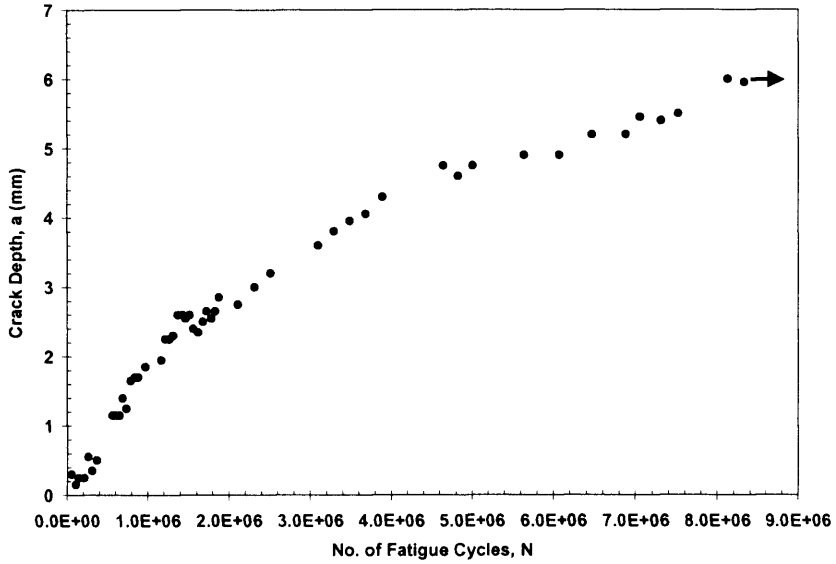

Figure 4.19: Fatigue crack growth data for Test CR5 (non-cold rolled length = 20mm)

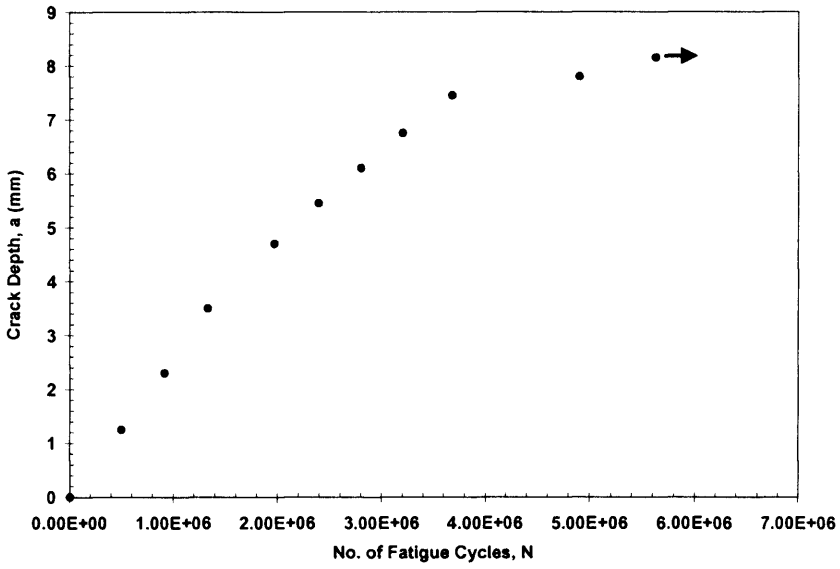

Figure 4.20: Fatigue crack growth data for Test CR6 (non-cold rolled length = 40mm)

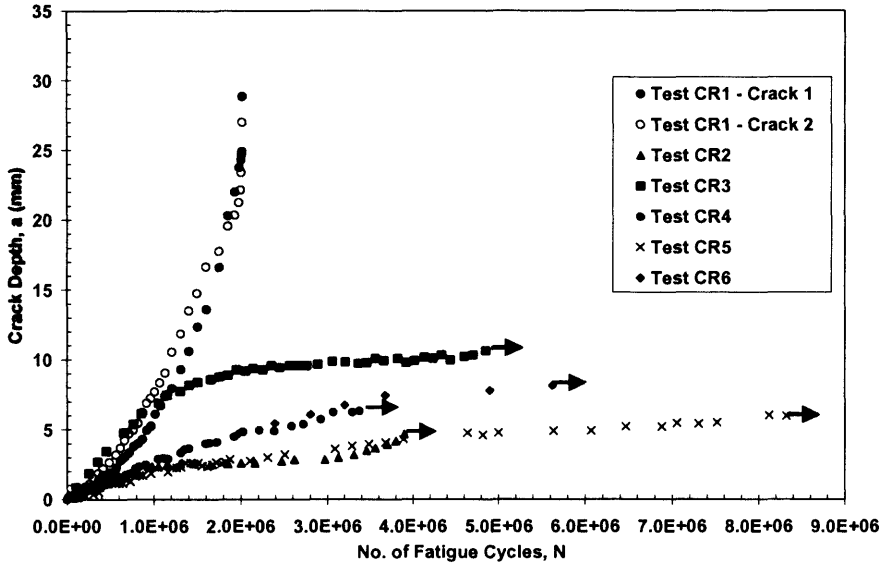

Figure 4.21: Fatigue crack growth data for all tests

4.5.3 Crack Shape Evolution Data

Periodic ACPD inspection performed along the width of the specimens (or along the length of the notch) had allowed the crack shape evolution to be constantly monitored throughout the fatigue tests. The crack shape evolution plots, together with the ACPD inspections intervals, are shown in Figs. 4.22 to 4.26 below. As stated earlier, two crack initiation sites were detected in Test CR1. The quarter-elliptical corner cracks are clearly shown in Fig. 4.22. The cracks coalesced to form a long edge crack after approximately 1.6 million fatigue propagation cycles. Semi-elliptical surface cracks were recorded in Tests CR2 to CR6. It is worth mentioning that the semi-elliptical crack shape is not evident in the figures shown since the axes are plotted on different scales. As can be seen from the figures, fatigue crack initiation was only detected in the non-cold rolled region. This is expected since surface compressive residual stress is known to deter fatigue crack initiation. It is demonstrated in Section 4.2 that a surface crack in a flat plate subjected to pure bending load will tend to extend faster at the surface (or length) direction as it propagates. The crack shape evolution results obtained, however, show very different crack growth behaviour. It can be observed in Figs. 4.23 to 4.26 that for most of the fatigue cycles applied, the crack growth rate in the depth direction was much higher than the surface (or length) direction and in some cases the crack length remained virtually unchanged. It is postulated that the induced compressive residual stress field not only influences the crack growth but controlled the crack growth in the surface direction.

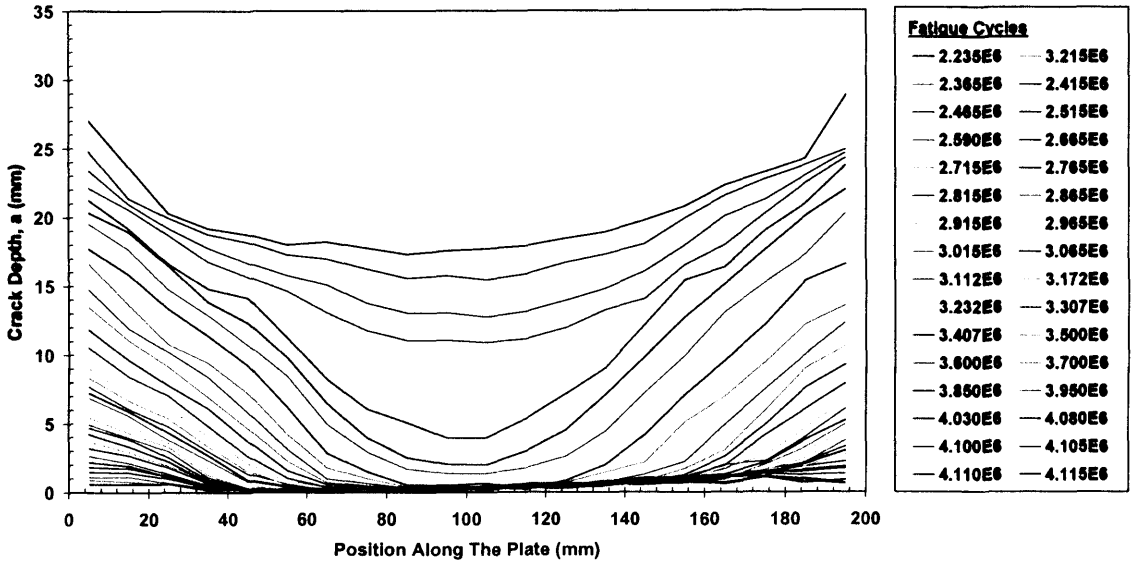

Figure 4.22: Crack shape evolution data for Test CR1

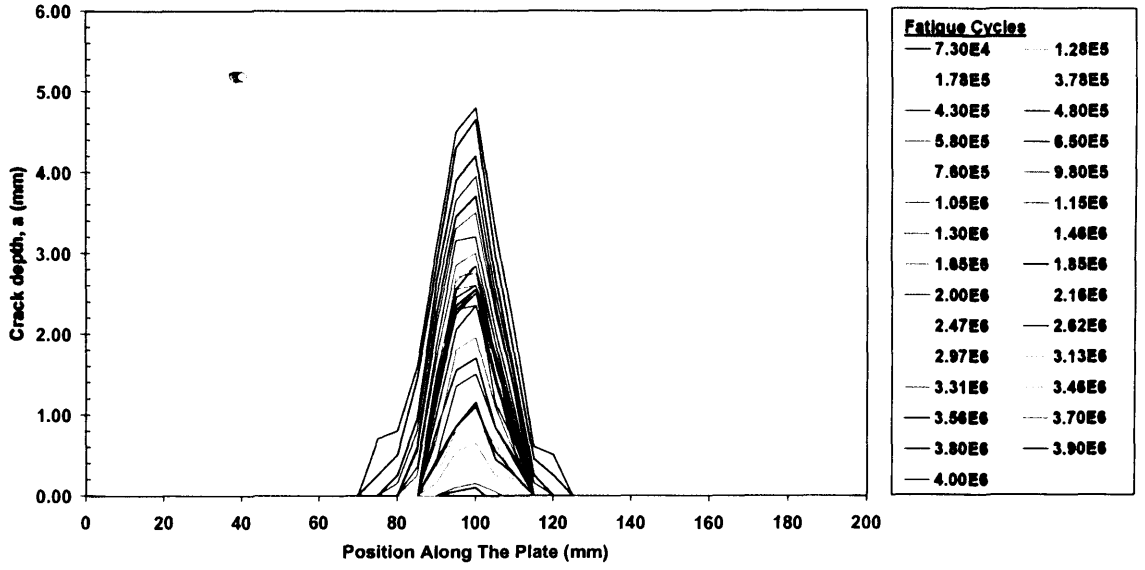

Figure 4.23: Crack shape evolution data for Test CR2

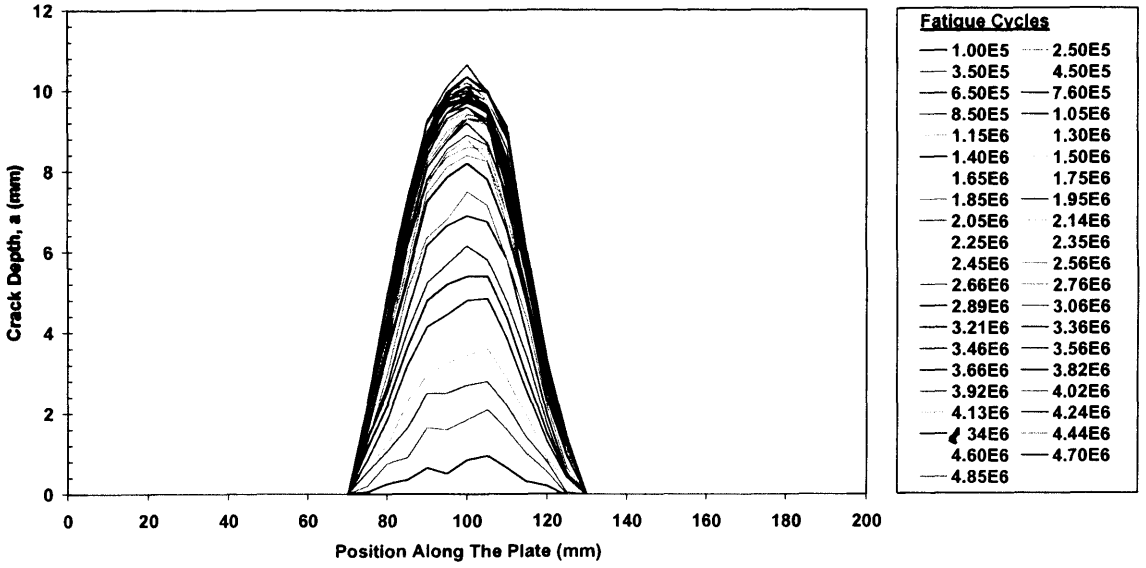

Figure 4.24: Crack shape evolution data for Test CR3

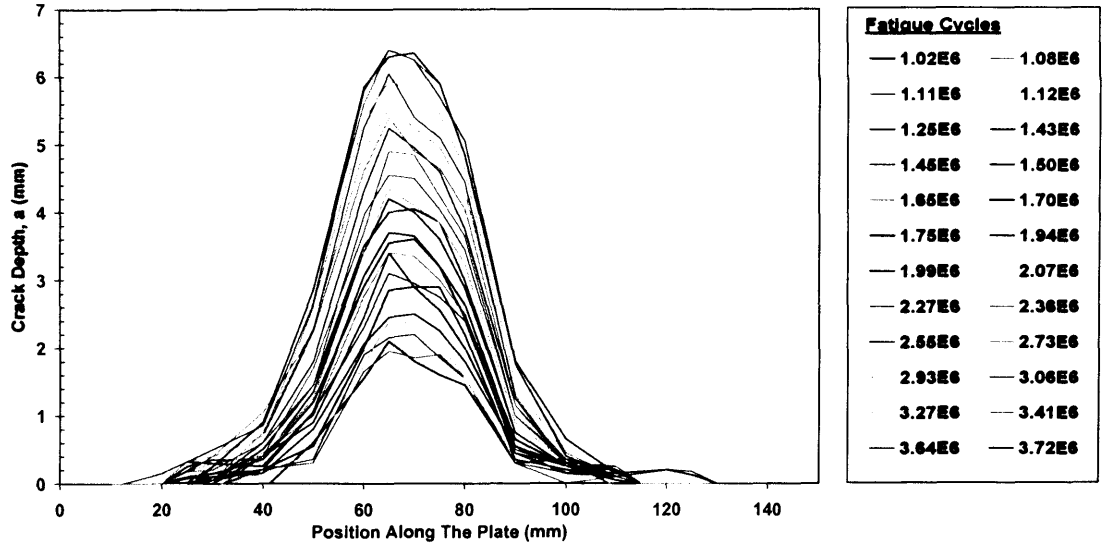

Figure 4.25: Crack shape evolution data for Test CR4

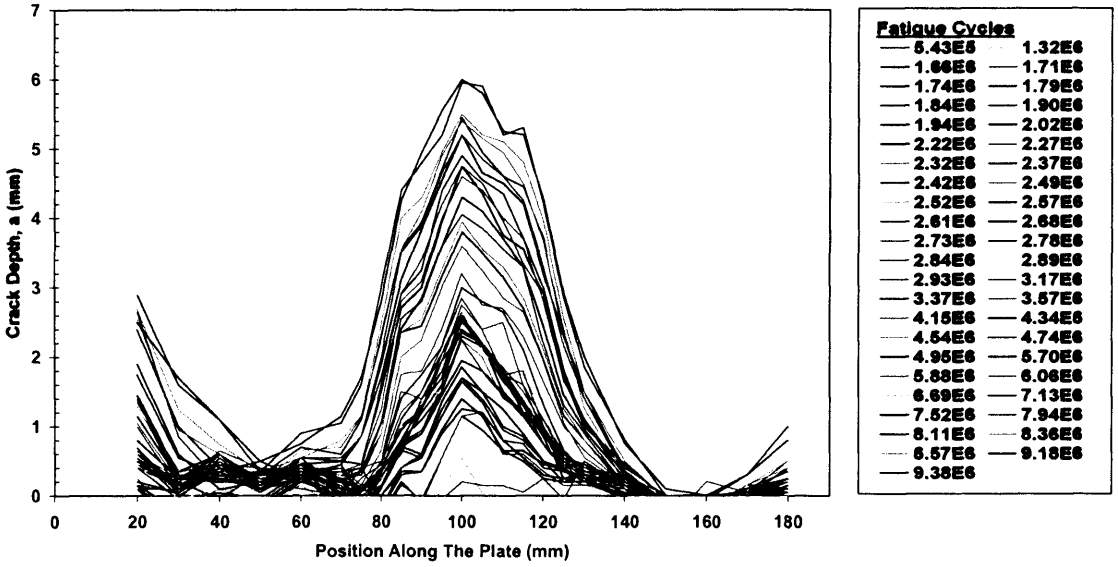

Figure 4.26: Crack shape evolution data for Test CR5

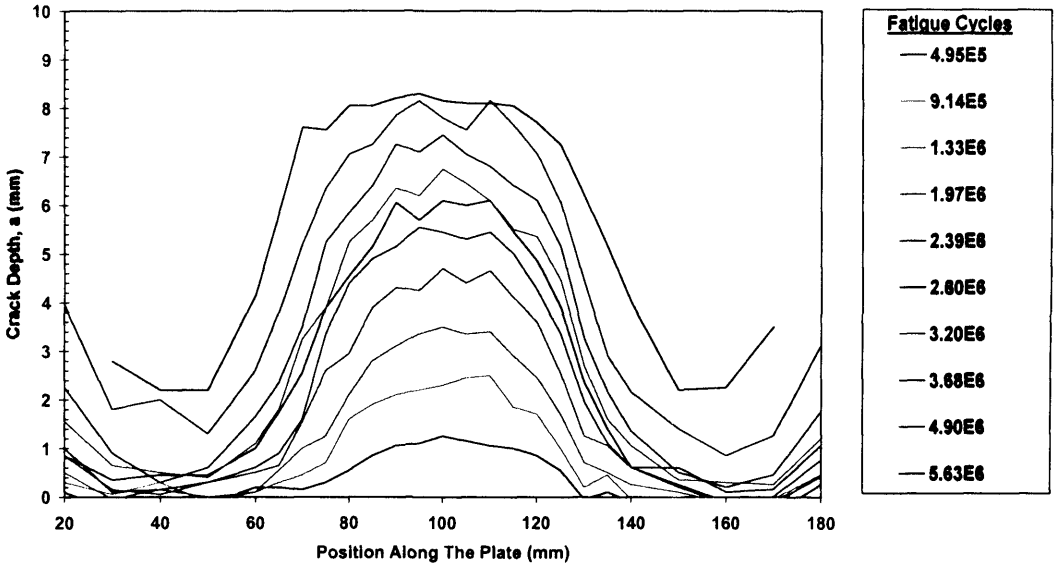

Figure 4.27: Crack shape evolution data for Test CR6

4.5.4 Fatigue Crack Surfaces

Following testing, the specimens were cooled in liquid nitrogen and broken open at a high strain rate to produce a fast-fracture surface which clearly demarcate the crack growth created during the fatigue tests. This procedure has enabled the examination of fatigue crack surface to be carried out. Fig. 4.30a below firstly shows a typical semi-elliptical crack grown from an artificial starter notch in a plate subjected to pure bending load and beachmarking technique was

employed to highlight the crack shape evolution. The fracture surfaces of Tests CR2, CR3, CR5 and CR6 are shown in Figs. 4.30b to e respectively.

(a) Typical semi-elliptical surface crack grown under pure bending

(b) Test CR2

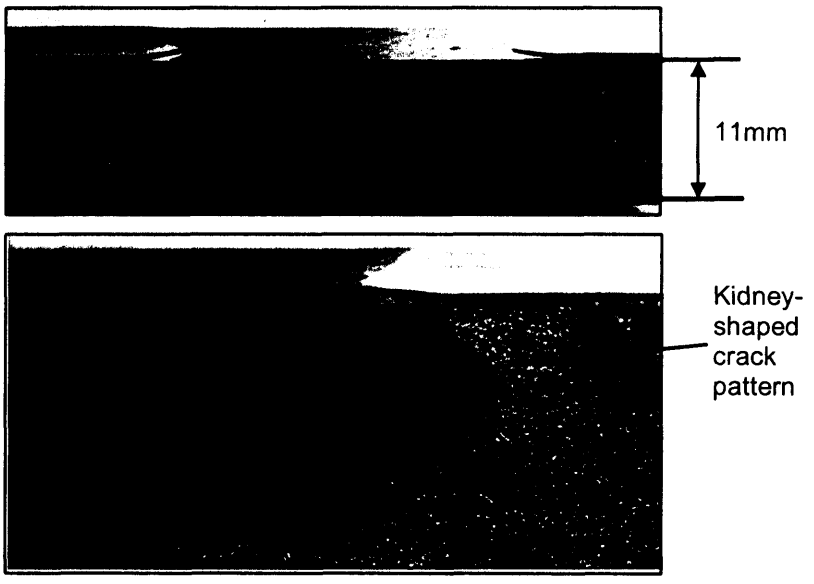

(c) Test CR3

(c) Test CR5

(d) Test CR6

Figure: 4.28: Fracture surfaces

4.6 Discussion of Fatigue Test Results

The results presented above clearly demonstrated that the stitch cold rolling technique significantly influenced the fatigue crack initiation, fatigue crack growth and crack shape evolution. As reported in Section 4.5.1, fatigue crack initiation was only detected in the non-cold rolled region in the stitch cold rolled specimens. This was an expected observation since notch-root cold rolling using an over-sized roller is widely known to have a double acting advantage of beneficial compressive residual stress combined with a lower SCF (due to larger root radius), resulting in crack initiation in the unprotected region in this case.

The fatigue crack growth data obtained have shown some unprecedented crack growth behaviour. It can be observed from Fig. 4.21 that the crack growth data are clearly unusual not only due to the relatively low crack propagation rate but also several tests show a significant retardation effect. In addition, both Tests CR2 and CR3 show that the crack growth was virtually retarded for almost 2 million fatigue cycles. It is worth noting that both of these specimens were re-rolled following crack initiation. In all the stitch cold rolled specimens, normal fatigue crack growth was recorded until the crack started to propagate into the cold rolled region. Once the surface crack encountered the cold rolled region, the crack growth was observed to retarded in

the length direction and advanced in the depth direction only. This is particularly evident in Figs. 4.16 and 4.23 for Test CR2. It is believed that the induced compressive residual stress and material anisotropy have acted as a barrier for fatigue crack growth, especially at the surface point. In other words, the surface compressive residual stress had "pinned" the crack ends, arresting it from propagating. Knight et al [4.4] called the beneficial surface compressive residual stress regions as surface "firewalls". It is postulated that during the crack growth retardation, the applied stress caused the relaxation of the remaining residual stress in the cold rolled region. As the residual stress was shaken-down, the crack propagated into the unprotected region (increase in crack length), resulting in the recovery of crack depth propagation, as can be observed in Tests CR2, CR4 and CR5. Test CR3 and CR6 on the contrary did not show a clear resumption of crack growth following crack retardation but again it should be noted that both tests were terminated prematurely. For all the stitch cold rolled specimens, the retardation effect on fatigue crack growth resulted in a significant improvement in fatigue crack propagation life compared to Test CR1 despite several tests having a smaller plate thickness. The comparison between the experimental results and Newman & Raju based fatigue life prediction for the 40mm and 20mm-thick tests are shown below in Figs. 4.29 and 4.30 respectively. For the 40mm-thick specimens, improvement in the fatigue crack propagation life by a factor of more than two fold can be observed while enhancement of crack propagation life by a factor of four fold was recorded for the 20mm-thick specimens. Test CR5 shows the extraordinary crack propagation life of approximately 8 million cycles, a comparative predicted life would only be in the order of 1.8 million cycles.

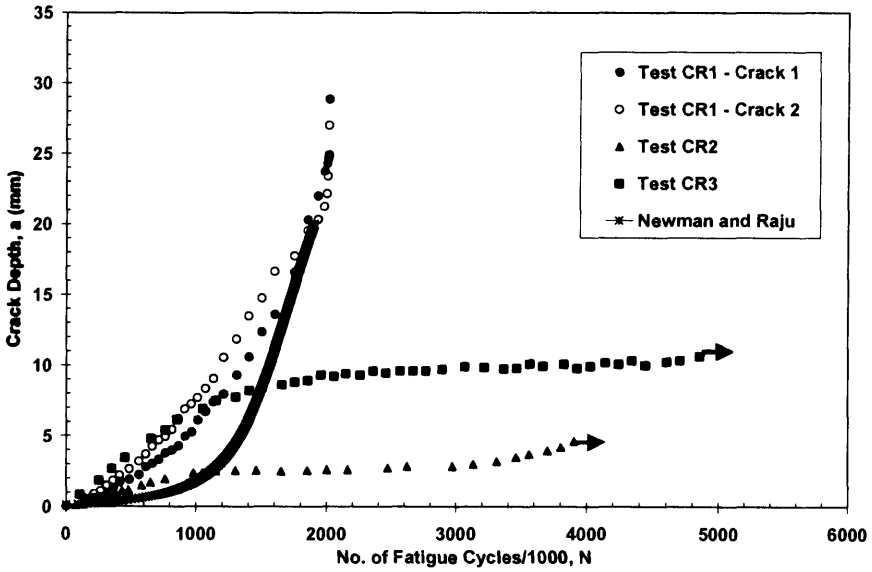

Figure 4.29: Comparison of fatigue propagation life for 40mm-thick specimens

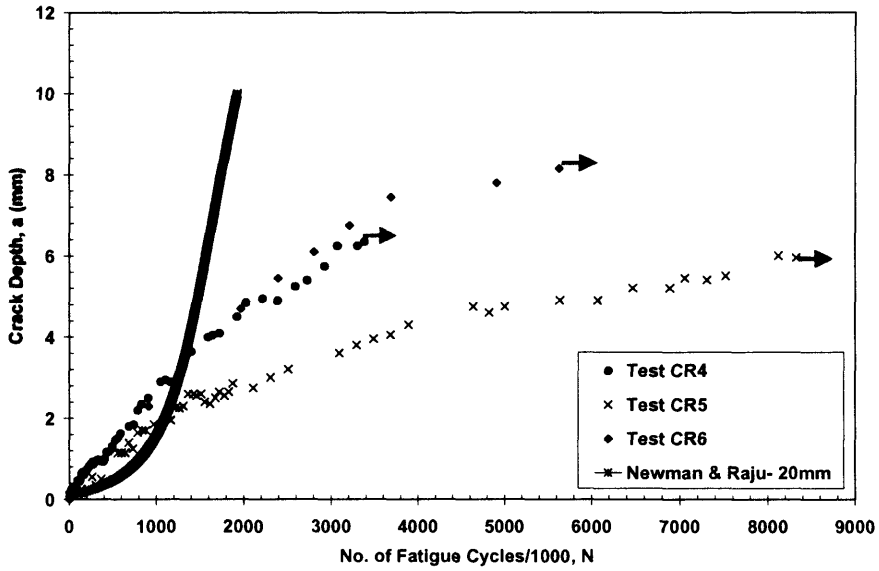

Figure 4.30: Comparison of fatigue propagation life for 20mm-thick specimens

It can be observed in Fig. 4.28 that the fatigue crack shapes of the stitch rolled specimens have unusual patterns. The conventional surface crack shape shown in Fig. 4.28a is contrasted by the crack shape observed from Tests CR2 and CR3 and to a lesser degree Tests CR5 and CR6. The crack surface shown in Test CR2 resembles a semi-circular crack rather than a semi-elliptical crack. Test CR3 even shows that the crack length stopped growing once it met with the cold rolled region and the crack had actually propagated underneath the cold rolled region, as illustrated in the close-up shot of the crack surface. The crack shape shown in Test CR3 is not symmetrical but skewed. It is believed that the contrast in the remaining residual stress had caused this, due to the fact that the stitch cold rolling technique employed is not a completely uniform process and needs further refinement. The beachmarks on Test CR5 and CR6 also show obvious similarities in the crack shape evolution behaviour seen in Tests CR1 and CR2. The "kidney" shape crack pattern observed is considered to be unusual and differs from a typical semi-elliptical crack. It is evident that the unique feature of stitch cold rolling, which applies differing intensities of surface compressive residual stress, has shown to promote crack growth in the depth direction by limiting the crack length growth.

Fig. 4.31 below shows the crack aspect ratio evolution predictions using a SIF weight function method [4.23, 4.24]. The development of the fatigue crack growth model will be further discussed in Chapter 6. The surface crack shape evolution predictions are plotted for different starting aspect ratio under bending. It can be seen from the figure that regardless of the initial crack shape, the crack will tend to grow to an optimum ratio. It is noteworthy that this crack shape evolution behaviour is independent of the applied stress magnitude but can be effected by

material anisotropy and loading modes [4.8]. The experimental crack aspect ratio evolution for all stitch cold rolled tests are shown in Fig. 4.32. Comparing the experimental data with the predictions, it will be appreciated that the crack shape evolution for all tests have been altered from their optimum ratio. It can be observed that most of the experimental data produced almost a straight line. This is because in most cases, the crack length was constantly increasing while the crack length remained constant, as the crack length growth was limited by the cold rolled region. Since the loading mode of the tests was identical to the prediction model, the only possible explanation for the crack shape differences is the introduction of material anisotropy in the stitch cold rolled specimens. From the experimental data, it can be seen that Tests CR2 and CR3 (40mm thick) recorded much higher aspect ratio than the thinner specimens. This implies that it is unlikely for a surface crack to grow through thickness or to achieve a high aspect ratio failure in a relatively thin plate under pure bending. Nevertheless, the crack retardation observed in the thinner specimens is extraordinary.

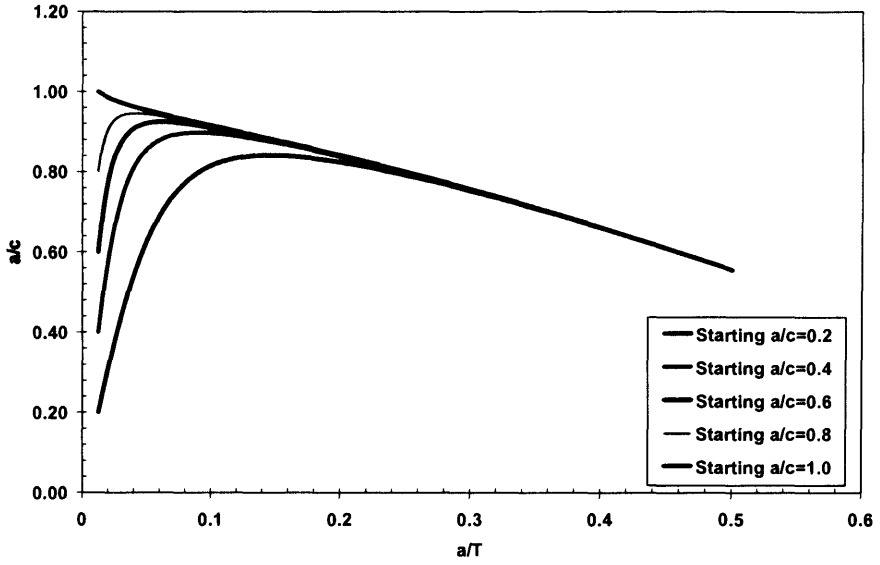

Figure 4.31: Crack aspect ratio evolution prediction using RMS SIF

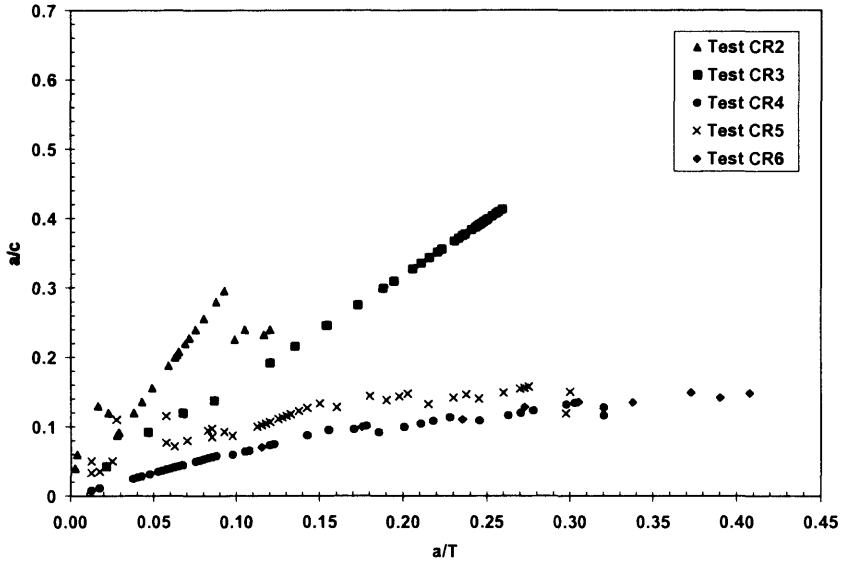

Figure 4.32: Crack aspect ratio evolution data for all stitch cold rolled specimens

4.7 Summary

This Chapter presented details of the fatigue testing of stitch cold rolled specimens. The use of periodic ACPD inspections enabled crack sizing and monitoring throughout the fatigue tests. The significance of crack shape on fatigue crack growth has been clearly illustrated using theoretical models and the experimental results. A total of six fatigue tests were carried out under different stitch cold rolling conditions. The experimental results undoubtedly demonstrated the beneficial effects of stitch cold rolling on fatigue endurance of structural components. The fatigue test data also proved that stitch cold rolling significantly influenced the fatigue crack initiation, crack propagation and crack shape evolution of cold rolled specimens. Based on the results obtained, it can be concluded that the induced surface compressive residual stress and introduction of material anisotropy are believed to be the major contributions in the improvement of fatigue life. Results have shown the potential of controlling the surface crack shape evolution and this may be used to promote short deep (or leak before break) fatigue cracks. In addition, the unique feature of stitch cold rolling was observed to have caused crack retardation, and even arrest in several tests. Since this technique is still at its infancy stage, more testing and development are required in order to fully discover its true potential and applications.

4.8 References

[4.1] Withers P. J. and Bhadeshia H. K. D. H., "Residual Stress – II: Nature and Origins", *Mater Sci Technol*, Vol. 17, 2001, pp. 366-375.

[4.2] Borland D. W., "Residual Stress Measurement – "Methods, Limitations and Significance", *Quality Ctrl Assurance Adv Surface Engng*, Inst of Materials, 1997, pp. 113-125.

[4.3] Knight M. J., Brennan F. P. and Dover W. D., "Fatigue Improvement of Threaded Connections by Cold Rolling", *J Strain Analysis Engng Design*, 2005, pp. 83-93.

[4.4] Knight M. J., Brennan F. P. and Dover W. D., "Controlled Failure Design of Drillstring Threaded Connections", *Fat Fract Engng Mater Struct*, 2003, pp. 1081-1090.

[4.5] Misumi M., Ohhashi T. and Ohkubo M., "Effect of Shot-Peening on Surface Crack Propagation in Plane Bending Fatigue", *Advances in Surface Treatment*, Vol. 3, 1986, pp. 55-74.

[4.6] Won J. P., Sun C. H. Kand Y. L., Sung H. P. and Hwa S. H., "The Effect of Compressive Residual Stress on the Fatigue Characteristics of Al6061", *Key Engng Mater*, Vol. 324-325 II, 2006, pp. 1181-1184.

[4.7] Hammersley G., Hackel L. A. and Harris F., "Surface Prestressing to Improve Fatigue Strength of Components by Laser Shot Peening", *Optics and Laser Engng*, Vol. 34, No. 4-6, 2000, pp. 327-337.

[4.8] Brennan F. P., Ngiam S. S. and Lee C. W., "An Experimental and Analytical Study of Fatigue Crack Shape Control by Cold Working", submitted to *Engng Fract Mech*, November, 2006.

[4.9] Han S. K., "Fatigue & Fracture Mechanics Analysis of Components Containing Residual Stress Fields", Ph.D. Thesis, University of London, 2002.

[4.10] Ngiam S. S. and Brennan F. P., "Crack Shape Control using Cold Rolling", In: *Proc Int Conf Fat Crack Paths*, Parma, 2003.

[4.11] Newman J. C. Jr. and Raju I. S., "Empirical Stress-Intensity Factor Equation for the Surface Crack", *Engng Fract Mech,* Vol. 15, No. 1-2, 1981, pp. 185-192.

[4.12] Knight M. J., "Reliable Operation of Drillstring Threaded Connections", Ph.D. Thesis, University of London, 2002.

[4.13] Ward A. P. and Parish H. E., "Choice of Fail Safe and Safe Life Fatigue Philosophies in Aircraft Design", In: *Proc Conf Safety and Failure of Components*, Inst Mech Eng, Vol. 184, Part 3B, 1969, p. 238-246.

[4.14] Dover W. D., Brennan F. P. and Etube L. S., "Structural Integrity Monitoring using Alternating Current Field Measurements", In: *Proc Structural Integrity in the 21st Century-The Lifetime of Plant, Structures and Components: Evaluation, Design, Extension and Management*, EMAS, 2000, pp. 307-315.

[4.15] British Standards Institute, "BS EN 10025:2004 – Hot Rolled Products of Non-Alloy Structural Steels", British Standards Institute, 2004.

[4.16] Peterson R. E., "Stress Concentration Factors – 2nd Edition", Wiley-InterScience Publication, ISBN 0471538493, 1997.

[4.17] Hibbert, Karlson and Sorenson Inc., *ABAQUS* User Guide Manual, v5.6, 1996.

[4.18] Brennan F. P. and Ngiam S. S., "Fatigue Crack Shape Control under Bending by Cold Working", In: *Proc Int Conf Fat Crack Paths*, Parma, 2006.

[4.19] Technical Software Consultants Ltd., "ACPD Crack Microgauge – Model U8 User Manual", Technical Software Consultants Ltd., Milton Keynes, UK, 1991.

[4.20] Gough H. J. and Wood W. A., "A New Attack upon the Problem of Fatigue of Metals, Using X-Ray Methods of Precision", In: *Proc Royal Soc London, Series A, Mathematical and Physical Sciences*, The Royal Society, 1936, pp. 510-539.

[4.21] Ishihara S. and McEvily A. J., "A Coaxing Effect in the Small Fatigue Crack Growth Regime", *Scripta Materilia*, Vol. 40, No. 5, 1999, pp. 617-622.

[4.22] Dover W.D. and Collins R., "Recent Advances in the Detection and Sizing of Cracks Using Alternating Current Field Measurements (A.C.F.M.)", *British J NDT*, Vol. 22, 1980, pp. 291-295.

[4.23] Shen G. and Glinka G., "Weight Functions for a Semi-Elliptical Crack in a Finite Thickness Plate", *Theore Applied Fract Mech*, Vol. 15, No. 3, 1991, pp. 247-255.

[4.24] Shen G. and Glinka G., "Weight Function for the Surface Point of Semi-Elliptical Surface Crack in a Finite-Thickness Plate", *Engng Fract Mech*, Vol. 40, No. 1, 1991, pp. 167-176.

CHAPTER 5

5.0 Fatigue Crack Shape Control Using Stitch Shot Peening

5.1 Introduction

The preceding Chapter has addressed the importance on the knowledge of fatigue crack shape evolution behaviour and its influence on fatigue crack growth in structural components. The experimental results reported have clearly demonstrated the feasibility of preferential cold working in controlling crack shape. Building on the success of the previous experimental study, a more quantitative experimental approach has been undertaken to better understand fatigue crack shape behaviour in the presence of residual stress fields and to maximise the potential of the preferential cold working technique. Based on the study reported in Chapter 4, a similar technique termed *stitch shot peening* has been introduced to further implement the preferential cold working concept.

Effects of shot peening on the fatigue strength of materials have been reported in many studies [5.1-5.5]. However, most of the work done to date on the effect of shot peening in fatigue has failed to address the important aspect of fatigue crack shape evolution and crack growth. In addition, little information can be found on the correlation between surface crack shape evolution behaviour in residual stress fields. One of the reasons for this may be that most of the studies conducted in the past have concentrated on observing one dimensional cracks in simple specimens (e.g. small hour-glass and compact tension specimens) which are not representative of many engineering components. Furthermore, most attention has been given to cracks initiating and growing in residual stress fields but few have studied the behaviour of cracks propagating "into" a cold worked region. The aim of the work described in this chapter is to achieve a better understanding of the fatigue crack shape evolution in shot peened components. Since the effective SIF range of a crack propagating through a cold worked region is known to be dependent on the residual stresses, the stress arising from shot peening and its relaxation behaviour were also investigated. Knowledge of these crucial characteristics is of immense importance in generating accurate SIF solutions.

This chapter presents the experimental fatigue testing programme of stitch shot peened specimens. Firstly, in order to demonstrate the practicality of stitch shot peening, the technique

will be compared to the stitch cold rolling technique. Specimen design and shot peening parameters are also presented. Experimental results are reported and a detailed discussion is presented on the data obtained. The experimental study reported here enabled the development of a fracture mechanics-based fatigue crack growth prediction model, which will be described in Chapter 6.

5.2 Stitch Cold Rolling versus Stitch Shot Peening

Even though stitch cold rolling had been proven to be an effective method in controlling fatigue crack shape, further development is needed as the intrinsic characteristics of the current cold rolling process have several drawbacks. Table 5.1 below tabulates the pros and cons of stitch cold rolling and the newly proposed stitch shot peening technique. It is noteworthy that the advantages and disadvantages presented are for the application of the stitch cold working technique in the present study, and might not apply to the conventional cold rolling and shot peening processes.

Stitch Cold Rolling Cold Rolling	Stitch Shot Peening
Advantages: • Relatively cheap compared to other surface treatment methods • Simple to employ • Does not involve special training or complicated equipments • Large deformation can be achieved Disadvantages: • Process is highly localised. Larger rolling area is possible but requires enormous rolling pressure • Difficult in-situ residual stress measurement on the processed surface • Introduction of residual stress is not completely uniform	Advantages: • Surface residual stress distribution is widely claimed to be uniform • Can be applied to complex geometries • Ability to cover a large surface area • Residual stress measurement on the processed surface is possible Disadvantages: • Relatively expensive • Increase in surface roughness • Requires highly trained operator • Involves specialised equipments and facilities • "Re-peen" following fatigue crack initiation is not practical if process is not performed in-house

Table 5.1: Comparison of the stitch cold rolling and stitch shot peening technique

The stitch cold rolling technique adopted is a highly localised process and complete uniformity (with respect to the distribution on the surface) of the induced residual stress cannot be assured.

Knight et al [5.6] reported large variations in residual stress level around the circumference of multi-pass stitch cold rolled drillstrings. They also showed that multi-pass stitch rolling does not significantly increase the residual stress magnitude but does make a more uniform residual stress distribution. Since one of the main objectives of the present experimental study is to monitor the characteristics of residual stress fields under cyclic loading, the ability to carry out reliable in-situ residual stress measurement is a prerequisite.

Shot peening is widely considered to be a highly-controllable process and its ability to cover a large surface area means that it is possible to mount a residual stress measuring sensor or probe onto the processed surface. The employment of the stitch shot peening technique in the current fatigue testing programme did have its disadvantages but they were considered to be surmountable. Following a thorough assessment of both techniques, it was decided that the advantageous features of shot peening have made stitch shot peening a more practical method in the investigation of fatigue crack shape behaviour under the influence of residual stresses as well as the study of residual stress relaxation under cyclic loading.

5.3 Experimental Test Details

5.3.1 Test Specimens

The study was carried out on specimens fabricated from BS EN 10025 Grade S275JR, a mild steel with a yield circa 275MPa [5.7]. The mild steel plates supplied were flame-cut from a cold rolled wide sheet. A request to keep the rolling direction constant for all the plates was made to the steel supplier. This precautionary step is very important in cancelling out the factor of material anisotropy (if any) induced by the cold rolling process during the production of the material. Fig. 5.1 below shows a machined specimen together with its rolling direction, which is along the length of the specimen.

All the specimens were machined on a high precision CNC (Computer Numerical Control) milling machine. A total of six tensile specimens were used in this study. Five specimens were assigned for the study of fatigue crack shape evolution while one was used for the investigation of residual stress relaxation behaviour. The machined test pieces had the shape of a typical hourglass specimen with a rectangular cross section. The test specimens were 1m in length and the middle section had a width of 150mm and thickness of 20mm. The detailed dimensions of the specimens can be found in Appendix H1. A semi-elliptical machined-notch of 18mm in width and 2mm in depth was introduced into the centre of all the specimens to encourage the growth of a surface crack.

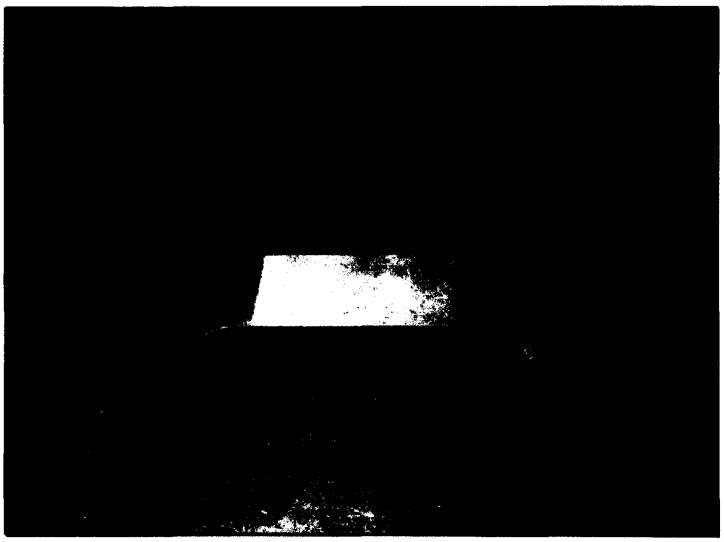

Figure 5.1: BS EN 10025 Grade S275JR test specimen

In order to ensure a uniform stress distribution in the middle section, the specimens were designed according to BS EN 1002-1:2001 [5.8]. All the dimensions satisfied the criteria described in the standard, with the exception of the gauge length. This is due to the reason that the overall length of the specimens was confined to the available daylight on the fatigue test machine used. Design optimisation and stress analysis was performed using the FE analysis software, ABAQUS [5.9]. Fig. 5.2 below shows an example of the quarter-symmetry 3D FE model of the test specimen.

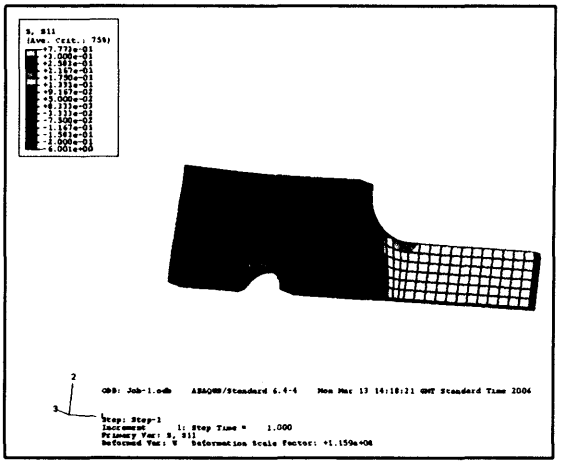

Figure 5.2: A quarter-symmetry 3D finite element mesh of the test specimens

5.3.2 Stitch Shot Peening Parameters

Table 5.2 below summarises the shot peening parameters and some examples of the stitch peened specimens are illustrated in Appendix H2. The shot peening process was provided by

Metal Improvement Company (MIC- Chester Division) and in order to fit into MIC shot peening facility's tight schedule, the shot peening work was carried out in two batches, with Test SP5 and SP6 being the first specimens to be shot peened. Tests SP2 to SP5 were shot peened with varying non-shot peened length to simulate failures with different crack aspect ratio. The non-shot peened length and the corresponding maximum possible/achievable through thickness crack aspect ratio of the stitch shot peened specimens are illustrated in Table 5.2. The edges of the specimens were shot peened to prevent fatigue crack initiation while the back of the specimens were shot peened to avoid distortion of the specimens during peening. However, the shot peened areas at the back of the specimens were kept to a minimum so that they would not interfere with the fatigue crack growth once the crack propagated deep into the plates. Cast iron steel shots were used to minimise surface roughness and 200% peening coverage was adopted to ensure residual stress distribution uniformity and to give maximum compressive residual stress near the yield point of the material.

Specimen	Shot Peening Intensity (Almen Intensity)	Coverage (%)	Shot Media	Non-shot peened Length (mm)	Max *a/c*
Test SP1	-	-	-	-	-
Test SP2	12C-16C	200	Cast Iron S930	20	2.00
Test SP3	12C-16C	200	Cast Iron S930	25	1.60
Test SP4	12C-16C	200	Cast Iron S930	35	1.14
Test SP5	12C-16C	200	Cast Iron S930	40	1.00
	12A-16A	200	Cast Iron S230		
Test SP6	3C-6C	200	Cast Iron S230	-	-
	12C-16C	200	Cast Iron S930		

Table 5.2: Summary of stitch shot peening parameters

Tests SP1 to SP5 were used for fatigue cracking while Test SP6 was used for the residual stress relaxation study. It must be noted that the naming of the specimens does not reflect the order in which the fatigue tests were carried out. Test SP1 was initially assigned to be shot peened with a non-shot peened length of 30mm but due to unforeseen technical problems at the facility, the shot peening process was unable to be carried out and therefore it was used as a control specimen for comparison purposes. An example of a stitch shot peened specimen is shown in Fig. 5.3 below. Test SP6 was shot peened with three different intensity bands so that the relaxation of residual stress with different initial magnitudes could be investigated. This also maximised the amount of

residual stress data that could be collected during the test. The three different shot peened bands of Test SP6 are illustrated in Fig. 5.4 below.

Figure 5.3: An example of a stitch shot peened test specimen

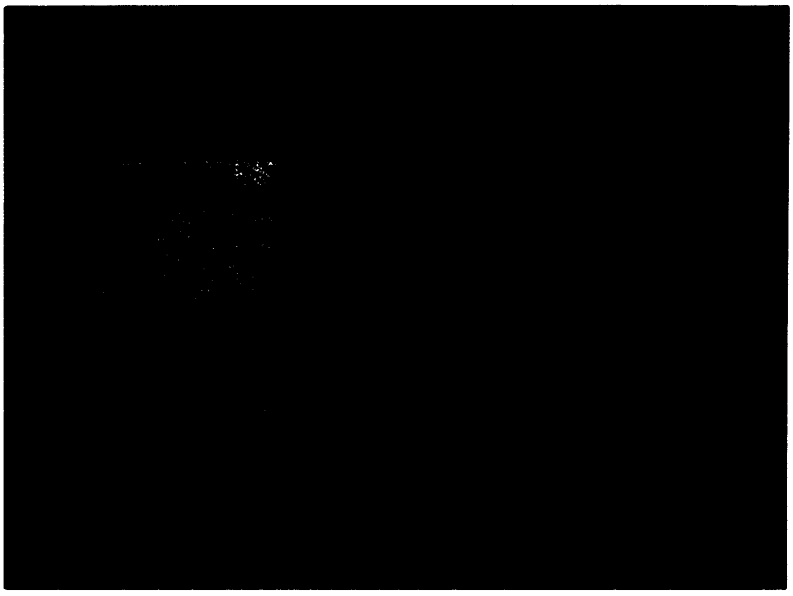

Figure 5.4: Shot peened bands on Test SP6

5.3.3 Fatigue Test Set-up

The previous chapter clearly demonstrated that a leak-before-break failure is more likely to occur in a component subjected to axial tension load compared to pure bending. In order to encourage

high crack aspect ratio failures, the fatigue tests were performed under axial tension. All the tests were conducted in ambient air on an Instron 1000kN servo-hydraulic fatigue test machine under constant amplitude loading at a nominal stress range of 200MPa, a stress ratio of $R \approx 0$ and a frequency of 2Hz. Crack sizing and monitoring was by periodic ACPD inspections along the width of the specimen, using a U9 Crack Microgauge [5.10].

The fatigue test set-up is shown in Fig. 5.5 below. As can be seen from the figure, a pin-and-clevis configuration was adopted for the end fitting arrangement to minimise possible misalignment as well as bending. The axiality of the test set-up was checked by strain gauging both sides of the specimen (Fig. 5.5b below) and the experimental strain readings during static loading were compared with the corresponding theoretical values (Fig. 5.6). As can be seen from the figure, there is virtually no difference between the theoretical and experimental strain readings, confirming the axiality of the test set-up.

(a) (b)

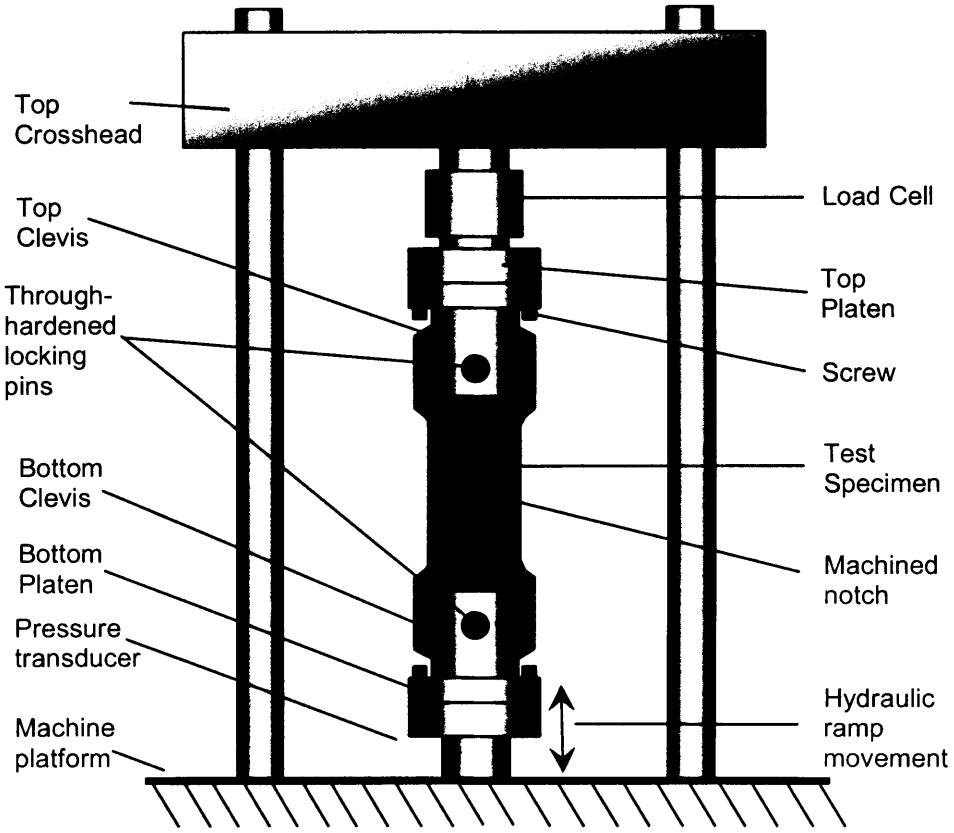

(c) 2D view of fatigue test set-up

Figure 5.5: Fatigue test set-up on an Instron 1000kN test machine

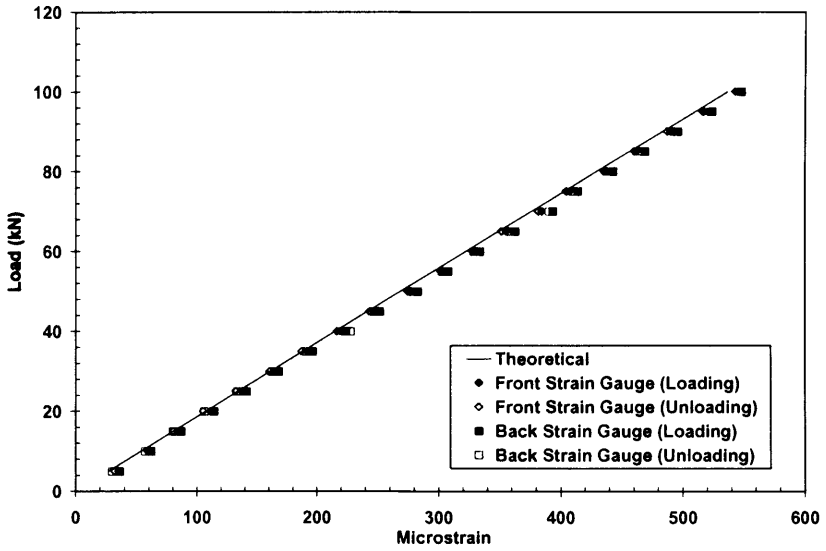

Figure 5.6: Comparison between theoretical and experimental strain data

Knowing that residual stress relaxation occurs to some extent under cyclic loading, it is important to ascertain that there was a significant magnitude of residual stress to influence the fatigue crack growth following crack initiation. Therefore, Tests SP1 to SP4 were fatigue pre-cracked under pure bending prior to shot peening and the four point bending set-up can be seen in Fig. 5.7 below. Another advantage of this procedure is that the initial magnitude of the surface residual stress could be assumed to be identical for all the stitch shot peened specimens before being tested under axial tension. Test SP5, which was the first test to be completed, was not fatigue pre-cracked as it was initially thought that the applied stress range would be sufficient for crack initiation. Further fatigue crack initiation details for Test SP5 will be discussed in Section 5.3.5.

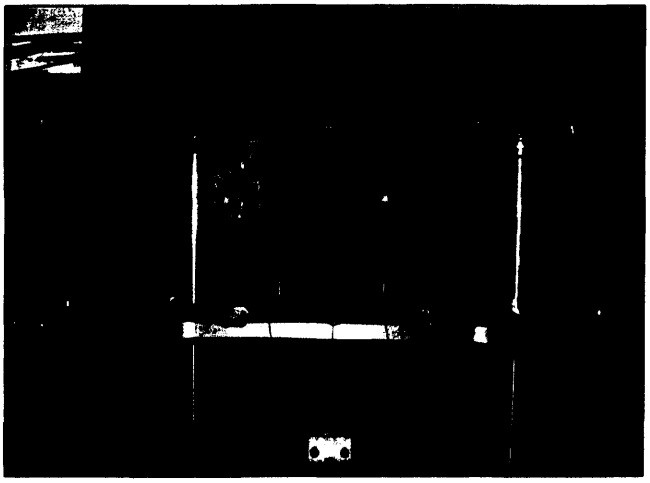

Figure 5.7: Fatigue pre-cracking of a test specimen

5.3.4 Residual Stress Monitoring Using the ICHD Technique

In order to develop an in-depth understanding of the influence of surface residual stresses on surface crack shape evolution, their characteristics throughout the course of the fatigue tests must be closely monitored. Examples of residual stress measurement techniques have been reviewed in Chapter 1 and the respective advantages were also compared. After careful consideration, it was decided that ICHD is the most suitable method in monitoring the surface residual stress relaxation behaviour in the current study. After the set-up of Test SP6 on the test machine, initial hole-drilling measurements were conducted before the commencement of cyclic loading. The specimen was then subjected to constant amplitude loading to cause gradual residual stress decay. A nominal stress range of 200MPa, stress ratio of $R \approx 0$ and a cycling frequency of 2Hz were used. Cyclic loading was then stopped following the prescribed number of fatigue loading cycles so that in-situ ICHD measurement could be carried out. This procedure continued until the specimen was exposed to a large number of fatigue cycles.

ICHD measurement was performed according to ASTM standard E837 [5.11] and Vishay Micro-Measurements Group (VMG) Inc. Technical Note TN-503-6 [5.12]. Strain gauge rosettes manufactured by VMG Inc., CEA-06-062UL-120 [5.13] with a rosette diameter of 5.13mm were used. The strain gauge rosette details can be found in Appendix H3. It has to be pointed out that the hole-drilling technique was particularly intricate on shot peened surfaces due to the increase in surface roughness and hence special care was taken during surface preparation. Before the installation of the strain gauge, it is common practice to remove the peaks of the dimples created by peening using a fine-grade Emery paper, as illustrated in Fig. 5.8 below. There is currently no standard regarding this procedure but a consistent application of this method on shot peened surfaces has been reported to yield good measurement results [5.14-5.16].

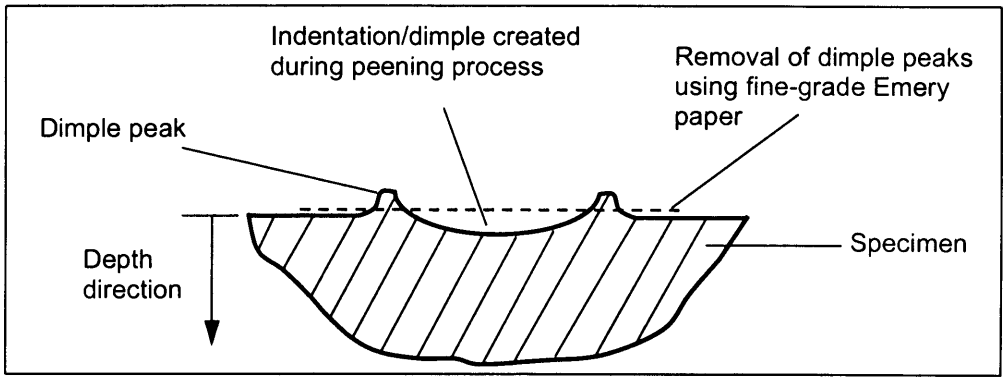

Figure 5.8: Removal of dimple peaks on shot peened surfaces

The holes were drilled incrementally using the RS-200 milling guide (Fig. 1.19) and high speed air turbine drill and the strain responses were acquired using the Vishay P-3500 [5.17] strain indicator connected to a multi-channel switching unit, as shown in Fig. 5.9 below. Drilling at incremental depth and the corresponding strain relief measurements enabled the residual stress distribution through the depth of the specimens to be determined. Fig. 5.10 shows the residual stress measurement performed on Test SP6 whilst in the fatigue test machine. Both the strain gauge installation and hole-drilling procedures were kept consistent in order to avoid causing discrepancies. The strain relaxation data recorded were analysed using the Equivalent Uniform Stress Method and the Integral Method, which will be further discussed in Chapter 6.

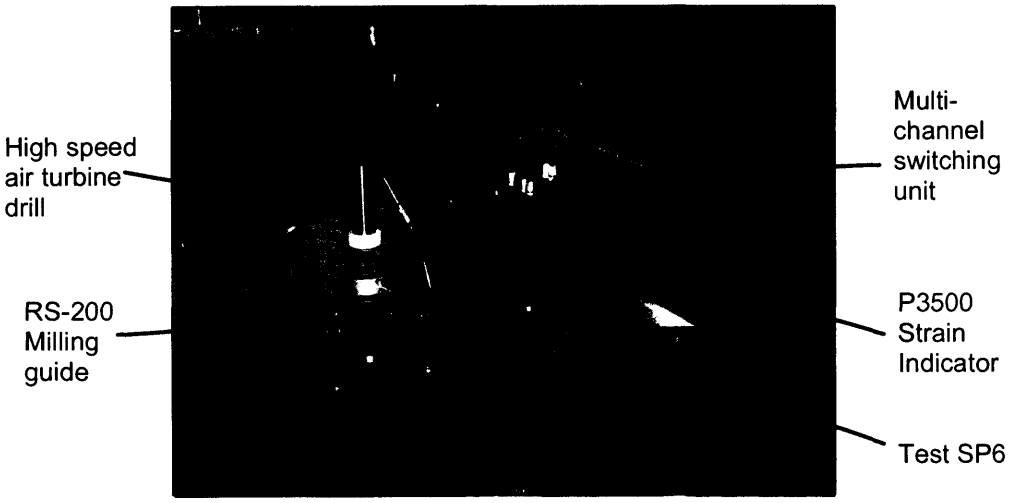

Figure 5.9: An example of the ICHD set-up

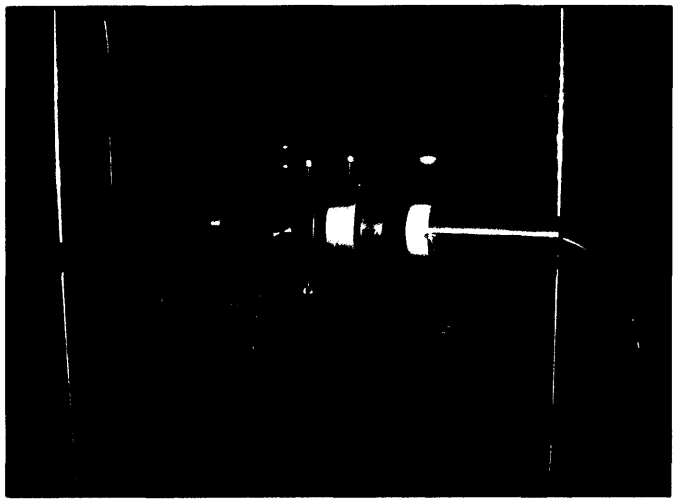

Figure 5.10: In-situ residual stress monitoring on Test SP6

5.4 Fatigue Test Results

5.4.1 Fatigue Crack Growth Data

The fatigue pre-cracking data for Tests SP1 to SP4 are tabulated in Table 5.3 and examples of fatigue crack initiation data and crack shape evolution are shown in Figs. 5.11 and 5.12 below respectively. Table 5.4 below summarises the fatigue test results for all the tests. It is worth mentioning that all the crack depth data plotted and tabulated in the following sections included the depth of the starter notch. The fatigue crack initiation lives under bending for Tests SP1 to SP4 were very similar. This is not unreasonable since the crack initiation mechanism in the non-

shot peened regions is free from the influence of the surface compressive residual zone. Tests SP1 to SP4 were fatigue pre-cracked to a certain crack depth so that the corresponding SIF range under axial tension would be above the threshold SIF of the material, which was obtained from Reference 5.18.

Specimen	Nominal Stress Range (MPa)	No. of Cycles to Crack Initiation	Total Pre-cracking Cycles	Crack Depth (mm)	Crack Aspect Ratio, *a/c*
Test SP1	225	250,000	530,000	4.20	0.24
Test SP2	225	294,000	654,600	3.75	0.38
Test SP3	225	234,341	610,940	4.20	0.42
Test SP4	225	270,000	485,000	3.95	0.34

Table 5.3: Summary of fatigue pre-cracking data

Specimen	Nominal Stress Range (MPa)	Crack Propagation Life	Total Fatigue Life	Non-shot peened Length (mm)	Final Crack Aspect Ratio, *a/c*
Test SP1	200	78,000	611,000	-	0.47
Test SP2	200	205,500	860,100	20	0.85
Test SP3	200	195,600	806,500	25	0.82
Test SP4	200	145,500	630,500	35	0.60
Test SP5	200 (Bending, no pre-cracking)	1,005,000	12,000,000	40	0.36

Table 5.4: Summary of fatigue test results

As previously stated, Test SP5 was the first test to be completed and it was initially thought that the introduction of a starter notch would be sufficient for crack initiation to take place under axial tension without fatigue pre-cracking. However, no crack initiation was detected after approximately 9.5 million fatigue cycles. In addition, a fatigue crack was found to have initiated at the upper locking-pin-hole of the specimen due to fretting fatigue and resulted the test being unable to be further tested in axial tension. The specimen was therefore tested under pure bending. It is important to note that Figs. 5.13 to 5.17 below only show crack propagation lives following an initial ≈2mm deep precrack. The total life is the sum of the initiation and propagation lives. Fig. 5.13 below shows the fatigue crack growth data for Tests SP5 together with the

corresponding stress history. The nominal bending stress range applied to Test SP5 prior to crack initiation ranged from 200MPa to 250MPa. Fatigue crack initiation was detected after 700,000 fatigue cycles at a nominal stress range of 250MPa. The relatively high crack initiation life of Test SP5 is believed to be caused by the effect of coaxing. As can be seen from the figure, Test SP5 experienced approximately 1 million fatigue crack propagation cycles and a final crack depth of 16.3mm was recorded.

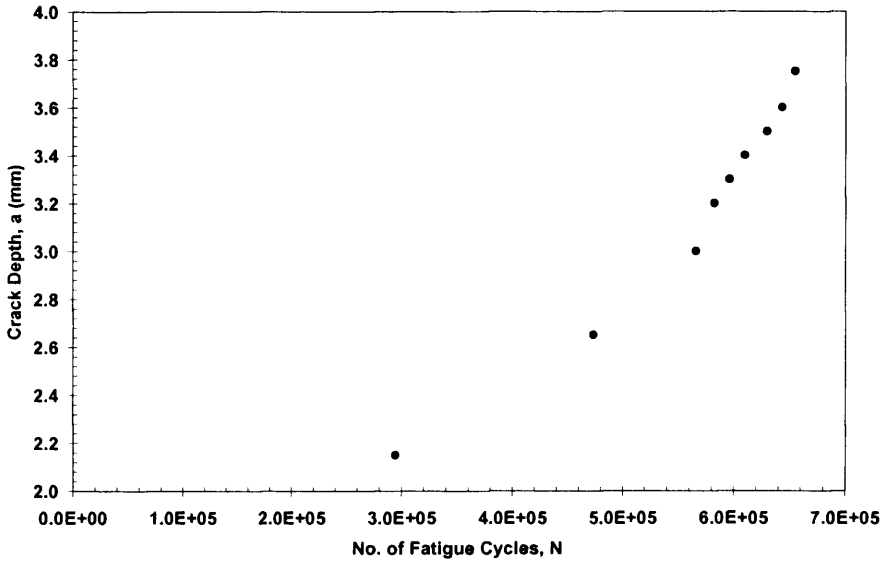

Figure 5.11: Crack initiation data for Test SP2 during fatigue pre-cracking

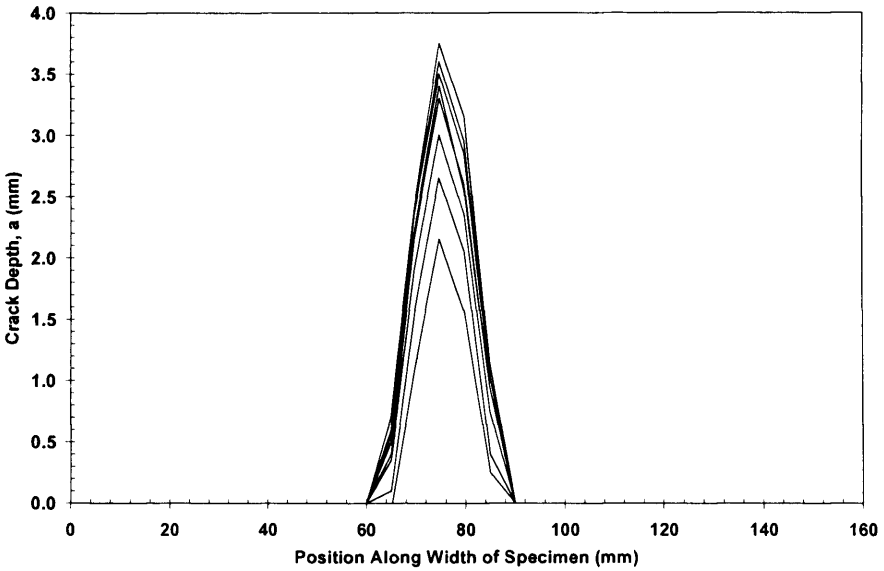

Figure 5.12: Crack shape evolution data for Test SP2 during fatigue pre-cracking

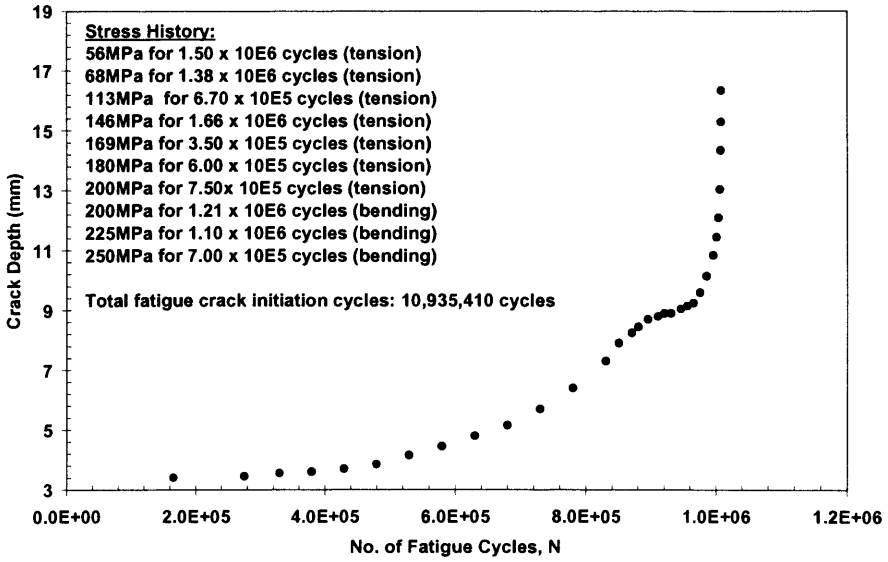

Figure 5.13: Fatigue crack growth data for Test SP5

Figs. 5.14 to 5.17 below show the fatigue crack growth data for Tests SP1 to SP4 respectively and all the crack growth results are compared in Fig. 5.18. All the stitch peened specimens had failed with a through thickness crack and the final crack aspect ratios are tabulated in Table 5.3 above. An example of the through thickness failure can be seen in Fig. 5.19. A significant improvement in the crack propagation life was observed for all the stitch shot peened specimens when compared to Test SP1. Test SP1 had a fatigue propagation life of 78,000 cycles and a final crack depth of approximately 18mm was recorded. Tests SP2, which had a non-shot peened length of 20mm recorded the highest fatigue propagation life of 205,500 cycles. Test SP3 (non-shot peened length = 25mm) and Test SP4 (non-shot peened length = 35mm) had crack propagation lives of 195,600 and 145,500 cycles respectively. In Tests SP1 to SP4, the specimen was considered to have failed once the ACPD technique was unable to measure the crack depth due to the fact that it had grown through thickness.

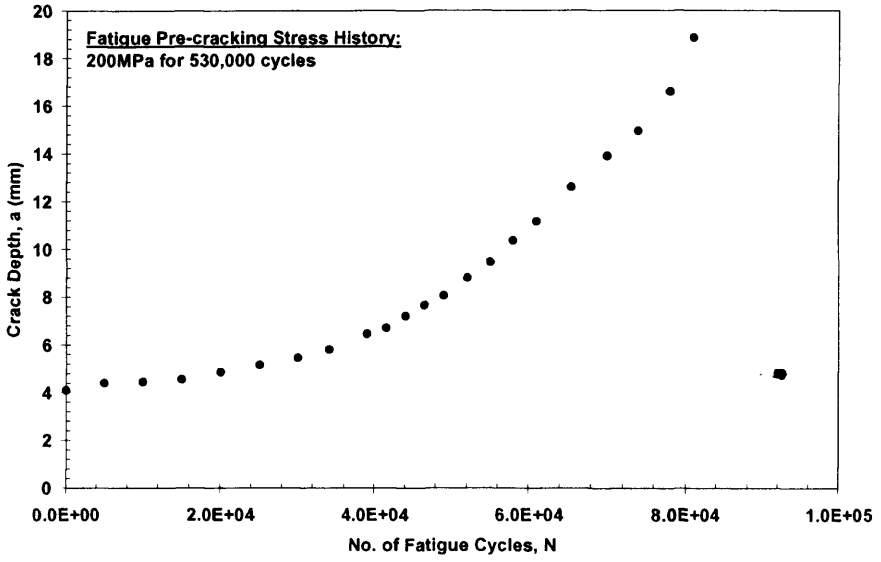

Figure 5.14: Fatigue crack growth data for Test SP1

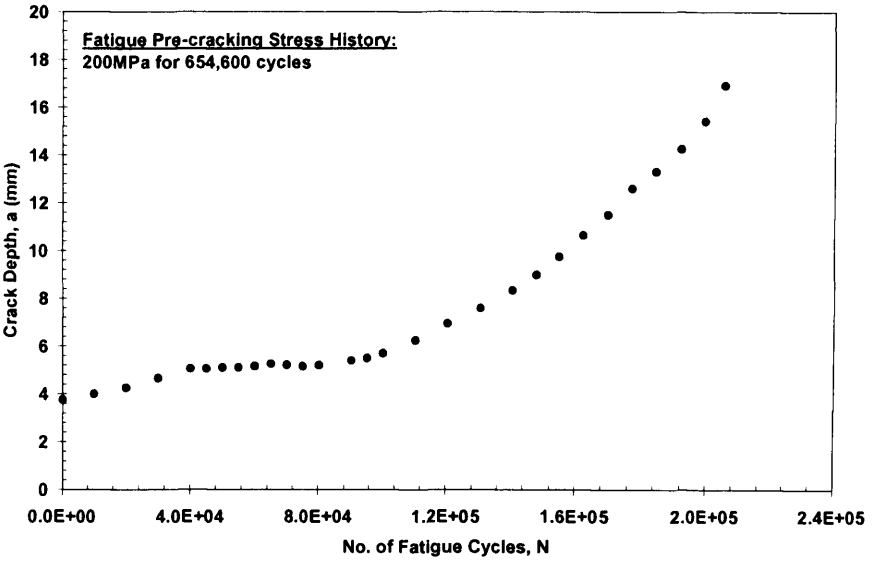

Figure 5.15: Fatigue crack growth data for Test SP2

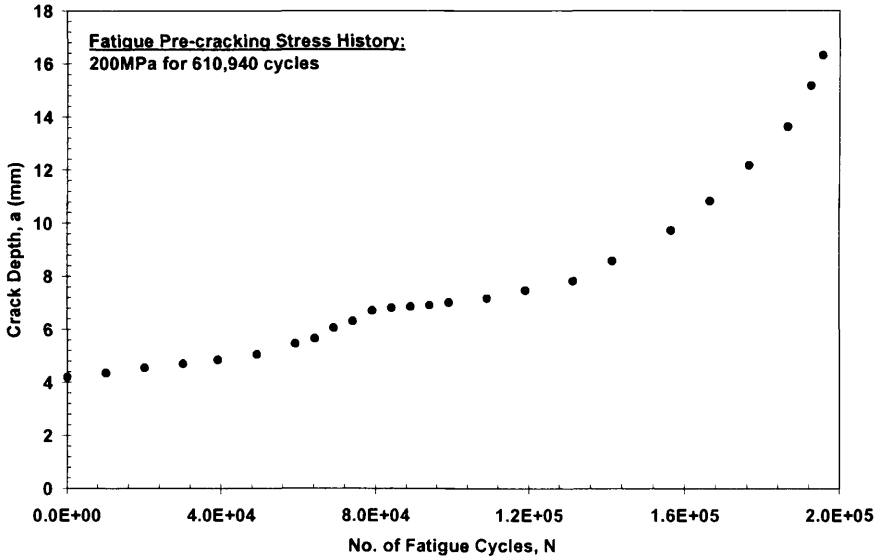

Figure 5.16: Fatigue crack growth data for Test SP3

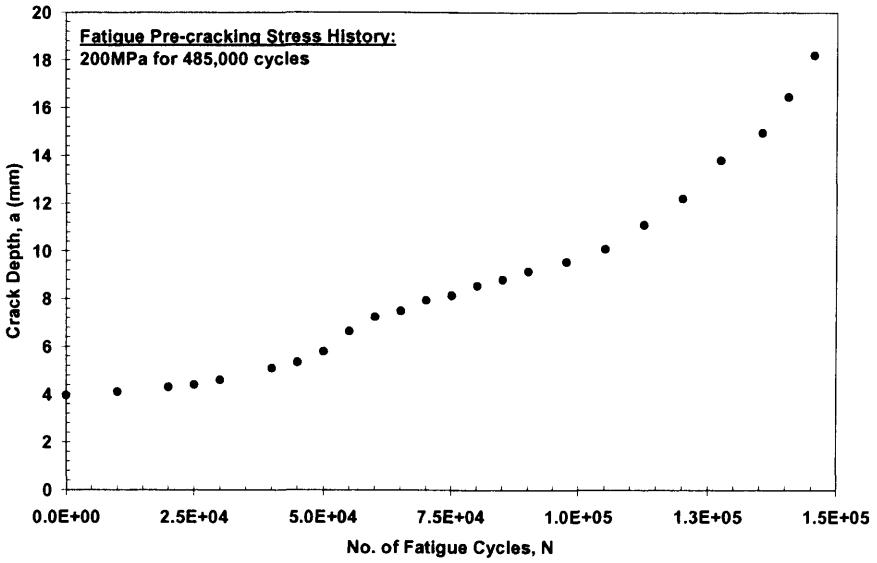

Figure 5.17: Fatigue crack growth data for Test SP4

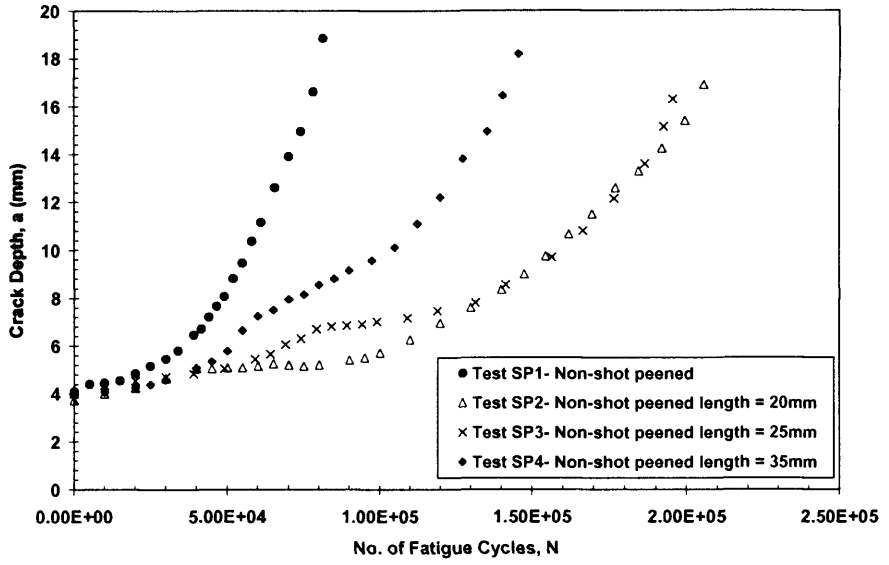

Figure 5.18: Comparison of fatigue crack growth data for Tests SP1 to SP4

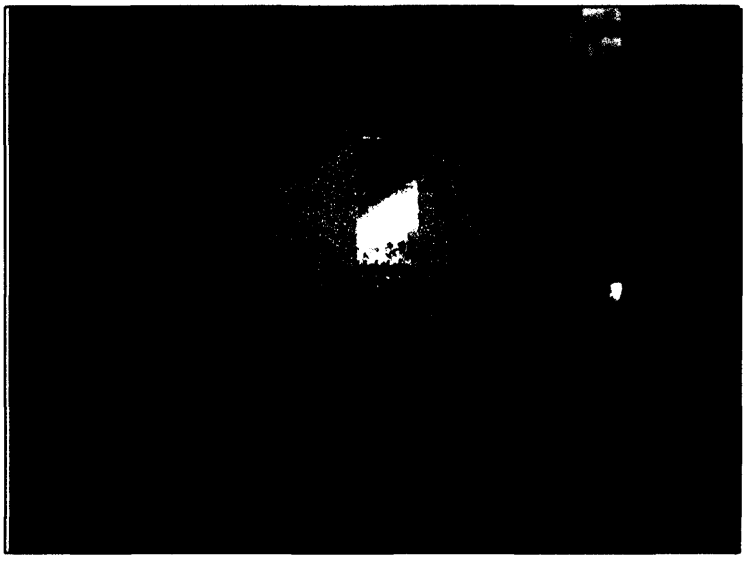

Figure 5.19: A through thickness crack in Test SP3

5.4.2 Crack Shape Evolution Data

For all the tests, periodic ACPD inspections were performed at 5mm intervals along the width of the specimens. The inspection rate was increased at the later stage of the crack growth so that the complete crack shape evolution behaviour could be established. Figs. 5.20 to 5.24 below illustrate the crack shape evolution for Tests SP1 to SP5 respectively. In all the tests, the introduction of the starter notch had encouraged the cracks to grow in a semi-elliptical manner but

again this is not evident in the plots as they are not plotted to scale. As can be seen from the figures, Tests SP1 to SP4 had deeper and shorter cracks when compared to Test SP5. This is expected since for a crack propagating through a section under bending, the SIF is greater at the crack surface point when compared to the value at the deepest point. Test SP5 failed with a crack aspect ratio of a/c = 0.36 while Tests SP1 to SP4 recorded final crack aspect ratios of a/c = 0.58, 0.85, 0.82 and 0.60 respectively.

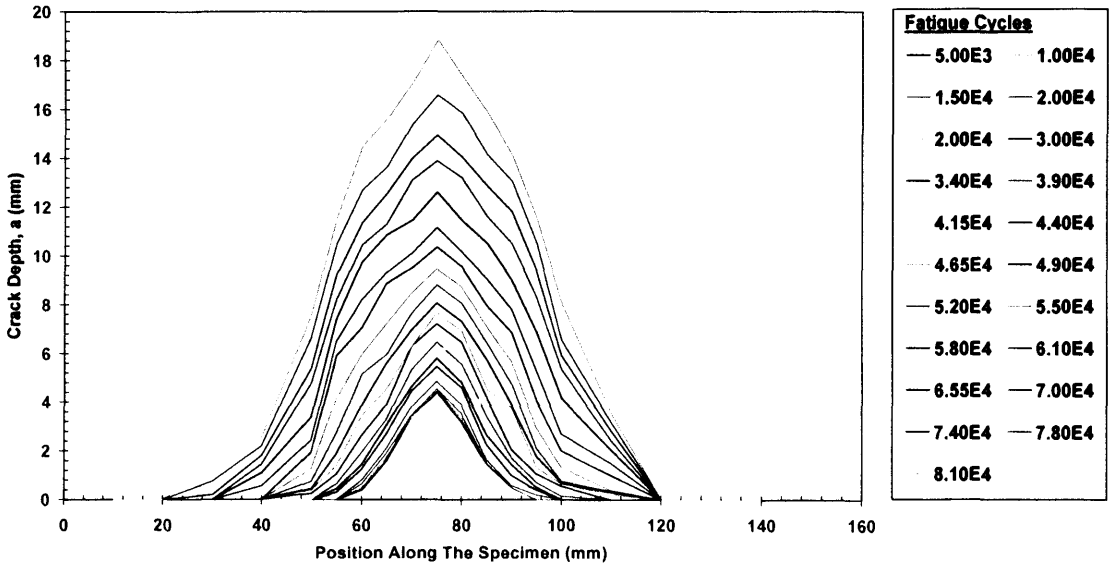

Figure 5.20: Crack shape evolution data for Test SP1

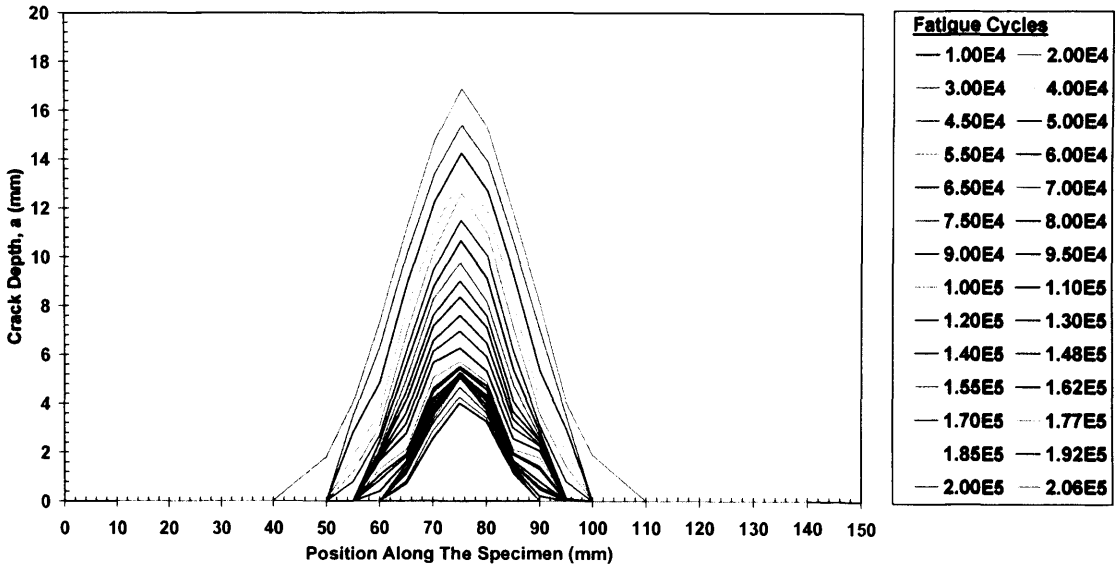

Figure 5.21: Crack shape evolution data for Test SP2

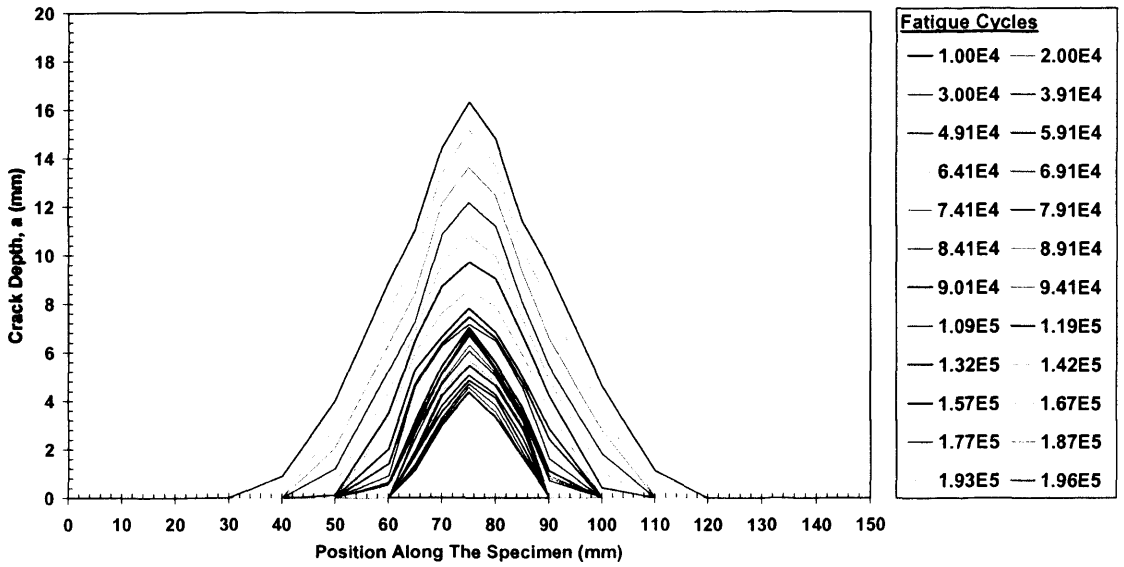

Figure 5.22: Crack shape evolution data for Test SP3

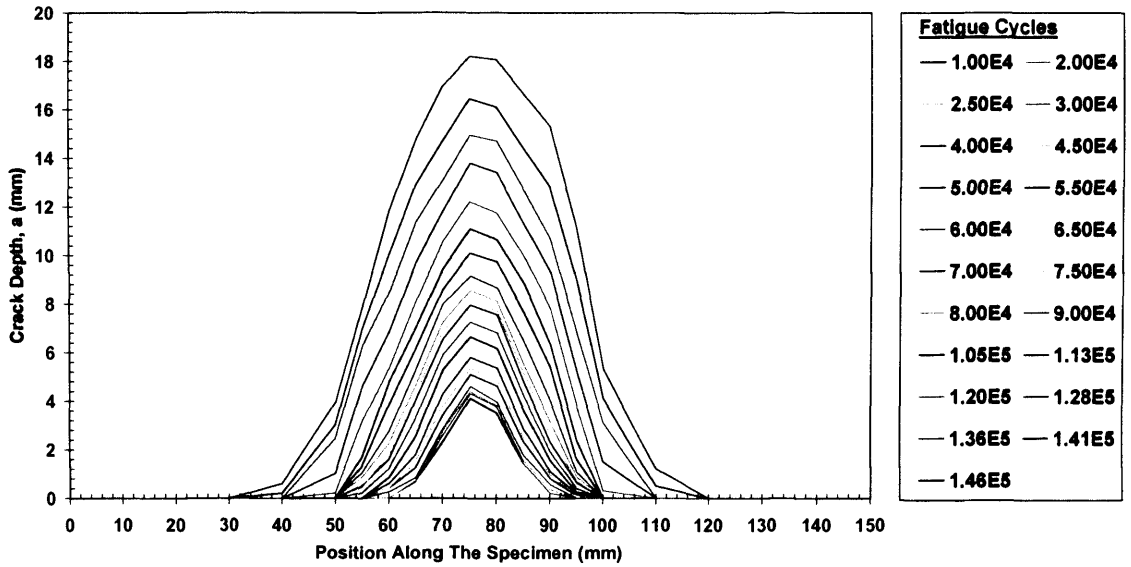

Figure 5.23: Crack shape evolution data for Test SP4

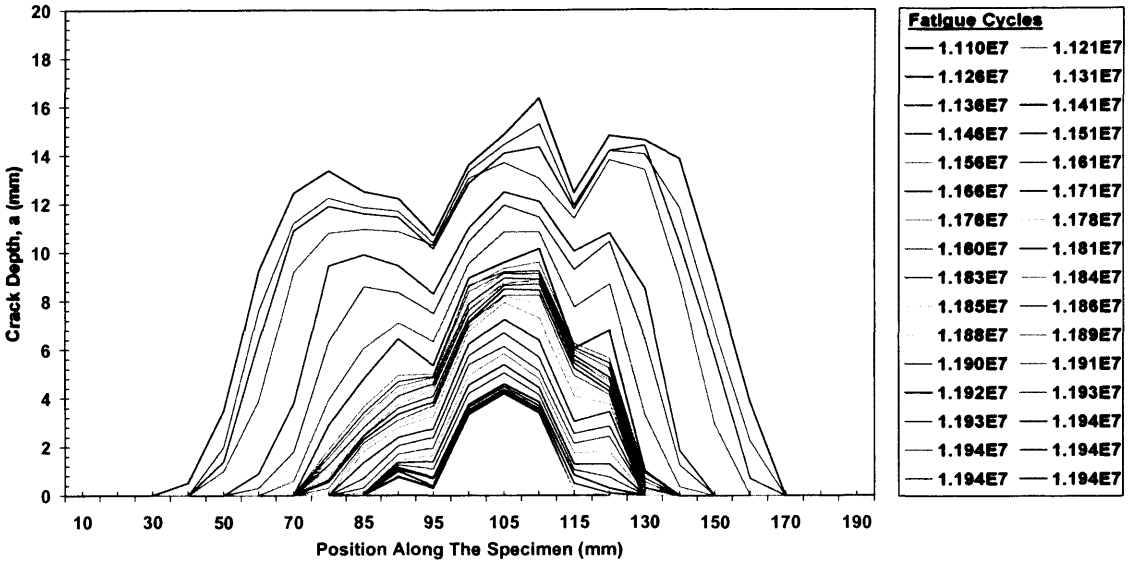

Figure 5.24: Crack shape evolution data for Test SP5

5.4.3 Fatigue Crack Surfaces

Following testing, the sectioned specimens were broken open by brittle fracture after immersion in liquid nitrogen so that fatigue crack surface examination could be carried out. Figs. 5.25a to d show the fracture surfaces of Tests SP1, SP2, SP3 and SP4 respectively while Fig. 5.25e shows the fracture surface of Test SP5, which was tested in pure bending. As can be seen from the figures, distinctive beachmarks can be observed in all the fracture surfaces with the exception of Test SP1, which was not shot peened. It must be noted that the beachmarks in some of the specimens can only be vaguely revealed in certain viewing angles even under a light source. Beachmarks were not intentionally introduced and are likely to have been caused by the different rates in crack propagation. The beachmarks observed have provided crucial information regarding the crack shape evolution behaviour.

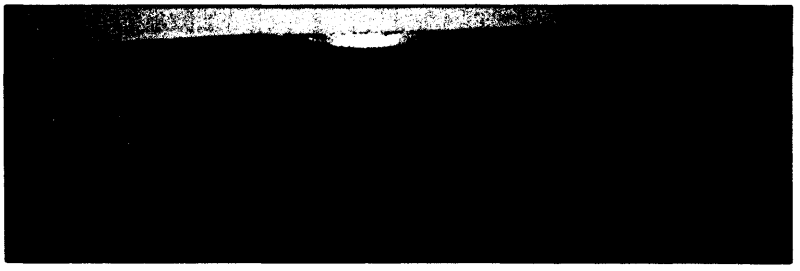

(a) Test SP1 (Control specimen)

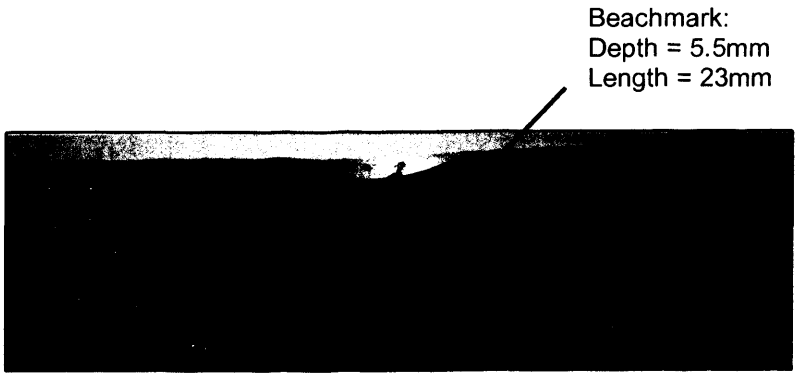

(b) Test SP2 (non-shot peened length = 20mm)

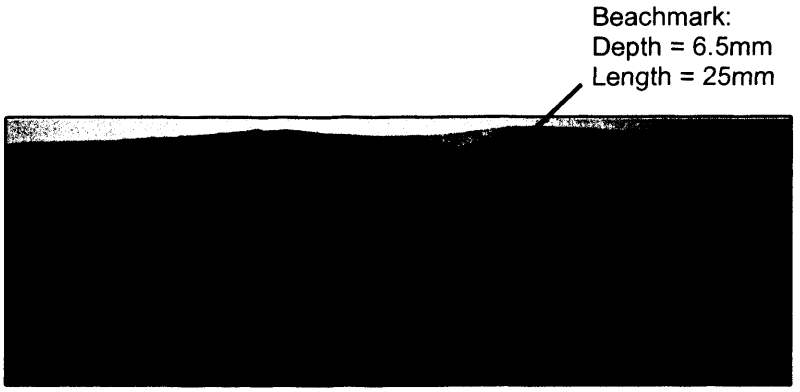

(c) Test SP3 (non-shot peened length = 25mm)

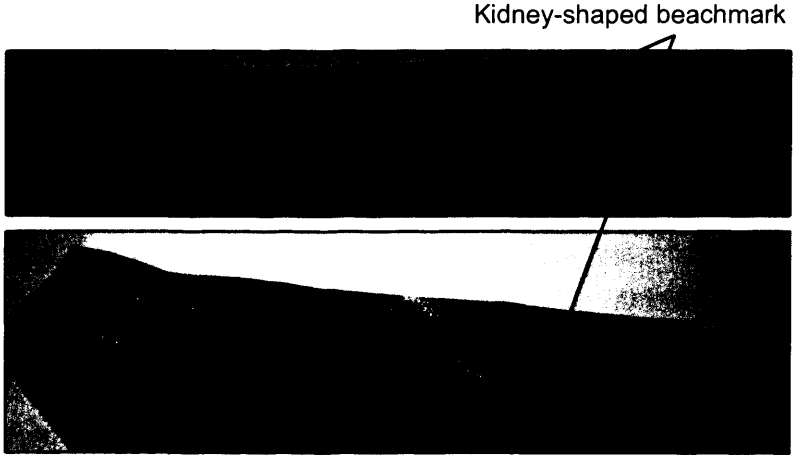

(d) Test SP4 (non-shot peened length = 35mm)

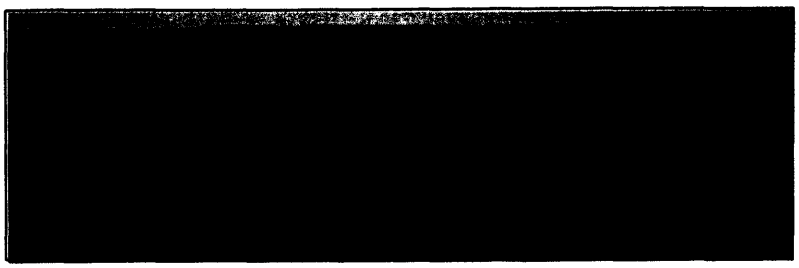

(e) Test SP5 (non-shot peened length = 40mm, under bending)

Figure 5.25: Fracture surfaces

5.5 Discussion of Fatigue Test Results

The practicality of the stitch shot peening technique in controlling the fatigue crack shape is evident in the test results. By comparing the fatigue test data of Test SP1 with Tests SP2 to SP4 in Table 5.3, it can be seen that the fatigue crack propagation lives of the stitch peened specimens have been significantly enhanced. An improvement in crack propagation life by a factor of up to 3 fold can be observed in Test SP2. In addition, fatigue crack retardation was observed in all stitch peened specimens.

Test SP2 recorded normal crack growth until the crack length extended to meet with the non-shot peened region. Crack retardation was then observed for the next 50,000 cycles and further fatigue cycling saw a recovery of crack growth in the depth direction. Test SP3 and SP4 clearly show unusual crack growth behaviour when the crack length equalled the non-shot peened length. However, the crack retardation observed is less severe compared to Test SP2. Similar to the stitch cold rolling technique, the surface compressive residual stress induced by shot peening had "pinned" the crack in the length direction, forcing growth in depth. All the specimens, except Test SP1, showed beachmarks on the fracture surfaces and these provided an insight into the crack shape evolution behaviour. For example in Fig. 5.25c, the labelled beackmark has a depth of 5.5mm and length of 22mm, which coincide with the dimensions of the crack in Test SP3 when crack retardation took place. The same can be observed in Tests SP2, SP3 and SP5 and the "kidney-shaped" crack behaviour can be vaguely seen in Test SP3. Hence, it is believed that the beachmarks are generated by the crack retardation effect.

In order to demonstrate the extent of the crack retardation observed, the normalised crack depth and length growth data for Tests SP1 and SP2 are compared in Fig. 5.26 below. In the graph, the crack depth is normalised with respect to the plate thickness (T) while the half crack length is normalised with respect to the plate half width (b). As can be seen from the figure, for most of the

fatigue cycles subjected to Test SP2, the crack length remained unchanged while the crack depth was constantly increasing. Test SP1, on the other hand, shows constant crack growth in both directions throughout the test. Perhaps the most striking feature in the graph is that at approximately 80,000 cycles, an increase in crack length had resulted in a resumption of crack depth growth in Test SP2. It is believed that subsequent fatigue cycling following the crack retardation had caused the compressive residual stress to decay, resulting in an increase in the effective SIF at the surface point and in turn crack length growth took place.

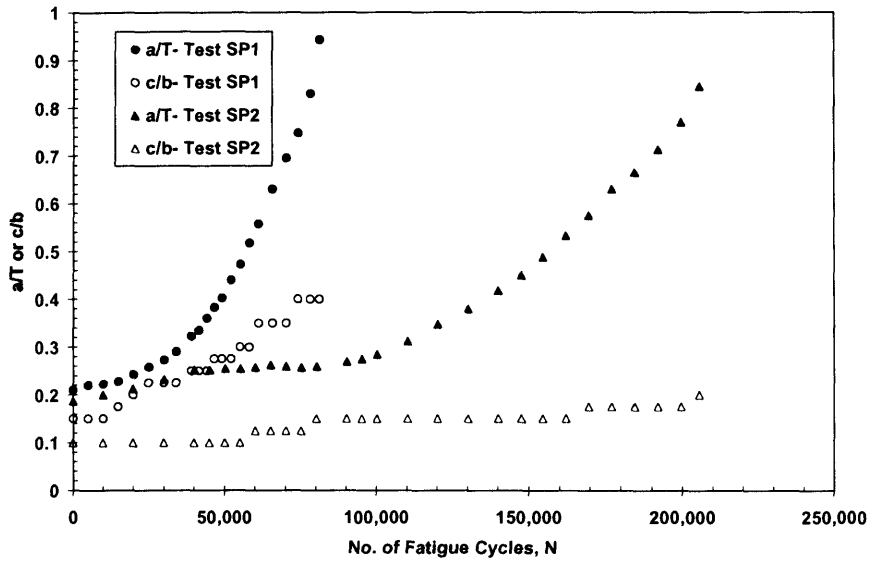

Figure 5.26: Comparison of crack depth and crack length growth for Tests SP1 and SP2

The crack retardation phenomena observed in the present study are less pronounced when compared to the test results obtained from the stitch cold rolled specimens but it must be noted that the stitch shot peened specimens were subjected to a much higher nominal stress range and the current tests were conducted in axial tension. The relatively high nominal stress range was adopted in order to cause residual stress relaxation (if any), since one of the main objectives of the present study was to investigate the effect of residual stress decay on fatigue crack shape evolution. In addition, medium-to-high-cycle fatigue tests were desired due to reasons of time and project resources.

Fig. 5.27 below shows the experimental crack aspect ratios for all the tests. For comparison purposes, the comparative SIF prediction for a surface crack under tension with starting a/c = 0.30 is included in the plot. The analytical work conducted on the fatigue crack growth prediction model will be discussed in Chapter 6. It can be seen that Tests SP2 to SP4 failed at a higher crack aspect ratio than Test SP1 and generally shorter non-shot peened lengths resulted in

higher aspect ratio. The comparable fatigue lives and crack aspect ratios of Tests SP2 and SP3 suggest that there may be an optimum configuration in the stitch peening parameters (e.g. non-shot peened length to thickness ratio) for a high aspect ratio leak before break crack to be achieved. All the experimental crack aspect ratios fall below the maximum possible values presented in Table 5.2. However, as illustrated in the figure below, Tests SP2 and SP3 had achieved higher aspect ratios than predicted, signifying the effectiveness of the stitch shot peening technique in promoting a high aspect ratio failure. Most remarkably, Test SP6 which was tested under bending shows comparable crack aspect ratio to Test SP1.

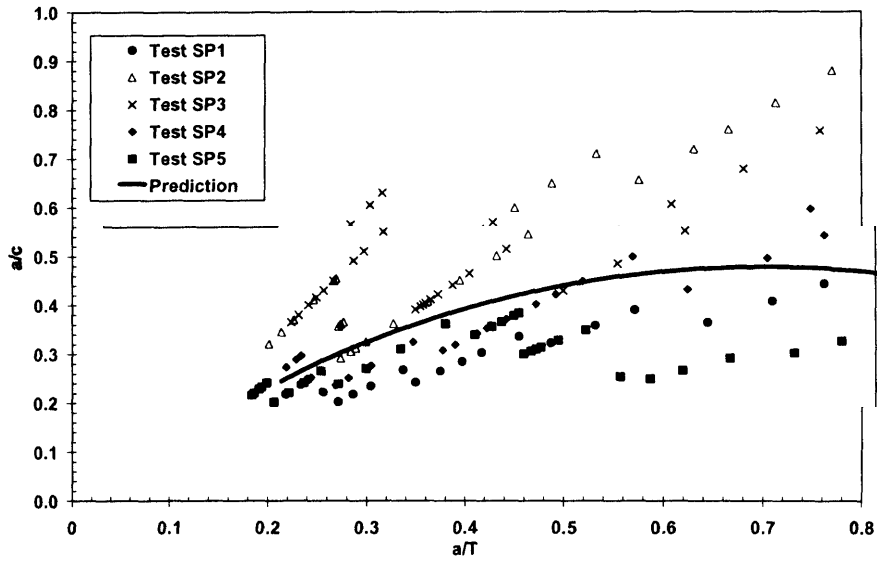

Figure 5.27: Comparison of crack aspect ratio evolution data

The results presented in the preceding sections clearly show that the crack sizing and monitoring data were much more consistent than those obtained in Chapter 4. The use of a more advanced crack sizing system, the U9 Crack Microgauge, had enabled high quality results to be recorded.

5.6 Summary

This chapter has presented details of the fatigue tests conducted on stitch shot peened specimens. The feasibility of the newly proposed stitch shot peening technique on controlling fatigue crack growth and crack shape evolution in mild steel plates was investigated. A total of six specimens were fatigue tested under different stitch peening parameters. The results obtained from the study have been presented in the form of initiation data, crack shape evolution curves, crack growth curves and crack aspect ratio evolution. The experimental results clearly show that stitch shot peening not only controlled the fatigue crack shape, but caused crack retardation. The

experimental results obtained from the tests described earlier have allowed the fatigue crack growth behaviour in compressive residual stress field to be characterised. The analysis of the fatigue test results and the residual stress measurement data will be discussed in Chapter 6.

5.7 References

[5.1] Bignonnet A., "Some Observations of the Effect of Shot Peening on Fretting Fatigue", In: *Fretting Fat*, Editors: Waterhouse R.W. and Lindley T. C., 1994, pp. 475-483.

[5.2] Farrahi G. H., Lebrun J. L. and Couratin D., "Effect of Shot Peening on Residual Stress and Fatigue Life of a Spring Steel", *Fat Fract Engng Mater Struct*, Vol. 18, No. 2, 1995, pp. 211-220.

[5.3] Ando L., Matsui K. and Ishigami H., "Study on Double Shot Peening and Fatigue Limit of Gear", *Key Engng Mater*, Vol. 183, No. 2, 2000, pp. 921-926.

[5.4] Park K. D. and Jun C.G., "The Effect of Compressive Residual Stresses of Two-Stage Shot Peening for Fatigue Strength of Spring Steel", In: *Proc Int Conf Offshore Polar Engng*, Vol. 12, 2002, pp. 220-223.

[5.5] Gao Y. K., Yao M., Shao P.G. and Zhao Y. H., "Another Mechanism for Fatigue Strength Improvement of Metallic Parts by Shot Peening", *J Mater Engng Performance*, Vol. 12, 2003, pp. 507-511.

[5.6] Knight M. J., Brennan F. P. and Dover W. D., "Fatigue Improvement of Threaded Connections by Cold Rolling", *J Strain Analysis Engng Design*, 2005, pp. 83-93.

[5.7] British Standards Institute, "BS EN 10025:2004 – Hot Rolled Products of Non-Alloy Structural Steels", British Standards Institute, 2004.

[5.8] British Standards Institute, "BS EN 10002-1:2001 – Metallic Materials- Tensile Testing Part 1: Method of Test at Ambient Temperature", British Standards Institute, 2001.

[5.9] Hibbert, Karlson and Sorenson Inc., *ABAQUS* User Guide Manual, v5.6, 1996.

[5.10] Technical Software Consultants Ltd., "ACPD/ACFM Crack Microgauge – Model U9 User Manual", Milton Keynes, UK, 1999.

[5.11] American Society for Testing and Materials, "Standard Test Method for Determining Residual Stresses by the Hole-Drilling Strain-Gage Method", ASTM E837-01e1, American Society for Testing and Materials, 2001.

[5.12] Vishay Micro-Measurements Group Inc., "Measurements of Residual Stresses by the Hole-Drilling Strain Gage Method", Tech Note TN-503-6, Revision 25-01-05, USA, 2005.

[5.13] Vishay Micro-Measurements Group Inc., "Special Purpose Sensors- Residual Stress Pattern". Document no. 11516, Revision 28-02-06, USA, 2006.

[5.14] Tanaka K. and Akiniwa Y., "Fatigue Crack Propagation Behaviour Derived from S-N Data in Very High Cycle Regime", *Fat Fract Engng Mater Struct,* Vol. 25, Issue 8-9, 2002, pp. 775-784.

[5.15] Soudan X., Lu J., Gillereau D. and Falvenot J. F., "Comparison of the X-ray Diffraction Method and the Hole-Drilling Method for the Measurement of the Residual Stress on the Aeronautical Materials", In: *Proc SEM Spring Conf Exper Mechs*, 1990, pp. 263-270.

[5.16] Lord J. D., Fry A. T. and Grant P. V., "A UK Residual Stress Intercomparison Exercise- An Examination of the XRD and Hole-Drilling Techniques", NPL MATC(A)98, National Physics Laboratory (UK), 1998.

[5.17] Vishay Micro-Measurements Group Inc., "Strain Indicator and Recorder- P3500", Document no. 11102, Revision 20-01-03, USA, 2003.

[5.18] Engineering Science Data Unit, "Fatigue Threshold Stress Intensity Factors and Slow Propagation Rates in Low and Medium Strength Low Alloy Steel", Stress and Strength Vol. 7, ESDU 81012, Engineering Science Data Unit, ISBN 085679 337 X, 1981.

CHAPTER 6

6.0 Development of a SIF Weight Function-Based Fatigue Crack Growth Evolution Prediction Model for Stitch Shot Peened Specimens

6.1 Introduction

The fatigue test results presented in Chapters 4 and 5 clearly show that the novel stitch cold rolling and the stitch shot peening techniques can be applied to control fatigue crack growth in structural steel components. These fatigue tests provided valuable information for the study of surface crack growth in compressive residual stress fields. The significance of residual stress and its influence on fatigue crack growth can be appreciated in the fracture mechanics analysis of the T-butt welded specimens reported in Chapter 3. It is also shown in Section 4.2 that the crack shape evolution has a profound effect on the fatigue crack growth behaviour of a surface crack. Hence, it would be extremely beneficial if the crack aspect ratio of surface cracks in flawed components can be modelled so that the component's residual strength can be accurately predicted. This becomes more significant when residual stress fields are present in the vicinity of the flaw. In order to further understand the mechanism of fatigue crack shape control using compressive residual stress induced by shot peening, a surface crack growth model is developed based on an existing surface crack SIF weight function and the Paris Crack Growth Law. For the generation of a representative fatigue crack growth model, the Paris material coefficients, C, and, m, of the BS EN 10025 GradeS275JR steel were determined using standard CT tests.

As described in Section 5.3.4, a residual stress monitoring programme was performed on Test SP6 to study the residual stress relaxation behaviour due to cyclic loading. This chapter will discuss in detail the analyses performed on the ICHD data obtained. Residual stress decay models at different plate-depth were proposed by using the measured strain relaxation data. The residual stress relaxation results were incorporated into the surface crack growth prediction model so that its "instantaneous" influence on the fatigue crack shape evolution could be modelled. It is believed that this is the first study to incorporate residual stress relaxation into a surface crack SIF weight function for fatigue crack shape evolution prediction.

6.2 Residual Stress Analyses

The residual stress monitoring by ICHD enabled the remaining residual stress to be determined at the desired fatigue intervals. The ICHD strain relief data obtained were analysed using the Equivalent Uniform Stress Method and the Integral Method. The main differences between these two methods and the resultant residual stress results are highlighted in the following sections. The strain hardening effect induced by shot peening and the validity of the residual stress data are also discussed.

6.2.1 The Equivalent Uniform Stress Method

When the hole-drilling method was first introduced, it was predominantly used for the measurement of uniform residual stress in relatively thin specimens. The hole-drilling method was subsequently extended by various researchers for the application to in-depth non-uniform residual stress measurement. Fig. 6.1 below illustrates the typical strain gauge rosette arrangement for the ICHD method. Based on this strain gauge rosette configuration, the governing equations for the residual stress analysis on uniform residual stress fields can be summarised using Equations 6.1 to 6.3 below. For a linear elastic isotropic material, the strain relaxation measured can be related to the principal stresses and the angle relative to the maximum principal stress direction as follows [6.1, 6.2]:

$$\varepsilon_r = A(\sigma_{max} + \sigma_{min}) + B(\sigma_{max} - \sigma_{min})\cos 2\alpha \qquad \text{- (6.1)}$$

$$A = -\frac{a'(1+\nu)}{2E} \qquad \text{- (6.2)}$$

$$B = -\frac{b'}{2E} \qquad \text{- (6.3)}$$

$$\sigma_{max}, \sigma_{min} = \frac{\varepsilon_1 + \varepsilon_3}{4A} \mp \frac{\left((2\varepsilon_2 - \varepsilon_1 - \varepsilon_3)^2 + (\varepsilon_1 - \varepsilon_3)^2\right)^{1/2}}{4B} \qquad \text{- (6.4)}$$

where ε_r is the measured strain relaxation

α is the angle from the nearer principal axis to Gauge 1

a', b' are the dimensionless strain relaxation calibration coefficients

E is the Young's modulus

ν is the Poisson's ratio

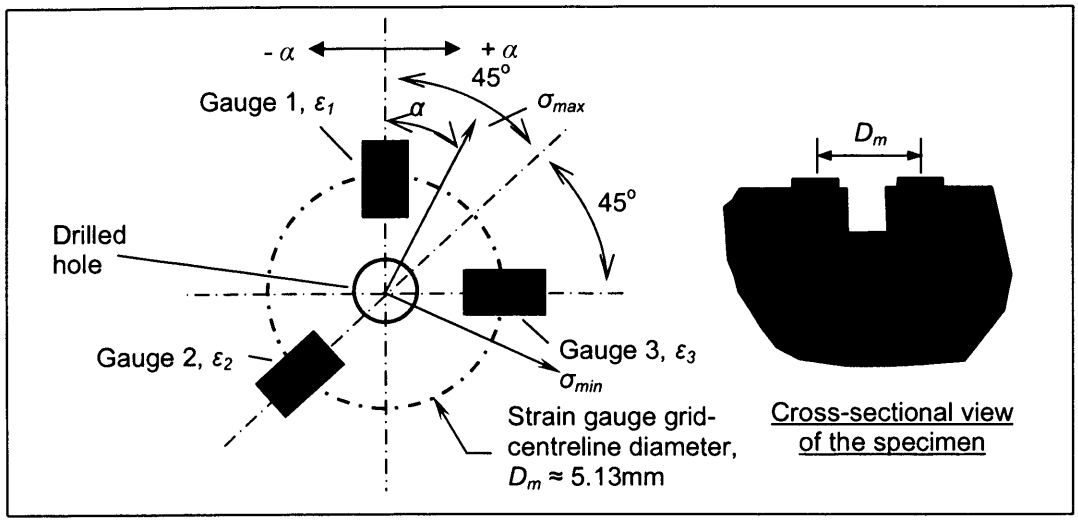

Figure 6.1: Schematic diagram showing a typical strain gauge rosette arrangement and the hole-drilling geometry used in the ICHD technique

The equations presented above form the basis of the Uniform Stress Method specified in ASTM E837. This method has no spatial resolution since it assumes that the residual stress is uniform with depth. In an attempt to measure the non-uniform residual stress distributions in spring steel specimens, Nickola [6.3] introduced the Average Stress Method. The Average Stress Method, or more often known as the Equivalent Uniform Stress (EUS) Method, is actually an approximation of the Integral Method (described in the next section) for the assessment of non-uniform residual stress fields. The EUS is defined as the average residual stress over the total hole-depth, which produces the same total strain relaxations as the actual non-uniform stress field. This method is outlined in the VMG Technical Note TN-503-6 [6.5]. For the strain gauge configuration illustrated in Fig. 6.1 above, the EUS method proposed by Nickola can be summarised as follows:

$$\sigma_{z+\Delta z}(z+\Delta z) = \sigma_z z + \sigma_{\Delta z}\Delta z \qquad \text{- (6.5)}$$

where σ is the equivalent uniform stress within subscript region
z is the hole depth before increment
Δz is the hole depth increment
$z+\Delta z$ is the hole depth after increment

The EUS is calculated by using the values of the dimensionless coefficients, *a'*, and, *b'*, presented in Equations 6.2 and 6.3 with the corresponding incremental strain relaxation values. Conventionally, the dimensionless calibration coefficients for a particular material were

determined experimentally by incremental hole-drilling on statically-loaded specimens. For better accuracy and greater flexibility of choice of hole-depth increment, Schajer [6.1, 6.4] applied Finite Element calculations for the evaluation of the dimensionless coefficients for a variety of steels and he concluded that the coefficients are almost material independent (with respect to steel grades). The coefficients developed by Schajer are valid for all steel grades and they are published in Reference 6.5. Although the EUS Method employs the hole-drilling procedures outlined in ASTM E837, it must not be confused with the Uniform Stress Method.

Figs. 6.2 and 6.3 below show examples of the strain relaxation data obtained from the 3C-6C and the 12C-16C shot peened band respectively. The data were acquired from the measurements performed on Test SP6 prior to fatigue loading. Both of the figures show typical strain relaxation curves plotted as a function of the hole-depth. Fig. 6.4 shows the corresponding principal stresses plotted using the strain relaxation data presented in Fig. 6.3. As can be seen from Figs. 6.2 and 6.3, the relieved-strains recorded from all three channels of the strain gauges have almost identical magnitudes close to the surface, indicating an equal biaxial compressive residual stress field. This is further confirmed in Fig. 6.3, where the principal stresses also show similar magnitude and trend. This observation is expected since surface compressive residual stress fields induced by shot peening is generally known to be biaxially equal in nature. It can be observed from the strain relaxation curves that the differences in the strain readings become much more obvious after approximately 1mm but this might be due to the fact that the influence of shot peening is less at greater hole-depths.

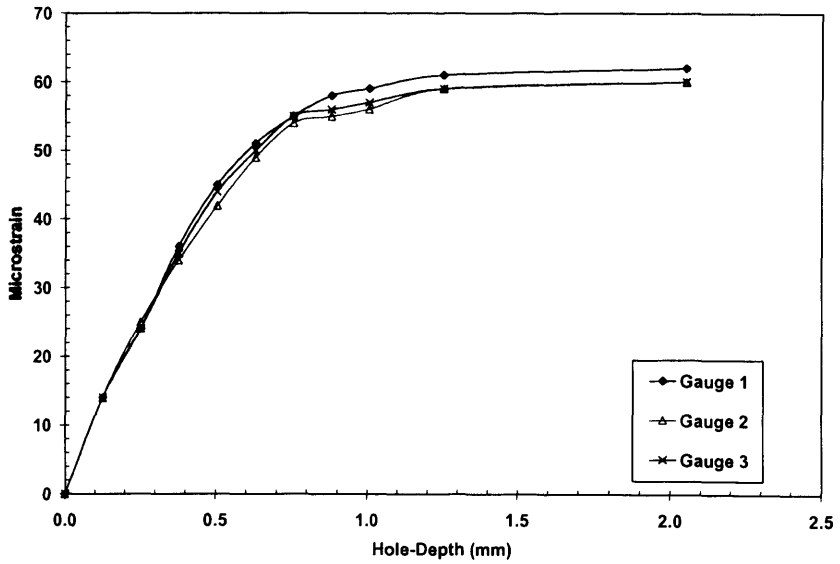

Figure 6.2: An example of the strain relaxation data obtained from the 3C-6C shot peened band prior to fatigue loading

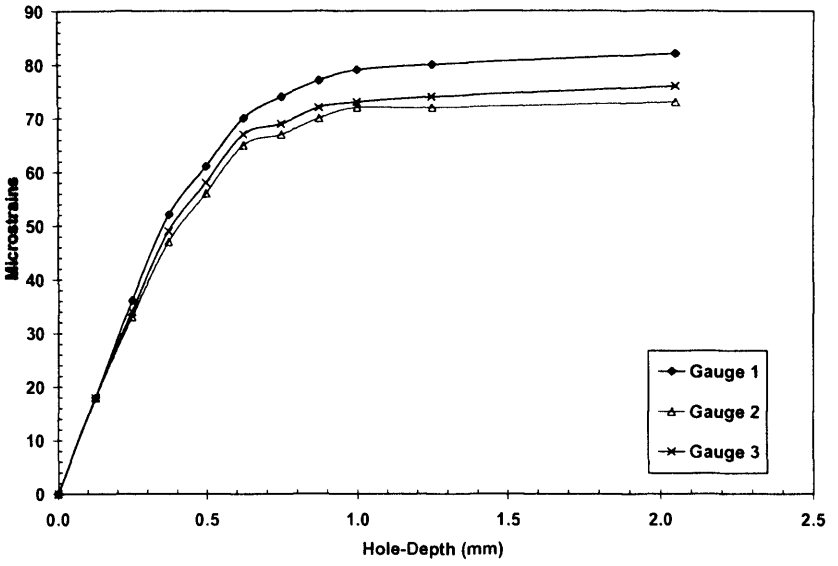

Figure 6.3: An example of the strain relaxation data obtained from the 12C-16C shot peened band prior to fatigue loading

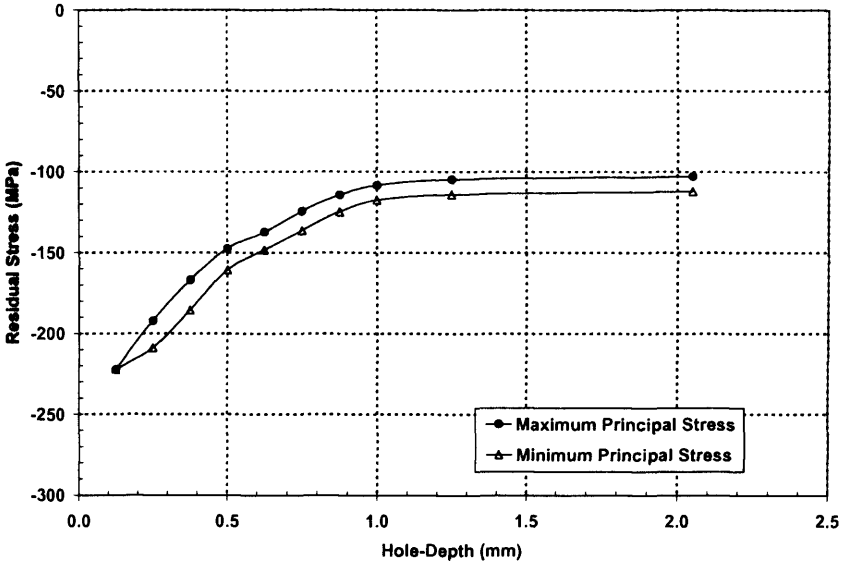

Figure 6.4: The principal residual stresses evaluated from the 12C-16C shot peened band prior to fatigue loading

The specifications of the strain gauge rosettes used in the present study can be found in Appendix H3. The ICHD measurements were performed at hole-depths of 0.13mm, 0.25mm, 0.375mm, 0.50mm, 0.625mm, 0.75mm, 0.875mm, 1.0mm and 2.05 mm. Since the residual stresses induced by shot peening were expected to have a steep gradient at near the surface, a relatively high spatial resolution was adopted for the first few hole-depth increments. The non-

dimensional strain relief calibration coefficients for the respective hole-depths were obtained from the VMG Technical Note TN-503-6 [6.5]. Although these coefficients are almost material independent, they were developed for the specific strain gauges with the corresponding standardised rosette geometries. The VMG Technical Note TN-503-6 recommends that the first hole-depth should be at least 0.13mm to avoid possible roughness and edge effects, and the full-depth of the blind-hole should be approximately 0.4 of the strain gauge grid-centreline diameter (Fig. 6.1 above).

Given that only the residual stress component on the maximum stress plane (i.e. transverse to the crack face and parallel to the cyclic loading direction) is considered to contribute to the Mode I crack opening, only the stress components parallel to the cyclic loading direction are presented and discussed in the following sections. The analysis concentrates on the residual stress data obtained from the 12C-16C shot peened band since the stitch peened specimens were shot peened with this intensity. Figs. 6.5 to 6.7 show the residual stress distributions for the 12A-16A, the 3C-6C and the 12C-16C shot peened band respectively. The data points show the residual stress magnitude at each respective incremental hole-depth and stress cycle interval. Hence, a separate hole was necessary to obtain each residual stress profile. These residual stress data were analysed using the EUS Method and the measurement procedures were consistent so that the results are comparative.

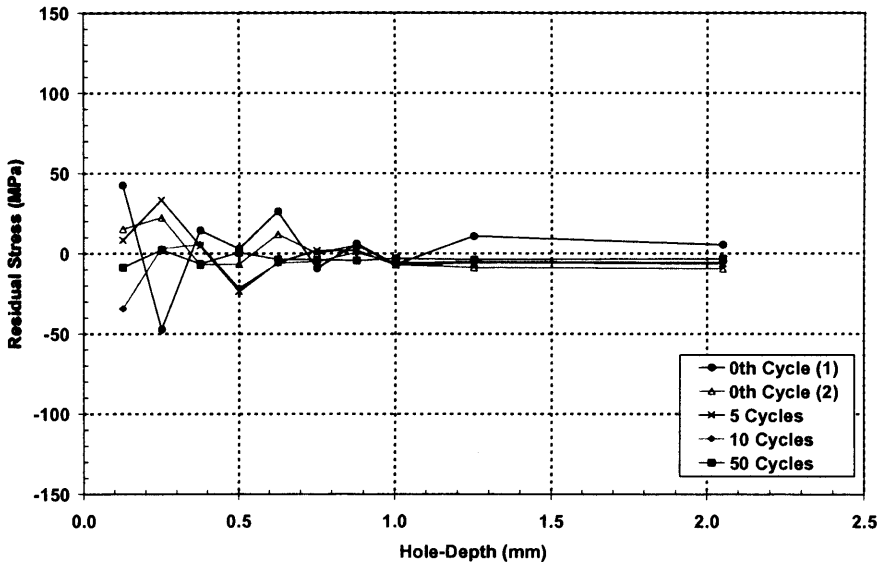

Figure 6.5: Residual stress data for the 12A-16A shot peened band (EUS Method)

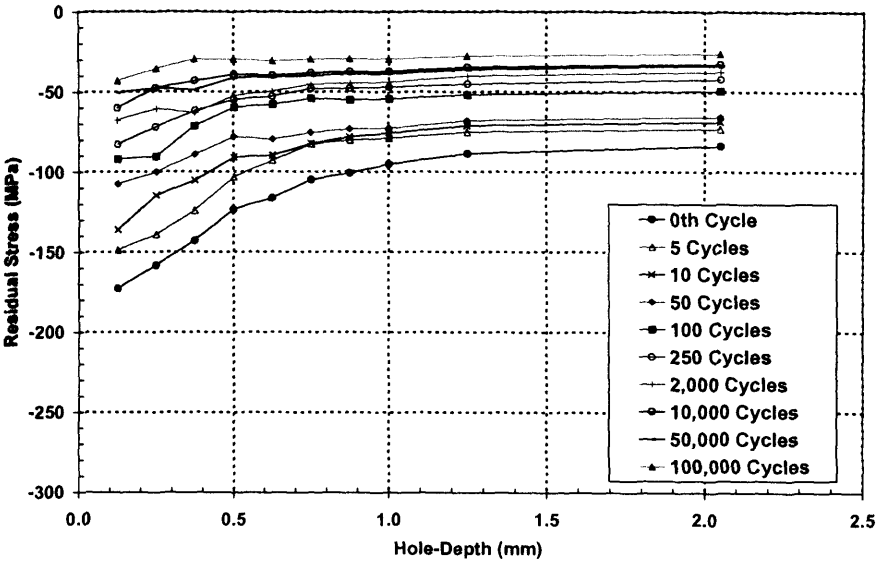

Figure 6.6: Residual stress data for the 3C-6C shot peened band (EUS Method)

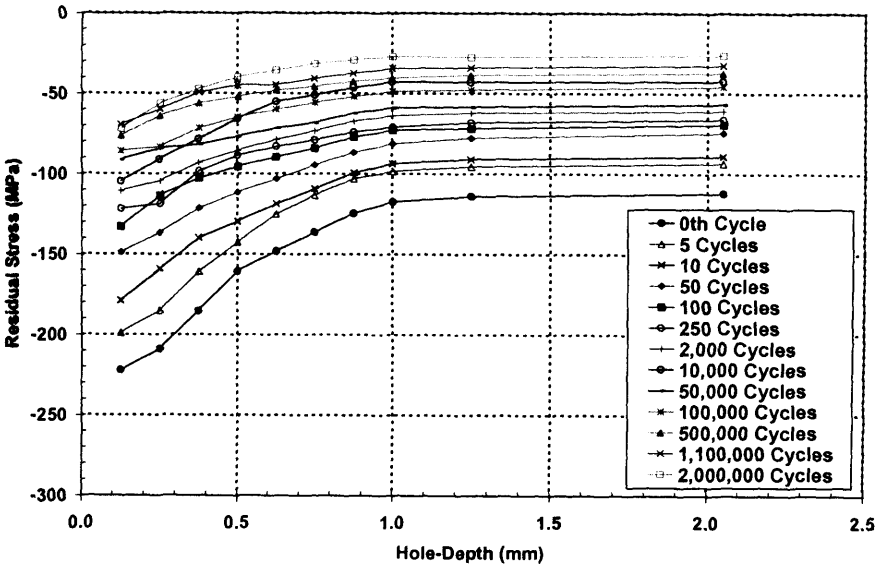

Figure 6.7: Residual stress data for the 12C-16C shot peened band (EUS Method)

As can be seen from Fig. 6.5, the residual stress monitoring on the 12A-16A shot peened band was terminated prematurely after five measurements. The residual stress data collected showed very low values and hence large scatter. Therefore, for clarity, the residual stress data for the 12A-16A shot peened band will not be further discussed. For the 3C-6C shot peened band, residual stress monitoring was carried out up to 100,000 stress cycles. It should be noted that two measurements were performed after 500,000 stress cycles but the strain relaxation data were erratic. Fig. 6.7 illustrates the residual stress data obtained from the 12C-16C shot peened band

up to 2,000,000 cycles. It is evident from Figs. 6.6 and 6.7 that the residual stresses redistributed and relaxed during the course of fatigue loading. Due to the higher shot peening intensity and the use of larger shot medias (Table 5.2), the initial residual stress (0th cycle) on the 12C-16C shot peened band has much higher magnitudes when compared to the 3C-6C band. It can also be observed from the figures that the compressive residual stress zone is much deeper for the 12C-16C case. A maximum sub-surface compressive residual stress of 222MPa and 173MPa was measured on the 12C-16C and the 3C-6C shot peened band respectively.

One of the shortcomings of the EUS Method is that it assumes that the EUS equals the average stress over the hole-depth. This is only true if the stresses at all depths within a given hole-depth contribute equally to the strain relaxations measured at the surface [6.1]. However, researchers [6.6-6.9] have shown that the strain relaxation measured at any given hole-depth increment (except the first) is caused only partly by the residual stress in that increment. The authors also concluded that the full-depth residual stress is predominantly influenced by the stresses closest to the surface and the relieved-strain corresponding to a normalised hole-depth of $Z/D_m>0.2$ (Fig. 6.1) has a negligible effect on the overall stress state. As stated previously, the EUS Method utilises the non-dimensional coefficients which were developed for uniform stress fields. As a result, the residual stresses illustrated in Figs. 6.6 and 6.7 do not resemble a typical residual stress profile induced by shot peening. In addition, the stresses presented are not self-equilibrating due to the intrinsic nature of the EUS Method. Despite the limitations described above, the EUS Method remains one of the most widely used in residual stress data reduction since it offers a rapid residual stress data reduction and it does not involve numerically-taxing analysis. Furthermore, provided that a high spatial resolution is used, the EUS Method does provide a good estimation of the "actual" residual stress at the first hole-depth increment.

6.2.2 The Integral Method

There is currently no standard procedure for verifying the non-uniformity of the full-hole-depth residual stress field based on measured strain relaxations but the Rendler-Vigness [6.10] percentage relieved-strain model is widely used as an aid in predicting non-uniform stress distribution. Since the strain relaxation calibration coefficients are almost material independent, Rendler-Vigness postulated the percentage relieved-strains in a uniform stress field should take the shape of the predicted curves presented in Fig. 6.8 below. By comparing the measured strain relaxation data with the Rendler-Vigness curves, it is evident that there is a high degree of non-uniformity in the residual stress distributions measured in the present study. It should be noted that the Rendler-Vigness model is not an absolute criterion in assessing the uniformity of a residual stress distribution. This is due to the fact that a non-uniform stress distribution can yield substantially similar percentage relieved-strains shown in Fig. 6.8 [6.5]. However, it is a good

indicator for verifying grossly non-uniform residual stress distributions if the data points vary considerably from the predicted curves, for example in this case. Cumulative

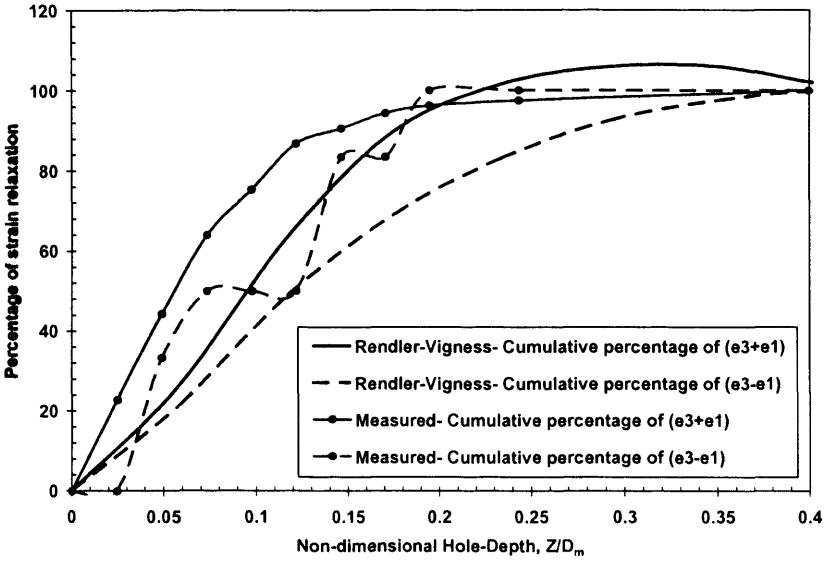

Figure 6.8: Comparison between the Rendler-Vigness percentage relieved-strain curves and the measured strain relaxation data

Bijak-Zochowski [6.11], Niku-Lari et al [6.12], and Flaman-Manning [6.13] pioneered the development of the Integral Method for the assessment of non-uniform residual stress field by the hole-drilling method. The Integral Method was not widely used until Schajer [6.9] implemented the application of FEA to the calculations of the non-dimensional strain relaxation coefficients, instead of relying on experimental calibrations. In conjunction with the development of the Integral Method, Schajer [6.1] also introduced the Power Series Method. The Power Series Method is generally employed in analysing linearly-varying residual stress fields while the Integral method is best suited for the case of residual stress fields with abrupt variations. Since only the Integral Method is adopted in the present study, the Power Series Method will not be further discussed.

According to the Integral Method, the measured strain relaxation, $p(h)$, is the integral of the infinitesimal strain components caused by the transformed stresses, $P(H)$, at all depths within the range $0 \leq H \leq h$:

$$p(h) = \frac{1+\nu}{E} \int_0^h A(H,h) P(H) dH \qquad \text{- (6.6)}$$

$$p(h) = \frac{1+\nu}{E} \int_0^h A(H,h) P(H) dH \qquad \text{- (6.6)}$$

where H is the non-dimensional depth from surface, Z/r_m

h is the non-dimensional hole-depth, z/r_m

z is the hole-depth

r_m is the strain gauge grid-centreline radius

$A(H,h)$ is the strain relaxation function

In practice, Equation 6.6 is more conveniently expressed in the discrete form of Equation 6.7:

$$\sum_{j=1}^{j=i} a'_{ij} P_j = \frac{E}{1+\nu} p_i \quad 1 \le j \le i \le n \qquad \text{- (6.7)}$$

where p_i is the measured strain relaxation after the *ith* hole-depth increment

P_j is the EUS within the *jth* hole-depth increment

a'_{ij} is the strain relaxation coefficient within increment of j of a hole i increments deep

n is the total number of hole depth increments

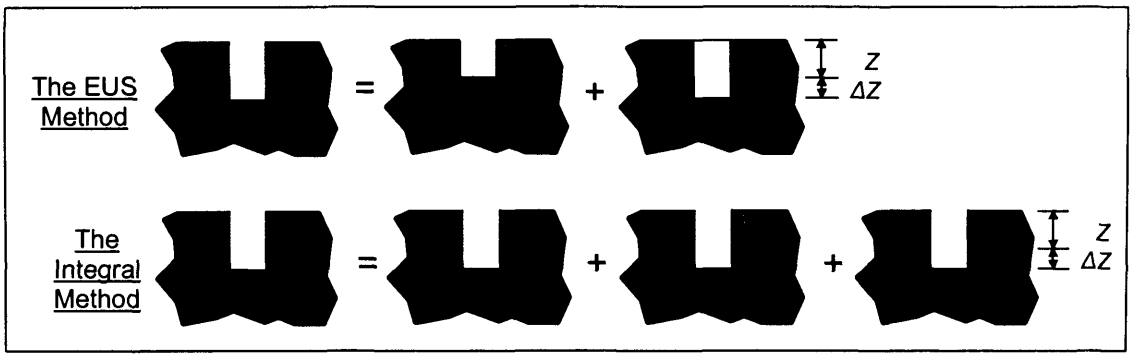

Figure 6.9: An illustration of the main difference between the EUS Method and the Integral Method

In contrast to the EUS Method, the Integral Method takes into account the contribution of the stresses at all depths simultaneously during the evaluation of the residual stresses at the instantaneous hole-depth, as demonstrated in the equations presented above. This significant difference between the EUS Method and the Integral Method can be illustrated with the aid of Fig. 6.9. Based on FE calculations, Schajer showed that the EUS within a hole-depth increment does not equal the average stress within that increment due to the increased sensitivity to the stresses closer to the surface [6.4, 6.9]. He also added that the deviation between the EUS and the "actual" stress becomes much more significant as the hole-depth increases. It must be pointed

out that all residual stress analysis methods only offer approximate values and it is impossible to evaluate the "actual" magnitude of the residual stress using these theoretical models. However, the Integral Method is widely regarded as one of the most reliable and robust approaches for the analysis of non-uniform residual stress fields.

The non-dimensional strain relaxation calibration coefficients for the Integral Method are presented in the form of tables in Reference 6.9. Since the tabulated coefficients do not coincide with the hole-depth increments used in the current study, a bivariate interpolation was performed to evaluate the intermediate values. In the present study, the residual stress analysis and the bivariate interpolation were computed using MATLAB®, according to the original scheme proposed by Schajer. Fig. 6.10 below shows the initial residual stress data for the 12C-16C shot peened band analysed using the EUS Method and the Integral Method. The differences between the stress profiles are evident from the figure, with both stress distributions having distinctive magnitude and trend as the hole-depth increases. The irregular shape of the residual stress distribution analysed (using the Integral Method) at hole-depth = 0.875 is believed to be caused by measurement error. As stated previously, the EUS Method does provide a good estimation of the magnitude of the residual stress at the first hole-depth increment and this is clearly shown in the figure, where only a 15% difference between the stress values at 0.13mm was calculated.

Figs. 6.11 and 6.12 illustrate the residual stress data analysed using the Integral Method, for the 3C-6C and the 12C-16C shot peened band respectively. Similar to the results obtained using the EUS Method, the residual stresses for the 12C-16C shot peened band have much higher magnitudes when compared to the values for the 3C-6C surface. It can be seen from the figures that the interior tensile residual stress zone could not be fully evaluated as a result of the hole-depth limitation of the ICHD technique and the loss of strain measurement sensitivity at greater hole-depth. Despite that, the residual stress profiles on both shot peened bands show clear self-equilibrating trends. Due to the inherent nature of the Integral Method of having a high spatial resolution, the residual stress data is very sensitive to strain measurement error, particularly at greater hole-depth. Therefore, it can be observed that the residual stress data becomes more unstable as the hole-depth increases. Overall, the Integral Method provides a more realistic estimation of the residual stresses and the distributions resemble a typical residual stress profile induced by shot peening. In addition, the trend of the residual stress data compare well with published literature.

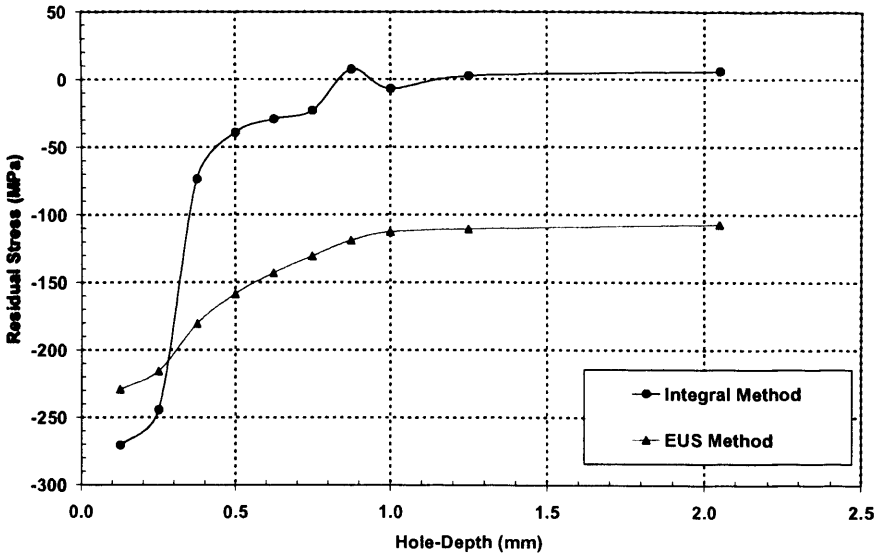

Figure 6.10: Comparison of the initial residual stress data analysed using the EUS Method and the Integral Method

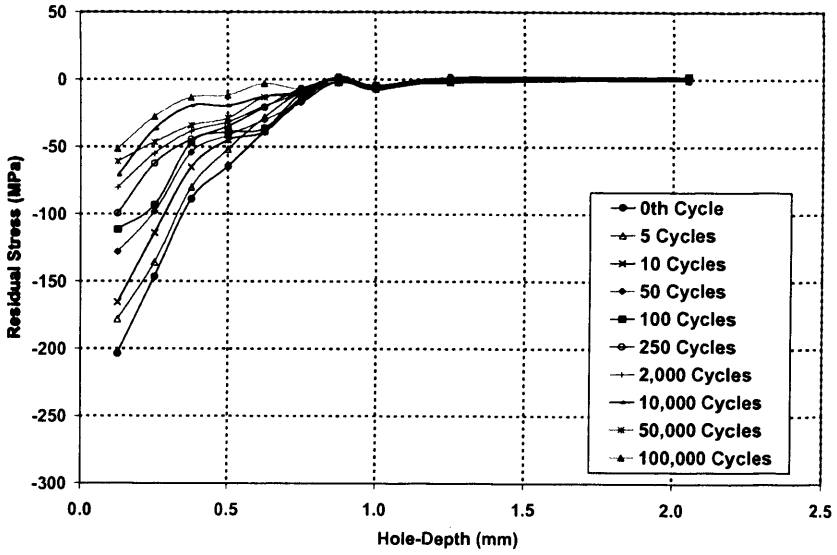

Figure 6.11: Residual stress data for the 3C-6C shot peened band (Integral Method)

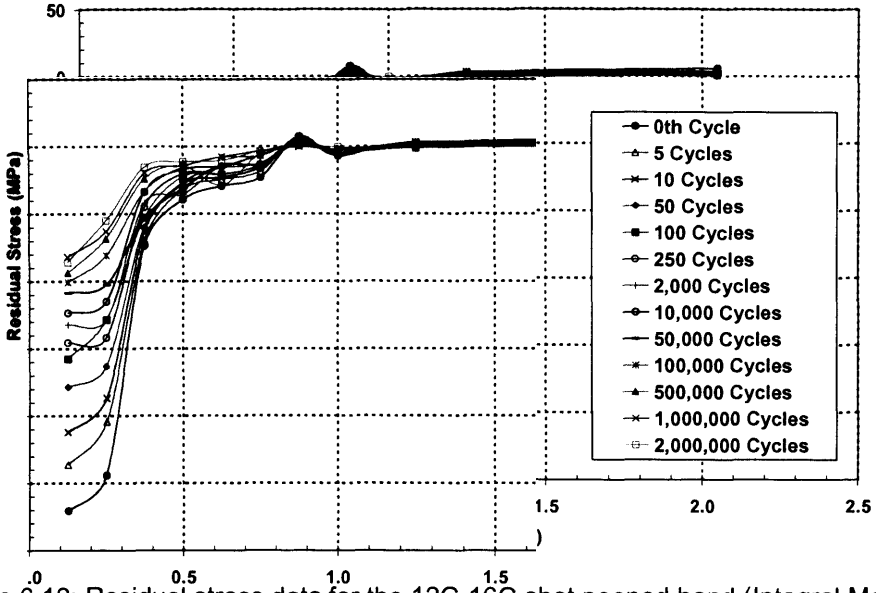

Figure 6.12: Residual stress data for the 12C-16C shot peened band (Integral Method)

6.2.3 The Strain Hardening Effect Induced by Shot Peening

All residual stress analyses by the hole-drilling method are based on linear elastic hypotheses. Hence, any local yielding caused by the stress concentration around the drilled hole can compromise the accuracy of the residual stress data. Since some of the residual stresses measured in the present study have magnitudes close to the yield strength of the material, the plasticity and the strain hardening effect on the residual stress data must be considered. ASTM E837 stated that the hole-drilling technique should only be used in the case where the magnitude of the residual stress is less than 50% of the bulk material's yield strength but the basis of this limitation is not addressed. Most of the residual stress analyses by the hole-drilling method published to date were either conducted on welded, cold-rolled or shot-peened components. These fabrication methods will inevitably induce a certain degree of plasticity onto the material due to the inherent nature of the process. Moreover, with these engineering components in their as-manufactured conditions, it is very rare that the magnitude of the residual stresses present is below 50% of the material's yield strength, and this is particularly true for welded components unless post weld treatments are carried out. Hence, in the majority of fabrication methods, the limitation presented in ASTM E837 will in all likelihood be violated.

In practice, the recommendations to take into account plasticity effects vary from 50% [6.2] to 70% [6.5, 6.6]. Based on numerical analyses, authors from References 6.14 and 6.15 stated that errors are only accountable when residual stresses exceed 60% of the material's yield strength. Beaney-Procter [6.6] observed an error of +16% in the stress calculation for a residual stress level corresponding to full yield, while Beghini et al [6.14] reported an overestimation of 20% for stress

magnitudes of 95% yield strength. On the contrary, various researchers [6.12, 6.16] have shown good agreement between hole-drilling and X-ray diffraction measurement data despite the magnitude of the residual stresses well above 50% of the material's yield strength.

In Reference 6.16, the hole-drilling residual stress data with 90% yield have a claimed accuracy of 10% when compared to the X-ray values. A recent study by Nobre et al [6.17] demonstrated that the residual stress data analysed using the Integral Method show good agreement with the X-ray measurement data. The measurements were performed on a wide range of structural steels with heavily shot peened surfaces. They found that overestimations are only significant when the residual stress magnitude exceeded 80% local yield strength of the work hardened surface. In an attempt to study the plasticity effect on hole-drilling data, Nobre et al [6.18] also found that the stress magnitude is much higher than 50% of yield strength despite using a mild shot peening intensity. They concluded that the strain hardening effect on the cold worked surface should be taken into account when assessing the plasticity effect in shot peened components.

In order to investigate the strain hardening effect, knowledge of the local material hardness and the yield strength of the shot peened surface is a prerequisite. The empirical equation proposed by Cahoon et al [6.19] is widely known to be able to provide an accurate calculation of the yield strength of metallic materials by using the Vicker's and Mayer's hardness, as described in the following equation:

$$\sigma_y = \left[(3.27HV)\cdot(0.1)^{m-2}\right] MPa \qquad \text{- (6.8)}$$

where HV is the material's Vicker's hardness

m is the Meyer's hardness exponent, ≈ 2.15 for mild steel [6.20]

Based on the proportionality between hardness and yield strength stated in Cahoon's equation, the increased local yield strength of the shot peened surfaces, σ^*_y, can be related to the yield strength of the bulk material, σ_y, using the following equation [6.18]:

$$\sigma^*_y = \sigma_y\left(1+\frac{\Delta HV}{HV}\right) \qquad \text{- (6.9)}$$

Prior to fatigue tests, the hardness of Test SP6 was evaluated using a UKAS calibrated Vicker's diamond hardness testing machine. The bulk material's hardness was determined from small samples extracted from the non-load-carrying sections of the specimens while the shot peened

surfaces' (12A-16A, 3C-6C and 12C-16C) hardness was tested on respective sections of the shot peened region. The surface roughness on the shot peened surfaces was carefully removed using a fine-grade Emery paper before each measurement. A total of five measurements were performed on each surface and the average values are tabulated in Table 6.1 below. The bulk material hardness (non-shot peened surfaces) of Test SP6 was calculated to be 134 ±6 HV.

Shot peened band	HV (shot peened surface)	ΔHV (%)
12A-16A	145 ±12	+8
3C-6C	167 ±15	+25
12C-16C	184 ±11	+48

Table 6.1: Measured Vicker's diamond hardness data

Specimen	S275 $\sigma_{y0.2}$ (MPa)	σ_y (MPa)	$\sigma_y/\sigma_{y0.2}$ (%)	σ^*_y (MPa)	σ^*_y / σ_y (%)	Max. σ_{res}/ σ_y (%)	Max. σ_{res}/ σ^*_y (%)
12A-16A	275	310	+13	336	+8	-	-
3C-6C	275	310	+13	387	+25	69	53
12C-16C	275	310	+13	458	+48	87	59

Table 6.2: Estimate of the material's yield strength from hardness data

A significant increase in the hardness of the shot peened surfaces can be observed in all the shot peened bands, confirming that the surfaces were highly cold worked. As expected, the 12C-16C shot peened band yielded the highest increase in hardness (+48%), followed by 3C-6C (+25%) and 12A-16A (+8%). Table 6.2 above shows the corresponding estimated yield strength of the bulk material and the shot peened surfaces using Equations 6.8 and 6.9. In order to examine the validity of Cahoon's equation in estimating the shot peened surfaces' yield strength and the suitability of using a Meyer's hardness exponent of 2.15, the yield strength of the bulk material is predicted directly from the hardness data. As shown in the table, a maximum error of +13% (with respect to the 0.2% offset yield strength, $\sigma_{y0.2}$) was calculated and this is considered to be acceptable since the Meyer's hardness exponent used is not specifically evaluated experimentally for the S275 steel. In addition, the S275 steel's 0.2% offset yield strength quoted in the British Standard [6.21] is the minimum yield strength and it is generally known that the mechanical properties of steels vary from batch to batch. Hence, Equation 6.8 is deemed to be valid to

provide a satisfactory estimation of the strain hardening effect. From the sixth column of Table 6.2, it can be observed that there is a 48% increase (with respect to the estimated yield strength, σ_y) in the local yield strength of the 12C-16C shot peened surface followed by 25% and 8% for 3C-6C and 12A-16A respectively. Therefore, it can be said that a higher shot peening intensity will result in higher local material yield strength. However, absolute correlation should not be drawn from the local yield strength values and the shot peening intensities since a different shot type was used for the 12C-6C surface and it is generally known that the magnitude of the induced residual stress induced does not solely depend on the shot peening intensity. The ratios between the maximum measured residual stress and the estimated bulk material yield strength are expressed in percentage form in the seventh column of Table 6.2. The last column of the table presents the ratios between the maximum measured residual stress and the estimated local yield strength. The maximum measured residual stresses using the Integral Method are 204MPa and 271MPa for the 3C-6C and the 12C-16C shot peened band respectively but no value can be calculated for the 12A-16A surface since the measured residual stress data were unreliable. The ratios using the estimated bulk material's yield strength as a reference are 69% and 87% for the 3C-6C and 12C-16C shot peened band respectively. The corresponding values using the estimated local yield strength as a reference are 53% and 59%. Without taking into account the strain hardening effect, the magnitude of the residual stresses, particularly for the 12C-16C case, is well above the 50% yield recommended by ASTM E837. On the contrary, the corresponding values are significantly reduced if the strain hardening effect is taken into account, with both ratios fallen below 60%, which is the currently accepted value in practice.

In recent research work assessing the plasticity and the strain hardening effect on hole-drilling data, Nobre et al [6.22] proposed a local stress-ratio criterion for verifying the validity of the measured hole-drilling data:

$$R_{\max} = \frac{\sigma_{Res}}{\sigma_y\left(1+2.8\frac{\Delta HV}{HV_{0.2}}\right)} \times 100\% \le k\%, \quad 60\% \le k \le 80\% \qquad \text{- (6.10)}$$

The above equation was derived based on an extensive hole-drilling measurement data, X-ray measurement data and FE calculations obtained from a wide range of steels with shot peened surfaces. Nobre et al stated that if the plasticity effect is to be considered, the stress-ratio should be evaluated with respect to the local yield strength of the work hardened surface instead of the bulk material's yield strength. They added that over-estimations were only detectable when the stress-ratio reaches 60% and becomes significant only when it exceeds 80%. In addition, the

plasticity effect on the hole-drilling data was determined by comparing the results of purely elastic FE simulations with those determined by elasto-plastic FE calculations and the results further confirmed the observations stated above. Based on these observations, Nobre et al concluded that plasticity effects are negligible if the maximum local-stress ratio, R_{max} does not exceed k% in Equation 6.10, with k = 60% used for a more conservative approach. Accordingly, the local stress-ratio calculated for the 3C-6C and the 12C-16C shot peened surfaces using Equation 6.10 are 42% and 43% respectively. It can be seen that the residual stresses measured in the present study are well below the 60%-mark proposed by Nobre et al and therefore plasticity effects (if any) are considered to be negligible in this case. Thus, it can be concluded that when verifying the validity of hole-drilling data due to plasticity, the strain hardening effect should be taken into account since it greatly reduces the possible effect of plastic yielding due to the drilled-hole. In addition, since the drilled hole resides in a significantly work hardened surface, it would be unreasonable to assess the plasticity effect based on the bulk material's yield strength.

6.2.4 Residual Stress Relaxation Data

This section will present the residual stress relaxation data obtained from the 3C-6C and the 12C-6C shot peened surfaces. Although it has been demonstrated that the EUS Method suffers from practical limitations when employed in non-uniform residual analysis, the residual stress data at the first hole-depth increment analysed using this method are included for comparison purposes. Figs. 6.13 and 6.14 below show the measured residual stress relaxation data at hole-depth = 0.13mm, for the 3C-6C and the 12C-16C shot peened surface respectively. The residual stress data are plotted on a semi-logarithmic scale. The error bars shown are based on a typical strain measurement error of ±3 microstrain at the first hole-depth increment, which corresponds to approximately ±32MPa. It is important to stress that strain values measured during hole-drilling are much less than those obtained from elastic loading of the material. Hence, similar to the determination of the magnitude of the residual stress, the error analysis also involves the strain relaxation calibration coefficients. The procedures for the residual stress error analysis based on the Integral Method can be found in Reference 6.23. Fig. 6.15 below shows examples of the residual stress relaxation curves for an SAE 1045 steel, plotted using the results reported by Landgraf [6.24] (Section 1.4.3). The graphs were plotted using different applied strain amplitudes and the yield strength of the material (500MPa) was used as the initial residual stress magnitude. It should be noted that the Landgraf residual stress decay model was developed based on strain-controlled experiments while the fatigue tests reported in the present study were conducted under stress-controlled conditions. Hence, the relaxation curves for the S275 steel are not included here. However, the general characteristics of the relaxation curves are not expected to vary significantly since the relaxation rate is proportional to the applied strain amplitude and the material hardness. Hence, the residual stress relaxation curves of SAE 1045 steel [6.24] (Fig.

6.15) are included in the following discussion to demonstrate the relaxation trend of the experimental residual stress data.

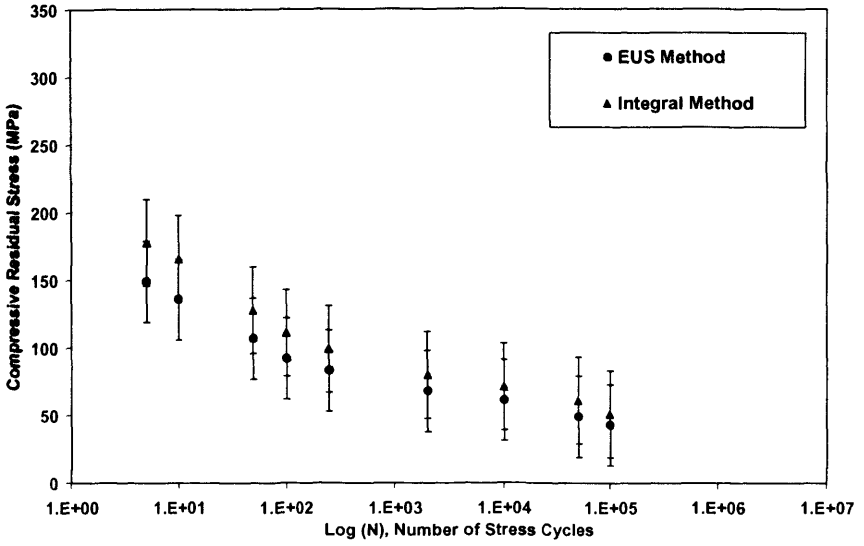

Figure 6.13: Residual stress relaxation data for the 3C-6C shot peened band

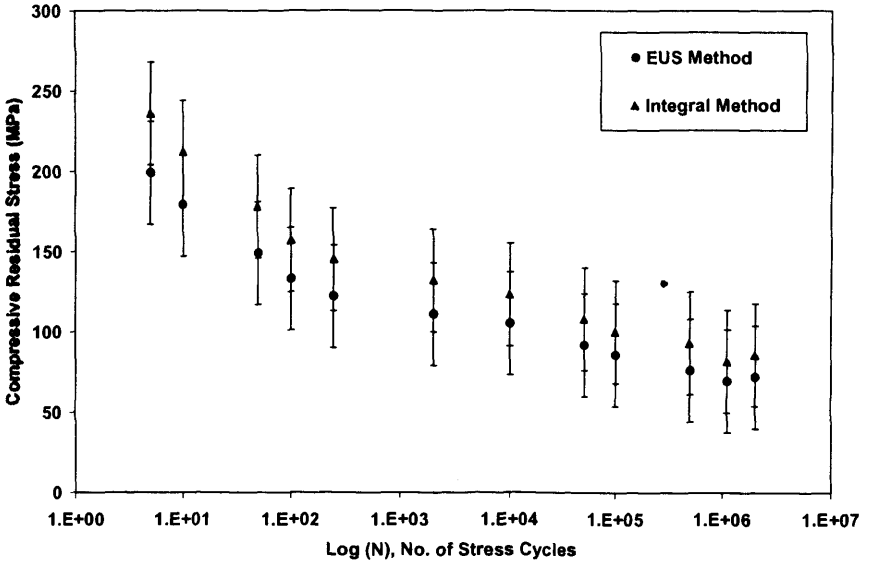

Figure 6.14: Residual stress relaxation data for the 12C-16C shot peened band

It can be clearly seen from Figs. 6.13 and 6.14 that the experimental residual stress data show exponential decay and a relaxation trend similar to Landgraf's model. It is evident in both figures that the magnitude of the remaining residual stress decreased drastically after the first few stress

cycles. This drastic decay behaviour of the remaining residual stress was also reported by Landgraf [6.24], Kodoma [6.25] and Farrahi et al [6.26] in shot peened components. From Fig. 6.14, it can be observed that the residual stress relaxation shows signs of reaching a plateau after approximately 1 x 10^6 cycles. It has been demonstrated that it is possible to use the ICHD method for the purpose of in-situ residual stress monitoring. The residual stress relaxation data presented above were incorporated into the SIF weight function-based crack growth model, which will be described in the following sections.

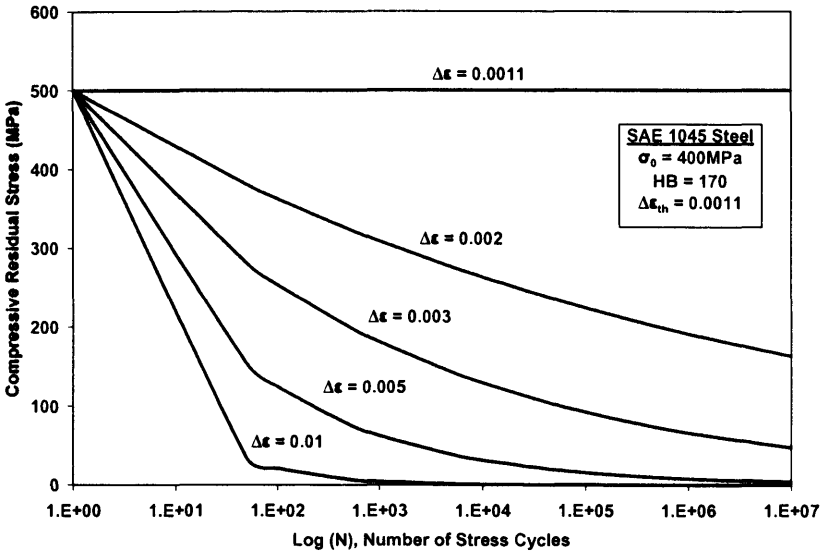

Figure 6.15: Examples of residual stress relaxation curves for an SAE 1045 steel [6.24]

6.3 A SIF Weight Function-Based Fatigue Crack Growth Prediction Model

6.3.1 Compact Tension (CT) Test

CT tests were carried out to obtain the Paris Law material coefficients (*C* and *m*) for the BS EN 10025 GradeS275JR steel. The test conditions followed the BS ISO 12108:2002 [6.27] and partly ASTM E647-05 [6.28]. The CT test details and the results obtained are presented in the following sections.

6.3.1.1 CT Test Details

A total of three CT specimens were extracted from a 170 x 120 x 70mm S275 steel plate, as shown in Fig. J3 in Appendix J. The parent steel plate was from the same batch material as for the stitch shot peened specimens. The direction of the CT specimens was chosen to avoid

material anisotropy effects, so that the crack growth is representative of those obtained from the stitch shot peened fatigue test specimens. The CT specimens were designed according to BS ISO 12108. The dimensions of the CT specimens can be found in Figs. J1 and J2 (Appendix J). An example of the CT test set-up on an Instron 1251 100kN servo-hydraulic fatigue test machine can be seen in Fig. 6.16 below. A load-ratio of $R \approx 0$ and a CA tensile load range of 8kN were adopted throughout the tests. All the tests were conducted in ambient air (temperature 16-19°C) at a frequency of 2.5Hz. A travelling microscope with an accuracy of 0.02mm was used to measure the crack length, at inspection intervals outlined in BS ISO 12108. Fatigue pre-cracking of the specimens was carried out according to BS ISO 12108. As can be seen from Fig. 6.16, the specimens were loaded using a pin-and-clevis arrangement, which was designed based on the suggested proportions and critical tolerances described in the aforementioned standard.

Figure 6.16: An example of the CT test set-up on an Instron 1251 100kN fatigue test machine

6.3.1.1 CT Test Results

Figs. 6.17 and 6.18 below show the fracture surfaces for Tests CT1 to CT3. Following the completion of each test, the fractured surfaces were examined to determine the extent of through-thickness crack curvature [6.27]. Since no visible crack contour was observed in the specimens, the crack curvature correction was not employed. The fracture surfaces were also checked for any asymmetrical crack growth, which can lead to erroneous crack length measurement. This phenomenon occurs if a specimen is subjected to asymmetrical loading (unbalanced moment) as a result of possible uneven contact between the loading pin and the specimen. In order to prevent the occurrence of this phenomenon, the pin-and-hole arrangement was adequately lubricated prior to the tests. As can be seen from Figs. 6.17 and 6.18, no visible asymmetrical crack fronts were observed.

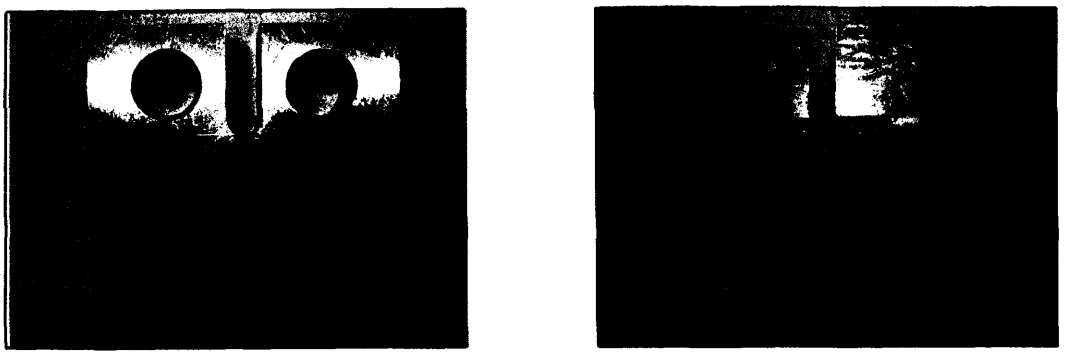

(a) (b)

Figure 6.17: (a) Test CT1 (b) Fracture surfaces of Test CT1

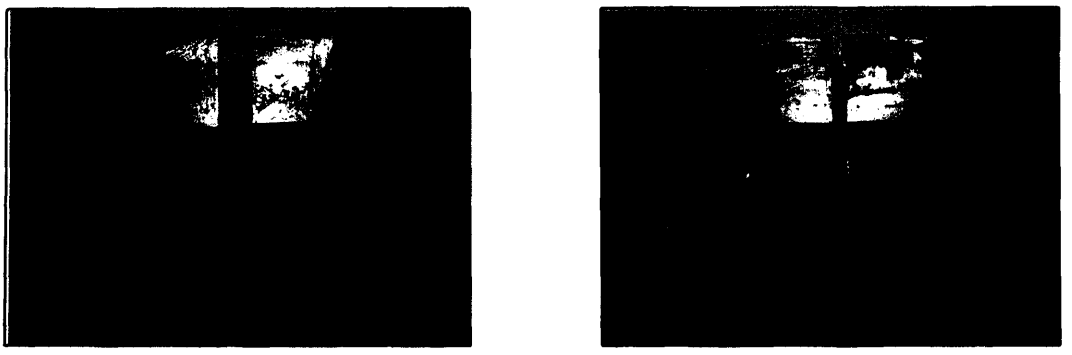

(a) (b)

Figure 6.18: Fracture surfaces of (a) Test CT2 and (b) Test CT3

Fig. 6.19 below shows the fatigue crack growth data for all the tests and the corresponding fatigue crack growth rate versus SIF range plots are shown in Fig. 6.20. The fatigue crack growth rates presented in Fig. 6.20 were determined using the incremental polynomial method outlined in ASTM 647. This involved fitting a second order seven-element polynomial to the fatigue crack growth rate data. The fatigue data reduction process was carried out using a program written in Digital Visual Fortran®. The corresponding SIF range was calculated according to the formula given in BS ISO 12108. The solid lines in Fig. 6.20 represent the crack propagation data for low-strength alloy steels (250MPa to 340MPa), obtained from ESDU 81011 [6.29]. It can be seen from the figure that the fatigue crack growth rate data obtained from all three specimens are consistent and the data scatter is minimal. In addition, all the measured data are within the limits of the ESDU crack propagation data. The measured crack growth rate data show three different segments, each with distinctive gradients at the respective SIF ranges, as indicated in Fig. 6.20. This observation is consistent with the typical sigmoidal behaviour of a fatigue crack growth rate plot, as shown in Fig. 1.4 in Section 1.3.3. The Paris Law material coefficients, C, and, m, were determined by combining the three scatter bands in Segment 2 (Paris Region) and by fitting a

power series line to the combined data. It is important to note that only the data points within the validity range recommended in BS ISO 12108 were used to evaluate the crack growth coefficients. Using the least square method, the material coefficients were calculated to be C = 4.162 and m = 1.26×10^{-10}, as shown in Fig. 6.21. These values were used in the Paris Law in conjunction with the fatigue crack growth model presented in the following sections, for the prediction of fatigue propagation life of the stitch peened specimens described in Chapter 5.

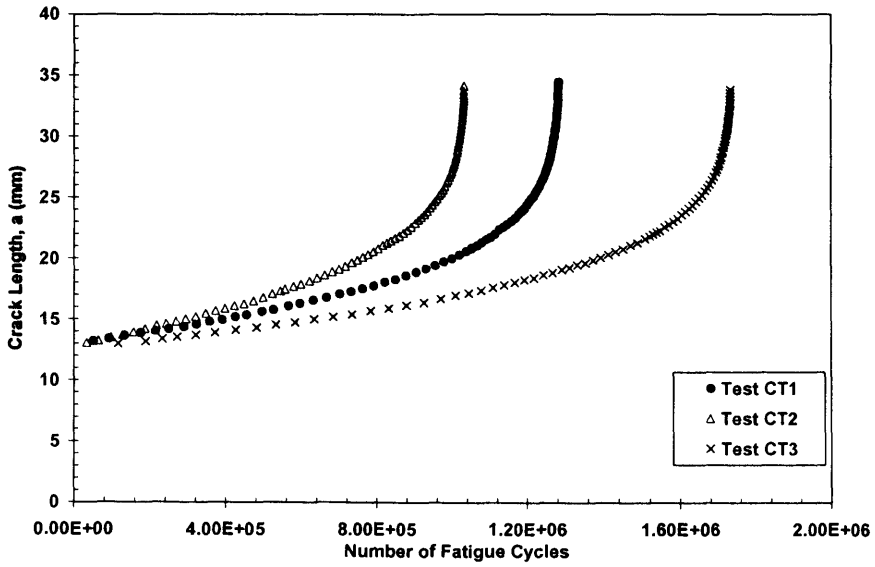

Figure 6.19: Fatigue crack growth data for all CT tests

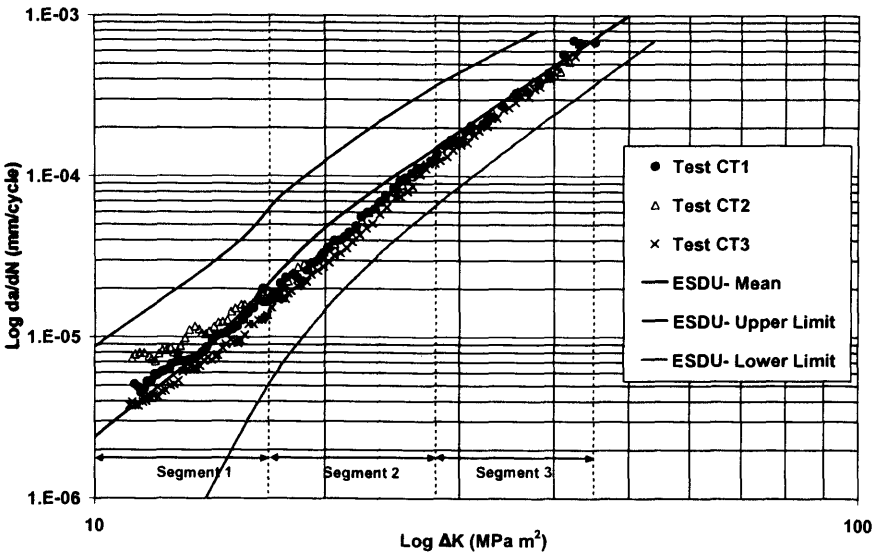

Figure 6.20: Fatigue crack growth rate vs. SIF range for all CT tests

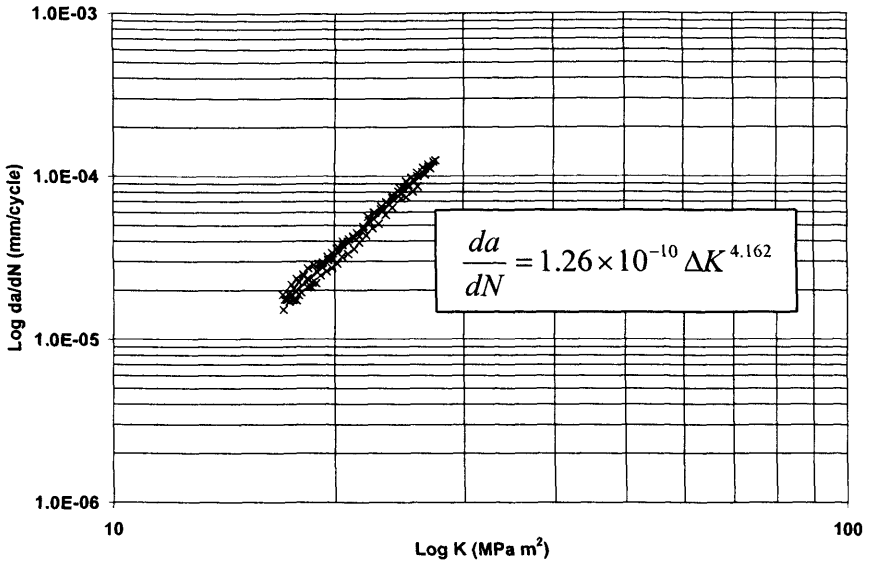

Figure 6.21: Combined fatigue crack growth data of Tests CT1 to CT3

6.3.2 Incorporation of the Residual Stress Data into the Fatigue Crack Growth Evolution Model

The calculation of SIFs using a weight function requires the knowledge of the full field stress distribution in the uncracked body. Similar to all experimental residual stress measurement methods, it is impossible for the ICHD technique to measure stresses at the plate's absolute surface point. Hence, the residual stress data presented in Sections 6.2.2 and 6.2.4 were required to be modified so that they could be incorporated into the weight function-based fatigue crack growth model. Since the stitch shot peened specimens were shot peened with an Almen Intensity of 12C-16C, only the residual stress data obtained from the 12C-16C shot peened surface are discussed in the following sections. Fig. 6.22 below shows the modified residual stress distributions based the original data presented in Fig. 6.12. As shown in the figure, the residual stresses at hole-depth = 0.13mm are linearly extrapolated to the plate's surface point. A linear extrapolation was adopted since the location of the maximum compressive residual stress in a shot peening induced residual stress field varies from case to case. Using X-ray residual stress measurement techniques, authors from References 6.30 and 6.31 observed maximum compressive residual stresses at layers close to the surface point of the shot peened components. In contrast, References [6.32, 6.33] show maximum stresses at relatively deeper sub-surface layers. Authors from References 6.17, 6.26, 6.34 and 6.35 reported mixed results even though the components being studied were shot peened with the same Almen Intensity. Therefore, for comparison purposes, the residual stresses at the surface point were assumed to be equal to those measured at the 0.13mm hole-depth. It can also be observed from the figure below that the residual stresses are modified to zero at hole-depth ≥ 0.875mm, based on the

assumption that the low-magnitude counter-balancing tensile residual stresses have negligible effect on the fatigue crack growth. This is not unreasonable since the tensile residual stresses are expected to relax drastically during the first few stress cycles.

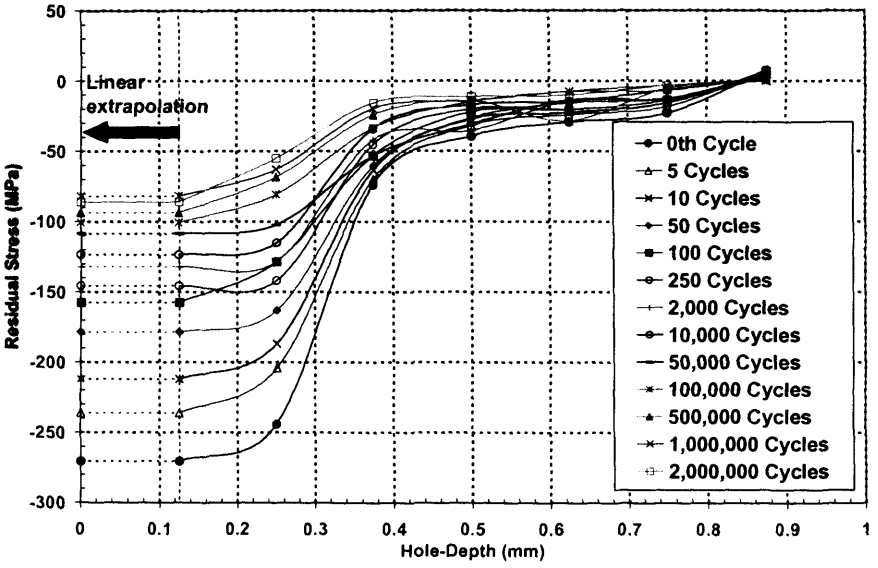

Figure 6.22: Linear extrapolation of the sub-surface residual stresses to the plate's surface point

For the generation of realistic SIF predictions, the residual stress relaxation effect was taken into account in the fatigue crack growth model. It is evident from Fig. 6.22 that the residual stress relaxation rates are not identical at all hole-depths. Hence, the residual stress relaxation rate at each hole-depth had to be evaluated individually. This was achieved by fitting a power series to the residual stress data which were plotted in a logarithmic scale and the relaxation constant and exponents (similar to Landgraf's model) were determined using the least square method. The individual residual stress relaxation function for all hole-depths can be found in Figs. K4 to K9 (Appendix K). A larger data scatter can be observed at greater hole-depth due to the fact that the Integral Method is much more prone to strain measurement errors as the hole-depth increases. Despite that, the residual stress relaxation data at relatively deeper layers in general still show a clear trend of exponential decay. By introducing the individual residual stress decay functions at the respective plate-depths, the relaxation behaviour was simulated in the fatigue crack growth model. It should be noted that the residual stress at the intermediate depths were calculated using linear interpolation. Since a high spatial resolution was used in the ICHD measurements, this procedure was found to be adequate and the errors resulted from the interpolation process are negligible.

6.3.3 SIF Weight Functions for Flat Plate Surface Cracks

The SIF weight function method was adopted for the calculation of SIFs due to its ability to accommodate complex stress fields, such as the measured residual stress distributions reported in previous sections. In order to simulate crack shape evolution in stitch peened specimens, knowledge of SIFs for both deepest point and surface point of a semi-elliptical surface crack is a prerequisite. In the present study, Shen-Glinka [6.36, 6.37] surface crack weight functions were adopted. Shen-Glinka's weight function for the deepest point, *A*, of a semi-elliptical crack in a plate of finite-thickness was derived using the universal weight function form, which is based on the COD proposed by Fett [6.38] (Section 1.3.5). The deepest point weight function can be written as:

$$m_A(x,a,c)=\frac{2}{\sqrt{[2\pi(a-x)]}}\left[1+M_{1A}\left(1-\frac{x}{a}\right)^{1/2}+M_{2A}\left(1-\frac{x}{a}\right)+M_{3A}\left(1-\frac{x}{a}\right)^{3/2}\right] \quad \text{- (6.11)}$$

The weight function for the surface point, *B*, of a semi-elliptical crack in a plate of finite-thickness was approximated by analogy to the weight function below using Equation 6.11 [6.37]:

$$m_B(x,a,c)=\frac{2}{\sqrt{\pi x}}\left[1+M_{1B}\left(\frac{x}{a}\right)^{1/2}+M_{2B}\left(\frac{x}{a}\right)+M_{3B}\left(\frac{x}{a}\right)^{3/2}\right] \quad \text{- (6.12)}$$

where M_{1A}, M_{2A}, M_{3A}, M_{1B}, M_{2B} and M_{3B} are the weight function coefficients determined from the reference state SIFs. Both the weight functions were derived using two reference SIF solutions; SIFs for semi-elliptical surface cracks under uniform tension and under pure bending, which were obtained from Shiratori et al [6.39]. In order to verify the accuracy of the weight functions, Shen-Glinka compared the generated SIF solutions with published FE data, including Newman-Raju [6.40] data for semi-elliptical cracks under pure bending and Shiratori et al [6.39] data for semi-elliptical cracks under quadratic and cubic stress distributions. Shen-Glinka reported that weight functions results compared well with published data and quoted differences of less than 3% for $0 \leq a/T \leq 0.8$ and $0.2 \leq a/c \leq 1$.

The SIF weight functions presented above form the framework of the surface crack growth evolution prediction model developed in the present study. The residual stress relaxation effect is taken into account by incorporating the modified residual stress distributions and the residual stress decay functions at different plate-depths into the fatigue crack growth model, which was computed using MATLAB®. Prior to the simulation of crack growth evolution under residual stress

fields, SIF predictions for simple loading conditions, generated using the current prediction model, were validated against published SIF solutions. This study, similar to that conducted by Shen-Glinka, was undertaken to validate the crack growth evolution model. An example of the validation process is presented in Fig. 6.23 below, which shows the comparison between weight function-based SIFs and Newman-Raju [6.40] SIFs for surface cracks under uniform tension. It should be noted that unlike the SIF predictions shown in Fig. 6.23, the current prediction model is capable of simulating "actual" crack growth evolution, which has a "naturally" varying *a/c* value. The validation data were plotted with fixed *a/c* values so that they are comparative with most published SIF solutions.

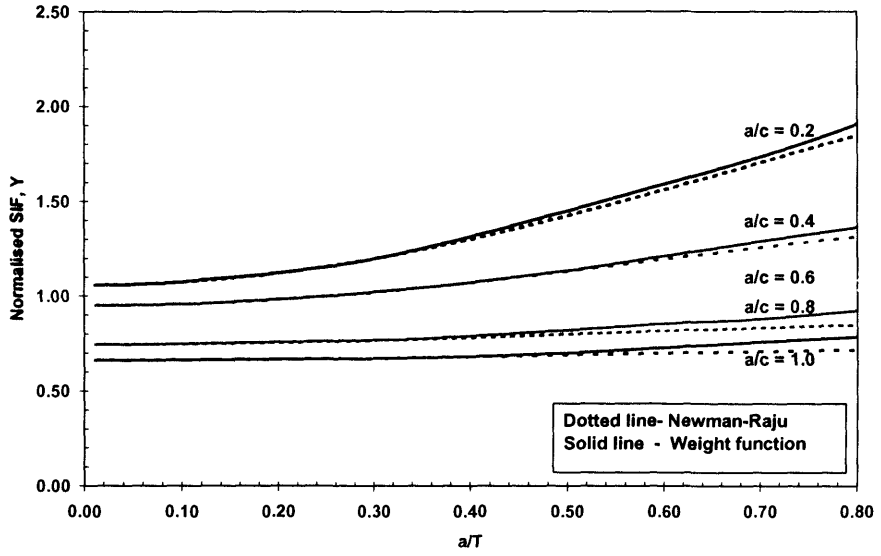

Figure 6.23: Comparison of weight function-based SIFs with Newman-Raju [6.40] SIFs for deepest point of semi-elliptical cracks in a finite thickness plate under uniform tension

A schematic of the crack growth evolution routine is shown in Fig. 6.24. The crack shape evolution computation shown in the figure produces a crack propagation prediction in terms of an *a-N* and *c-N* curve and crack aspect ratio evolution. The program is designed to "loop" for increasing values of crack depth, *a*, and crack half-length, *c*, until it reaches the prescribed final normalised crack depth, a_{Final}/T. The stress relaxation functions shown in Figs. K4 to K9 were used in the residual stress decay model. The effective applied stress distribution includes the remaining compressive residual stresses once the crack length equals the prescribed non-shot peened length. One shortcoming of simulating the stitch peening effect using this method is that the non-shot peened region is subject to the remaining compressive residual stress once the surface point enters the stitch peened region, as illustrated in Fig. 6.25.

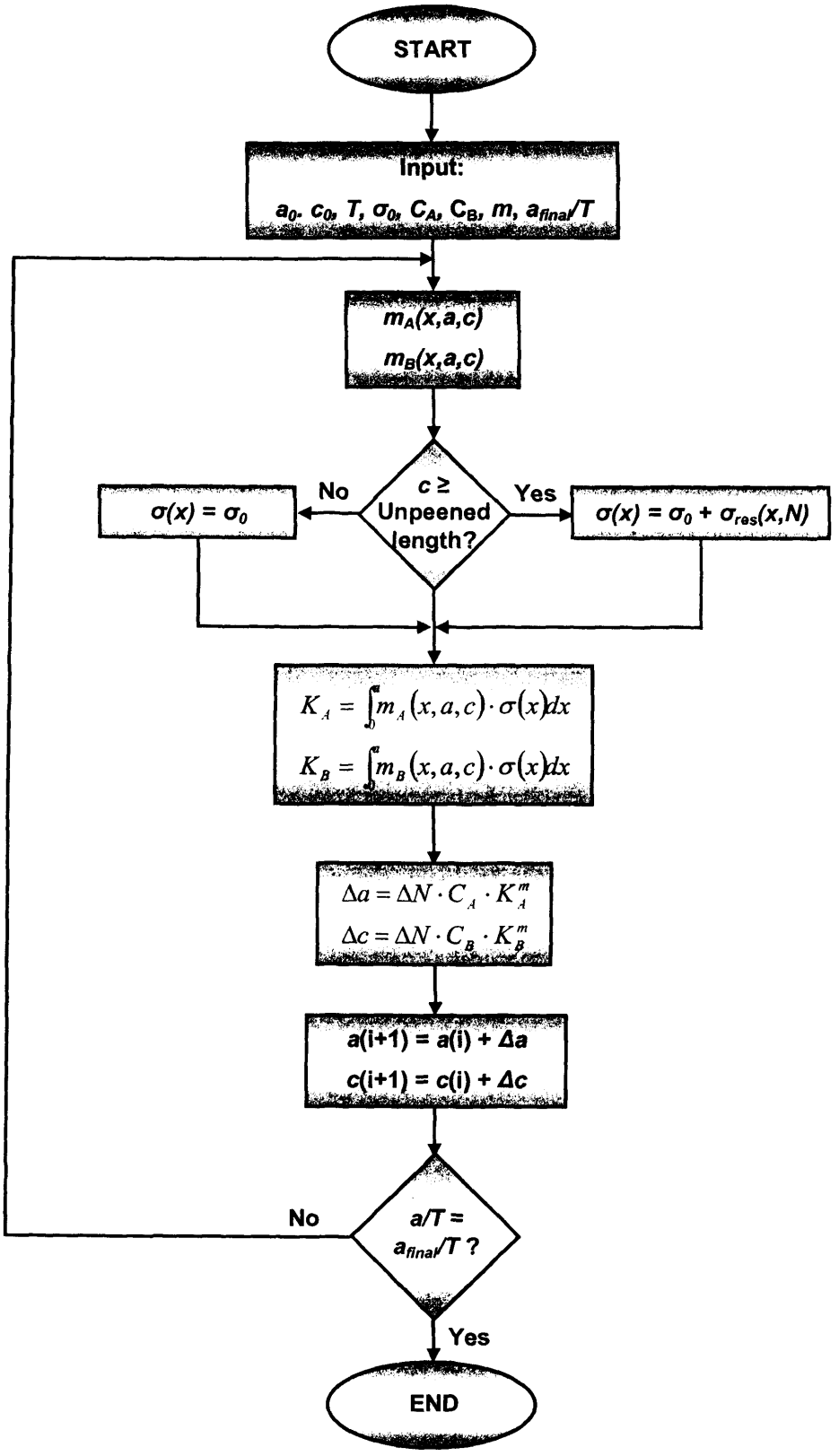

Figure 6.24: Schematic flowchart of the crack growth evolution model

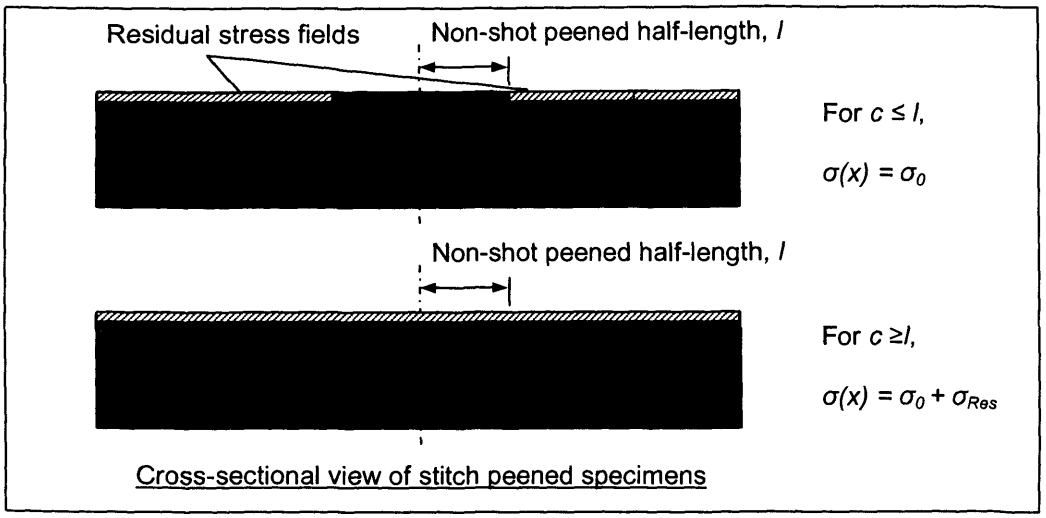

Figure 6.25: Simulation of the stitch shot peening effect

However, the residual stresses in the non-shot peened region are expected to have only a small influence on the crack growth at the deepest point since all the stitch peened specimens had a minimum initial 3.5mm-deep pre-crack while the modified residual stress fields only had a depth of 0.875mm. In other words, the crack front at the deepest point was sufficiently remote from the surface layers to be considered free from the influence of the remaining residual stresses. Although residual stresses at the non-shot peened region have a greater influence on the surface point SIF, there is no existing weight function that is able to overcome this limitation.

The "real-time" SIFs for the deepest point and the surface point of the surface crack are determined by numerical integration of the Paris Law, based on the material coefficients (C and m) determined from the CT tests. The crack growth rates were calculated by assuming that the Paris relationship between crack growth rate and SIF range is applied at points A and B on the crack front. Thus [6.40]:

$$\frac{da}{dN} = C_A \Delta K_A^{\ m} \quad \text{- (6.13)}$$

$$\frac{dc}{dN} = C_B \Delta K_B^{\ m} \quad \text{- (6.14)}$$

Normally, C_A and C_B are assumed to be equal. However, many researchers [6.40-6.42] have demonstrated that experimental results for surface cracks under tension and bending loads show

distinctively different crack growth behaviour at low *a/t* ratios when compared to predictive models. They added that the SIF at the surface point is approximately 10% higher than the value at the deepest point. Based on these observations, the crack growth coefficient C_B was assumed to be:

$$C_B = 0.9^m C_A \quad \text{- (6.15)}$$

Accordingly, Equation 6.15 was used in the current crack growth evolution model. Newman-Raju postulated that one of the reasons behind the difference between C_A and C_B may be the changing relationship between the SIF and the crack growth rate as the stress state changes from plane stress on the surface point to plane strain within the material. Equation 6.15 is widely adopted in the calculation of surface crack SIF and many researchers have shown that a semi-elliptical crack can be successfully modelled using the proposed relationship.

6.3.4 Discussion

Figs. 6.26 and 6.27 below show the crack depth and the crack half-length growth predictions respectively, for specimens with different non-shot peened length. The corresponding crack aspect ratio evolution predictions are illustrated in Fig. 6.28. For comparison purposes, these prediction curves were simulated using the same starting *a/c* and *a/T* and hence these are not the exact predictions for their experimental counterparts. It should also be noted that Test SP5, which was tested under bending, is not included in the following discussions. It can be observed from Fig. 6.26 that stitch shot peened specimens are predicted to have higher fatigue crack propagation life when compared to a non-shot peened specimen. Due to the presence of the surface compressive residual stress, the crack half-length growth in stitch shot peened specimens are also predicted to be much lower. It can be appreciated from Fig. 6.27 that all stitch peened specimens are expected to fail with a higher crack aspect ratio, illustrating that the stitch shot peening technique can be implemented to promote a leak-before-break failure. It can also be seen from the figures that a relatively short non-shot peened length will result in a much higher growth in the depth direction, when compared to longer non-shot peened lengths. For example, a stitch shot peened specimen with a non-shot peened length of 20mm is expected to attain a maximum crack aspect ratio of approximately 0.9 while a value of 0.7 is predicted for a specimen with a non-shot peened length of 35mm. Fig. 6.28 shows unusual crack aspect ratio evolution predictions, where an abrupt change of gradient can be observed for all stitch shot peened specimens. This phenomenon is a result of the surface compressive residual stress preventing crack growth in the length direction, forcing growth in depth.

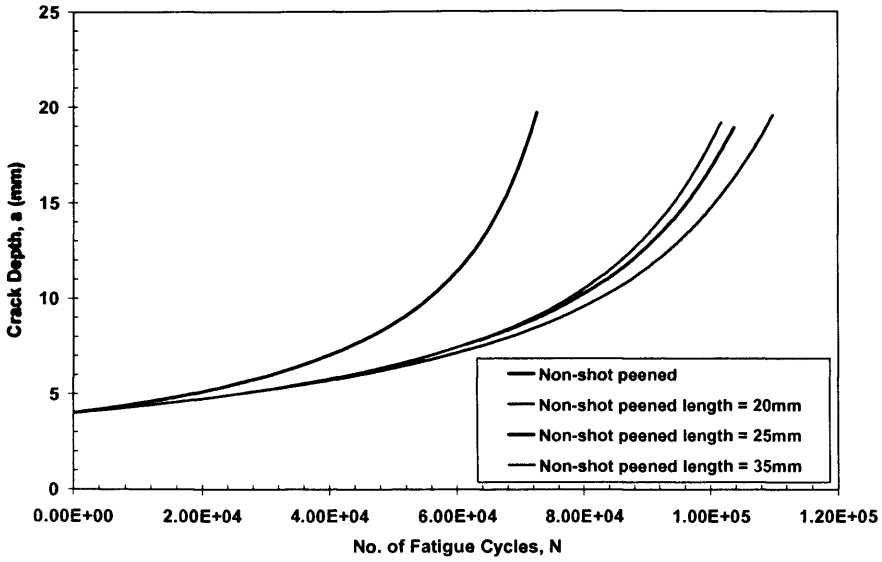

Figure 6.26: Fatigue crack growth prediction

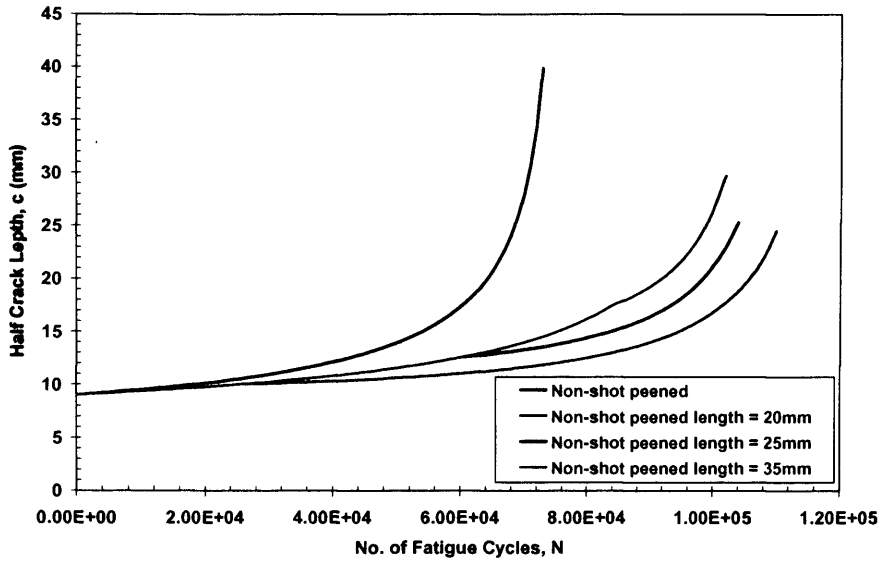

Figure 6.27: Half-crack length growth prediction

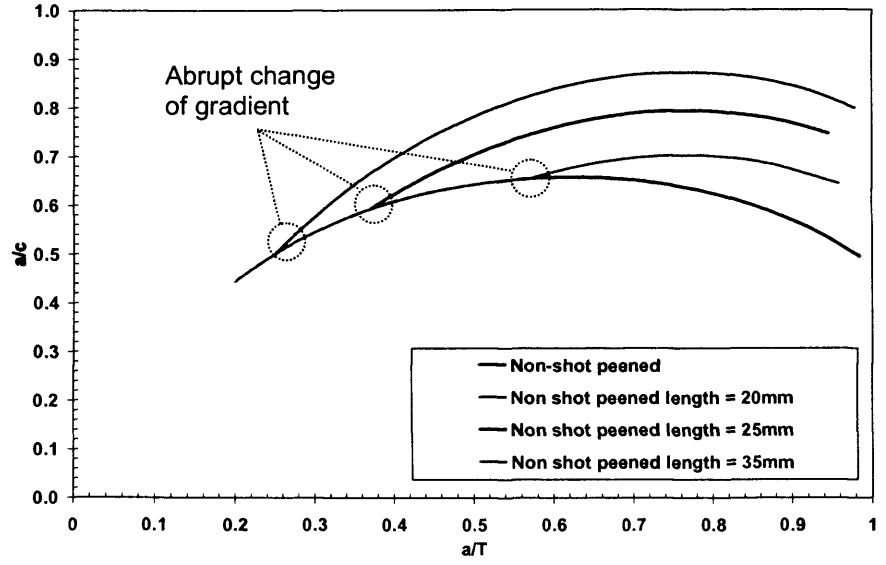

Figure 6.28: Simulation of crack aspect ratio evolutions

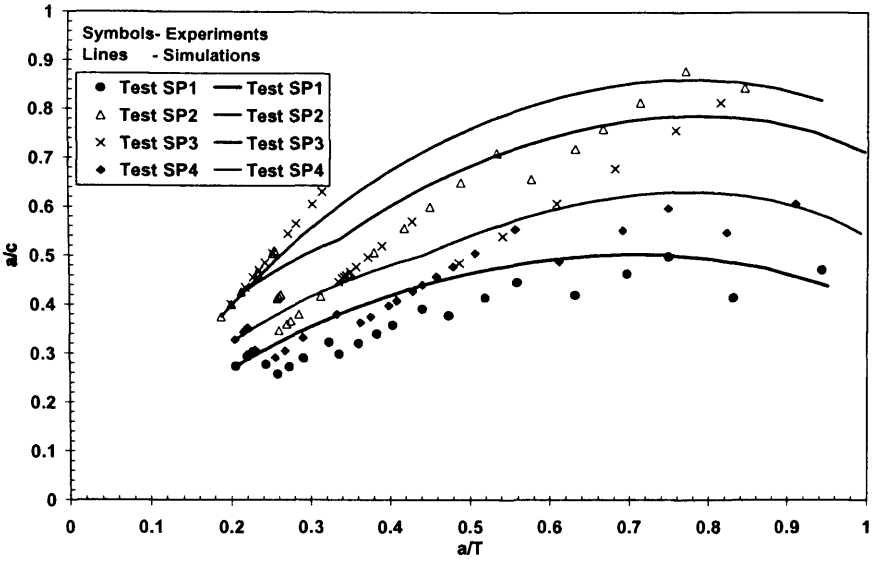

Figure 6.29: Comparison between the experimental and the simulated crack aspect ratio evolutions

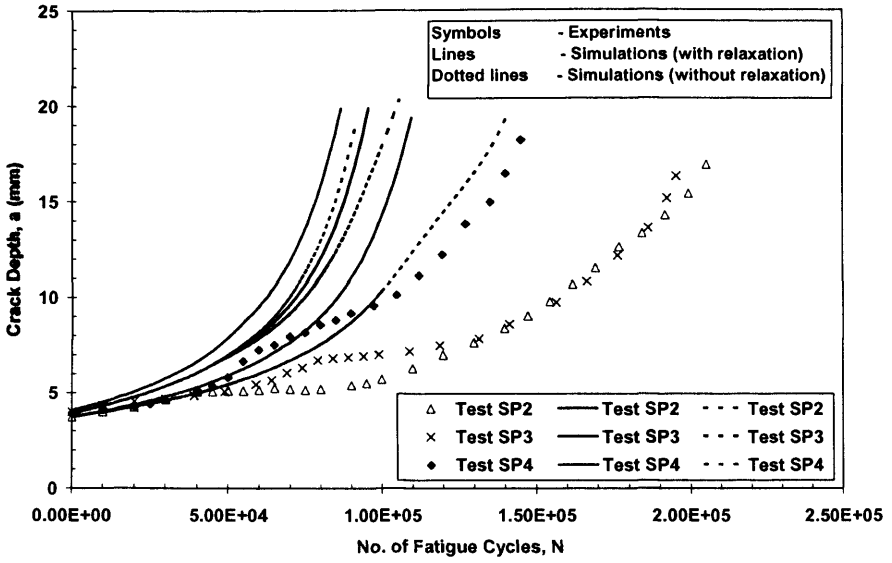

Figure 6.30: Comparison between the experimental and the simulated fatigue crack propagation lives

Fig. 6.29 above shows the comparison between the experimental and the predicted crack aspect ratio evolution for Tests SP1 to SP4. The predicted curves were generated using the corresponding experimental starting *a/c* and *a/T* values. It can be appreciated that the crack growth evolution model is able to predict the general trend of the crack aspect ratio evolutions and the enhancement caused by stitch shot peening. Moreover, the crack aspect ratio evolutions of Test SP1 and SP4 were simulated with good accuracy. It is believed that the irregularities in experimental data are caused by the coarse ACPD crack length inspection interval (5mm) adopted. Hence, a better agreement between the experimental and the predicted data is expected if a high accuracy crack length measurement technique (e.g. optical technique) was employed.

Fig. 6.30 shows the comparison between the experimental and the predicted fatigue crack propagation lives for Tests SP1 to SP4. The graph shows that the crack growth prediction model provides a good estimation of the fatigue crack propagation life of Test SP1. The prediction data indicate that the Paris Law material coefficients determined from the CT tests are applicable in modelling surface crack growth. The fatigue lives of Tests SP2 to SP4 are however greatly underestimated. For example, Tests SP2 and SP3 recorded approximately 150% increase in fatigue crack propagation life but and the corresponding lives predicted by the crack growth evolution model are only a 20% and 40% increase. Overall, the crack growth model tends to be over-conservative on the fatigue propagation life prediction of stitch shot peened specimens.

In order to demonstrate the influence of residual stresses on the prediction data, Figs. 6.31 and 6.32 below include the simulated data with and without residual stress relaxation effects. Without residual stress relaxation, all the cracks were predicted to achieve higher crack aspect ratios, as shown in Fig. 6.31. However the crack aspect ratio shows signs of decreasing as the cracks grow considerably deep into the plate. This suggests that surface residual stress fields have less influence on the final phases of the crack propagation as the surface cracks tend to a certain crack shape. Fig. 6.32 shows the fatigue crack propagation life predictions without inclusion of residual stress relaxation. It can be seen from the figure that the predicted lives without residual stress relaxation effects are closer to the experimental data but they are still significantly underestimated.

Since over-conservatism is observed in the prediction data generated with and without residual stress relaxation effects, it is believed that the unusual crack growth behaviour observed in the experiments might be influenced by other factors. The discrepancies between the experimental and the prediction data are likely to be caused by the following reasons:

1. The work hardening effect on the shot peened surfaces was not taken into account in the current predictive model. Hence, the improvement in the fatigue crack propagation lives observed in the predictions is solely caused by the introduction of the remaining surface compressive residual stress. This is a significant factor since an enhancement in the mechanical properties of the shot peened surfaces is very much expected, as evidently demonstrated in Section 6.2.3.

2. The crack growth evolution model assumed that the shot peened surfaces had the same Paris Law material coefficients (C and m) as a non-shot peened S275 steel. The material coefficients of the shot peened surfaces are however expected to be greatly influenced by shot peening.

3. Since linear elastic conditions are hypothesised in the SIF weight function method, the plasticity effect induced by shot peening is not considered in the crack growth evolution model.

Despite the limitations presented above, the SIF weight function-based crack growth evolution model provided valuable information on the shot peening residual stress effect on crack growth and crack shape evolution behaviour in stitch shot peened specimens.

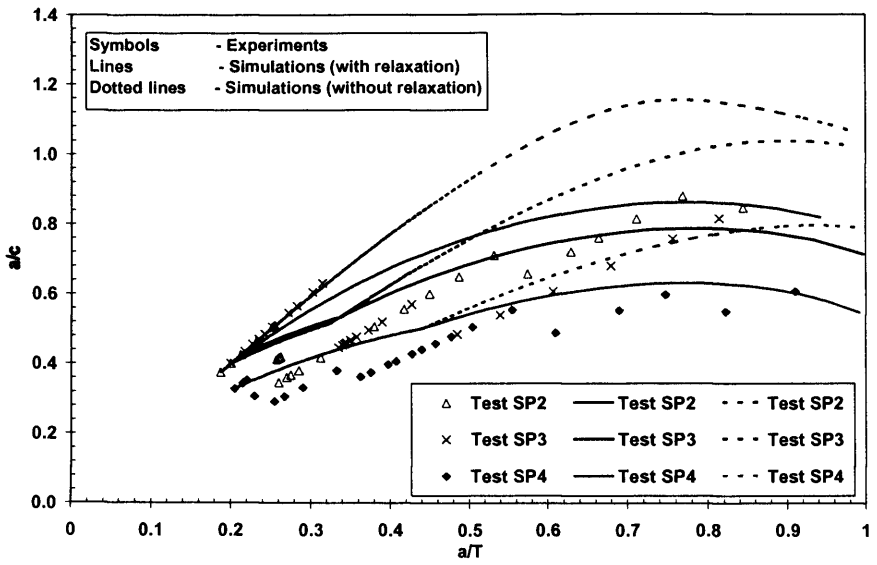

Figure 6.31: Illustration of the crack aspect ratio simulation data with and without residual stress relaxation effects

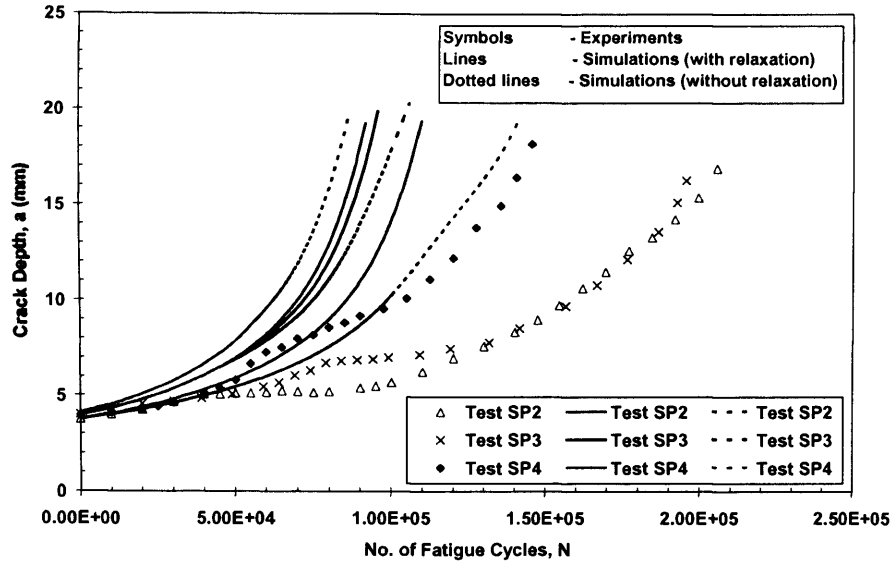

Figure 6.32: Illustration of the fatigue crack propagation prediction data with and without residual stress relaxation effects

6.4 Summary

This Chapter presented the analyses involved in the development of a SIF weight function-based fatigue crack growth model. The strain relaxation data collected from the residual stress monitoring programme were analysed using the EUS Method and the Integral Method. The

differences between the two methods have been clearly demonstrated in the analysed results. The EUS Method provided a rapid data reduction for the measured strain relaxation data but the calculated results have been shown to be unrepresentative of the actual residual stresses. On the contrary, the Integral Method provided a more realistic estimation of the residual stresses present and the trend of the measured data compares well with published literature. A detailed analysis of the strain hardening effect induced by shot peening revealed that the mechanical properties of the shot peened surfaces have been greatly enhanced. Hence, the so-called plasticity effect is considered to have negligible effect on the validity of the hole-drilling strain relaxation data if the plasticity effect is assessed based on the yield strength of the work hardened surfaces. The residual stress monitoring programme also enabled the shot peening residual stress relaxation behaviour under cyclic loading to be studied. Overall, it has been shown that it is possible to monitor residual stress relaxation in shot peened components using the ICHD technique. However, the hole-drilling procedures must be applied consistently and an adequate residual stress analysis method must be chosen so that the results are representative of the residual stress present.

This chapter also calculated the effective SIFs for the surface point and the deepest point of a surface crack under residual stress fields using a weight function method. The development of a surface crack growth evolution prediction model is made possible with the integration of the weight function method, the Paris Crack Growth Law and the proposed residual stress relaxation functions. The unique features of the crack growth model allowed the "instantaneous" crack shape evolution in stitch shot peened specimens to be simulated. Although the predictive model is capable of simulating crack shape evolution and fatigue crack propagation life of a non-shot peened specimen, it suffers from practical limitations when applied to the simulation of stitch shot peening effects. The fatigue crack propagation life predictions in general show a high level of conservatism. Hence, further work is needed to enhance its ability to model crack shape evolution in anisotropic materials.

6.5 References

[6.1] Schajer G. S., "Application of Finite Element Calculations to Residual Stress Measurements", *J Engng Mater Technol*, Transactions of the ASME, Vol. 103, 1981, pp. 157-163.

[6.2] American Society for Testing and Materials, "Standard Test Method for Determining Residual Stresses by the Hole-Drilling Strain-Gage Method", ASTM E837-01e1, American Society for Testing and Materials, 2001.

[6.3] Nickola W. E., "Practical Subsurface Residual Stress Evaluation By The Hole-Drilling Method", In: *Proc Spring Conf. Exper Mech*, Society for Experimental Mechanics, New Orleans, 1986, pp. 47-58.

[6.4] Schajer G. S., "Measurement of Non-Uniform Residual Stresses Using the Hole-Drilling Method. Part I- Stress Calculation Procedures", *J Engng Mater Technol*, Transactions of the ASME, Vol. 110, 1988, pp. 338-343.

[6.5] Vishay Micro-Measurements Group Inc., "Measurements of Residual Stresses by the Hole-Drilling Strain Gage Method", Tech Note TN-503-6, Revision 25-01-05, USA, 2005.

[6.6] Beaney E. M. and Procter E., "A Critical Evaluation of the Centre-Hole Technique for the Measurement of Residual Stresses", *Strain Journal BSSM*, Vol. 10, No. 1, 1974, pp. 7-14.

[6.7] Ajovalasit A., "Measurement of Residual Stresses by the Hole-Drilling Method: Influence of Hole Eccentricity", *J Strain Analysis*, Vol. 14, No. 4, 1979, pp. 171-178.

[6.8] Flaman M. T., Mills B. E. and Boag J. M., "Analysis of Stress-Variation-With-Depth Measurement Procedures for the Centre Hole Method of Residual Stress Measurements", *Exper Techniq*, Vol. 11, 1987, pp. 35-37.

[6.9] Schajer G. S., "Measurement of Non-Uniform Residual Stresses Using the Hole-Drilling Method. Part II- Practical Application of the Integral Method", *J Engng Mater Technol*, Transactions of the ASME, Vol. 110, 1988, pp. 344-349.

[6.10] Rendler N. J. and Vigness I., "Hole-drilling Strain-gage Method of Measuring Residual Stresses", In: *Proc SESA XXIII*, Vol. 2, 1966, pp. 577-586.

[6.11] Bijak-Zochowski M., "A Semidestructive Method of Measuring Residual Stresses", *VDI-Berichte*, Vol. 313, 1978, pp. 469-476.

[6.12] Niku-Lari A., Lu J. and Flavenot J. F., "Measurement of Residual-Stress Distribution by the Incremental Hole-Drilling Method", *Exper Mech*, Vol. 25, No. 6, 1985, pp. 175-185.

[6.13] Flaman M. T. and Manning B. H., "Determination of Residual Stress Variation with Depth by the Hole-Drilling Method", *Exper Mech*, Vol. 25, No. 9, 1985, pp. 205-207.

[6.14] Beghini M., Bertini L. and Raffaelli P., "An Account Of Plasticity In The Hole-Drilling Method Of Residual Stress Measurement", *J Strain Analysis*, Vol. 30, No. 3, 1995, pp. 227-233.

[6.15] Kornmeier M., Forschungsberichte Institut für Werkstofftechnik, Uni-Gh Kassel, No. 23, 1999.

[6.16] Belassel M., Lebrun J. L., Denis S., Gautier E. and Bettembourg J. P., "Effect of Thermal and Mechanical Loading on the Generation of Macro and Micro Stresses in Eutectoid Steel", In: *Proc 4th Int Conf Residual Stresses*, Baltimore, 1994, pp. 392-401.

[6.17] Nobre J. P., Kornmeier M., Dias A. M. and Scholtes B., "Comparative Analysis of Shot-Peening Residual Stresses Using Hole-Drilling and X-ray Diffraction Methods", *Mater Sci Forum,* Vols. 347-349, 2000, pp. 138-143.

[6.18] Nobre J. P., Kornmeier M., Dias A. M. and Scholtes B., "Use of the Hole-Drilling Method for Measuring Residual Stresses in Highly Stressed Shot-Peened Surfaces", *Exper Mech*, Vol. 40, No. 3, 2000, pp. 289-297.

[6.19] Cahoon J. R., Broughton W. H. and Kutzak A. R., "The Determination of Yield Strength from Hardness Measurements", *Metall Trans*, Vol. 2, 1971, pp. 1979-1983.

[6.20] Tabor D., "A Simple theory of Static and Dynamic Hardness", In: *Proc Roy Soc Lon*, Vol. 192, 1948, pp. 247-274.

[6.21] British Standards Institute, "BS EN 10025:2004 – Hot Rolled Products of Non-Alloy Structural Steels", British Standards Institute, 2004.

[6.22] Nobre J. P., Dias A. M., Gibmeier J. and Kornmeier M., "Local Stress-Ratio Criterion for Incremental Hole-Drilling Measurements of Shot Peening Stresses", *J Engng Mater Technol*, Vol. 128, 2006, pp. 193-201.

[6.23] Schajer G. S., "Stress Calculation Error Analysis for Incremental Hole-Drilling Residual Stress Measurements", *J Engng Mater Technol, Transactions of the ASME*, Vol. 118, 1996, pp. 120-126.

[6.24] Landgraf R. W., "Cyclic Deformation Behavior of Engineering Alloys", In: *Proc Fatigue-Fundamental Applied Aspects*, Sweden, 1977.

[6.25] Kodoma S., "The Behavior of Residual Stress During fatigue Stress Cycles", In: *Proc 2nd Int Conf Mechanical Behavior of Metals*, Society of Material Science, Vol. 2, 1972, pp. 111-118.

[6.26] Farrahi G. H., Lebrun J. L. and Courtain D., "Effect of Shot Peening on Residual Stress and Fatigue Life of a Spring Steel", *Fat Fract Engng Mater Struct*, Vol. 18, No. 2, 1995, pp. 211-220.

[6.27] British Standards Institute, "BS ISO 12108:2002 – Metallic Materials – Fatigue Testing – Fatigue Crack Growth Method", British Standards Institute, 2002.

[6.28] American Society for Testing and Materials, "Standard Test Method for Measurement of Fatigue Crack Growth Rates", ASTM E647-05, American Society for Testing and Materials, 2005.

[6.29] Engineering Science Data Unit, "Fatigue Crack Propagation in Low and Medium Strength Allow Steel Plate, Bar and Forgings", Stress and Strength Vol. 7, ESDU 81011, Engineering Science Data Unit, ISBN 0 85679 336 1, 1981.

[6.30] Holzapfel H., Schulze V., O. and Macherauch E., "Residual stress Relaxation in An AISI 4140 Steel Due to Quasistatic and Cyclic Loading at Higher Temperatures", *Mater Sci Engng*, Vol. A248, 1998, pp. 9-18.

[6.31] Webster G. A. and Ezeilo A. N., "Residual Stress Distributions and Their Influence on Fatigue Lifetimes", *Int J Fat*, Vol. 23, 2001, pp. S375-S383.

[6.32] Menig R., Pintschovius L. Schulze V. and Vöhringer O., "Depth Profiles of Macro Residual Stresses in Thin Shot Peened Steel Plates Determined by X-ray and Neutron Diffraction", *Scripta Materialia*, Vol. 45, 2001, pp. 977-983.

[6.33] Torres M. A. S. and Voorwald H. J. C., "An Evaluation of Shot Peening, Residual Stress and Stress Relaxation on the Fatigue Life of AISI 4340 Steel", *Int J Fat*, Vol. 24, 2002, pp. 877-886.

[6.34] Özdemir A. T. and Edwards L., "Relaxation of Residual Stresses at Cold-Worked Fastener Holes Due to Fatigue Loading", *Fat Fract Engng Mater Struct*, Vol. 20, No. 10, 1997, pp. 1443-1451.

[6.35] Sabelkin V. Martinez S. A., Mall S., Sathish S. and Blodgett M. P., "Effects of Shot-Peening Intensity on Fretting Fatigue Crack-Initiation Bahaviour of Ti-6Al-4V", *Fat Fract Engng Mater Struct*, Vol. 28, 2005, pp. 321-332.

[6.36] Shen G. and Glinka G., "Weight Functions for a Semi-Elliptical Crack in a Finite Thickness Plate", *Theore Applied Fract Mech*, Vol. 15, No. 3, 1991, pp. 247-255.

[6.37] Shen G. and Glinka G., "Weight Function for the Surface Point of Semi-Elliptical Surface Crack in a Finite-Thickness Plate", *Engng Fract Mech*, Vol. 40, No. 1, 1991, pp. 167-176.

[6.38] Fett T., Mattheck C. and Munz D., "On the Calculation of Crack Opening Displacement from the Stress Intensity Factor", *Engng Fract Mech*, Vol. 27, 1987, pp. 697-715.

[6.39] Shiratori M., Niyoshi T. and K. Tanikawa, "Analysis of Stress Intensity Factors for Surface Cracks Subjected to Arbitrarily Distributed Surface Stresses", In: *Stress Intensity Handbook*, Ed: Murakami et al, Pergamon Press, Vol. II, ISBN: 0 08 034809 2, 1987, pp. 698-705.

[6.40] Newman J. C. Jr. and Raju I. S., "Empirical Stress-Intensity Factor Equation for The Surface Crack", *Engng Fract Mech*, Vol. 15, No. 1-2, 1981, pp. 185-192.

[6.41] Corn D. L., "A Study of Cracking Techniques for Obtaining Partial Thickness Cracks of Pre-selected Depths and Shapes", *Engng Fract Mech*, Vol. 3, No. 1, 1971, pp. 45-52.

[6.42] Yen C. S. and Pendleberry S. L., "Technique for Making Shallow Cracks in Sheet Metals", *Mater Res Standards*, Vol. 2, No. 11, 1962, pp. 913-916.

CHAPTER 7

7.0 Conclusions and Recommendations for Future Work

7.1 Conclusions

The main objective of this study was to better understand the influence of surface residual stress on fatigue crack growth in structural components. The increasing trend of the use of welding, cold rolling, shot peening etc. as fabrication techniques means the fatigue performance of many engineering components is affected by the presence of residual stress fields. In order to obtain accurate structural integrity assessments of flawed components when residual stresses are present, it is necessary to account for residual stress distributions. This thesis documents the experimental and analytical work conducted on components containing residual stress fields. Both the damaging effects of surface tensile residual stress and the beneficial effects of surface compressive residual stress are investigated. This current chapter draws together and reviews the work undertaken, summarising the main observations. Areas of future work that will contribute to the knowledge in this field are also presented.

7.1.1 JOSH and VACF Testing of SE 702

Chapter 2 reported the analytical work conducted on the generated JOSH load-time sequence. Although the main constituents employed in the JOSH model are widely regarded as statistically stationary processes individually, appropriate wave and numerical parameters must be used for the generation of a stationary load-time history. It has been shown that the generated VA load-time sequence can be characterised by its ESR, the sea state distribution and the PSD. The post sequence-generation analyses demonstrated that the long term statistical nature of the load-time sequence should be assessed in order to ascertain its validity and suitability for laboratory testing of jack-up structures. The convergence of the sequence parameters and the stationary point of the load-time sequence must be monitored in order to generate an adequately mixed sea state distribution. This is extremely important for load-time history standardisation purposes, so that the VA fatigue test results are representative and comparable with those completed elsewhere.

The validated JOSH sequence was successfully employed in the medium-to-long-life VACF testing of SE 702 presented in Chapter 3. A total of one air test and four corrosion fatigue tests were carried out. The effect of cathodic over-protection and hydrogen embrittlement on the

fatigue performance of SE 702 was simulated using an environmental chamber. The main conclusion drawn from the testing of the SE 702 T-butt welded plates is that the effect of cathodic over-protection and hydrogen embrittlement on HSS is not as critical as reported by previous VACF studies on other HSS. The fatigue results also show that higher negative CP levels resulted in shorter fatigue lives but this was not observed to be as detrimental as suggested by the UK HSE offshore design guidance. In general, SE 702 shows superior fatigue performance in air and under CP when compared to the conventional S355 steel. The fatigue results obtained from the present study are considered to be more appropriate for indicating the long-life service performance of jack-up steels, with two specimens representing a twenty-year round service loading of a jack-up structure. In addition, the fatigue crack growth data collected from the present study are much more stable when compared to previous VACF studies on HSS, illustrating the significance of a statistically stationary load-time sequence.

7.1.2 Residual Stresses in T-butt Welded Joints

The current recommendations by published standards and literature on the inclusion of tensile residual stresses in the assessment of T-butt welded joints containing a crack-like flaw are critically reviewed. The through-thickness residual stress distributions recommended by British Energy Generation Ltd. R6, BS 7910:1999, BS 7910:2005 and API RP 579 are based on published experimental data. These data are predominantly obtained from measurements conducted on medium-strength steels and the validity ranges are limited. These residual stress distributions might not be representative of engineering components manufactured from HSSs but the applicability of these distributions to HSSs is not addressed in the standards. Furthermore, these recommended distributions are shown to be over-conservative when compared to recent residual stress measurement studies by Wimpory and Hyeong et al. Hence, further work is very much needed to verify and expand the validity of the recommended residual stress distributions.

The through-thickness tensile residual stresses in two of the T-butt welded plates were measured using a neutron diffraction technique. Although the trend of the residual stresses is similar, distinctive stress magnitudes can be observed when the data were compared to those obtained from a SE 702 T-butt plate welded with different heat input. Based on the comparison between the residual stress data obtained in the present study and published data, it is believed that the peak transverse residual stresses may be related to the heat input rate to material's yield strength ratio, but further work needs to be carried out to confirm this observation.

For comparison purposes, a tri-linear upper bound residual stress distribution was proposed, based on the neutron diffraction measurement data. Expressed as a continuous piecewise linear function with appropriate intervals, the proposed residual stress field was successfully employed

in the calculation of the effective weld toe SIFs in the T-butt welded joints using SIF weight function methods. The SIF solutions were applied to the experimental data and the results evidently demonstrated the significance of tensile residual stress on the fatigue crack growth data. The fatigue life predictions of T-butt welded joints also clearly show the deleterious effect of tensile residual stress on crack propagation. Hence, it must be taken into account when assessing the residual strength of welded joints.

7.1.3 Preferential Cold Working Methods

Chapter 4 presented the experimental work conducted on stitch cold rolled specimens. The aim of this study was to investigate fatigue crack shape evolution in compressive residual stress fields. A cold rolling rig, capable of applying a cold rolling pressure of 21kN, was designed and constructed. A total of six mild steel specimens, each cold rolled with different stitch rolling parameters, were fatigue tested under pure bending. Fatigue crack growth evolution was monitored using a periodic ACPD inspection technique. The fatigue test results show unprecedented crack growth behaviour and crack retardation effects. Crack initiation was only detected in the unprotected regions. The fatigue lives of all stitch cold rolled specimens were considerably enhanced and the effect of cold working was observed for several million cycles at a nominal cyclic stress close to half yield stress. Furthermore, the crack shapes in all stitch cold rolled specimens were significantly altered. It is shown in the experimental results that cracks loaded under bending extended only very slowly in depth when the length was contained by cold working meaning that through-thickness cracks are unlikely. Despite this, the novel stitch cold rolling technique clearly demonstrated its feasibility in controlling fatigue crack shape by manipulating the surface compressive residual stress fields.

The preferential cold working method was further studied using the stitch shot peening technique. Large scale fatigue tests were carried out on five mild steel specimens under axial tension. The specimens were shot peened with varying stitch peening parameters to promote different crack aspect ratio evolutions. The fatigue test results are similar to those obtained from the stitch cold rolling tests, showing significant crack retardation effects once the crack length met with the shot peened region. All stitch peened specimens show much higher crack aspect ratios at failure when compared to the control-specimen. Residual stress monitoring was also conducted on a test specimen peened with three different shot peening intensity bands.

The fatigue test results obtained from the aforementioned experimental studies illustrate the capability of preferential cold working methods in promoting a localised failure. The stitch shot peened test specimens also show that controlled cold working can be applied to produce high

aspect ratio leak-before-break cracks. These "designer crack" techniques can be implemented to extend components' fatigue life and develop the concept of controlled failure design.

7.1.4 Residual Stress Monitoring and Analyses

The residual stress relaxation behaviour due to cyclic loading was investigated through in-situ residual stress measurements conducted on Test SP6 at different stress cycle intervals. The residual stress data presented in Section 6.2 shows that it is possible to use the ICHD technique in monitoring residual stresses in structural components. However, measured strain relaxation data must be analysed using adequate residual stress analysis methods so that the results are representative of the "actual" residual stress present. In the present study, the EUS Method and the Integral Method were adopted and the differences between the two methods are discussed. The Integral Method has been shown to be most suitable in analysing shot peening residual stresses and the trend of the data obtained in the current study compared well with published literature. The hardness measurement data show that the shot peened surfaces were highly work hardened, resulting in a significant increase in the local material hardness and yield strength. Based on these observations and the recommendations by published literature, the measured residual stress data are considered to be free from the so-called plasticity effect.

The residual stress monitoring programme reported in the present study is considered to be unique in several aspects. Firstly, it is in the author's opinion that this is a rare but comprehensive residual stress relaxation study that utilises a hole-drilling technique. This is due to the fact that most of the residual stress relaxation studies conducted to date are based on X-ray methods and very often they are approached in a qualitative manner to confirm that residual stress decay does occur and measurements were only taken for a few stress cycle intervals. In addition, the use of the ICHD technique also means that depth profiling of residual stresses was made possible without resorting to layer removal techniques, which are known to significantly alter the initial residual stress state. Layer removal techniques have to be employed in X-ray methods for sub-surface measurements. The relatively large dimensions of the specimen used in this study had the advantage of accommodating many measurements and the three different shot peened bands also maximised the number of measurements that could be obtained from a single specimen. This is significant as it was not necessary for the residual stress monitoring test set-up used in this study to be disassembled between measurements. Using a single specimen for residual stress measurement also eliminates possible material anisotropy and batch to batch variation in material mechanical properties and chemical composition. Furthermore, the variation in the initial residual stress state in the respective shot peened surfaces can be assumed to be negligible since they were shot peened in identical conditions.

7.1.5 Surface Crack Growth Evolution Prediction using a SIF Weight Function-Based Model

As stated previously, it is possible to include residual stress fields in the calculation of effective SIFs using a weight function method. This method was further extended in the development of a fatigue crack growth model, as presented in Chapter 6. SIF weight functions coupled with the Paris Law were used as a tool to evaluate "real" surface crack growth behaviour in residual stress fields. Three CT tests were successfully carried out to determine the Paris crack growth coefficients for a S275 steel. The measured residual stress data were incorporated into the crack growth model in the form of relaxation functions at different depths. The stitch peening effect was simulated and the prediction of crack shape evolution provided valuable information on the effect of surface compressive residual stress on surface crack growth behaviour. The crack growth evolution model has been shown to be able to predict crack aspect ratio evolution in stitch peened specimens with reasonable accuracy. In addition, the fatigue crack propagation life of the controlled specimen (Test SP1) was predicted with good accuracy. However, it is clear that the SIF weight function method suffers from practical limitations when applied to surface crack growth prediction in surface cold worked components. Therefore, empirical corrections are needed to enhance its reliability and to extend its applicability in modelling crack shape evolution in anisotropic materials.

7.2 Summary of Main Conclusions and Findings

The preceding section presented the conclusions and observations based on the work conducted in the present study. The main conclusions and findings can be summarised as follows:

- This thesis demonstrated the importance of the long-term statistical nature and stationary effect of a standardised VA load-time sequence. The stationary effect of a load-time sequence has been shown to have a profound effect on the fatigue crack growth data obtained from VA fatigue tests.

- There is still limited data on the characteristics and through-thickness profile of residual stresses present in welded components. Hence, further work is needed so that relevant guidance can be incorporated into existing standards.

- SE 702 showed superior corrosion fatigue performance under VA loading when compared to the conventional medium strength S355 steel. Cathodic over-protection has

a detrimental effect on the fatigue lives but not as critical as suggested by the UK HSE offshore design guidance.

- It is possible to employ a SIF weight function method in the calculation of effective SIFs in tensile residual stress fields. The inclusion of residual stress fields has been shown to significantly alter the fatigue crack growth rate data.

- The two newly developed preferential cold working methods, the stitch cold rolling and stitch shot peening techniques, have been demonstrated to be able to promote localised failures, control fatigue crack shape evolution and extend the service life of structural components.

- The ICHD technique has been employed in the study of residual relaxation behaviour due to cyclic loading on shot peened components. Residual stress relaxation has been clearly demonstrated to be a function of applied cyclic stress range.

- SIF weight functions have been used to simulate crack shape evolution of surface cracks reside in residual stress fields. The novel fatigue crack growth model developed in the present study takes into account residual stress relaxation effects and can be used to predict fatigue crack propagation life of components containing residual stress fields.

7.3 Recommendations for Future Work

This thesis presented novel approaches to fatigue and fracture mechanics of structural components containing residual stress fields. Based on the findings obtained, the following future work is identified for further development of the methodologies presented in the present study:

- Further develop the JOSH model using service data obtained from different jack-up platform installation sites apart from the North Sea region. This will help to expand the validity of the JOSH framework and increase confidence in the use of this model in analysing jack-up structures at different jack-up operating locations.

- Conduct more long-life VACF tests using different CP levels. Other influencing factors such as mean stress should also be investigated for the corrosion fatigue resistance of HSSs under VA loading. This will enhance the library of data for such steels and verify the overall trend in the fatigue performance of HSSs so that the results can be incorporated into a suitable jack-up platform installation design guidance.

- Investigate the relaxation behaviour of residual stresses in welded joints under realistic loading. This could be achieved using non-destructive residual stress measurement techniques such as ultrasonic and magnetic methods. Alternating Current Stress Measurement (ACSM) [7.1-7.3], a non-contacting magnetic method, has recently been demonstrated to be able to measure residual stresses in bi-axial stress systems.

- Modify the current cold rolling rig to accommodate a higher rolling capacity (i.e. large roller) so that the area of cold rolled regions could be increased. This will allow residual stresses on the cold worked surface to be measured using different measurement techniques. An automated jacking system should also be included for the purpose of residual stress field uniformity during the cold rolling process.

- Further implement the preferential cold working method using the recently developed state-of-the-art laser shock peening technique [7.4]. This technique has been shown to be able to introduce compressive residual stress field onto metallic components up to a penetration depth of 10mm. It has also been demonstrated to significantly enhance mechanical properties and fatigue strength of treated components. Another main advantage of this technique over shot peening is that the process does not introduce surface roughness.

- Conduct more fatigue tests on preferential cold worked specimens in a systematic manner with varying parameters such as unprotected length and plate thickness. These tests will provide an empirical basis for a wider analysis of crack shape evolution under residual stress fields and allow the optimum preferential cold working parameters to be studied.

- Apply ACSM to the investigation of residual stress relaxation under cyclic loading and compare the results with the residual stress data obtained in the present study. The ACSM technique could compliment ICHD measurements since it has a good accuracy for near-surface measurements but a low penetration depth.

- Further extend the application of SIF weight functions in crack shape evolution prediction by incorporating anisotropy effects into the model. The crack growth model can be modified to accommodate different crack growth coefficients for the work hardened surfaces. The plasticity effect induced by cold working processes could be investigated through elasto-plastic fracture mechanics analysis.

7.4 References

[7.1] Dover W. D. and Zhou J., "Non-contacting Stress Measurement", *Insight*, Vol. 40, No. 5, 1998, pp. 340-343.

[7.2] Chen K. and Brennan F. P., "A Theoretical and Experimental Study of Alternating Current Stress Measurement Under Different Loading Modes", *J Strain Analysis Engng Design*, Vol. 212, No. 5, 1998, pp. 291-303.

[7.3] Han S., Brennan F. P. and Dover W. D., "Development of the Alternating Current Stress Measurement Model for Magnetostriction Behaviour of Mild Steel Under Orthogonal Magnetic Fields for Stress Measurement", *J Strain Analysis*, Vol. 37, No. 1, 2001, pp. 21-31.

[7.4] Hammersley G., Hackel L. A. and Harris F., "Surface Prestressing to Improve Fatigue Stength of Components by Laser Shot Peening", *Optics Lasers Engng*, Vol. 34, 2000, pp. 327-337.

Appendix A

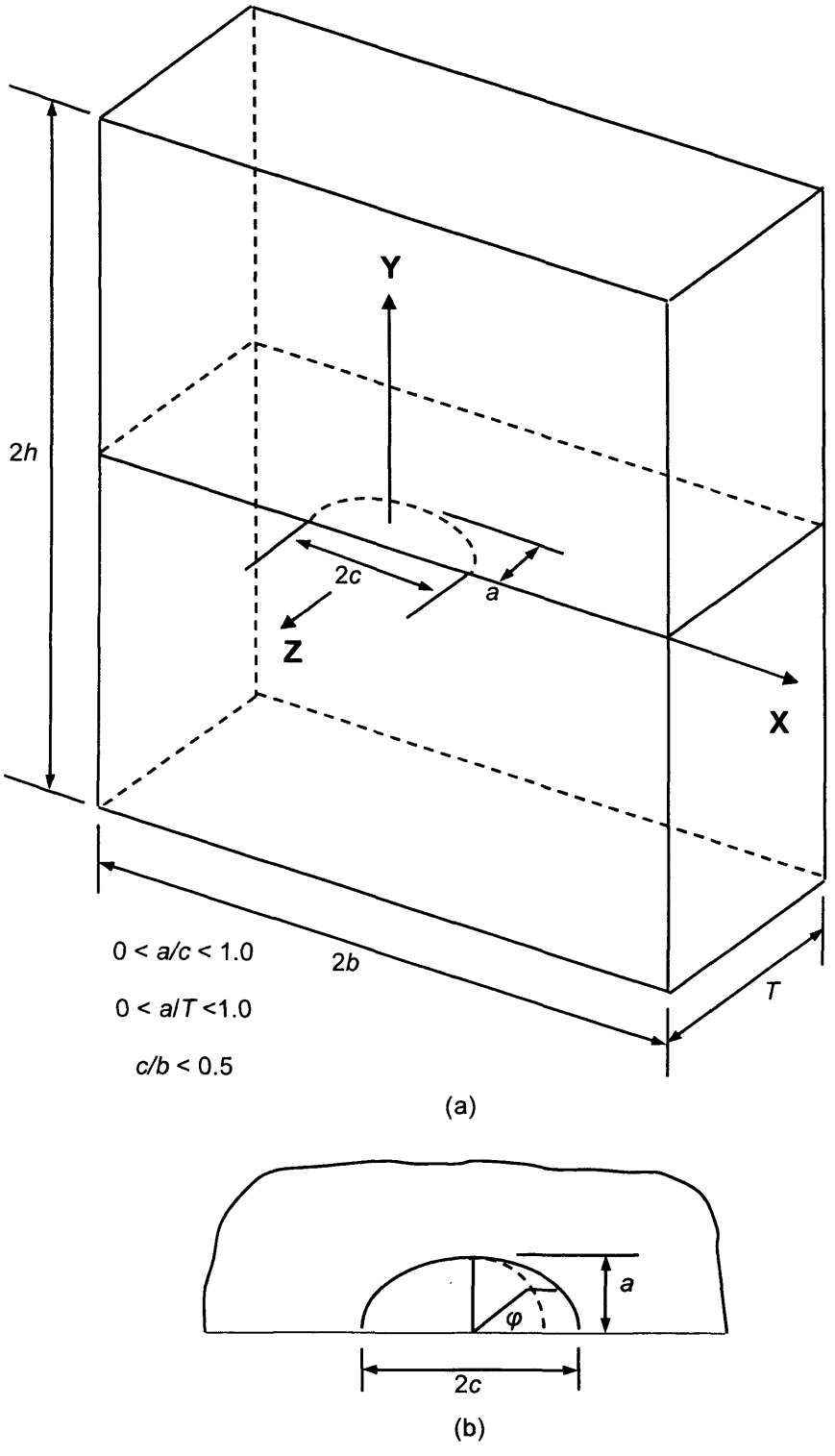

Figure A1: Notation of Semi-elliptical Surface Crack (a) Surface Crack in a Finite Thickness Plate, (b) Semi-elliptical Surface Crack

Appendix B

B.1 Pseudo-Random Binary Shift (PRBS) Generator

Similar to the WASH model, the JOSH framework generates the random load history within the duration of any particular sea state from the corresponding power spectral density function. There are several methods that can be used to perform this process, and these include the random range generator, the Markovian load range generator, Fourier summation random walk technique and the pseudo-random binary shift technique [B1]. The Pseudo-random Binary Shift (PRBS) Generator was adopted for both the WASH and JOSH framework because it provides a good simulation of the frequency content, which is of primary importance for corrosion fatigue testing. Besides that, the versatile nature of the generator enables the simulation of all types of spectrum.

The PRBS technique makes use of a shift register (a series of 0 and -1; On and Off) of arbitrary length and the schematic diagram of this technique is shown in Fig. B1. The length of the shift register determines the resolution of the power spectrum to be generated. A white noise $\varepsilon(t)$ (the time history corresponding to a uniform power spectrum) can be easily generated with this register. At each clock pulse (signal output time), all the digits are shifted one place to the right, with the last digit abandoned and the first is formed from either a two way (M, L) or a four way (M, L, M_1, L_1) feed back loop (see Fig. B1). In this study, a four way feed back loop was adopted. This white noise is then passed through a digital filter $h_x(\tau)$ (Equation B1), which amplifies all the desired frequency components so that unwanted frequencies remain, but only as an insignificant part of the time history. For any particular power spectral density function, the filter function is taken as the inverse discrete Fourier transform of the function, $H_x(f)$ before the loading characteristics can be generated. The inverse Fourier transform function is obtained from the white noise spectrum, $S_\varepsilon(f)$, relevant to the power spectral density function (PSD), $S_x(f)$ (Equation B2).

$$h_x(\tau) = \int_0^\infty H_x(\omega) e^{-i\omega t} d\omega \qquad \text{- (B1)}$$

$$S_x(f) = |H_x(f)|^2 S_\varepsilon(f) \qquad \text{- (B2)}$$

This technique features a programmable return period and the sequence is also reproducible across different machines because the shift register consists of integers 0 and 1 and there will neither be rounding error nor overflow. The detailed procedure used in implementing this technique can be found in References B1 and B3. However, the PRBS technique utilised in generating the random load history can be summarised as follow:

- Given power spectrum
- Calculation of transfer function
- Evaluation of filter function
- Construction and preparation of shift register
- Signal generation by shifting register and then filtering

B.2 The Markov Chain Technique

After generating a random loading sequence from the relevant power spectral density function using the PRBS technique, the next step is to reproduce the long term behaviour for a combination of naturally-occurring multiple sea states. The long term multiple sea state behaviour of the load history is widely regarded as a random process. The Markov Chain technique is adopted for generating a transition matrix for multi-sea state modelling. This technique analyses the tendency of the likelihood of one event to be followed by another. According to the Markov Chain technique, each sea state can either transit to another sea state which is directly above or below itself, or remain unchanged. The occurrence of any single sea state does not affect the long term distribution of the complete sequence and the long term occurrence probabilities should coincide with the long term sea state distribution in the system. This technique assumes that the present is independent of the prior events occurred. Hence, the robustness of the Markov Chain technique is suitable for dependent random events such as multi-sea state modelling, where the outcome depends only on the present state and its long term statistic.

In this method, the random sea state sequence is generated using the calculated probability transition matrix which can be mathematically expressed as:

$$\Pi(p+1) = T^i \, \Pi(p) = T^{i,p+1} \, \Pi(0) \qquad \text{- (B3)}$$

Where $\Pi(p)$ is the transition matrix containing the probability of occurrence of each sea state after p transitions and T^i is the transpose of the Markov Chain matrix. After a large number of

transitions, the long term probability distribution of sea states can be represented by the state transition matrix as:

$$\Pi(p+1)=\Pi(p)=\Pi(\infty) \qquad \text{- (B4)}$$

In JOSH, the significant wave height and their average occurring duration of the individual sea states were used as the primary parameter to evaluate the state transition matrix. Although the most realistic approach to obtain the real sea-states transition would be the long term real-time recording of the wave movements, it is a highly impractical and expensive process. Hence, Olagnon [B4] proposed an alternative method in which a tri-diagonal transition matrix (Fig. B2) can be estimated from the long-term probability distribution of the sea states. The elements of T can be determined from $\Pi(\infty)$ and other state duration information. Olagnon proposed that the expected duration of sea state (in seconds) in the North Sea according to its significant wave height can be estimated by the following equation:

$$D = e^{\left\{\frac{5.6-H_s}{1.4}\right\}} \quad \text{for } H_s < 5\text{m} \qquad \text{- (B5)}$$

$$D = e^{\left\{\frac{8.0-H_s}{5.5}\right\}} \quad \text{for } H_s > 5\text{m} \qquad \text{- (B6)}$$

Once a current sea state is known (either input as the first state or resulted from a previous transition), the next state can be determined by using the Monte Carlo method [B5]. This is schematically illustrated in Fig. B3 and can be mathematically expressed as:

$$T_{ii} = 1 - \frac{B}{D} \qquad \text{- (B7)}$$

$$\frac{F_i}{D_i} = \frac{F_{i-1}}{D_{i-1}} * \frac{T_{i-1,i}}{1-T_{i-1,i-1}} + \frac{F_{i+1}}{D_{i+1}} * \frac{T_{i+1,i}}{1-T_{i+1,i+1}} \qquad \text{- (B8)}$$

where T_{ij} is the probability of transition from sea state i to sea state j

B is the (sub) block duration

D_i is the average duration of sea state i, D

F_i is the fraction of time spent in sea state i $(\Pi(i)(p=\infty))$

During this process, uniformly distributed random numbers between 0 and 1 are generated by using a congruential expression and this is used to indicate a certain state transition probability (up, down or remain) (Fig. B3). In order to achieve machine independence, long return period, numerical stability (no rounding errors) and high resolution are recommended. This is achieved by utilising a variant of the PRBS-based random number generator. Pre-shifts are introduced into the sequence generation to eliminate all transient behaviour. It must be noted that in order to generate a statistically stable and reproducible sequence, the combination of the number of shift register elements, return period, resolution and the number of pre-shifts, must be adequately implemented in both the PRBS technique and Markov Chain method. The details of the numerical parameters can be found in [B6].

B.3 References

[B1] J. C. P. Kam, Wave Action Standard History (WASH) for Fatigue Testing Offshore Structures, Applied Ocean Research, Vol. 14, Issue 1, pp.1-10, 1992.

[B2] L. S. Etube, Fatigue and Fracture Mechanics of Offshore Structures, Engineering Research Series- ERS-4, Professional Engineering Publishing Ltd., ISBN 1-86058-312-1, 2001.

[B3] J. C. P. Kam and W. D. Dover, The Procedures to Generate the Wave Action Standardised History (WASH)- The Manual, UCL Report to the WASH Committee, 1988.

[B4] M. Olagnon, G. Lebas and J. Thebault, Characterisation of Sea-States for Fatigue Testing Purposes, Proceeding of 7th International Symposium of Offshore Mechanics and Artic Engineering, ASME, Houston, 1988.

[B5] J. C. P. Kam, Wave Action Standard History (WASH) for Fatigue Testing Offshore Structures, Applied Ocean Research, Vol. 14, Issue 1, pp.1-10, 1992.

[B6] Press W. H., Flannery B. P., Teukolsky S. A. and Vetterling W. T., "Numerical Recipes in C: The Art of Scientific Computing- 2nd Edition", Cambridge University Press, ISBN 0521431085, 1992.

.4 Figures

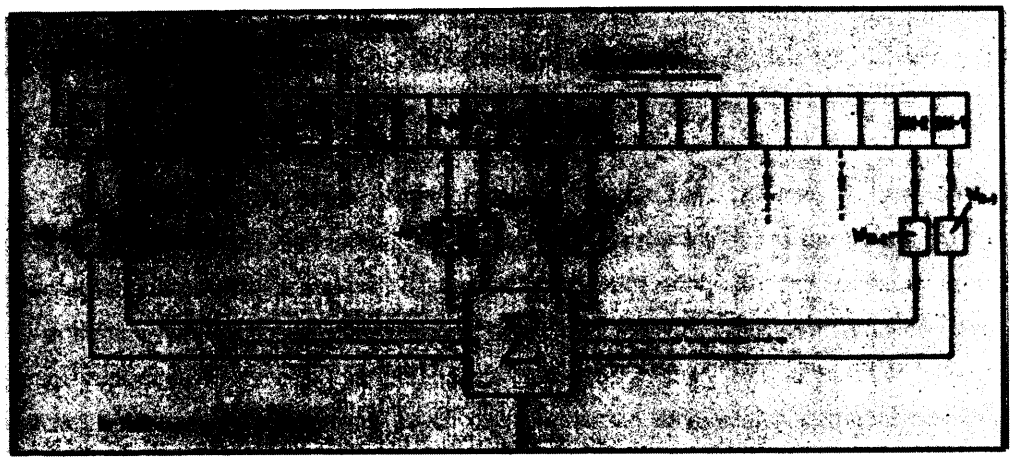

Figure B1: Schematic diagram of the PRBS technique [B2]

$$T = \begin{bmatrix} T_{11} & T_{12} & 0 & 0 & 0 & 0 & 0 & 0 \\ T_{21} & T_{22} & T_{23} & 0 & 0 & 0 & 0 & 0 \\ 0 & \bullet & \bullet & \bullet & 0 & 0 & 0 & 0 \\ 0 & 0 & \bullet & \bullet & \bullet & 0 & 0 & 0 \\ 0 & 0 & 0 & T_{i,i-1} & T_{i,i} & T_{i,i+1} & 0 & 0 \\ 0 & 0 & 0 & 0 & \bullet & \bullet & \bullet & 0 \\ 0 & 0 & 0 & 0 & 0 & \bullet & \bullet & \bullet \\ 0 & 0 & 0 & 0 & 0 & 0 & T_{n,n-1} & T_{nn} \end{bmatrix}$$

Figure B2: Illustration of the tri-diagonal nature of the transition matrix

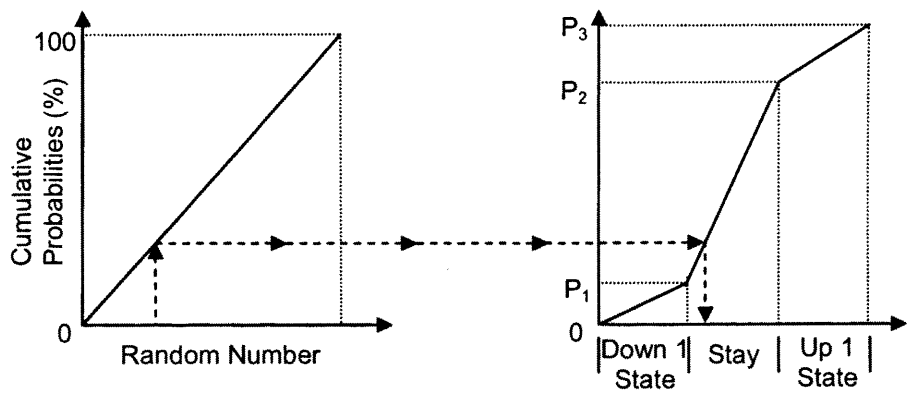

$P_1 = T_{i,\,i-1}$
$P_2 = P_1 + T_{i,\,i}$
$P_3 = P_2 + T_{i,\,i+1} = 100\%$

Figure B3: Sea state transitions by Monte Carlo Method

Appendix C

C.1 Cycle Counting

It is well known that fatigue crack growth behaviour is strongly affected by the load history, especially in variable amplitude loading, where the fatigue characteristics cannot be expressed in fundamental fatigue parameters alone. Hence, it is vital that adequate and representative fatigue damage accumulation is implemented during fatigue and fracture analysis. Cycle counting is the process of reducing a complex variable amplitude load history into a number of equivalent constant amplitude stress excursions which can be related to available constant amplitude test data. In order to evaluate the cumulative fatigue damage analysis, the load history has to be 'broken down' into individual cycles using the appropriate counting method. The most commonly used methods include simple range counting, peak counting, level-crossing counting and rainflow counting.

Simple range counting is considered to be the simplest method of all, which only requires the stress or strain ranges between successive reversals are counted. This is done by extracting the half cycles and counting from local maximum to local minimum. However, it does not give any information on the actual peaks unless the stress returns to zero between cycles and often larger ranges normally associated with fatigue damage can be missed. Hence, this technique is considered not very reliable and unrepresentative of the true fatigue damage. On the other hand, peak counting is based on the identification of local maximum and minimum stresses in the continuous sequence. In this method, the peaks above a prescribed mean level are counted, with the troughs below the mean. This implies that troughs which are negative peaks above or positive peaks below zero are not directly taken into account. Hence, peak counting method is more suitable for narrowband signal. In level-crossing counting method, a count is made when the stress in the sequence crosses an arbitrary level, usually the mean level of the complete history. When zero is set to be the reference level, this method is usually known as zero-crossing counting. The individual crossings counted will then be combined to form complete cycles. Zero-crossing is widely used in offshore wave modelling to identify wave height, which is then used to establish multi-sea states data. Like other cycle counting methods, the level-crossing counting method tends to give a conservative fatigue live estimates and does not lead to a complete reproduction of the original sequence.

C.1.1 Rainflow Counting

The rainflow counting method is generally considered to be the best approach for estimating the fatigue damage caused by variable amplitude loading conditions. The method was developed by Endo et al [C1, C2] and it was named after a rainflow analogy adopted in their early work on cycle counting. The main advantage of this counting method is that it can be used for both narrowband and broadband signals. In addition, its generic nature of identifying closed stress-strain hysteresis loops in cyclic loading makes it the most reliable and accurate counting technique. This unique feature also makes it the most realistic fatigue damage summation and fatigue life prediction method available. In variable amplitude loading conditions, a commonly used damage model, the Palmgren-Miner Linear Rule [C3, C4], is implemented. When used in conjunction with the predicted stress-strain response of a material, this technique provides vital insight into the effect of a given strain history on the materials response. One shortcoming of this method is that it requires a complete load history for accurate analysis.

Since its recognition, a series of counting techniques have been developed under the principle of rainflow method. These include range-pair counting, hysteresis loop counting and ordered overall range counting. Although the main features of these methods vary, the unique characteristics of rainflow concept can still easily be identified. Knowing the advantages of the rainflow method and after prudent consideration, the rainflow cycle counting method was used as the primary cycle counting technique in the current JOSH framework.

C.2 References

[C1] Endo T., Misunaga K. and Nakagawa H., "Fatigue of Metals Subjected to Varying Stress-Prediction of Fatigue Lives", *Preliminary Proceedings of The Chugoku-Shikoku District Meeting*, The Japan Society of Mechanical Engineers, 1967, pp. 41-44.

[C2] Matsuishi M. and Endo T., "Fatigue of Metals Subjected to Varying Stress- Fatigue Lives under Random Loading", *Preliminary Proceedings of The Chugoku-Shikoku District Meeting*, The Japan Society of Mechanical Engineers, 1968, pp. 37-40.

[C3] Palmgren A., "Durability of Ball Bearings", *Z Ver Deut Ing*, Vol. 68, No. 14, 1924, pp. 339-341.

[C4] Miner M. A., "Cumulative Damage in Fatigue", *J Appl Mech*, Vol. 12, Trans. ASME Vol. 67, 1945, pp. A159-A164.

Appendix D

D.1 The Equivalent Stress Range Concept

Paris et al [D1] first proposed the equivalent fatigue damage concept for relating fatigue damage under constant amplitude to variable amplitude loading. It was proposed that the loading stresses can be averaged using the root mean square method. However, this method is not suitable for fatigue, as most of the damage is caused by the magnitude of the stress range applied. Dover et al [D2, D3] extended the concept as the weight average stress range (WASR) or the equivalent stress range approach, for more realistic representation of the fatigue crack growth analysis of tubular joints.

The equivalent stress range is basically an imaginary constant amplitude stress range which would cause the same fatigue damage as the total linearly cumulated damage caused by the variable stress cycles in random stress history. For this approach to be valid, the effects due to stress cycle interaction [D4] and the mean stress level are assumed to be negligible. This assumption has been shown adequate in analysing the fatigue behaviour of offshore structures under variable amplitude loading conditions [D5-D7]. Using this approach and assuming that Paris Law applies, the equivalent stress range can be mathematically expressed as:

$$\frac{da}{dN} = C\left(Y\sqrt{\pi a}\right)^m S_h{}^m \qquad \text{- (D1)}$$

$$S_h = \left[\int_0^n \Delta S^m p(\Delta S) d(\Delta S)\right]^{\left(\frac{1}{m}\right)} \qquad \text{- (D2)}$$

$$= \left[\Sigma(\Delta S)^m P(\Delta S)\right]^{\left(\frac{1}{m}\right)} \qquad \text{- (D3)}$$

where S_h is the weighted average or equivalent stress range
ΔS is an individual stress range
m is the Paris crack growth constant
$p(\Delta S)$ is the probability density of the stress range, ΔS
$P(\Delta S)$ is the probability of occurrence of the stress range, ΔS

In other words, the expression simply weights the individual stress range to the power of the materials crack growth constant, m, and then take the m^{th} root of the average result. The main drawback of this approach is that it ignores the load interaction effect, which becomes more critical in multi-sea state corrosion fatigue. In order to eliminate the load interaction effect, Etube [D6] proposed the sea state equivalent stress concept, which relies on using sea state parameters to determine the sea state equivalent stress range. However, this can be a tedious and time-costing process since a complete realistic load history will contain thousands of sea state transitions and there are 2000 sea states transitions used in the current sequence. This means that the sea state equivalent fatigue crack growth analysis will become extremely difficult as the instantaneous crack growth at a particular sea state can only be estimated. This is due to the fact that it would be impractical to adopt a small crack measurement inspection interval.

It has been demonstrated that when coupled with the rainflow cycle counting method, the equivalent stress range approach produced satisfactory results. If the clipping ratio of the stress history ($\sigma_{max}/\sigma_{RMS}$) is kept low, the load interaction effect is believed to be negligible. Hence, the conventional equivalent stress range concept is adopted for the fatigue and fracture analysis of the specimens.

D.2 References

[D1] Paris P. and Erdogan F., "A Critical Analysis of Crack Propagation Laws, *J Basic Eng*, Transactions of the American Society of Mechanical Engineers, 1963, pp. 528-534.

[D2] Chaudhury G. K. and Dover W. D., "Fatigue Analysis of Offshore Platforms Subject to Sea Wave Loading", *Int J Fatigue*, Vol. 7, 1985, pp. 13-19.

[D3] Hibberd R. D. and Dover W. D., "Random Loading Fatigue Crack Growth in T-Joints", Offshore Technology Conference, 1977, pp. 365-373.

[D4] Skorupa M., "Load Interaction Effects during Fatigue Crack Growth under Variable Amplitude Loading- A Literature Review. Part I: Empirical Trends", *Fatigue Frac Eng Mat Struc*, Vol. 21, 1998, pp. 987-1006.

[D5] Kam J. C. P., "Wave Action Standard History (WASH) for Fatigue Testing Offshore Structures", *Appl Ocean Research*, Vol. 14, Issue 1, 1992, pp. 1-10.

[D6] Etube L.S., Myers P., Brennan F. P. and Dover W. D., "Constant and Variable Amplitude Corrosion Fatigue Performance of a High Strength Jack-up Steel", Proc of The International Offshore and Polar Engineering Conference, Vol. IV, 1998, pp. 123-130.

[D7] Tantbirojn N., Bowen R. J., Etube L. S., Dover W. D., Kilgallon P. J., Roberts T. and Spurrier J., "Variable Amplitude Corrosion Fatigue of Jack-up Steels", Health and Safety Executive Offshore Technology Report, 2001/79, ISBN 0 7176 2319 X, 2001.

Appendix E

Groupe Arcelor

Project :
SE 702

Centre for research on materials in Le Creusot
Edition: 19 février 2003 Schéa 1/2

Date :	10 février 2003
Process :	SAW / 121
Welder :	JCW

Record n°

Base material

Mark:	1
Type:	Plate
Trade mark:	SE 702 TSS3
Standard name:	/
Supplier:	Industeel
Heat number:	S51-1523701-1
Product number:	677379-3-63783
Thickness: (mm)	50
Size: (mm)	(2) 1000 x 500 (250)

Filler material

Welding sequence:	A
Type:	Flux cored wire
Trade mark:	Fluxocord 42
Standard name:	/
Supplier:	Oerlikon
Diameter: (mm)	3,2
Heat number:	8M4561
Baking: (°C-h)	/
Storage: (°C)	20°C

Shielding gas or flux

Welding sequence:	A
Type:	Powder flux
Trade mark:	OP 121 TT W
Standard name:	/
Supplier:	OERLIKON
Composition:	/
Heat number:	
Baking: (°C-h)	350°C/2h
Storage: (°C)	150°C

Specified welding conditions

Welding sequence:	A
Heat input: (kJ/mm)	1,8
Voltage: (V)	30
Amperage: (A)	550
Travel speed: (cm/min)	55
Current polarity:(DC+/-)	DC -
Wire feed rate: (m/min)	/
Joint preparation:	Machining
Welding position:	PA /1G
Gas flow rate: (l/min)	/
Gas nozzle Ø: (mm)	/
Bead push / pull:	Perpendicular
Stick-out: (mm)	32
Tungsten electrode: Ø	/
Back shielding: (y/n)	no
Gas flow rate: (l/min)	/
Back gouging: (y/n)	no
Back gouging method:	/
Clamping : (y/n)	yes
Preheating: (°C)	100°C
Interpass temp.: (°C)	180°C
Postheating: (°C-h)	150°C/2h

N.D.E.

Visual:	yes
Dye penetrant:	no
Magnetoscopic:	no
Ultrasonic exam. :	no
Radiograph:	no
Design code:	ASME IX

PWHT

Type :	/
Furnace temp.: (°C)	/
Heating: (°C/h)	/
Holding temp.: (°C)	/
Holding time: (h)	/
Cooling: (°C/h)	/
End temp.: (°C)	/

Power-source

Brand:	LINCOLN
Type:	DC 1000
Current: (AC / DC)	DC
Pulsed / Cunstant:	Cunstant
Auto/Manual:	Auto

Welding sequence

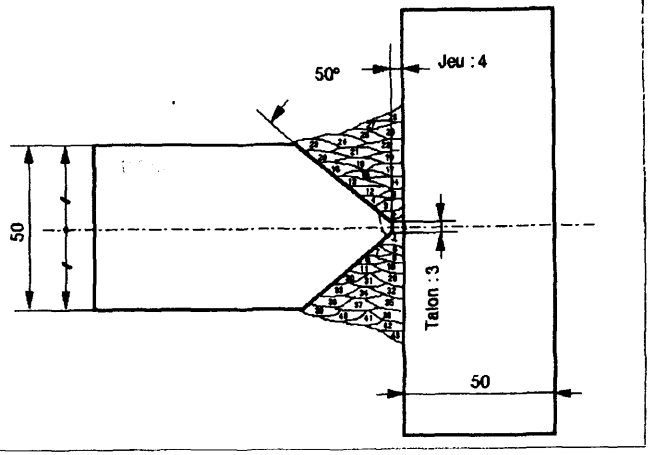

Approbation welding report

	Welder	Welding technicien	Metalurgist	Engineer
Date				
Surname	J-Cl.Wang	J-Cl.Wang	F.Reverdiau	D.Cardamone
Visa				

Figure E1: Welding technical sheet for SE 702 T-butt welded plate specimens

E.1 Alternating Current Potential Difference Method (ACPD)

The Alternating Current Potential Difference (ACPD) [E1, E2] technique is a contacting non-destructive inspection (NDI) method. Other alternating current NDI which utilise the skin effect of an AC passing through an electrical conductor to measure flaws and stress includes Alternating Current Field Measurement (ACFM) and Alternating Current Stress Measurement (ACSM) [E3, E4]. By choosing suitable inspection intervals it was possible to use this technique to monitor crack growth from initiation to specimen failure.

The ACPD technique involves applying an alternating current to the specimen, using contacting probes to establish a uniform thin-skin electric field on the surface of the specimen as shown in Fig. E1a. A surface breaking crack disturbs the current flow, resulting in a potential drop in across the crack. This potential drop can be measured* using point contact techniques and the crack depth can then be calculated from the ratio of the surface potential difference measure across the crack, V_1 and on an unflawed region adjacent to the crack, V_2 as illustrated in Fig. E1b. During measurements, a suitable static load (usually the mead load) is normally applied to the specimen so that the crack surfaces will stay opened. Assuming that the material is homogeneous and the electric field remains uniform on the specimen surface and crack faces, the crack depth can be calculated using a simple one-dimensional calculation. It can be shown that the crack depth is related to the two voltages by the formula [E1]:

$$d = \left(\frac{V_2}{V_1} - 1\right)\frac{\Delta}{2} \qquad \text{- (E1)}$$

where d is the estimated crack depth
V_2 is the voltage across crack
V_1 is the reference voltage across unflawed region
Δ is the distance between voltage probe electrodes

The one dimensional solution given above was based on an infinitely long crack in an infinite plate. Hence, discrepancies will arise in crack depth estimates for semi-elliptical cracks compared with actual values. This problem has been investigated by Dover et al [E2] and it was concluded that it can be solved as a 2-dimensional Laplacian problem. By using this method with conformal mapping techniques and other numerical methods, an appropriate modifying factor was introduced. The details can be found in Reference E2.

The ACPD technique had been employed because of its robustness and relative simplicity compared to other crack measurement techniques. Crack depth predictions are based on mathematical modelling, therefore do not require calibration and can provide a rapid crack depth measurement. In addition, the accuracy of this technique in crack sizing is well established and it has been successfully used in many applications [E5-E7].

E.2 References

[E1] Dover W.D. and Collins R., "Recent Advances in the Detection and Sizing of Cracks Using Alternating Current Field Measurements (A.C.F.M.)", *British J NDT*, Vol. 22, 1980, pp. 291-295.

[E2] Dover W.D., Charlesworth F. D. W., Taylor K. A., Collins R. and Michael D. H., "The Use of AC Field Measurement to Determine the Shape and Size of a Crack in a Metal", Eddy Current Characterisation of Materials and Structures, Editors: Birnbaun G. and Free G., American Society of Testing Materials Publications, STP 722, 1982, pp. 401-427.

[E3] Dover W. D. and Zhou J., "Non-Contacting Stress Measurement", *Insight*, Vol. 40, No. 5, 1998, pp. 340-343.

[E4] Chen K. and Brennan F. P., "A Theoretical and Experimental Study of Alternating Current Stress Measurement under Different Loading Modes", *J Strain Analysis Eng Design*, Vol. 212, No. 5, 1998, pp. 291-303.

[E5] Dover W. D. and Bond L. J., "Crack Characterisation in Welded Nodes As Found in Offshore Structures Using ACPD and Ultrasonic Techniques", 11th *Int Conf Nondestructive Testing*, 1985, pp. 1539.

[E6] Livingstone F. and Kilpatrick I. M., "On-line Fatigue Crack Growth Monitoring in Externally Pressurised Vessels using the Alternating Current Potential Drop (ACPD) Technique", *Review of Progress in Quantitative Nondestructive Evaluation*, Vol. 7B, 1998, pp. 1531-1539.

[E7] Michael D. H., Collins R. and Dover W. D., "Detection and Measurement of Cracks in Threaded Bolts with an AC Potential Difference Method", In: *Proc Royal Society London*, Vol. A385, 1983, pp. 145-168.

E.3 Figures

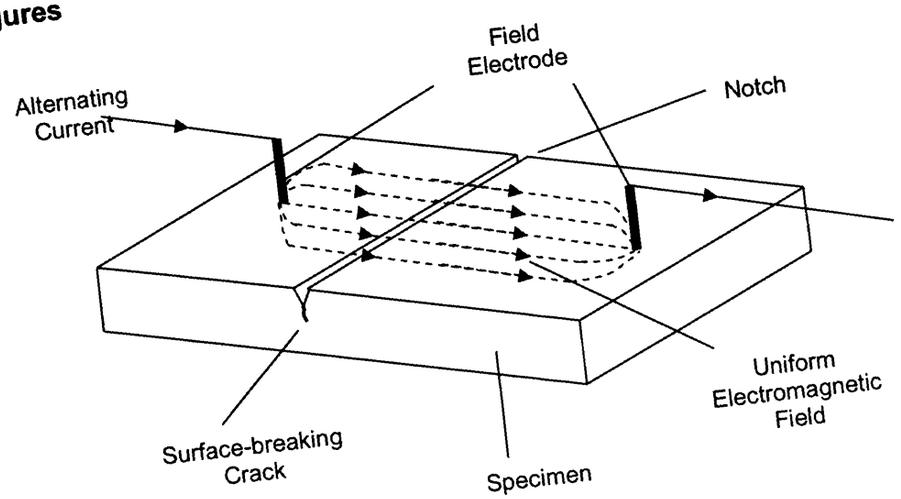

(a)

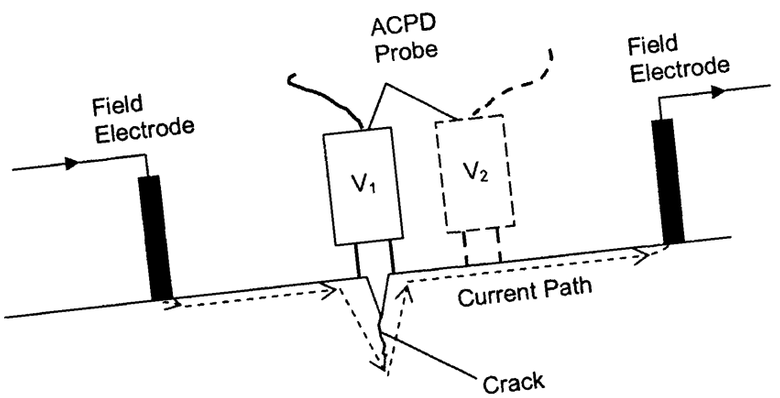

(b)

Figure E1: Schematic illustration of the ACPD technique

Appendix F

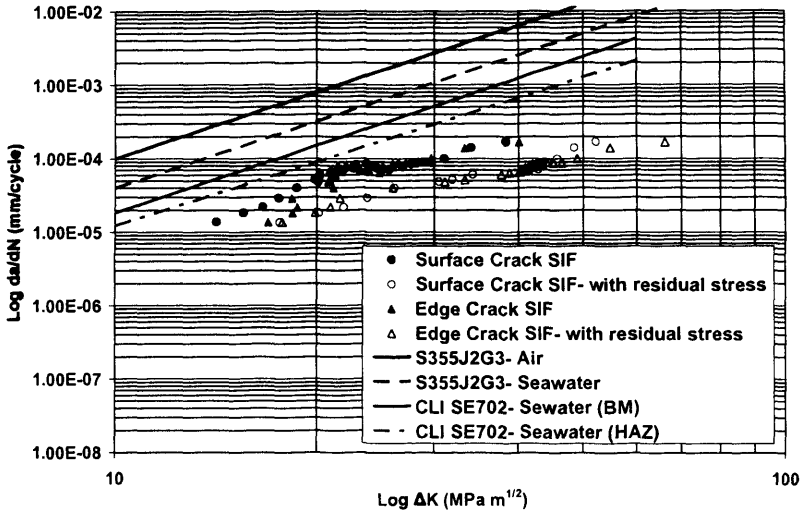

Figure F1: Fatigue crack growth rate vs. SIF range for Test 1

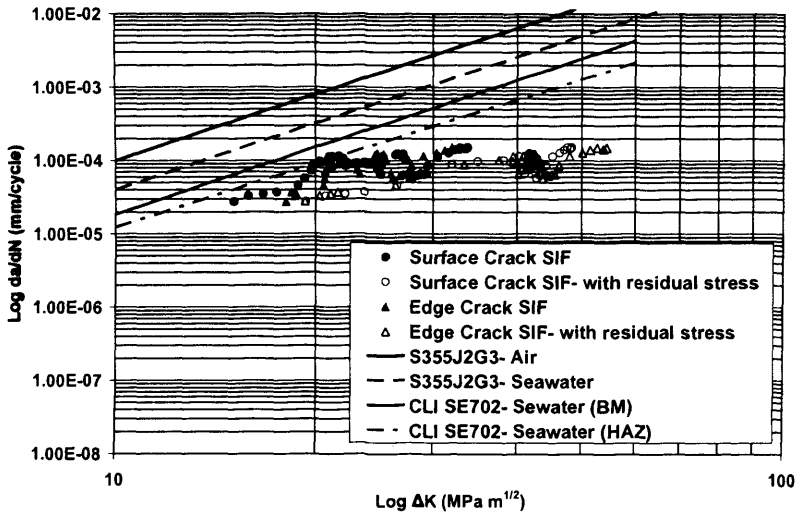

Figure F2: Fatigue crack growth rate vs. SIF range for Test 2

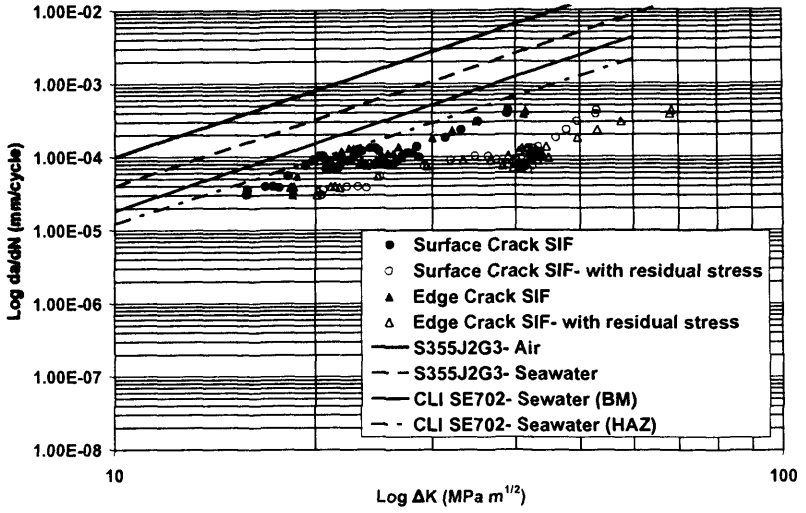

Figure F3: Fatigue crack growth rate vs. SIF range for Test 3

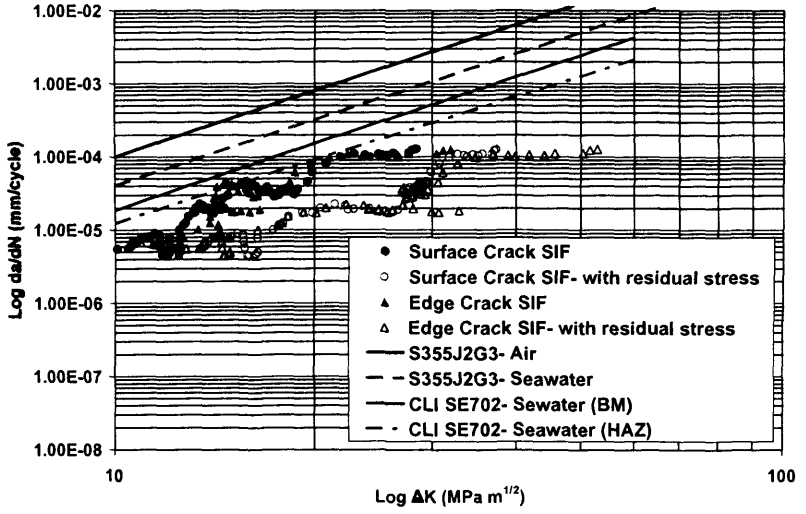

Figure F4: Fatigue crack growth rate vs. SIF range for Test 4

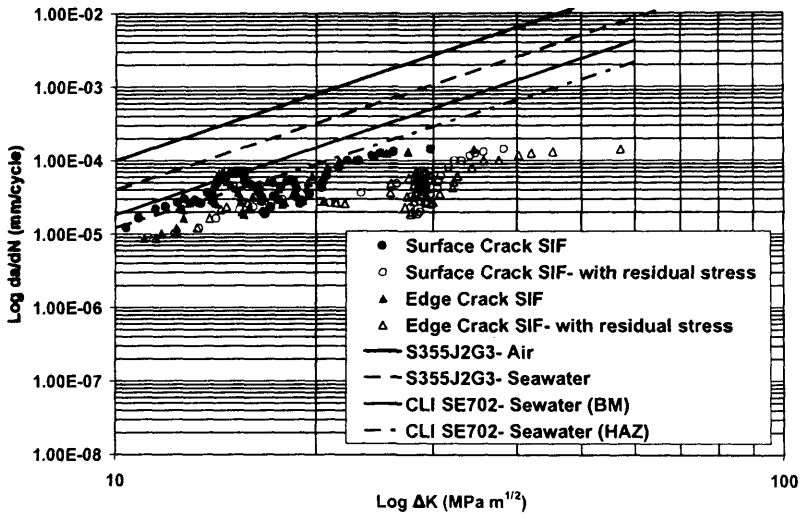

Figure F5: Fatigue crack growth rate vs. SIF range for Test 5

Appendix G

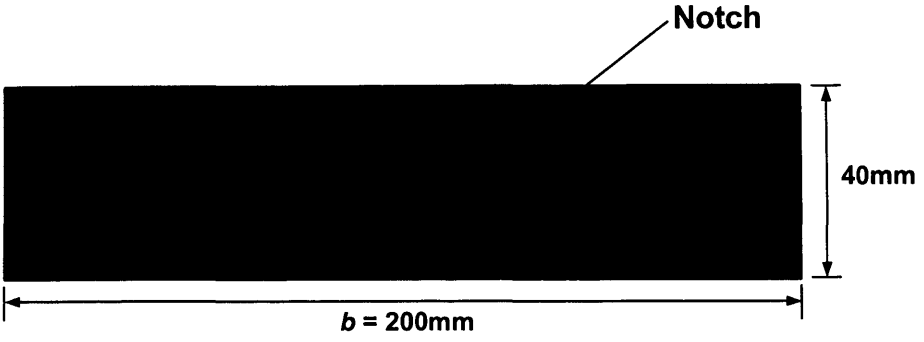

(a) Test CR1: Non-cold rolled

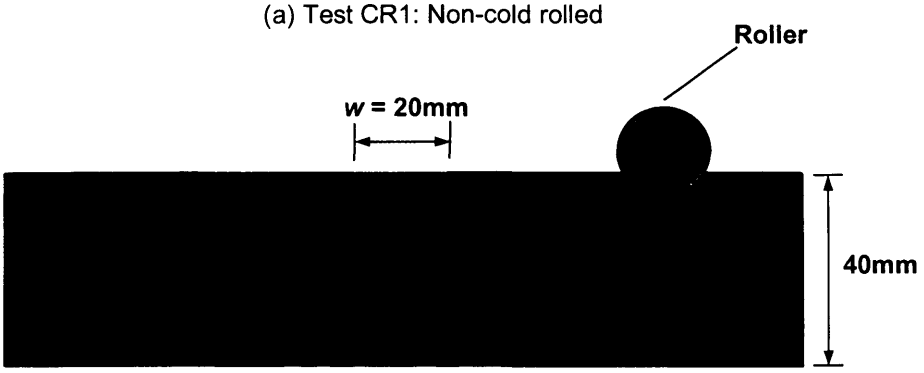

(b) Test CR2: Non-Cold Rolled Length = 20mm, $\frac{w}{2b} = 0.1$

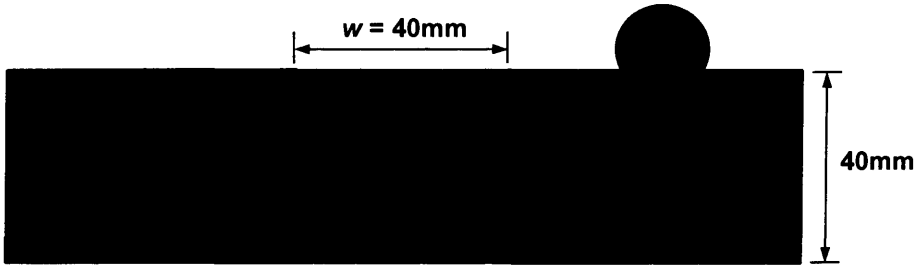

(c) Test CR3: Non-Cold Rolled Length = 40mm, $\frac{w}{2b} = 0.2$

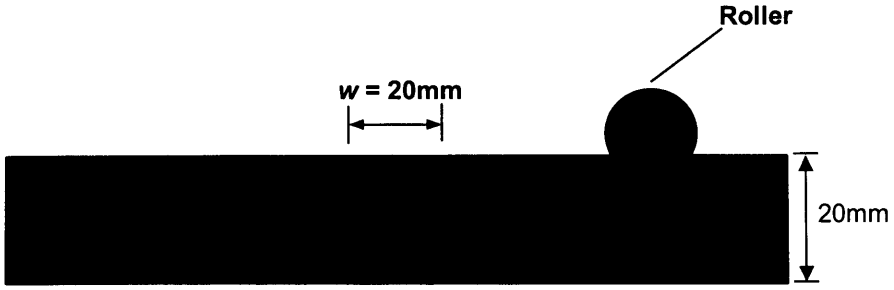

(d)Test CR4 : Non-Cold Rolled Length = 20mm, $\frac{w}{2b} = 0.1$

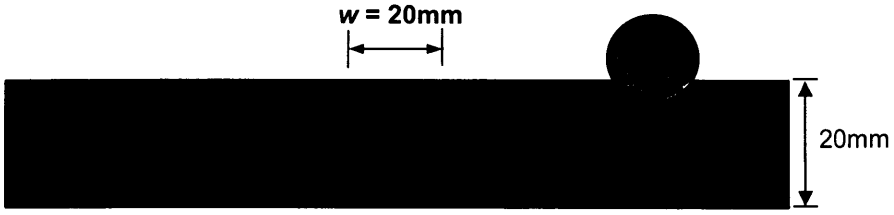

(e) Test CR5: Non-Cold Rolled Length = 20mm, $\frac{w}{2b} = 0.1$

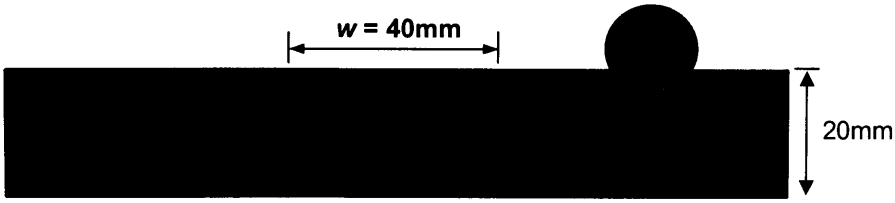

(f) Test CR6: Non-Cold Rolled Length = 40mm, $\frac{w}{2b} = 0.2$

Figure G1: Side views of test specimens with their respective stitch cold rolling parameters

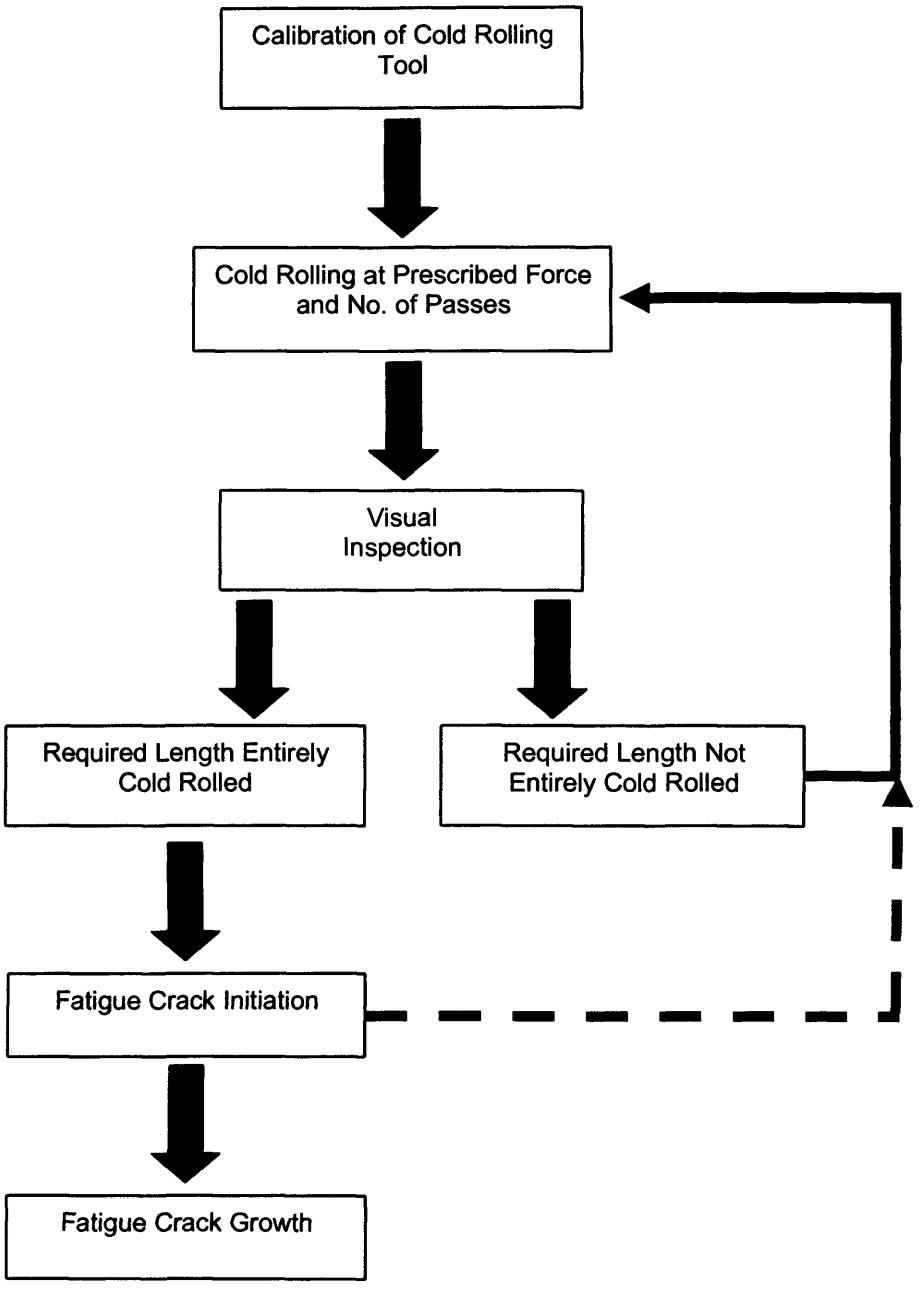

Figure G2: Summarised flow chart of stitch cold rolling procedures

Appendix H

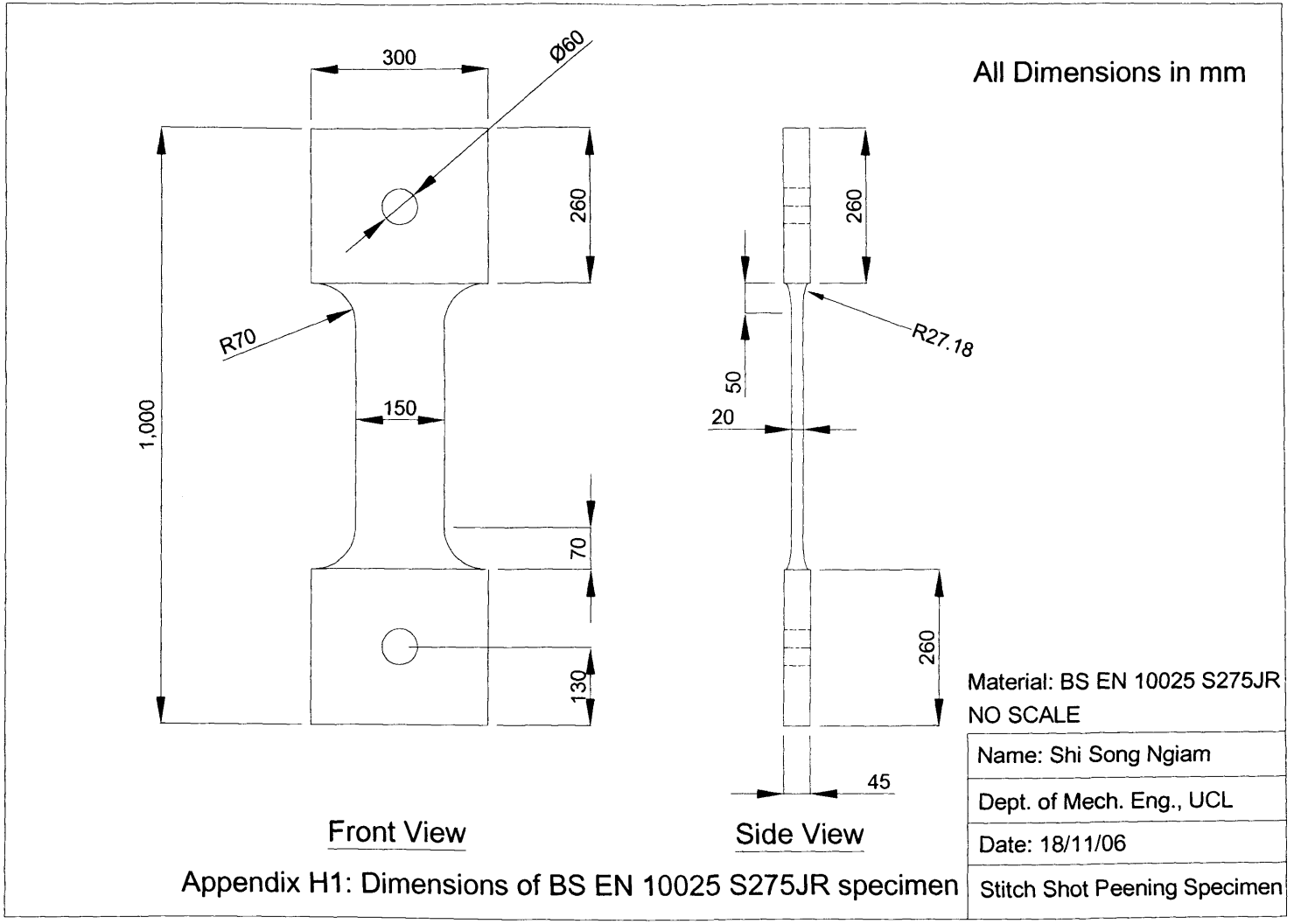

Appendix H1: Dimensions of BS EN 10025 S275JR specimen

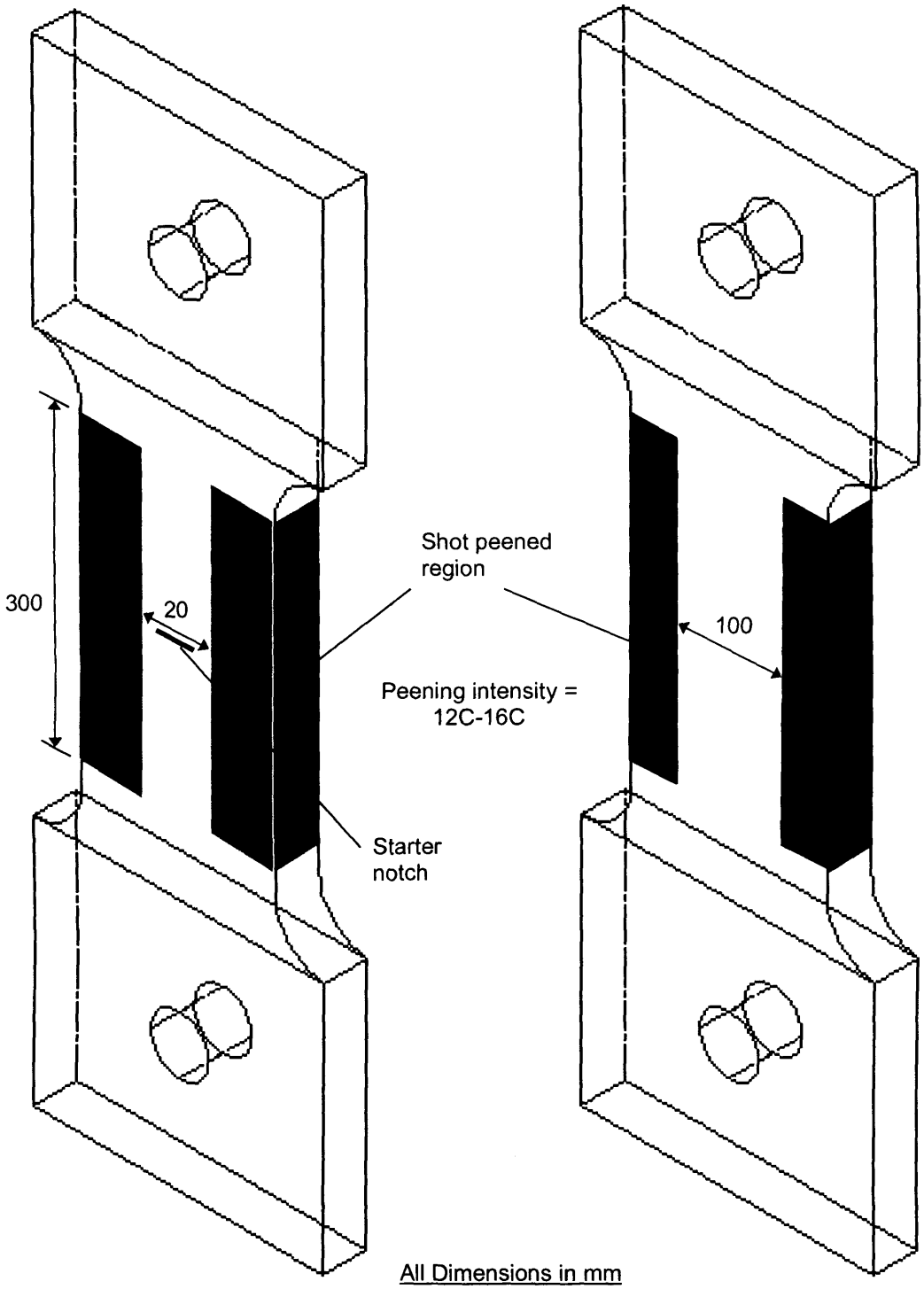
300
20
Shot peened region
100
Peening intensity = 12C-16C
Starter notch
All Dimensions in mm
Front of Specimen
Back of Specimen

(a) Test SP2

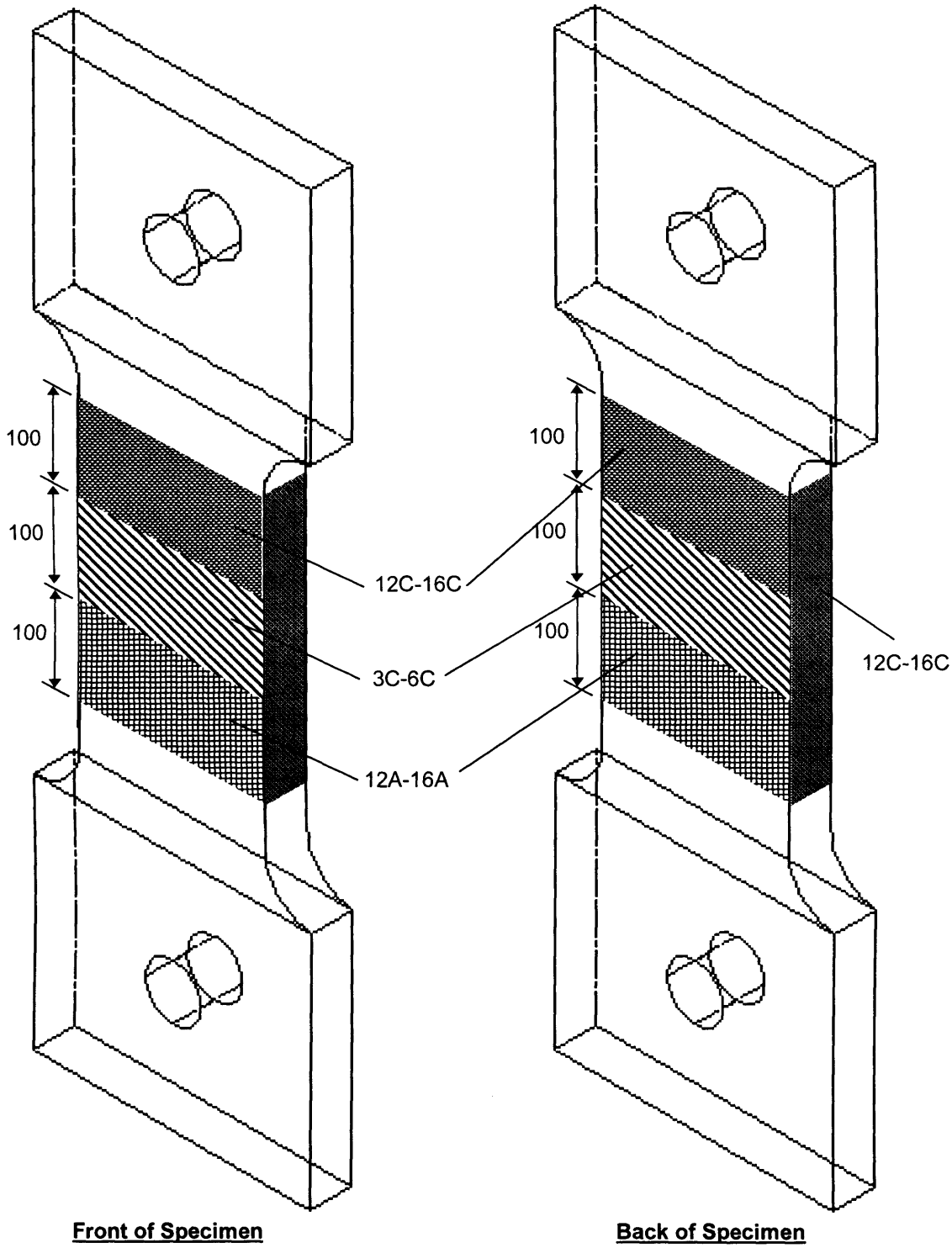

(b) Test SP6

Appendix H2: Examples of stitch shot peened specimen

Item	Specification
Gauge type	CEA-06-062UL-120
Gauge factor	2.04
Gauge length	1.57mm
Resistance	120ohm
r_0	0.875
r_m	2.565
R_2-R_1	1.57

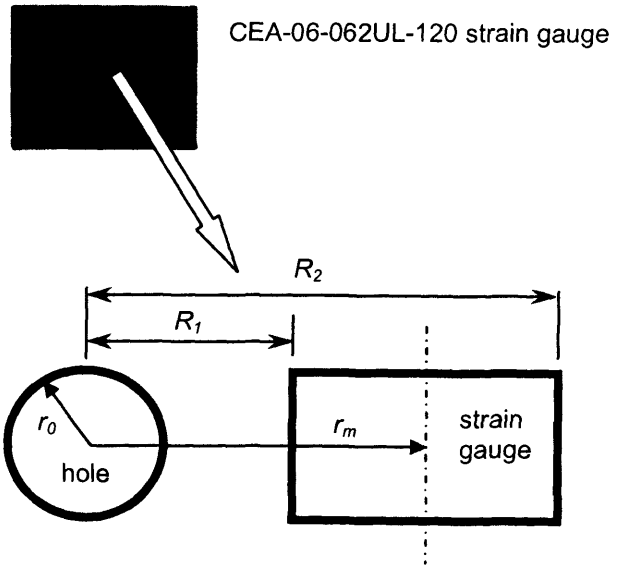

Appendix H3: Specification of CEA-06-062UL-120 residual stress strain gauge [5.13]

Appendix J

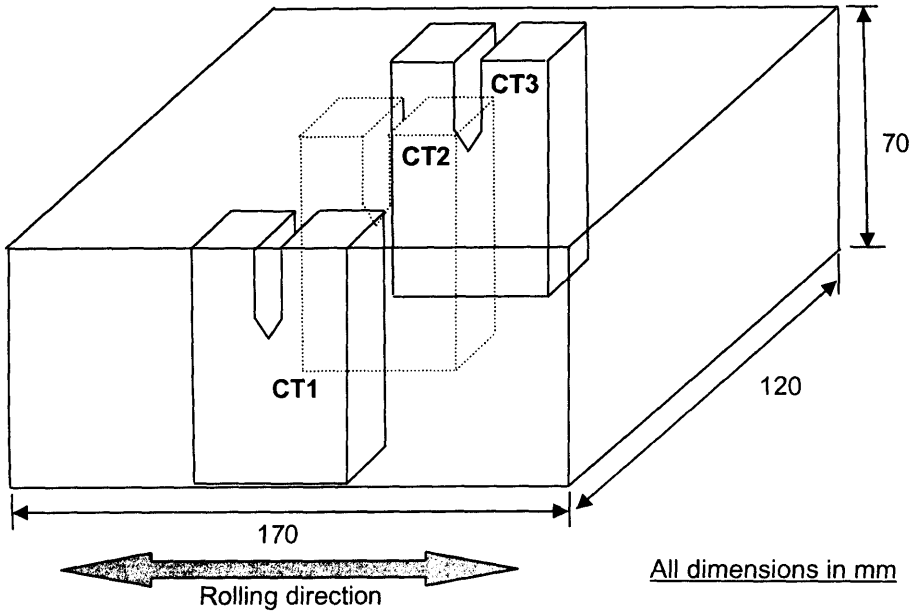

Figure J1: The details of the CT specimen types

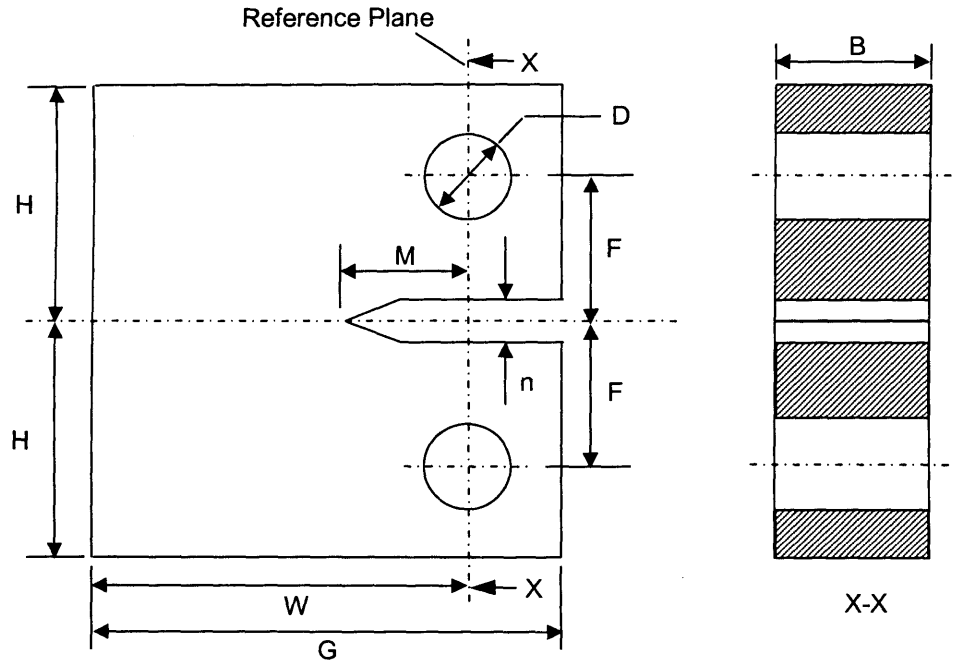

Detail	Size (mm)	Tolerances (mm)
B (thickness)	17.300	±0.15
D	12.100	+0.05
F	13.310	±0.09
G	60.500	±0.15
H	29.040	±0.15
n	3.146	±0.05
M	9.680	±0.05
W	48.400	±0.15

Figure J2: Specifications for the CT specimens according to BS ISO 12108:2002

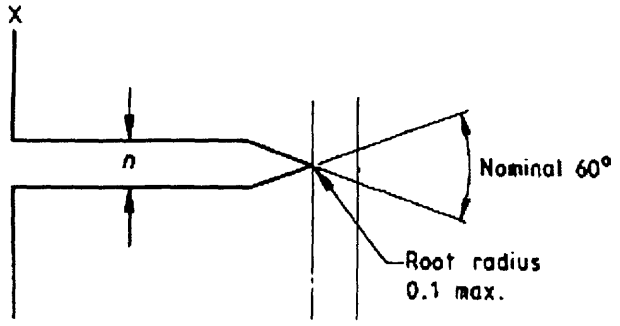

Figure J3: Notch geometry

Appendix K

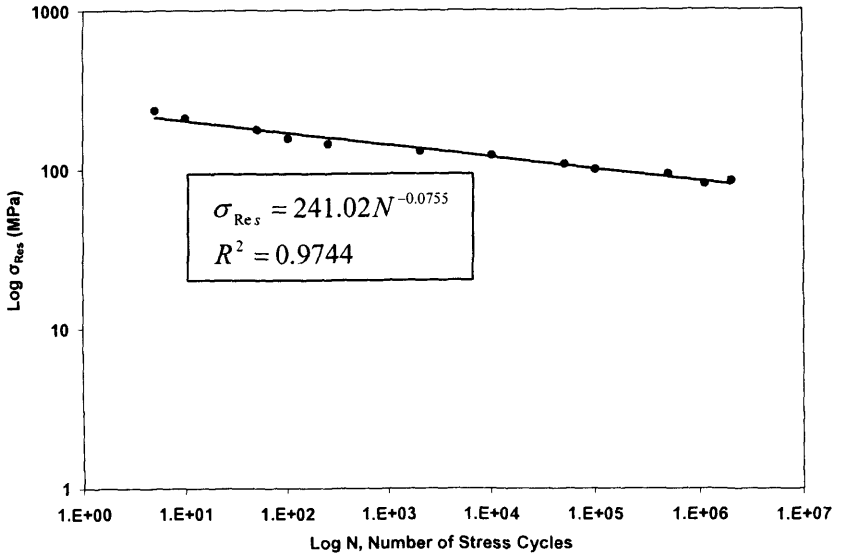

Figure K4: Residual stress relaxation function at hole-depth = 0mm and 0.13mm

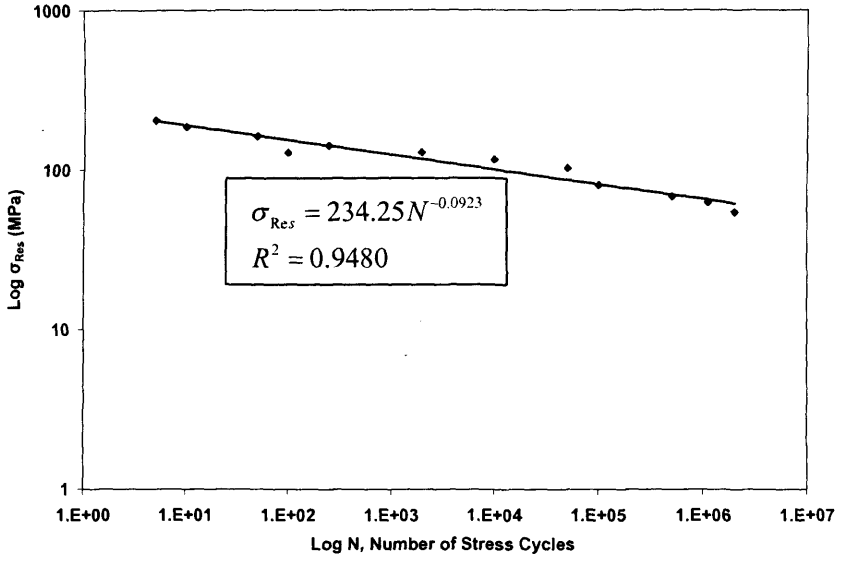

Figure K5: Residual stress relaxation function at hole-depth = 0.25mm

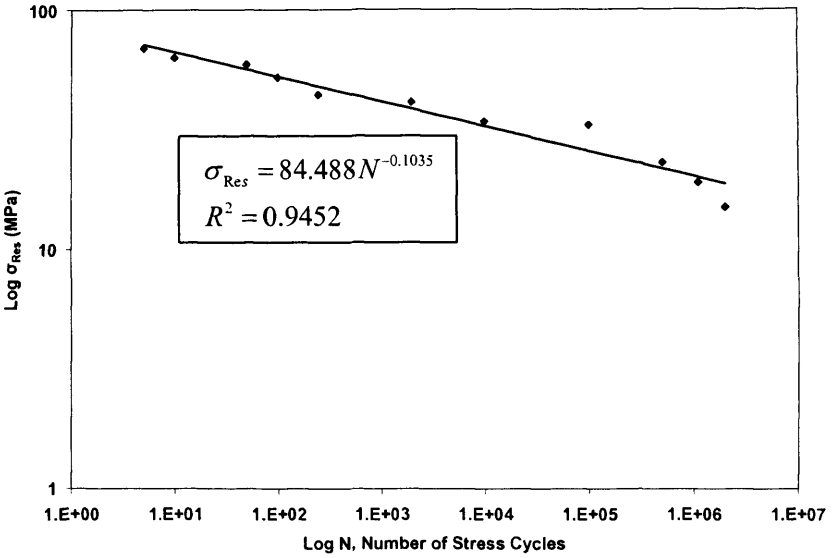

Figure K6: Residual stress relaxation function at hole-depth = 0.375mm

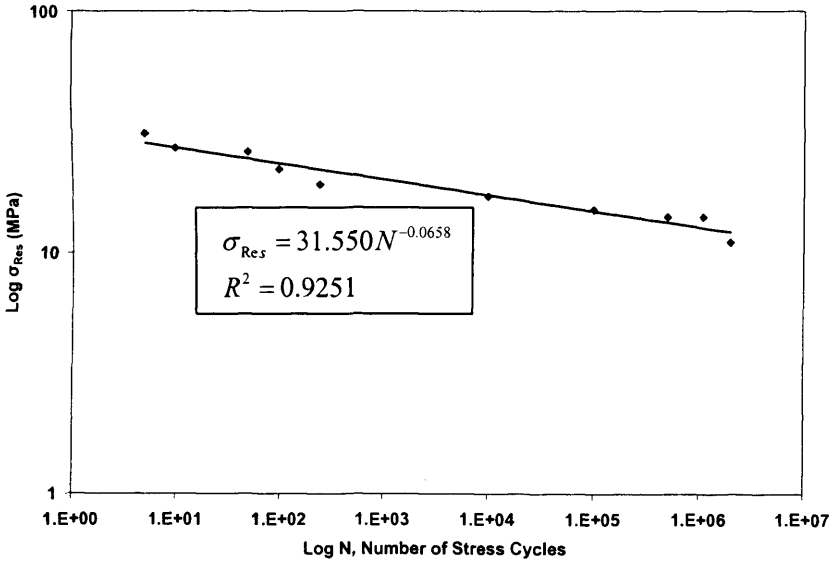

Figure K7: Residual stress relaxation function at hole-depth = 0.5mm

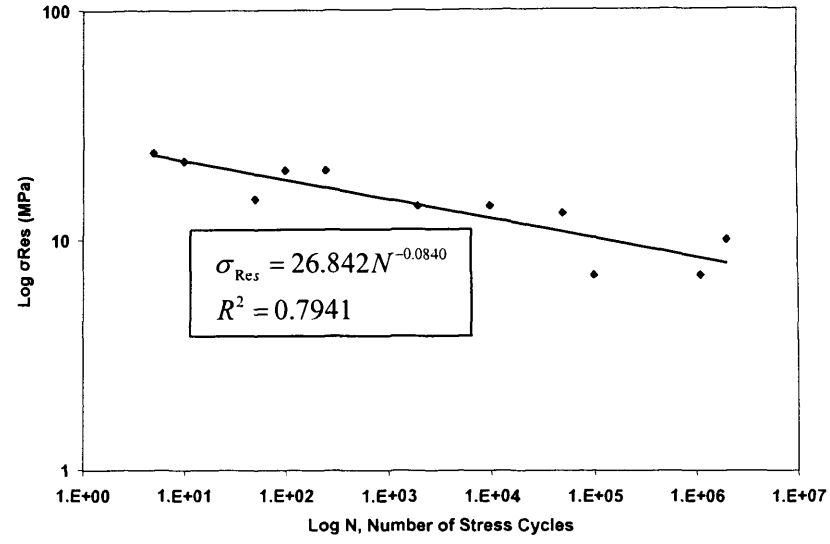

Figure K8: Residual stress relaxation function at hole-depth = 0.625mm

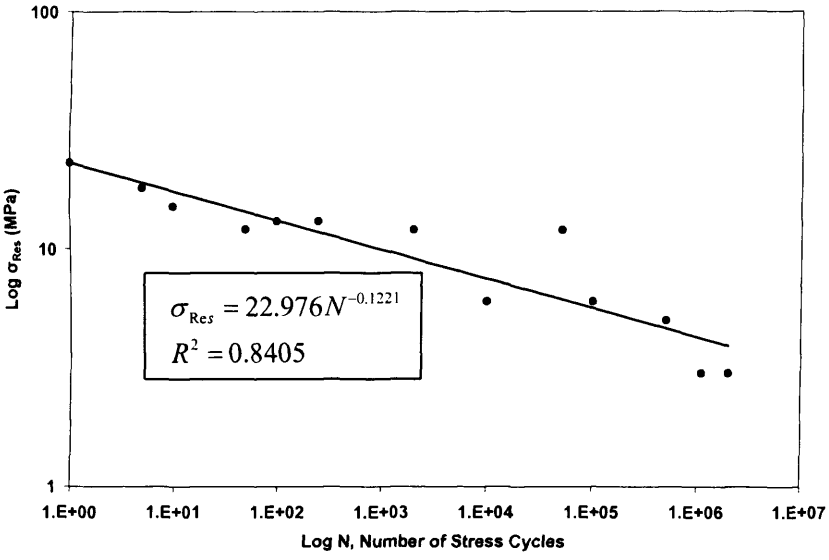

Figure K9: Residual stress relaxation function at hole-depth = 0.75mm